Gold Nanoparticles Used in Cancer Cell Diagnostics, Selective Photothermal Therapy and Catalysis of NADH Oxidation Reaction

A Dissertation
Presented to
The Academic Family

By

Xiaohua Huang

In Partial Fulfillment
Of the Requirements for the Degree
Doctor of Philosophy in Chemistry

Georgia Institute of Technology
May, 2006

Gold Nanoparticles Used in Cancer Cell Diagnostics, Selective Photothermal Therapy and Catalysis of NADH Oxidation Reaction

Approved by:

Dr. Mostafa A. El-Sayed, advisor
Laser Dynamics Laboratory
School of Chemistry and Biochemistry
Georgia Institute of Technology

Dr. Bridgette Barry
School of Chemistry and Biochemistry
Georgia Institute of Technology

Dr. Zhong L. Wang
School of Materials Science and Engineering
Georgia Institute of Technology

Dr. Nicholas Hud
School of Chemistry and Biochemistry
Georgia Institute of Technology

Dr. Z. John Zhang
School of Chemistry and Biochemistry
Georgia Institute of Technology

Data approved: March 31, 2006

This thesis is dedicated to my husband, Xiaobing Yi, who always takes considerate care of me, always loves me in his heart and always be there in my life. Without him, I could not walk through the past four years during my PH. D study and research. He let me realize that I am precious and it is so worthy to live in this world.

ACKNOWLEDGEMENTS

Firstly, I would like to thank my advisor, Dr. Mostafa A. El-Sayed. I appreciate that he gave me the valuable opportunity to come to Georgia Tech and his lab for my PH. D study. I also appreciate that he let me work on this project which I like very much and I can do well on it. During those years in my study and research as a graduate student, I learned a lot from him. He taught me how to become a real scientist. His patience and wisdom impressed me very much. Instead of blaming, he always encouraged and helped me when I was not doing well on experiments, papers and presentations. I really appreciate his support and advisements from my heart. Without him, I could not achieve so much today. Secondly, I would like to express my sincere gratitude to Dr Ivan H. EL-Sayed, son of Dr EL-Sayed and also a surgeon and an assistant professor in Department of Otolaryngology-Head and Neck Surgery, Comprehensive Cancer Center, University of California at San Francisco. He not only provided cell lines for the research, but also he taught me the cell culture technique and much knowledge on molecular biology. Without him, I could not start my research. I also appreciate him for his patience and confidence in me and so many valuable discussions on our experiments. Thirdly, I would like to thank Prof Paul Edmonds in the Department of Biology at Georgia Tech, who provided the cell culture facilities for our experiments. He is so unselfish and so kind. Without him, I can not carry on my experiments. In addition, I would like to thank Dr Randall H. Kramer, who is so kind and let me use his lab without conditions when I visited UCSF. I also like to thank Dr Mohan Srinivasarao who let me use his micro-absorption spectrometer, micro-Raman spectrometer and the confocal microscope at any time. I also want to thank Dr Robert M. Dickson who let us use his dark field microscope at the

beginning of our project and his former students, Mr Jie Zheng, Ms Lynn Peyser and Mr Sandeep Patel for the help on the dark field imaging.

In addition, I would like to thank Laurie Sanni, who was a former student in our lab. She is so nice and so helpful at any time. When I came to the lab, it was her who taught me everything and let me acquaint myself with the lab. Whenever I asked for her help, she was always trying to help me out without any consideration. I also like to thank Prashant for his help on the calculation about my experimental results. Other lab members, including Dr Qian Wei, Wenyu Huang, Alexander Schill, Qusai Darugar, Susie Eustis and Christopher Tabor and former lab member Radha Narayanan are all acknowledged for their help.

Finally, I would like to thank my dear husband, Xiaobing Yi who always loves and supports me at any time. I also want to thank my father, Mingxue Huang and mother, Jiayu Zhou, my three sisters, Lihua Huang, Shuhua Huang, Junhua Huang and my brother, Xinghua Huang for their support on my study.

TABLE OF CONTENTS

LIST OF TABLES

LIST OF FIGURES

SUMMARY OF THE DISSERTATION

This thesis is aimed at exploring the application of gold nanoparticles in cancer cell diagnostics and therapy. Cancer is a public leading cause of death in the world. Searching for efficient method of diagnostics of cancer and selective therapy are extremely active field today. With the great development of nanotechnology, various nanoparticles in different structures, shapes and composites provides good potential for their application in cancer diagnostics and therapy. Compared to other nanoparticles, gold nanoparticles have great advantages in cancer applications due to their easy preparation, efficient bioconjugation, potential noncytotoxicity, tunable and enhanced scattering and absorption properties. The strong scattering of gold nanoparticles provides an opportunity for their use in cancer cell imaging. Their strong absorption provides a possibility for them to be used in photothermal therapy. In this thesis, we will show that both gold nanospheres and gold nanorods can be used as molecular contrast agents for dual efficient cancer diagnostics and selective photothermal therapy.

Gold nanospheres of 40 nm in diameter were synthesized by the citrate reduction method. The nanospheres were conjugated to anti-epidermal growth factor receptor (anti-EGFR) monoclonal antibodies and then incubated with a nonmalignant epithelial cell line (HaCat) and two malignant oral epithelial cell lines (HOC 313 clone 8 and HSC 3). The cells were imaged under dark field at 100x using an inverted IX70 Olympus microscope. The absorption spectra of gold nanoparticles on single cells were measured using a SEE1100 micro-spectrometer. The dark field light scattering images show distinct

difference between the cancerous and noncancerous cells due to the overexpression of the EGFR on the cancer cells. The anti-EGFR antibody conjugated nanoparticles specifically and homogeneously bind to the surface of the cancer cells with higher affinity than to the noncancerious cells. The peak position of the surface plasmon absorption spectra of gold nanoparticles also show difference between cancer and noncancer cells due to the difference in the dielectric constant of the surrounding environment on the surface of the gold nanoparticles.

After the incubation with anti-EGFR/gold conjugates, the cells were exposed to a cw argon ion laser at 514 nm. Due to the overloading of gold nanoparticles on the cancer cells, it is found that the malignant cells require less than half the laser energy to be killed than the healthy cells. No photothermal destruction is observed for all types of cells in the absence of nanoparticles at four times the energy required to kill the malignant cells with ant-EGFR/Au. This demonstrates that gold nanospheres can be used as a novel class of selective photothermal agents using a cw laser at low powers in the visible region.

By oven-heating experiment, it is found that cells without nanoparticles are thermally destroyed between 70 – 80 ^{o}C. This temperature is found to be in agreement with the calculation results by Prashant (another member in our group) from the amount of gold loading at the threshold laser power.

For clinical application of treating cancer in vivo under the skin, it is necessary to use nanoparticles absorbing in the near infrared (NIR) region of the radiation spectrum to minimize the light extinction by intrinsic chromophores in native tissue. Gold nanorods with suitable aspect ratios (length divided by width) can be synthesized which absorb and

scatter strongly laser light in the NIR region (650-900 nm). Thus gold nanorods were synthesized by the seed-mediated growth method and conjugated to anti-epidermal growth factor receptor (anti-EGFR) monoclonal antibodies and incubated in cell cultures with the cancer and healthy cells. Like the nanospheres, the anti-EGFR antibody conjugated nanorods bind specifically to the surface of the malignant type cells with a much higher affinity due to the overexpressed EGFR on the cytoplasmic membrane of the malignant cells. As a result, they strongly scattered red light from gold nanorods in dark field using a laboratory microscope, the malignant cells are clearly visualized and distinguished from the nonmalignant cells.

It is found that malignant cells require half the laser energy to be photothermally destroyed than the nonmalignant cells if exposed to a continuous Ti:Sapphire laser at 800 nm. Compared to other contrast agents for photothermal therapy in NIR region such as Si/Au nanoshell and carbon nanotubes, solid gold nanorods have several advantages. The synthesis of gold nanorods with various aspect ratios, which enable tunable absorption wavelength in NIR is quite simple and well-established. The size of the nanorods needed is quite small and is potentially useful in applications such as drug delivery and gene therapy. In addition, the biosafety of gold nanorods has been proven is well known and they have been used in vivo since the 1950's. Recently the noncytotoxicity of gold nanoparticles in human cells has been studied in detail by Wyatt et al.

The addition of gold nanoparticles is found to quench the NADH fluorescence intensities but has no effect on the fluorescence lifetime. This suggested that the fluorescence quenching is not due to coupling with the excited state, but due to changing

the ground state of NADH. In support of this, the intensity of the 340 nm absorption band of NADH is found to decrease while that of the 260 nm band of NAD^+ is found to increase as the concentration of gold nanoparticles increase. This conversion reaction is further supported by nuclear magnetic resonance and mass spectroscopy. The linear dependence of the initial reaction rate of NADH on the concentration of gold nanoparticles gives strong support that the conversion of NADH to NAD^+ is occurring on the surface of the gold nanoparticles, i.e. NADH is surface catalyzed by the gold nanoparticles.

CHAPTER 1
INTRODUCTION

When the size of a material is reduced to the nanometer length scale (which is the length scale of the electronic motion that determines the material's properties), its electronic and thus chemical properties change tremendously. In semiconductor nanoparticles, the property change results from quantum confinement of the electronic motion (1). In metals, the properties of the surface become dominant and give nanoparticles new properties (2). In noble metals the coherent collective oscillation of electrons in the conduction band induces large surface electric fields which greatly enhance the radiative properties of gold and silver nanoparticles when they interact with resonant electromagnetic radiation (3). This makes the absorption crossection of these nanoparticles orders of magnitude stronger than the strongest absorbing molecules (4) and the scattered light becomes orders of magnitude more intense than the fluorescence of organic dyes (5). These unique properties provides great potential for the nanoparticles to be used in many applications, such as biochemical sensors (6), biological imaging and medial therapeutics (7-12) as well as in catalysis because of their high surface-to-volume ratios (13-14).

1.1 Important properties of gold nanoparticles

1.1.1 Surface plasmon absorption property of gold nanoparticles

Gold nanoparticles show a strong absorption band in the visible region when the frequency of the electromagnetic field is resonant with the coherent electron motion, which is called surface plasmon resonance absorption (15). The surface plasmon

absorption results from the dipole oscillations of the free electrons with respect to the ionic core of a spherical nanoparticle (16). A net charge difference is shown on the nanoparticle surface when interaction with an electric field which results in a polarization of the electrons with respect to the ionic core of a nanoparticle (see Figure 1).

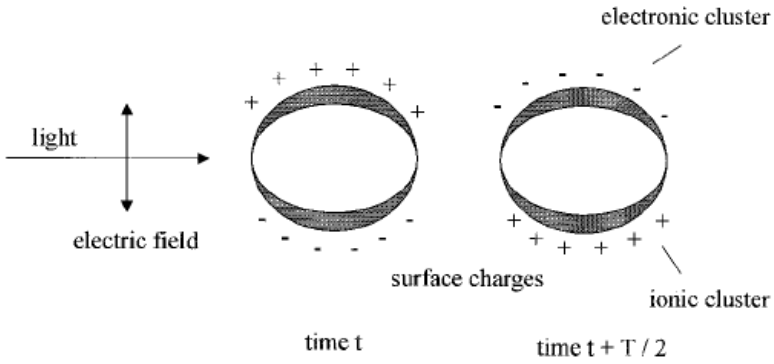

Figure 1-1: A scheme of surface plasmon absorption of spherical nanoparticles illustrating the excitation of the dipole surface plasmon oscillation (16).

This induces a dipolar oscillation of all the electrons in the same phase. When the frequency of the electromagnetic field becomes resonant with the coherent electron motion, a strong absorption band around 520 nm in the spectrum is observed (Figure 1-2), which is the origin of the observed brilliant color of the nanoparticles in solution.

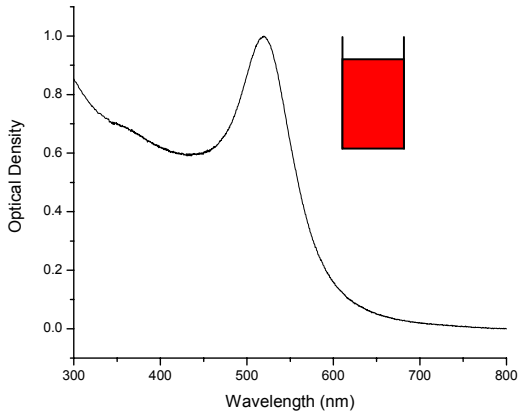

Figure 1-2: Typical surface plasmon absorption spectrum of spherical nanoparticles. Strong absorption band around 520 nm in the spectrum is the origin of the observed red color of the nanoparticle solution.

Mie (17) is the first to explain the surface plasmon resonance behavior of the spherical metal nanoparticles. He solved maxwell's equation for an electromagnetic light wave interactiong with a small sphere. For nanoparticles much smaller than the wavelength (< 20nm), only the dipole oscillation contributes significantly to the extinction cross section and thus Mie's theory reduced to the following equation:

$$\sigma_{ext}(\omega) = 9\frac{\omega}{c}\varepsilon_m^{3/2} V \frac{\varepsilon_2(\omega)}{[\varepsilon_1(\omega)+2\varepsilon_m]^2+\varepsilon_2(\omega)^2}, \quad (1\text{-}1)$$

Where V is the particle volume, x is the angular frequency of the exciting light, c is the speed of light, and ε_m and $\varepsilon(\omega) = \varepsilon_1(\omega) + i\ \varepsilon_2(\omega)$ are the dielectric functions of the surrounding medium and the material itself respectively. The resonance condition if fulfilled when is $\varepsilon_1(\omega) = -2\ \varepsilon_m$ if ε_2 is small or weakly dependent on ω. But for larger nanoparticles, the light can not polarize the nanoparticles homogeneously and retardation effects lead to the excitation of higher-order modes (2).

From equation (1-1), it can be seen that the peak intensity and position of the surface plasmon absorption band is dependent on the size and shape of the metal nanoparticles as well as the dielectric constant of the metals as well as the medium surrounding the particles (18). As the size increases, the absorption maximum is red shifted slightly (See Figure 1-3). The bandwidth also changes when the sizes changes. Link and El-Sayed (4) have shown that the bandwidth decreases with the increase of the nanoparticles size when the nanoparticles are less than 20 nm in diameter (Figure 1-4, left) and the bandwidth increases with the increase of the nanoparticle size when the nanoparticles are larger than

20 nm. He also found that the absorption coefficient is linearly dependent on the volume of the nanoparticles which is in agreement with the Mie theory (17).

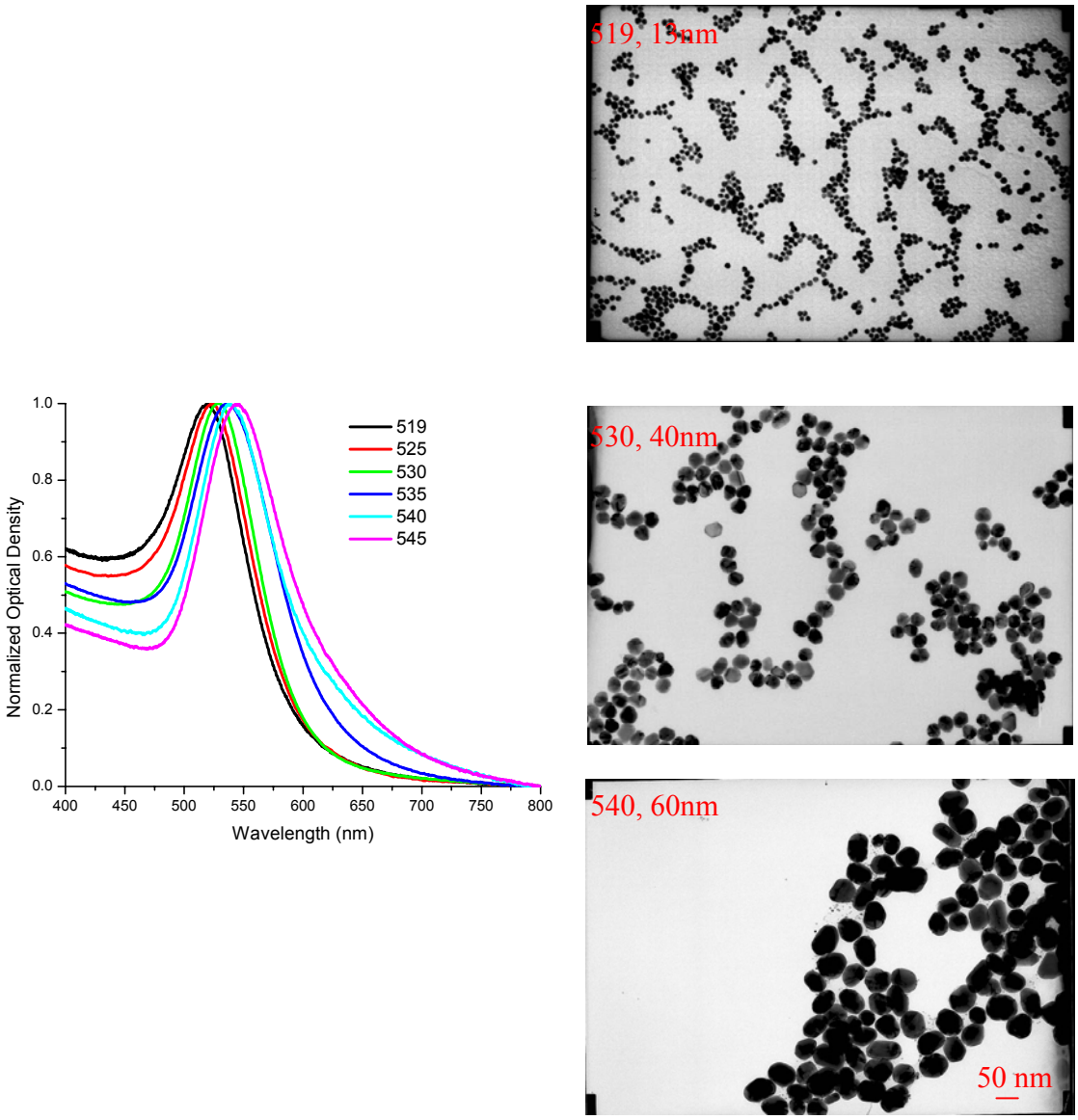

Figure 1-3: Surface plasmon absorption spectra (left) and TEM (right) of spherical gold nanoparticles in different sizes. The surface plasmon absorption maximum is weakly dependant on the size of the nanospheres.

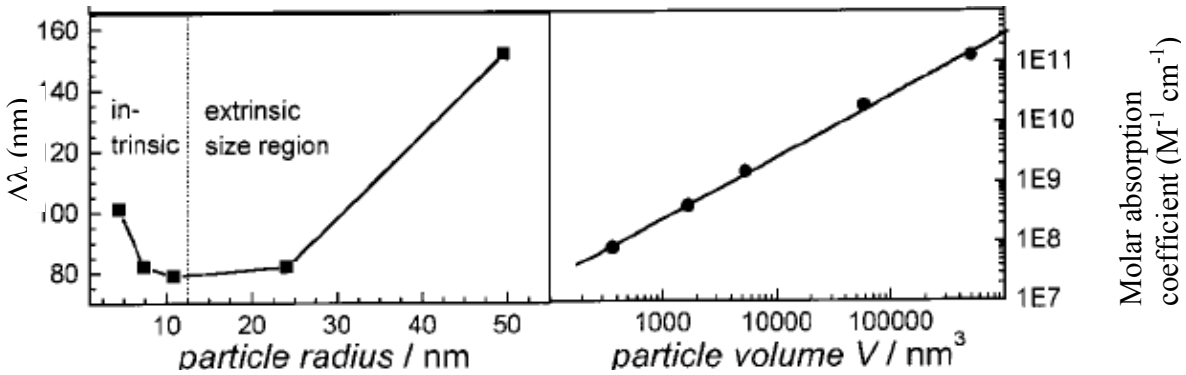

Figure 1-4: Left: the relationship of the absorption bandwidth with the size of the nanoparticles; Right: the relationship of the absorption coefficient with the size of the nanoparticles (4). The bandwidth increases with decreasing nanoparticle radius in the intrinsic size region and also with increasing radius in the extrinsic size region as predicted by Mie theory. The extinction coefficients of these gold nanoparticles against their volume show a linear dependence (4).

When the shape of the nanoparticles changes from nanosphere to nanorods, the surface plasmon absorption spectrum also changes. Figure 1-5 shows a typical absorption spectrum of nanorods. The surface plasmon absorption of gold nanorods have two bands: a strong long wavelength band in the near infrared region due to the longitudinal oscillation of electrons and a weak short wavelength band in the visible region around 520 nm due to the transverse electronic oscillation.

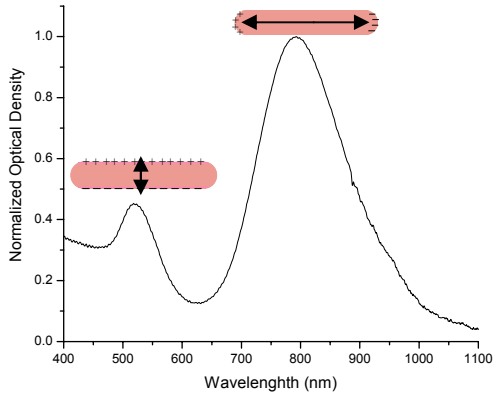

Figure 1-5: Typical surface plasmon absorption spectrum of gold nanorods. The strong long wavelength band in the near infrared region around 800 nm is due to the longitudinal oscillation of electrons and the weak short wavelength band in the visible region around 520 nm is due to the transverse electronic oscillation.

The optical absorption spectrum of gold nanorods with aspect ratio *R* can be modeled using an extension of the Mie theory. Within the dipole approximation according to the Gans (19) treatment, the extinction cross-section *r*ext for elongated ellipsoids is given by the following equation (20):

$$\sigma_{\text{ext}} = \frac{\omega}{3c}\varepsilon_{\text{m}}^{3/2} V \sum_j \frac{(1/P_j^2)\,\varepsilon_2}{\{\varepsilon_1 + [(1-P_j)/P_j]\,\varepsilon_{\text{m}}\}^2 + \varepsilon_2^2}, \tag{1-2}$$

Where *Pj* are the depolarization factors along the three axes *A*, *B* and *C* of the nanorod. with $A > B = C$, defined as

$$P_A = \frac{1-e^2}{e^2}\left[\frac{1}{2e}\ln\left(\frac{1+e}{1-e}\right) - 1\right], \tag{1-3}$$

$$P_B = P_C = \frac{1-P_A}{2},$$

and the aspect ratio *R* is included in *e* as follows:

$$e = \left[1 - \left(\frac{B}{A}\right)^2\right]^{1/2} = \left(1 - \frac{1}{R^2}\right)^{1/2}. \tag{1-4}$$

Different from spherical nanoparticles, the absorption spectrum of the gold nanorods is very sensitive to the aspect ratio (length/width). Figure 1-6 shows experimentally how the absorption maximum of the nanorods shifted with the aspect ratios. When the aspect ratio increases, the absorption maximum of the longitudinal band is greatly red shifted. The absorption difference of the longitudinal band caused the color difference of the nanorod solution. For short nanorods with the longitudinal maximum lower than 700 nm, the

nanorods appear in blue color. When the longitudinal maximum is between 700 nm and 800nm, the solution appears in deep red color and the nanorods with longitudinal maximum larger than 800 nm, the nanorods appears in pink color. Figure 1-7 shows theoretically the changes of the absorption intensity and the position with the change of the dimension of the nanorods (21) according to equation (1-2). From Figure 1-7, it can be seen that with the increase of the aspect ration, the absorption intensity increases.

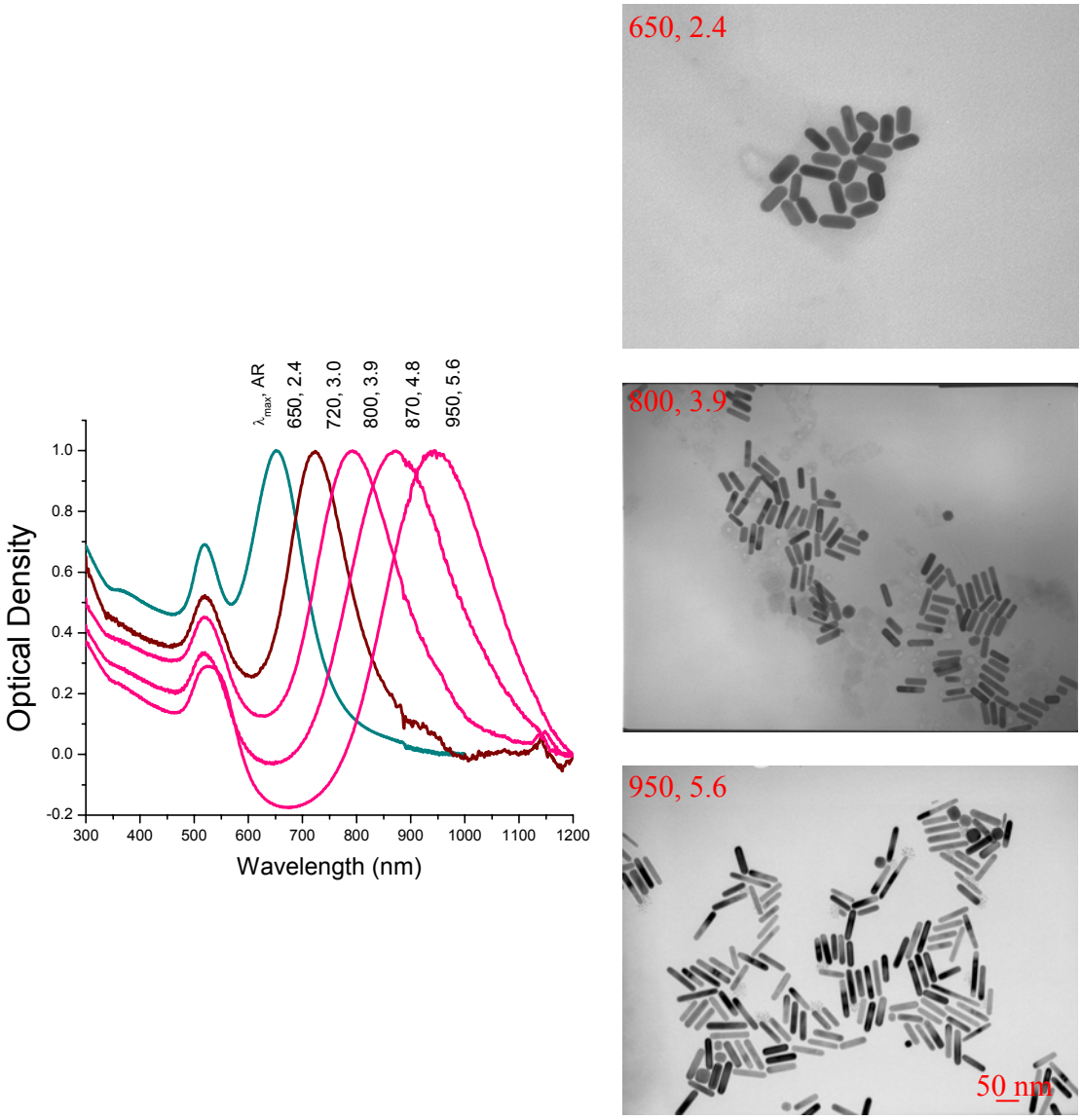

Figure 1-6: The absorption spectra of gold rods of different aspect ratios (left) and TEM of the rods with aspect ratios at 2.4, 3.9 and 5.6.

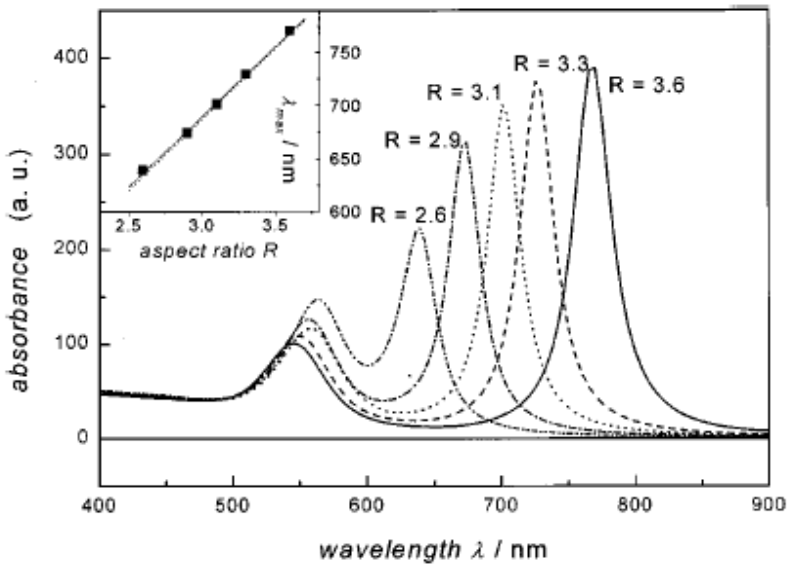

Figure 1-7: Calculated absorption spectra of elongated ellipsoids with varying aspect ratios *R* according to equation (1-2). (21).

From the inset of Figure 1-7, it can be seen that the absorption maximum of the longitudinal band is linearly dependant on the aspect ratio of the nanorods while there is no change on the transverse band. This gives a simple guess of the aspect ratio according to the known absorption maximum without TEM experiments.

Due to the strong surface plasmon absorption, gold nanoparticles offer great potential in photothermal therapy applications. It has been found that the strong absorbed radiation is converted efficiently into heat on a picosecond time domain due to electron-phonon and phonon-phonon processes (18). Thus, upon the laser irradiation at the surface plasmon absorption band, the nanoparticles absorb photon energy and then immediately transfer into heat energy. If the nanoparticles are incorporated or incubated with biomolecules, cells or tissues, this heat energy will cause the sharp increase on the local temperature around the nanoparticles and thus cause the damage of the surrounding materials. This photothermal destruction can be used for disease or cancer therapy.

Compared to the strongly absorbing Rhodimine 6G (ε = 1.16 x 10^5 M^{-1} cm^{-1} at 530 nm (22)) dye molecules, gold nanoparticles absorb about 10^3 stronger (for nanospheres of 40 nm in diameter, ε = 2.74 x 10^9 M^{-1} cm^{-1} at 530 nm, (4)). Thus gold nanoparticles provide a novel class of photo-absorber in medical applications.

For clinical application of treating cancer in vivo under the skin, one need to use near infrared (NIR) laser light which has larger penetration depth. Light in the region between 650 – 900 nm has a penetration depth of at least several centimeters depending on the types of the tissue (23). From Figure 1-6 we can see that the gold nanorods absorb strongly in the NIR region. This offers the great opportunity for the nanorods to be used as the photo-absorbers in NIR and realize photothermal therapy.

1.1.2 Surface plasmon light scattering property of gold nanoparticles

It is known that gold particle suspensions scatter colored light when illuminated by a beam of white light (24). The light-scattering gold nanoparticle suspensions have the same appearance as fluorescent solutions as shown in Figure 1-8 (5).

The light scattering is sensitive to the size, shape and the composite of the nanoparticles. Nanoparticles with 58 nm in diameter scatter green light while 78 nm in diameter scatter yellow light (Figure 1-8, b and c) while gold nanorods scatter red light under illumination of a beam of white light (Figure 1-9, (25)). Figure 1- 10 shows how the scattered light is different for compositions and shapes (26).

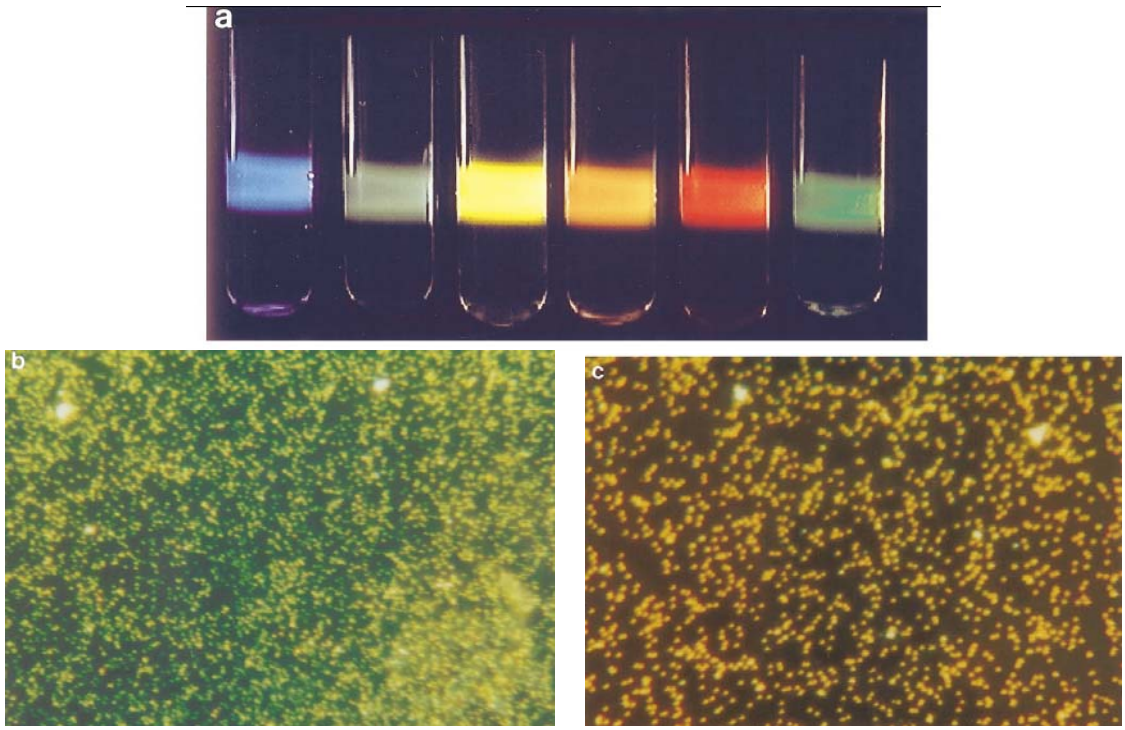

Figure 1-8: a: the gold nanoparticles of different sizes irradiated by a beam of white light, b: the light scattering imaging of 58 nm gold nanoparticles, c: the light scattering imaging of 78 nm gold nanoparticles (5).

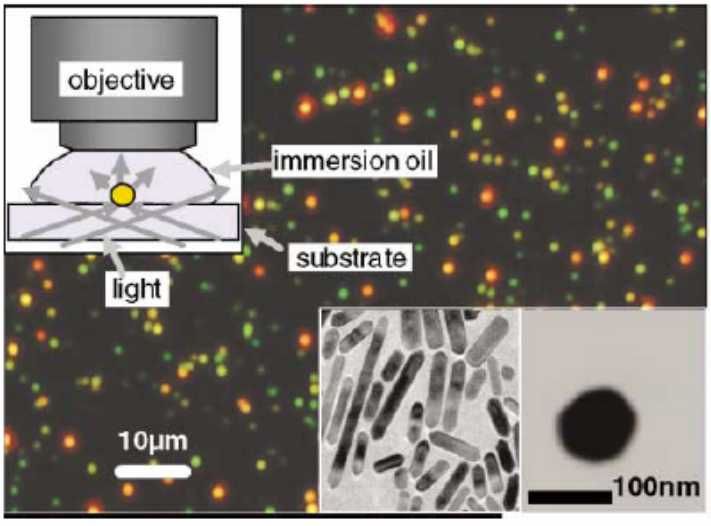

Figure 1-9: True color photograph of a sample of gold nanorods (red) and 60 nm nanospheres (green) in dark-field illumination (inset upper left). Bottom right: TEM images of a dense ensemble of nanorods and a single nanosphere (25).

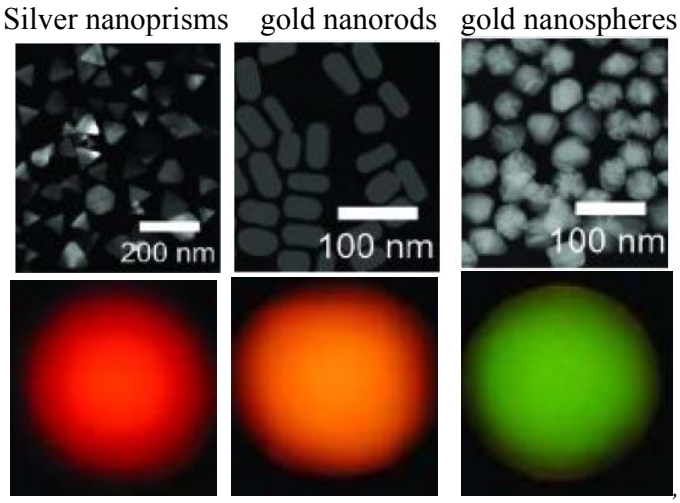

Figure 1-10: Light scattering of silver nanoprisms, gold nanorods, and gold nanospheres (26).

Juan Yguerabide and Evangelina E. Yguerabide (5) have presented the theory of the light-scattering properties. The light scattering intensity is described by equation (1-5), which depends on the detection direction of the scattered light. The light scattering cross section is defined by the express in equation (1-6).

$$I = \frac{16\pi^4 a^6 n_{\text{med}}^4 I_0}{r^2 \lambda_0^4} \left| \frac{m^2 - 1}{m^2 + 2} \right|^2 \sin^2(\alpha), \tag{1-5}$$

$$C_{\text{sca}} = \frac{128\pi^5 a^6 n_{\text{med}}^4}{3\lambda_0^4} \left| \frac{m^2 - 1}{m^2 + 2} \right|^2, \tag{1-6}$$

Where a is the particle radius, n_{med} is the refractive index of the medium surrounding the particle, I_0 is the intensity of the incident monochromatic light, m is the relative refractive index of the bulk particle material, α is the angle between the detection direction **r** and the incident beam, λ_0 is the wavelength of the incident beam and Im is the imaginary part of the complex expression within the parenthesis.

From equation (1-5 and 1-6), we can see that the light scattering power is proportional to the sixth power of the particle radius. Thus by changing the size of the nanoparticles, the strength and the light scattering profile can be tuned. Figure 1-11 shows the normalized light scattering profile of the gold nanospheres in different sizes and Table 1-1 shows the relative strength of the light scattering of these particles. Thus, by changing the size of the gold nanoparticles, light scattering color and power can be tuned.

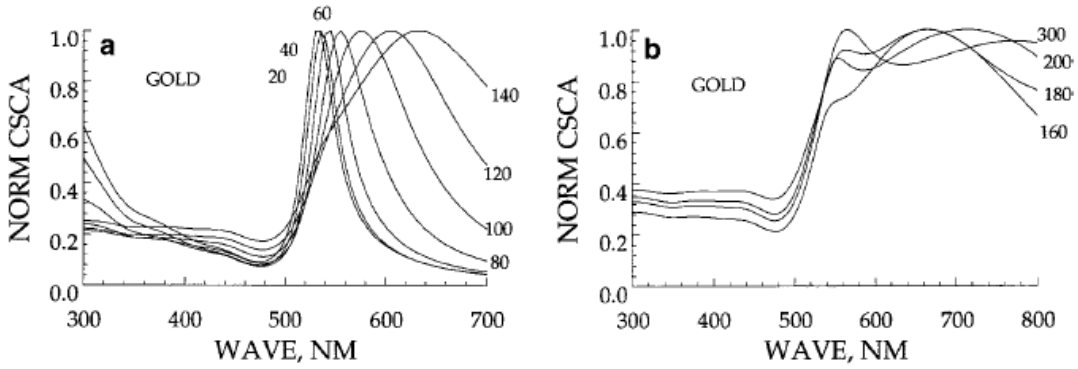

Figure 1-11: Calculated light scattering cross section vs wavelength for homogeneous, spherical gold particles with different diameters (23).

Table 1-1: Comparison of calculated intensity of light Scattered at 90° by gold particles illuminated with monochromatic (I_u) and white unpolarized Light ($I_{u,INT}$) (19).

Diameter (nm)	$I_{U,INT}(90)$	$I_U(90)^a$
20	1	1
40	71.3	72.5
60	859	973
80	4.42×10^3	5×10^3
100	1.33×10^4	1.5×10^4
120	2.74×10^4	3.1×10^4
140	4.34×10^4	4.92×10^4
160	5.79×10^4	6.56×10^4
180	7.15×10^4	8.1×10^4
200	8.3×10^4	9.4×10^4
300	1.76×10^4	2×10^4

Lu et al. (27) theoretically derived the resonant light scattering cross section of gold nanorod according to the quasi-static theory, shown in equation (1-7) (27):

$$\sigma_{sca} = \frac{128\pi^5 a^2 b^4}{3\lambda^4}|A + iB| \tag{1-7}$$

Where

$$A = \frac{\begin{array}{c} n_x^2(\varepsilon_2^4(n_x-1)^2 + 2\varepsilon_{1r}^3\varepsilon_2(1-2n_x)n_x + (\varepsilon_{1r}^4+\varepsilon_{1i}^4)n_x^2 - 2\varepsilon_{1r}\varepsilon_2(2n_x-1)(\varepsilon_2^2(n_x-1)+\varepsilon_{1i}^2 n_x) \\ +\varepsilon_2^2\varepsilon_{1i}^2(2n_x^2-2n_x-1) + \varepsilon_{1r}^2(2\varepsilon_{1i}^2 n_x^2 + \varepsilon_2^2(1-6n_x+6n_x^2))) \end{array}}{((\varepsilon_2+\varepsilon_{1r}n_x-\varepsilon_2 n_x)^2 + (\varepsilon_{1i}n_x)^2)^2} \tag{1-8}$$

$$B = \frac{\begin{array}{c} n_y^2(2\varepsilon_2^3\varepsilon_{1i}(n_y-1) + \varepsilon_2^4(n_y-1)^2 + 2\varepsilon_2\varepsilon_{1i}^3 n_y + 2\varepsilon_{1r}^3\varepsilon_2(1-2n_y)n_y + (\varepsilon_{1r}^4+\varepsilon_{1i}^4)n_y^2 \\ -2\varepsilon_{1r}\varepsilon_2(2n_y-1)(\varepsilon_2\varepsilon_{1i}+\varepsilon_2^2(n_y-1)+\varepsilon_{1i}^2 n_y) + \varepsilon_2^2\varepsilon_{1i}^2(2n_y^2-2n_y-1) \\ +\varepsilon_{1r}^2(2\varepsilon_2\varepsilon_{1i}n_y + 2\varepsilon_{1i}^2 n_y^2 + \varepsilon_2^2(1-6n_y+6n_y^2)))((\varepsilon_2+\varepsilon_{1r}n_x-\varepsilon_2 n_x)^2 + (\varepsilon_{1i}n_x)^2)^2 + 2\varepsilon_2\varepsilon_{1i}n_x^2(\varepsilon_2^2(n_x-1) \\ +(\varepsilon_{1r}^2+\varepsilon_{1i}^2)n_x + \varepsilon_{1r}(\varepsilon_2-2\varepsilon_2 n_x))((\varepsilon_2+\varepsilon_{1r}n_y-\varepsilon_2 n_y)^2 + (\varepsilon_{1i}n_y)^2)^2 \end{array}}{((\varepsilon_2+\varepsilon_{1r}n_x-\varepsilon_2 n_x)^2 + (\varepsilon_{1i}n_x)^2)^2((\varepsilon_2+\varepsilon_{1r}n_y-\varepsilon_2 n_y)^2 + (\varepsilon_{1i}n_y)^2)^2} \tag{1-9}$$

$$n_x = \frac{-a^2b^2 + b^4 + ab^2\sqrt{a^2-b^2}\,\ln(a+\sqrt{a^2-b^2}/b)}{(a^2-b^2)^2} \tag{1-10}$$

$$n_y = \frac{-a^2b^2 + a^4 - ab^2\sqrt{a^2-b^2}\,\ln(a+\sqrt{a^2-b^2}/b)}{2(a^2-b^2)^2} \tag{1-11}$$

Where a is the half of rod length, b is half of the rod width, $\varepsilon 1$ and $\varepsilon 2$ are the dielectric functions for the ellipsoid and embedding regions, respectively. Figure 1-12 shows the numerical calculation results of light scattering spectra of gold nanorods with different aspect ratios according to equation (1-7) (27).

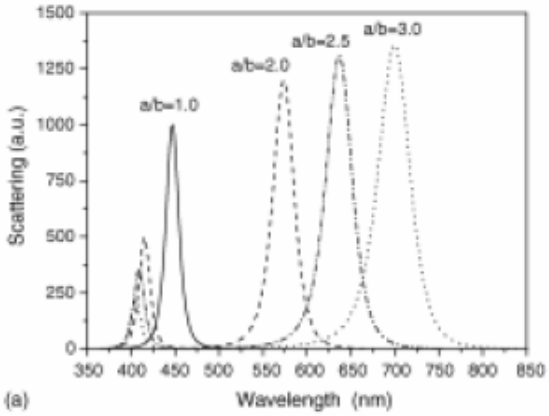

Figure 1-12: Calculated resonance scattering spectra of gold nanorods with varying aspect ratios a/b (27).

Using the light scattering properties, gold nanoparticles offer great potential for applications in biomedical imaging. A 60 nm gold nanoparticles is 10^5 stronger in the scattered light than the fluorescence light of a fluorescein molecule. Also, the scattered light color and intensity can be tuned by changing the size and shapes of the nanoparticles. Compared to fluorescent molecules, the use of gold nanoparticles for imaging is simple. There are no photobleach problems which always exist for fluorescence molecules.

From above introduction, we know that the peak intensity and position of both surface plasmon absorption and scattering bands are dependent on the size and shape of the metal nanoparticles. Since the total extinction efficiency is equal to the sum of the scattering and absorption efficiency, the absorption and scattering percentage will vary depending on the size and shape of the nanoparticles. Figure 1-13 shows the calculated size and shape dependence of the percentage of the absorption and scattering efficiency (28) using Mie theory, separation of variables method and discrete dipole approximation method. For a 40 nm nanospheres, the absorption cross section is higher than the light scattering cross section. But when the shapes change to spheroid with aspect ration of 2, they are equal and when the aspect ration change to 3 for the spheroid nanoparticles, scattering cross section dominates. Figure 1-14 shows the percentage of the absorption and scattering efficiency for gold nanorods (28) using discrete dipole approximation method. It can be see that the absorption and scattering efficiency can be tuned by changing the aspect ratio of the nanorods. This tunability between the absorption and scattering provides great flexibility for their use in imaging and photothermal therapy.

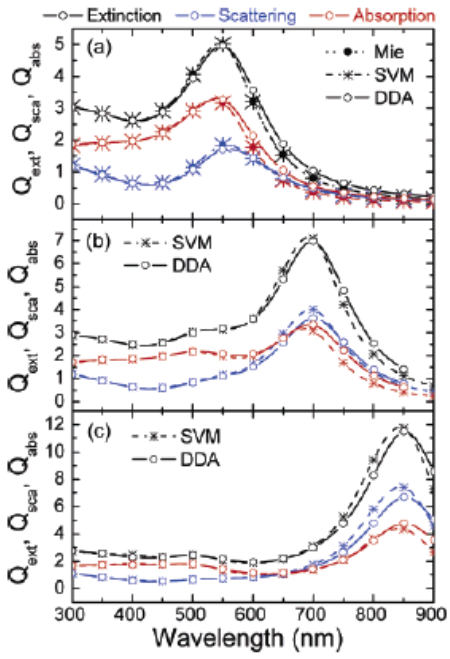

Figure 1-13: Calculated optical extinction, absorption, and scattering spectra (a) for a Au sphere with a radius of 40 nm in water and for a prolate Au spheroid with an aspect ratio *R* of (b) 2 and (c) 3, using different computational methods (29).

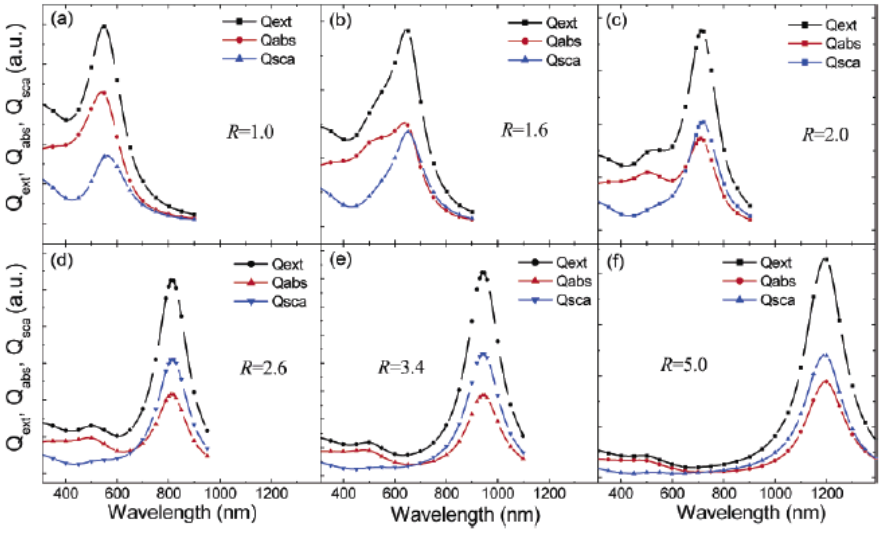

Figure 1-14: A series of calculated spectra for optical extinction, absorption, and scattering efficiencies for Au nanorods with different aspect ratios *R* (28).

1.1.3 Catalytic property of gold nanoparticles

Gold nanoparitcles have large surface-to-volume ratio compared to bulk materials, thus they are attractive to be used as catalysts. Figure 1-15 shows the publication of gold catalysis since 1901 from Scienfinder Scholar and Figure 1-16 shows the patens on the gold catalysis in the last decades (29). Traditionally gold was thought to be inert in catalysis. But within decades, gold nanoparticles have received wide interests due to the availability of small size nanoparticles which provides higher percentage of surface atoms and thus become active for catalysis.

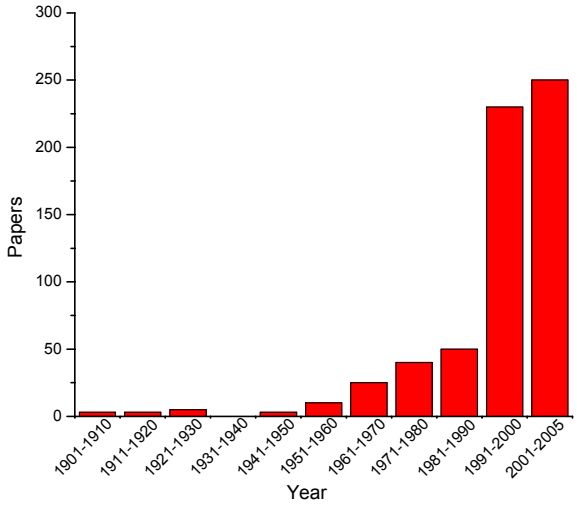

Figure 1-15: Gold catalysis publications from 1901 to 2005 (29).

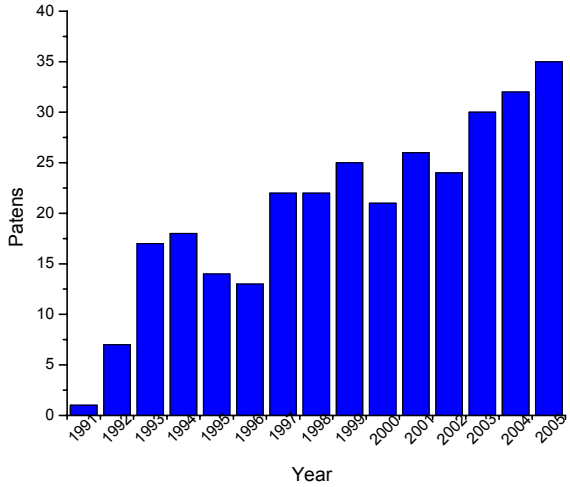

Figure 1-16: Gold catalysis patents from 1991 to 2005 (29).

The use of supported gold nanoparticles in heterogeneous catalysis accounts for most publications. The most reported catalysis is the low-temperature oxidation of carbon oxide (29-32), propylene epoxidation (33, 34), combustion of hydrocarbons (35, 36), NOx reduction (37, 38), hydrogenation reactions (39) and some other reactions (40-42). The activity of the gold nanoparticles depends on the size of the nanoparticles, the surface property of the nanoparticles (Au^+ might be involved) and the interaction of the particle with the supported substrates (43).

In homogeneous catalysis colloidal nanoparticles are used. Citrate-stabilized colloidal gold nanoparticles have been shown to be an active redox catalyst in the reaction between hexacyanoferrate (III) and thiosulfate ions (13, 14, 44) by Freund and Spiro. They found that the initial reaction rate is linearly dependent on the concentration of the gold nanoparticles. Compared with the theoretical results, they found the reaction is surface controlled catalysis, not diffusion controlled. Poly (N-vinyl-2-pyrrolidone) (PVP) capped colloidal gold nanoparticles can catalyze the homocoupling of phenylboronic acid in water (45). Some other reactions such as thiol oxidation under UV radiation are also catalyzed by gold nanoparticles (46). For the colloidal nanoparticle catalysis, the stabilizer is most important. Weak stabilizer will not keep the nanoparticle stable during reactions while stronger stabilizer will cap the nanoparticle too strongly thus the surface activity is limited. So gold nanoparticles prepared in different methods and capped by different materials affect greatly the catalytic activity of the nanoparticles (47).

1.2 Cancer

Cancer is the leading killer in the United States under the age of 85, surpassing heart disease in 2004 (48). Currently, one in four deaths in the United States is due to cancer (49). Nearly half of all men and a little over one third of all women in the United States will develop cancer during their lifetimes (50). Cancer can strike people at any age; although about 77% of all cancers are diagnosed in people age of 55 and older (50).

Cancer begins when the DNA of a normal cell changes, or "mutates". Most of the time when DNA becomes damaged, the body is able to repair it. In cancer cells, the damaged DNA is not repaired (51). People can inherit damaged DNA, which accounts for inherited cancers. More often, though, a person's DNA becomes damaged by exposure to something in the environment, like smoking (52). Cancer usually forms as a tumor. Some cancer, like leukemia, does not form tumors. Instead, these cancer cells involve the blood and blood-forming organs and circulate through other tissues where they grow. Often, not all tumors are cancerous. Benign (noncancerous) tumors do not spread (metastasize) to other parts of the body and, with very rare exceptions, are not life threatening (53).

Cancer develops when cells in a part of the body begin to grow out of control. Although there are many kinds of cancer, they all start because of out-of-control growth of abnormal cells. Under normal conditions, the cells in the human body divide and grow in an orderly, controlled manner. Cancer occurs when cells grow in an uncontrolled manner. Instead of dying, they outlive normal cells and continue to form new abnormal cells (54).

The cancer cell is profoundly abnormal cells which can be observed under simple optical microscope. Cancer cell's morphology is different from that of a normal cell. Its nucleus is larger and irregular.

1.2.1 ErbB receptors

The growth of cells requires signal transduction between cells. The "conversation" between two cells involves a molecular messenger (called a ligand) from the sender and a site (called a receptor) on the membrane surface of the cell receiving the signal. When the signal is received, it is passed along within the cell. In this way, the message is communicated from the outer surface of the cell to the cell's nucleus (55).

One of common signaling pathways involve proteins called receptor tyrosine kinases, which have three components: An extracellular ligand-binding domain receptor that is located outside the cell and receives incoming signals; A transmembrane domain that crosses the cell membrane and conveys information from the outside to the inside; An intracellular tyrosine kinase domain that adds a phosphate molecule to tyrosine, a type of protein. This process initiates an internal messaging cascade and is referred to as "phosphorylation" (56).

In oncology, the most important tyrosine kinase signaling networks is a group of receptors belonging to the "HER" family, also known as the ErbB signaling network (see Figure 1-17) (57). The HER family of receptors consists of four main members commonly called as HER1/EGFR (ErbB1), HER2 (ErbB2), HER3 (ErbB3) and HER4

(ErbB4), which demonstrate homology in their kinase domains, but diverge in their extracellular regions and C-terminal tails (see Figure 1-18) (58).

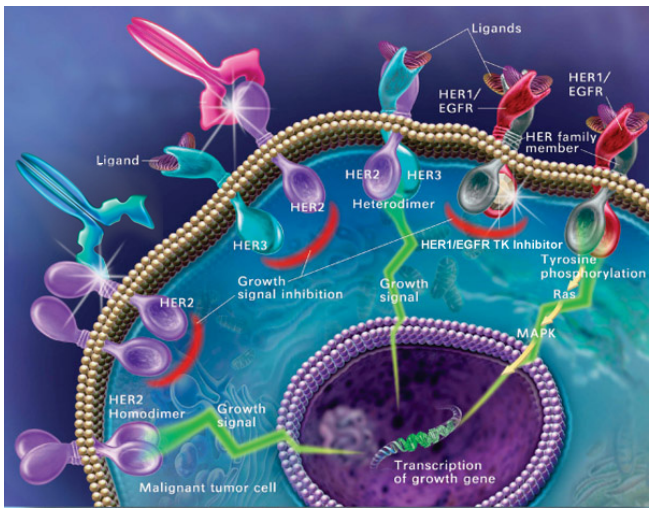

Figure 1-17: Her Signaling (57).

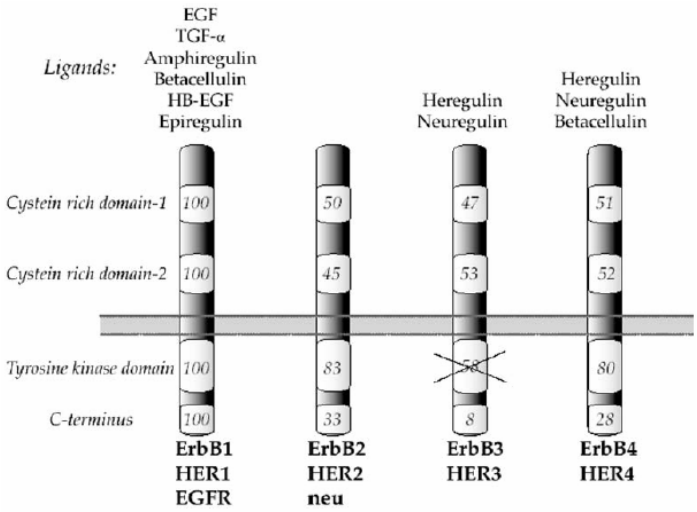

Figure 1-18: Schematic diagram of the four ErbB family members and their ligands. Numbers denote the degree (expressed as a percentage) of homology relative to ErbB1/EGFR (58).

These receptors are widely expressed in all tissues where they regulate diverse functions, including mitogenesis, differentiation, and cell survival. Different ligands and

protein-protein interactions contribute to the diverse signaling networks that characterize each receptor. Each of these receptors is in some way involved in the development of malignant tumors, although some are more involved than others in different cancers. In all cells, some level of growth-signal transduction is normal and is part of the regular growth cycle. It is the overexpression, or activation, of these signals - or the failure to counterbalance or block those signals -- that leads to uncontrollable growth and lead to cancer (see Table 1-2) (59). In the case of the HER2, for example, overexpression is the

Table 1-2: Her receptors and cancers (59).

Name	Types of dysregulation	Cancer type
HER1/ErbB1/EGFR	Overexpression and/or mutation leading to non-stop activity	head and neck, brain, bladder, stomach, breast, lung, endometrium, cervix, vulva, ovary, esophagus, stomach, prostate, renal, pancreatic, glioblastoma and in squamous cell carcinoma
HER2/ErbB2/c-erbB-2	Overexpress and/or coexpression with HER1 improves the possibility of beast cancer	breast, ovarian
HER3/ErbB3	Coexpression with HER2 improves the possibility of breast cancer	breast, colon, gast, prostate
HER4/ErbB4	lower expression in breast and prostate tumors relative to normal tissue	breast, prostate, childhood medullot

result of a genetic alteration that generates multiple copies of a gene that encodes a growth receptor. Because of the surplus of growth receptor genes in the cell, excessive numbers of growth receptors are created that, when activated, enlarge the number growth signals stimulating the cell, accelerating cell division and tumor growth.

1.2.2. EGFR

The epidermal growth factor receptor (EGFR) is a cell surface receptor that directs the initiation of processes such as growth, proliferation, apoptosis, adhesion, migration, and differentiation, when it is activated by specific growth factors (60-62). Overexpression, or increased abundance, of EGFR in cancers was first identified by LICR (Ludwig Institute for Cancer Research) investigators who also have done dominant research in the EGFR area (63). EGFR is overexpressed (it can also be mutated) with high frequency in most cancers (see Table 1-3) (64). EGFR expression in normal cells ranges from 40,000–100,000 receptors per cell (65). In many cases, the number of EGFRs expressed in malignant cells is greater than that expressed in normal cells; up to 2 million EGFRs per cell were reported to be demonstrated in human epidermoid carcinoma cells A431 (66).

Table 1-3: EGFR overexpression in tumors (64).

Tumor type	Percentage of tumors overexpressing EGFR
Cervix/uterus	90%
Head and Neck	80-100/%
Renal carcinoma	50-90%
Esophagael	43-89%
Nonsmall cell lung carcinoma	40-80%
Prostate	40-80%
Glioma	40-63%
Ovarian	35-70%
Bladder	31-48%
Pancreatic	30-50%
Colon	25-77%
Breast	14-91%
Gastric	4-33%

Epidermal growth factor receptor (EGFR) is the prototype member of the type I receptor tyrosine kinases (67-69). The EGFR is a 170-kDa plasma membrane glycoprotein containing an extracellular ligand-binding domain, a single transmembrane region, a

cytoplasmic domain which is composed of a tyrosine kinase domain and a C-terminal tail (67, 70, 71). The amino acid sequence of EGFR has been deduced by Ullrich et al. in 1984 (72). From this information and subsequent structure studies the structure features of EGFR has been constructed as in Figure 1-19 (72-76).

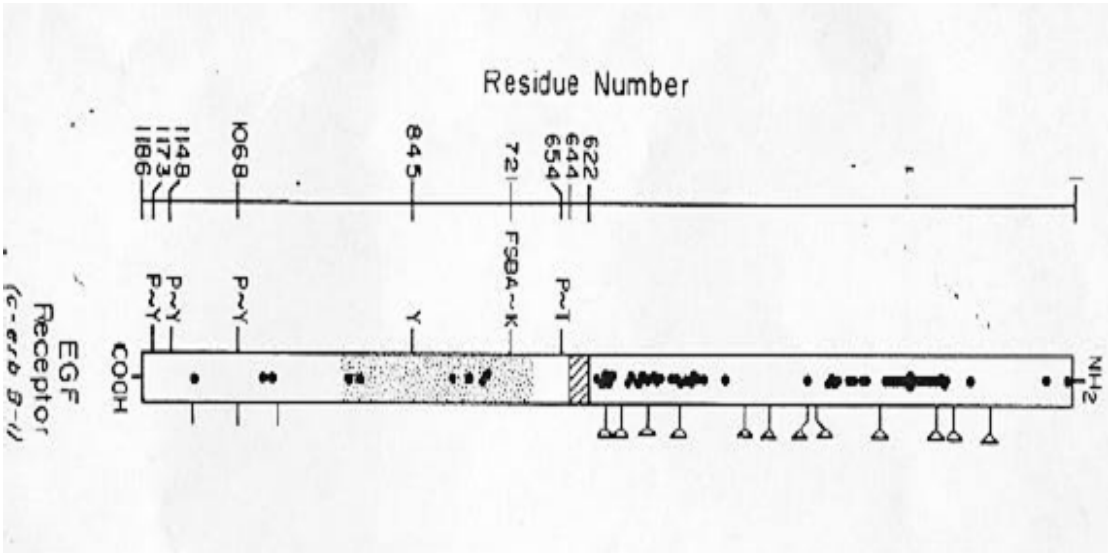

Figure 1-19: Structure features of EGFR._ ： canonical sequences for N-linked glycosylations; —◃: probable sites of N-linked oligosaccharide chains, ●: cysteine residues, Y: tyrosine residues, P ~ Y: phosphotyrosine residues, T: threonine residues, P ~ T: phosphothreonine residues, K: lysine residues, FSBA ~ K: lysine residue covalently labeled with p-fluorosulfonylbenzoyl adenosine, crosshatched area: membrane-spanning region, stippled area: sequences similar to src kinase (76).

The extracellular domain of EGFR contains 621 amino acid residues (70) and it folded into four domains in three dimension, domain I, II, III and domain IV (77) (see Figure 1-20). Domain I and III are regions with a relatively large number of canonical sequences for N-linked glycosylation and domain II and IV regions containg a high content of cysteine [76]. The ligands for EGFR such as EGFRand TGF-α binds to both domain I

and III (78). The transmembrane domain is a single polypeptide chain of 22 amino acids (79). Immediately adjacent to the transmembrane sequence, there is at the cytoplalsmic interface a 13-residue sequence that is highly enriched in basic amino acids (76). The tyrosine kinase is located in the endoplasmic domains and the c-terminal regions contains the major sites of autophosphorylation.

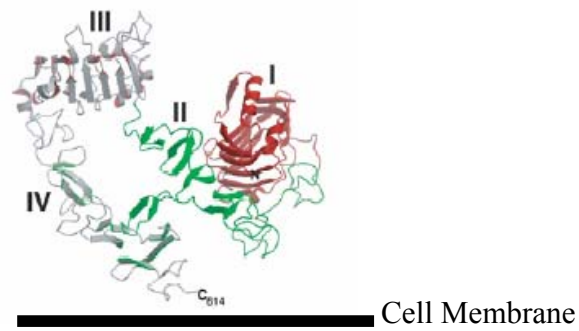

Figure 1-20: Three dimensional structure of the extracellular domain of EGFR (77).

EGFR realize its function in the initiation of cell growth processes by binding with EGF. Upon binding of a specific growth factor ligand to its extracellular ligand-binding domain, the EGFR receptor pairs, or 'dimerizes', with another ErbB family member (see Figure 1-21, 1-22) (80,81). This dimerization may be homodimerization (i.e. EGFR dimerizes with another EGFR) or heterodimerization (e.g. EGFR dimerizes with ErbB-2, ErbB-3, or ErbB-4) determined by the levels of each receptor, and the particular ligand bound to the receptor. After dimerization, the receptors' intrinsic tyrosine kinase activity phosphorylates tyrosine amino acid residues in both receptors.

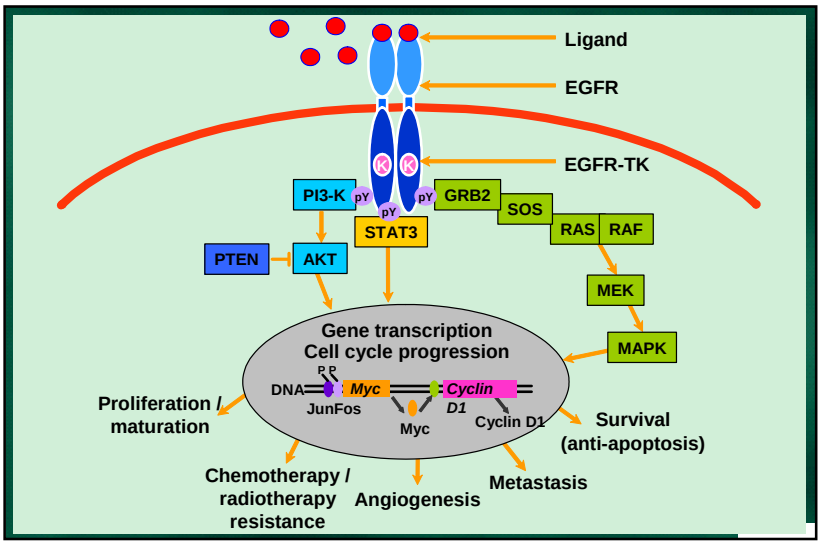

Figure 1-21: EGFR signaling transduction in tumor cells (80).

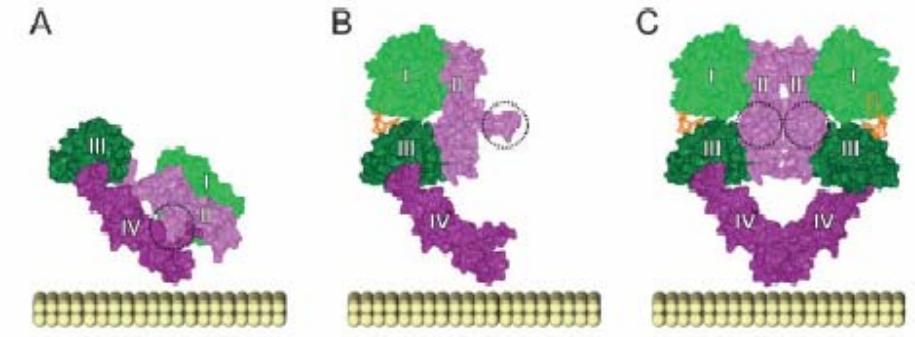

Figure 1-22: Ligand activation of EGFR. A: Structure of unbound extrocellular domain (autoinhibited, tethered state); B: Structure of 1:1 EGF: EGFR extrocellular complex (dimerization-competent state) and C: structure of 2:2 EGF: EGFR extrocellular complex (dimerized, activated state) (81).

Various 'adaptor' proteins, such as Shc and Grb2, are then recruited to the phosphorylated tyrosines, and transduce signals via major cell signaling pathways that are comprised of signaling molecules such as the nitogen-activated protein kinase (MAPK), and the p70 S6 α kinase, and also multiple phosphoinositide 3-kinases (PI3K), protein

kinase C (PKC), and the p70 S6β kinase, many of which were discovered and/or characterized by Ludwig Institute for Cancer Research (LICR) teams (82). The sequential activation of these and other molecules transmit signals from the receptor dimers at the cell surface through particular pathways to, ultimately, the transcription machinery in the nucleus. The final aspect of the EGFR signaling process occurs with the receptor undergoing a conformational change (concomitant with ligand binding) that results in the exposure of motifs for endocytosis (removal from the cell surface) and degradation. The endocytosis of the receptor is the mechanism for down-regulation of signaling from the activated EGFR (83-84).

1.2.3. Cancer diagnostics

Conventional cancer diagnostics depends on the cell pathology, such as biopsy, endoscopy, and imaging which all looked at the cell appearance under microscope (85, 86). Biopsy is the only sure way to test for cancer. In biopsy, the doctor removes a sample of the tissue on the abnormal area or may removes the whole tumor and then a pathologist examines the tissue under microscope.

Endoscopy is to look into the body by using a thin, lighted tube. Sample tissue or cells can be collected for further examination through the forcep on the tip of the tube.

Imaging is to look at the inside of the body using X-ray, or CT (computed tomography), ultrasonography and MRI (magnetic resonance imaging). It usually uses a special dye that is put into the body to stain certain organs and increase the imaging contrast. X-ray imaging is the most common way to make pictures of the inside of the body. CT,

sometimes called CAT (computed angled tomography) scan, uses special x-ray equipment to obtain image data from different angles around the body and then uses computer processing of the information to show a cross-section of body tissues and organs. Ultrasonography uses high-frequency sound wave to enter the body and then use the echoes to produce a picture called a sonogram. MRI uses radiofrequency waves and a strong magnetic field to provide remarkably clear and detailed pictures of internal organs and tissues. The technique has proven very valuable for the diagnosis of a broad range of pathologic conditions in all parts of the body including cancer, heart and vascular disease, stroke, spinal and joint problems.

With the advanced development of molecular biology in the last decade, enormous progress has been made to understand the molecular events that accompany maglignant transformation and progression by genomics and proteomics (87). Molecular diagnostics determines how the genes and proteins in cancer cells and or organism are interacting in a cell by expressing these molecular signatures as patterns (88, 89). Compared to the conventional pathology methods, these patterns improve the clinical's ability to diagnostics cancers with more accuracy and they assist early cancer detection. However, these advances have not yet impacted on diagnostics and staging of the majority of cancer cells in real time (90).

1.2.4. Cancer therapy

It is well know that the tradition cancer treatment includes surgery, radiation, hormone therapy and more recently chemotherapy, immunotherapy and combines strategies (91). Surgery is the oldest form of treatment for cancer. It offers the greatest chance for cure

for many types of cancer, especially those that have not yet spread to other parts of the body but not for cancers at late phase. It will continue to be an extremely important weapon against cancer.

Radiation is the second weapon against cancer. Radiation therapy involves treating cancer with beams of high-energy particles, or waves (radiation), such as X-rays, gamma rays, neutrons or pimesons (92). Radiotherapists often implant radioactive materials or radioisotopes into tumors. The particles transfer their energy into electrons which ionize the matter they reach such as water and/or the solid constituents of cytoplasm, RNA and DNA. This ionization damages the molecules and leads the free radicals to recombine with oxygen available in the environment. Thus changes the biological properties of the biomolecules such as causing the cell to die or make it impossible to divide. Radiation is much more harmful to cancer cells than it is to normal cells. This is because cancer cells divide more rapidly than do healthy cells. Cells are more vulnerable to damage when they're dividing, making cancer cells to be more susceptible to radiation than normal cells. In addition, normal cells can recover from the effects of radiation more easily than cancer cells. But still it is nonetheless true that it is impossible to kill a tumor without harming the surrounding healthy cells.

Hormone therapy changes the internal environment and prevents the growth of cancers that are hormone-dependent such as breast and prostate cancers. It is usually called androgen deprivation therapy (ADT) or androgen suppression therapy. Controlling cancer of the prostate is the triumph of hormone therapy. Androgens, produced mainly in the testicles, can actually stimulate prostate cancer cells to grow. Hormone therapy is to

lower androgen levels (either by surgery or drugs such as pituitary down-regulators and anti-androgens) can usually make prostate cancers shrink or grow more slowly.

Chemotherapy is most often used to mean taking medicines, or drugs, to treat cancer, especially suitable for those cancers that have been spread out and can not be used by the local methods such as surgery and radiation. Normal cells grow and die in a controlled way. Cancer cells keep dividing and forming more cells without control. Anticancer drugs destroy cancer cells by stopping them from growing or multiplying. They also go after and damage any healthy cells that are quickly dividing, whether it's a cancer cell or not. Lately emerged photothermal therapy have greatly improved the therapy efficiency by injecting contrast agents such as weak emitting dyes (93, 94) into the tumer sites which convert the photoengergy into thermal engery and thus kill the cancer cells. Photosensitizers are also been reported for photodynamic therapy which use photoexcited molecules to transfer their energy to oxygen forming excited singlet oxygen which injures cancer cells (95, 96).

With the development of immunology, immunotherapy (also known as biologic therapy) is emerged as a more specific cancer treatment method. Immunotherapy is a treatment that uses certain parts of the immune system to fight diseases, including cancer. This can be done by stimulating your own immune system to work harder or by using an outside source, such as manmade immune system proteins (97). Compared to other forms of cancer treatment, such as surgery, radiation therapy, or chemotherapy, immunotherapy is relatively new. One of the immunotherapy is to use monoclonal antibody which specifically target the cancer cells and then block the cancer cell activation or cure the

cancer cells by attaching radioactive chemicals on the antibodies (98). Some monoclonal antibodies that react with specific antigens on certain types of cancer cells have been used in clinical trials (see Table1-4) (64). Compared with side effects of standard chemotherapy, the side effects of naked MAbs are usually relatively mild and are often related to an "allergic" reaction.

Table 1-4: Monoclonal antibodies in clinical trials (64).

MAb Name	Trade Name	Type	Used to Treat:	Approved in:
Rituximab	Rituxan	Anti-CD20 antigen	Non-Hodgkin lymphoma	1997
Trastuzumab	Herceptin	Anti-HER2 receptor	Breast cancer	1998
Gemtuzumab ozogamicin*	Mylotarg	Anti-CD33 antigen	Acute myelogenous leukemia (AML)	2000
Alemtuzumab	Campath	Anti-CD52 antigen	Chronic lymphocytic leukemia (CLL)	2001
Ibritumomab tiuxetan*	Zevalin	Anti-CD20 antigen	Non-Hodgkin lymphoma	2002
Tositumomab *	Bexxar	Anti-CD20 antigen	Non-Hodgkin lymphoma	2003
Cetuximab	Erbitux	Anti-EGFR receptor	Colorectal cancer	2004
Bevacizumab	Avastin	Anti-VEGF receptor	Colorectal cancer	2004

1.3 Nanotechnology in cancer applications

With the tremendous development of nanotechnology, a variety of nanostructures with different shapes and structures of different composites (1, 4, 99-107) has been provided.

These nanostructures demonstrate unique electronic, photonic, catalytic and highly controlled and interesting properties as a consequence of the size reduction from bulk to nanoscale (16, 18, 108-111). These nanoparticles exhibit similar size dimensions to many common biomolecules such as proteins and DNA, thus offer great possibilities for the integration of nanotechnology to biotechnology. Typical applications include contrast agents for disease diagnostics and therapies (112-115), developing homogenous immuassay [116-118] and assembling new materials (119, 120).

The use of nanoparticles in medicine is one of the important directions that nanotechnology is taking at this time. Their applications in drug delivery [121-123], cancer cell diagnostics (124-129) and therapeutics (12, 130, 131) have been active fields of research.

1.3.1 Quantum dots in cancer imaging

One of the most widely used nanoparticles in the cancer applications are the semiconductor nanocrystals, also referred to as quantum dots, due to their wide absorption ranges and unique size dependent fluorescence properties (see Figure 1-23, (126), Figure 1-24, (127)). They are highly fluorescent and photobleach resistant (113, 114). They can be used for imaging cancer cell markers (see Figure 1-25) (125). They can provide single excitation for multicolor images, which is not possible for molecular fluorophors because of their narrow excitation spectra. But the potential human cytotoxicity of the semiconductor material is one major problem for its *in vivo* application.

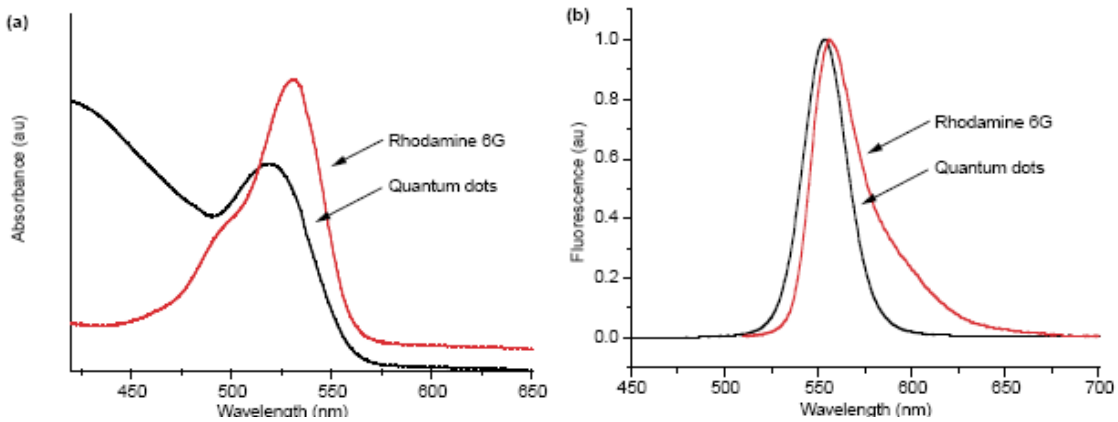

Figure 1-23: The wide absorption spectrum (a) and the narrow emission spectrum (b) of CdSe QDs compared to rhodamine 6G dye molecules (126).

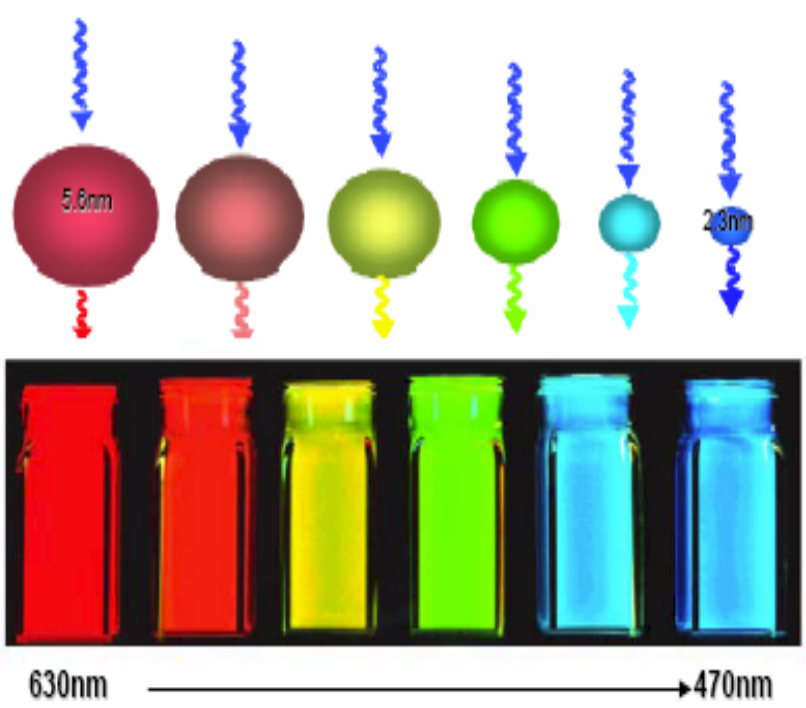

Figure 1-24: The size dependant fluorescence property of CeSe QDs (127).

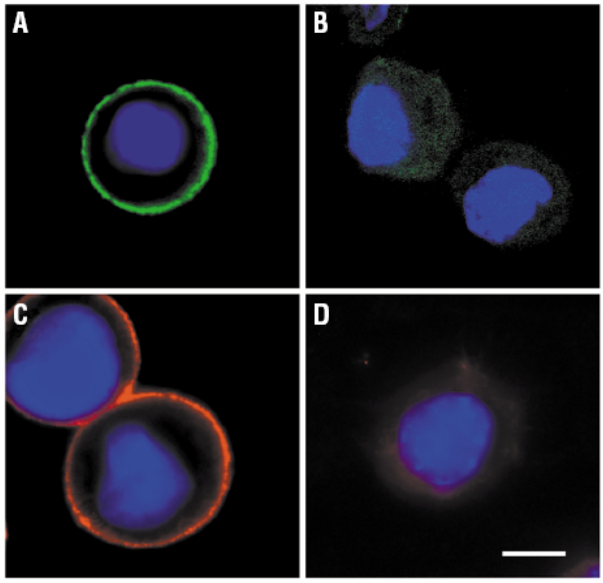

Figure 1-25: Detection of cancer marker Her2 with QD-IgG. (A), (C) fixed cells Sk-BR-3 cells were incubated with monoclonal anti-Her2 antibody and goat anti-mouse IgG conjugated to QDs. (A) QD535-IgG, (c): QD630-IgG. (B) and (D) cells were incubated with normal mouse IgG and QD-IgG (125).

1.3.2 Gold nanoshell in cancer imaging and photothermal therapy

Another kind of nanoparticles for cancer applications is called gold nanoshell nanoparticles (12, 128, 132-135). It contains silica core (about 140 nm in diameter) with a thin laser of gold shells (about 10 nm). The absorption band of core-shell particles can been tuned by adjusting the ratio of the thickness of the gold shell to the diameter of the silica core (Figure 1-26, (132)) and thus enables both strong scattering and absorption efficiency. Therefore they can be use as dual imaging/therapy contrast agents (see Figure 1-27, 128). Figure 1-28 is the photothermal cancer therapy using gold nanoshell in vivo experiment.

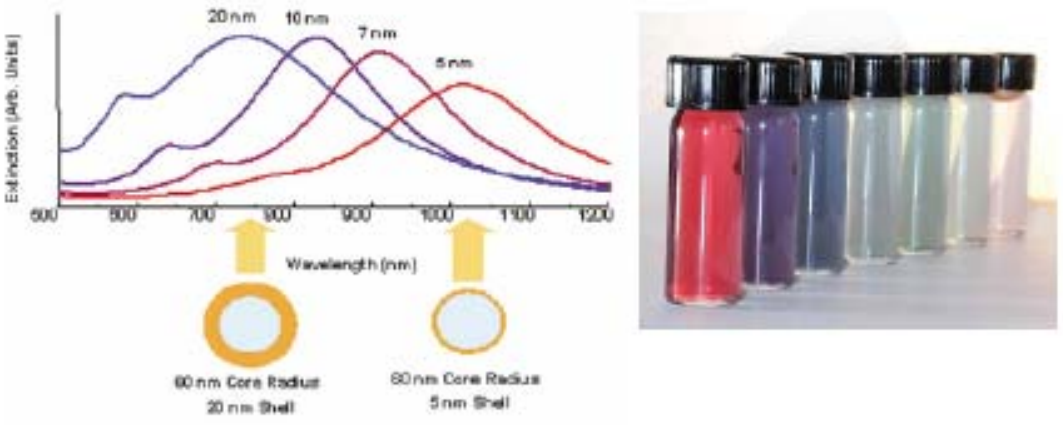

Figure 1-26: The optical tenability of Si/AU core shell nanoparticles by changing the ration of the shell to core (132).

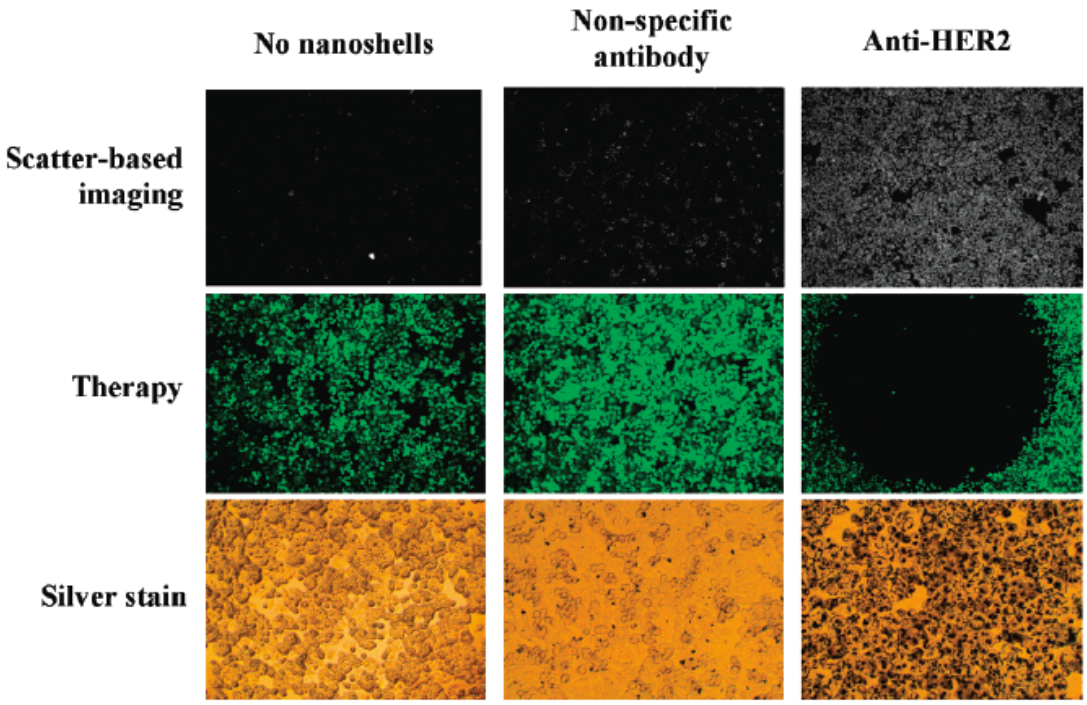

Figure 1-27: Combined imaging and therapy of SKBr3 breast cancer cells using HER2-targeted nanoshells. Scatter-based darkfield imaging of HER2 expression (top row), cell viability assessed via calcein staining (middle row), and silver stain assessment of nanoshell binding (bottom row) (128).

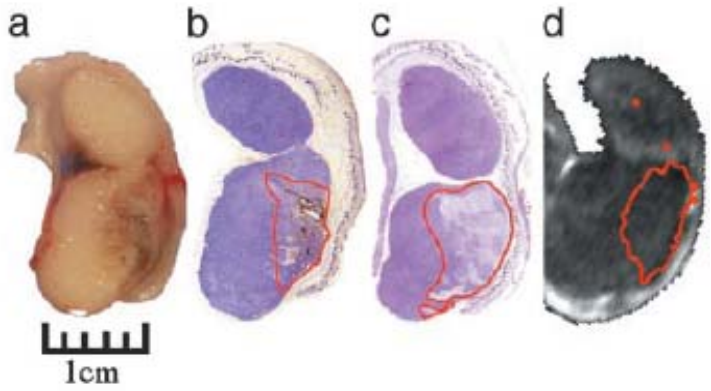

Figure 1-28: (*a*) Gross pathology after *in vivo* treatment with nanoshells and NIR laser reveal hemorrhaging and loss of tissue birefringence beneath the apical tissue surface. (*b*) Silver staining of a tissue section reveals the region of localized nanoshells (outlined in red). (*c*) Hematoxylin_eosin staining within the same plane clearly shows tissue damage within the area occupied by nanoshells. (*d*) Likewise, MRTI calculations reveal an area of irreversible thermal damage of similar dimension to *a*, *b*, and *c* (12).

1.3.3 Polymer nanoparticles in drug delivery

Nanoparticles have become a greatly studied for use in drug delivery for therapeutic applications due to their small size which is suited for intravenous delivery. Polymer has several advantages over other nanoparticles such as easy incorporation or incubation of the drug with the nanoparticles, the ability to stabilize the drugs in vivo and no side effects (especially for the biodegradable polymers) (136-140). Figure 1-29 (141) shows a common way of the drug delivery into cells and the later releasing to target. Polymer can also be functionized with cancer marker targeting molecules as other nanoparticles. So the polymer can specifically target the cancer cells and then release the drugs to the cancer (142).

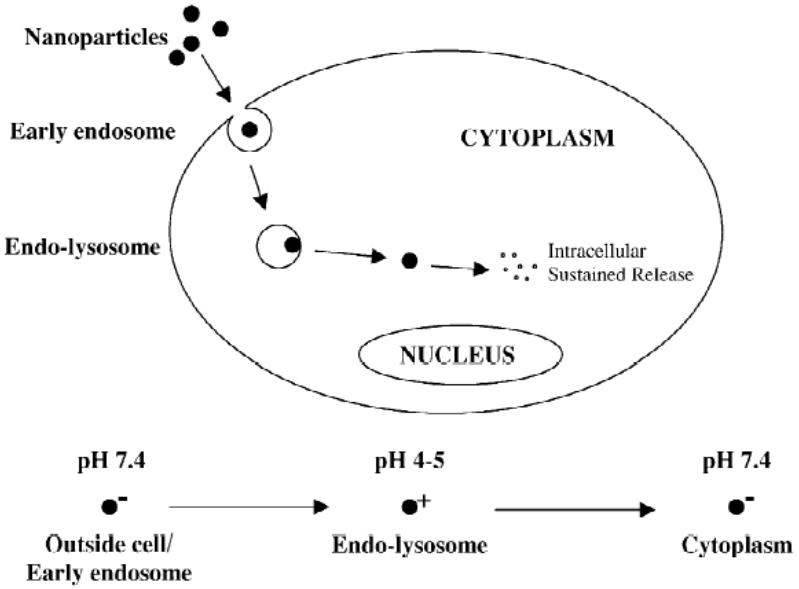

Figure 1-29: Intracellular trafficking of nanoparticles. Following their uptake, nanoparticles are transported through early endosomes to the sorting endosomes. A fraction of nanoparticles recycles back to the cell exterior while another fraction is transported to secondary endosomes/lysosomes from where nanoparticles escape into the cytoplasm. Nanoparticles that escape into the cytoplasm could act as intracellular reservoirs for sustained release of the encapsulated therapeutic agent (141).

1.3.4 Gold nanoparticles in cancer imaging

Solid gold nanoparticles have been widely interested due to its easy preparation, ready bioconjugation and potential noncytotoxicity (143). Various methods for the preparation of gold colloids were reported in the 20th century (144). It only takes several minutes to synthesize the nanoparticles in a boiling auric solution that is reduced by citrate molecules, which is the most popular synthesis method. The sizes of the nanoparticles can be easily changed by changing the citrate concentration (145). The citrate capped nanoparticles are very stable but the citrate ion can be replaced and functionized with various ligands for specific applications. The safety of gold nanoparticles is well-known.

Gold nanoparticles have already been used in vivo since the 1950's as a radiaotracer (143).

Using the light scattering properties of gold nanoparticles, preliminary studies have reported their use as contrast agents for biomedical imaging using multiphoton plasmon resonance microscopy (9), third-harmonic microscopy (11), optical coherence microscopy (10) and confocal scanning optical microscopy (8) (see Figure 1-30, 1-31).

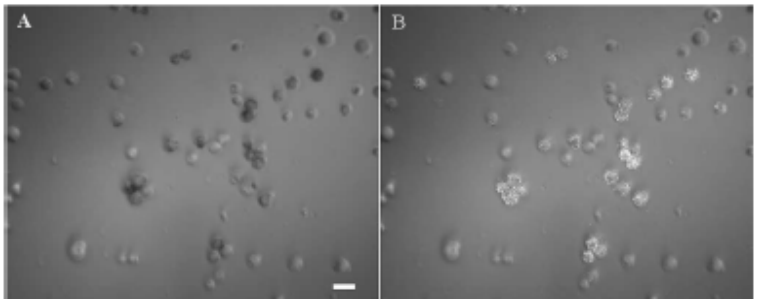

Figure 1-30: SiHa cells labeled with anti-EGFR gold conjugates in (**a**) brightfield (**b**) in brightfield with laser pointer illumination (8).

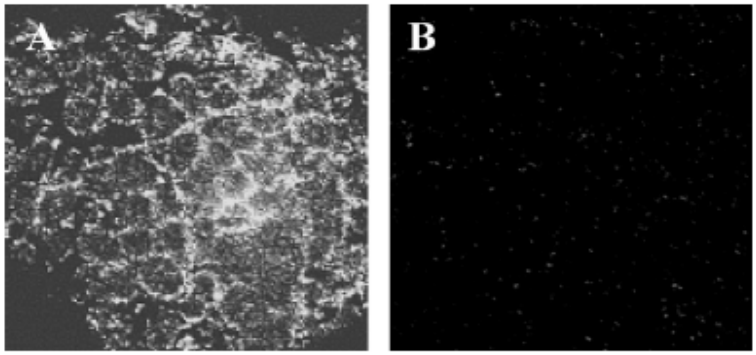

Figure 1-31: Cervical biopsies labeled with anti-EGFR antibodies/gold nanoparticles conjugates: (**A**) clinically abnormal; (**B**) clinically normal obtained under the same acquisition conditions as (**A**) (8).

Gold nanoparticles have several advantages for imaging application compared to other agents. The scattered light is very strong and they are much brighter than chemical fluorophores. They are photobleach resistant and can be easily seen in as low as 10^{-16} M

concentration (147). Sokolov (8) have used confocal microscope to detect the scattering of anti-EGFR/Au nanoparticles for cervical cancer. Irradiation with a laser will only produce single color which is close to the laser wavelength used. When illuminated with a beam of white light, gold nanoparticles will scatter light of many colors. The color of the light is determined by the absorption spectrum of the nanoparticles which depends on the shape and size of the nanoparticles (8). This color dependent scattering property provides the potential for imaging studies with a simple white light source.

In this thesis, the application of gold nanospheres (129, 130, 148) and nanorods (131) in the cancer cell diagnostics and therapy are demonstrated in detail. This includes using the surface plasmon absorption band of gold nanoparticles and the strong scattering properties for diagnostics of cancer cells from healthy cells, using the particle's strong absorption properties. The efficient energy conversion process from photo energy to local heat energy (18) is used for photothermal cancer therapy.

The catalytic property of gold nanoparticles for the NADH oxidation to NAD^+ is also described. In addition, the application of gold nanospheres and nanorods as substrates for surface enhanced Raman of small molecules, large biomolecules and living cells is also described and demonstrated. Furthermore, some other related studies such as the biological synthesis of gold nanoparticles inside cells are also discussed.

1.4 References

(1) Alivisatos, A. P. *Science*, **1996**, *271*, 933-937.

(2) Kreibig, U.; Vollmer, M. *Optical Properties of Metal Clusters*; New York: Springer, **1995**.

(3) El-Sayed, M. A. *Acc. Chem. Res*. **2001**, *34(4),* 257.

(4) Link, S.; El-Sayed, M. A. *J. Phys. Chem. B* **1999**, *103*, 8410.

(5) Yguerabide, J.; Yguerabide, E. E. *Anal. Biochem*. **1998**, *262*, 137.

(6) Mirkin, C. A.; Letsinger, R. L.; Mucic, R. C.; Storhoff, J. J. *Nature*, **1996**, *382*, 607

(7) Sokolov, K.; Aaron, J.; Hsu, B.; Nida, D.; Gillanwater, A.; Follen, M.; Macaulay, C.; Adler-Storthz, K.; Korgel, B.; Discour, M.; Pasqualini, R.; Arap, W.; Lam, W.; Richartz-Kortum, R. *Technol. Cancer Res. & Treat.* **2003**, *2(6)*, 491.

(8) Sokolov, K.; Follen, M.; Aaron, J.; Pavlova, I.; Malpica, A.; Lotan, R.; Richartz-Kortum, R. *Cancer Res*. **2003**, *63*, 1999.

(9) Yelin, D.; Oron, D.; Thiberge, S.; Moses, E.; Silberberg, Y. *Optics Express* **2003**, *11*, 1385-1391.

(10) Raub, C. B.; Orwin, E. J.; Haskell, R. *J. Biomech. Eng.* **2003**, *125*, 1-6.

(11) Yelin, D.; Oron, D.; Korkotian, E.; Segal, M.; Silberberg, Y. *Apply. Phys. B*: Lasers and Optics **2002**, *74* (Suppl.), S97-S101.

(12) Hirsch, L. R.; Stafford, R. J.; Bankson, J. A.; Sershen, S. R.; Rivera, B.; Rrice, R. E.; Hazle, J. D.; Halas, N. J.; West, J. L. *Proc. Natl. Acad. Sci. USA* **2003**, *100*, 13549.

(13) Freund, P. L.; Spiro, M. *J. Phys. Chem*. **1985**, *89*, 1074.

(14) Freund, P. L.; Spiro, M. *J. Chem. Soc., Faraday Trans.* 1 **1986**, *82*, 2277.

(15) Bohren, C. F.; Huffman, D. R. *Absorption and Scattering of Light by Small Particles*. New York: Wiley, **1983**

(16) Link, S.; El-Sayed, M. A. *Annu. Rev. Phys. Chem.* **2003**, *54*, 331.

(17) Mie, G. *Ann. Phys*. **1908**, *25*, 377.

(18) Link, S.; El-Sayed, M. A. *Int. Reviews Phys. Chem.* **200**0, *19(3),* 409.

(19) Gans, R. *Ann. Phys* **1915**, *47*, 270.

(20) Papavassiliou, G. C. *Prog. Solid State Chem*. **1980**, *12*, 18.

(21) Link, S.; Mohamed, M. B.; El-Sayed, M. A. *J. Phys. Chem. B* **1999**, *103*, 3073.

(22) Du, H.; Fuh, R. A.; Li, J.; Corkan, A.; Lindsey, J. S. *Photochem. Photobiol*. **1998**, *68*, 141.

(23) Weissleder, R. *Nat. Biotechnol*. **2001**, *19*, 316.

(24) Van De Hulst, H. C. *Light Scattering by Small Particles*, pp. 397–400, Dover, New York, **1981**.

(25) Sönnichsen, C.; Franzl, T.; Wilk, T.; Plessen, G. V.; Feldmann, J. *Phys Rev. Lett*. **2002**, *88 (7),* 077402-1.

(26) Freemantle, M. *Science* **2001**, *79(49),* 10.

(27) Zhua, J.; Huanga, L.; Zhaoa, J.; Wang, Y.; Zhaoa, Y.; Haoa, L.; Lu, Y. *Materials Science and Engineering B* **2005**, *121*, 199.

(28) Lee, K. S.; El-Sayed, M. A. *J. Phys. Chem. B* **2005**, *109*, 20331.

(29) Hutchings, G. J. *Gold Bulletin* **2004**, *37*, 3.

(30) Okamura, M.; Nakamura, S.; Tsubota, S.; Nakamura, T.; Azuma, M.; Haruta, M. *Catal. Lett.* **1988**, *51*, 53.

(31) Grisel, R.; Weststrate, K. J.; Gluhoi, A.; Nieuwenhuys, B. E. *Gold Bulletin* **2002,** *35/2*, 39.

(32) Hutchings, G. J.; Haruta, M. *Applied Catalysis A: General*, **2005**, *291*, 2.

(33) Stangland, E. E.; Stavens, K. B.; Andres, R. P.; Delgass, W. N. *J. Catal*. **2000**, *191*, 332.

(34) Sinha, A. K.; Seelan, S.; Tsubota, S.; Hayashi, M. *Topics in Catalysis* **2004**, *29*, 95.

(35) Griesel, R. J. H.; Kooyman, P. J.; Nieuwenhuys, B. E. *J. Catal.* **2000**, *191*, 430.

(36) Waters, R. D.; Weimer, J. J.; Smith, J. E. *Catal. Lett*. **1995**, *30,* 181.

(37) Salama, T. M.; Ohnishi, R.; Ichikawa, M. *Chem. Commun*. **1997**, 105.

(38) Lee, J. Y.; Schwank, J. *J. Catal*. **1986**, *102*, 207.

(39) Sakurai, H.; Tsubota, S.; Haruta, M. Appl. Catal. A **1993**, *102*, 125.

(40) H. Sakuri and M. Haruta, *Catal.Today*, **1996**, *29*, 361.

(41) T. Aida, R. Higuchi and H. Niiyama, *Chem. Lett.,* **1990**, 2247.

(42) G. Hutchings, *Catal. Today*, **2002**, *72*, 11.

(43) Meyer, R.; Lemire, C.; Shaikhutdinov, S. K.; Freund, H. J. *Gold Bulletin* **2004**, *37(1–2),* 72.

(44) Spiro, M. J.; Freund, P. L.; *J. Chem. Soc. Faraday Trans. 1* **1983**, *79*, 1649.

(45) Tsunoyama, H.; Sakurai, H.; Ichikuni, N.; Negishi, Y.; Tsukuda, T. *Longmuir* **2004**, *20(26),* 11293.

(46) Li, J. J.; Peng, X. *J. Nanosci. Nanotechnolo*. **2004**, *(6),* 565.

(47) Li, Y.; Hong, X. M.; Collard, D. M.; El-Sayed, M.A. *Organic Letters*, **2000**, *2 (15),* 2385.

(48) *Released News*, 2/8/05, News target network.

(49) Jemal, A.; Tiwari, R. C.; Murray, T.; Ghafoor, A.; Samuels, A.; Ward, E.; Feuer, E. J.; Thun, M. J. *CA Cancer J. Clin*. **2004**, *54(1)*, 8.

(50) *American Cancer Society report*, **02/01/2005.**

(51) Stein, G. S.; Pardee, A. B. *Cell cycle and growth control: biomolecular regulation and cancer***, 2004,** Hoboken, NJ: Wiley-Liss.

(52) *Clinical trials* [electronic resource]: questions and answers, **2004**, Bethesda, Md.: National Cancer Institute.

(53) *Oncologie* [electronic resource], **2004,** Paris; New York: Springer.

(54) *Released news,* **6/6/05**, National Cancer Institute.

(55) Genentech Inc, *research reports*, **2004**.

(56) Lodish, H.; Berk, A.; Zipursky, L. S.; Matsudaira, P.; Baltimore, D.; Darnell, J. *Molecular Cell Biology,* **2002,** 4th Ed., W. H. FREEMAN.

(57) http://www.biooncology.com/biooc/approach/HERPathway.m.

(58) Harari, P. M.; Huang, S. M.; Herbst, R.; Quon, H. *Moleculartargeting of the epidermal growth factor receptor in head and neck cancer.* In Head and Neck Cancer: a Multidisciplinary Approach, pp 1001–1016. **2003**, Eds Harrison LB, Sessions RB & Hong WK. Philadelphia, PA, USA: Lippincott, Williams and Wilkins.

(59) http://www.gene.com/gene/products/education/oncology/herpathway.jsp.

(60) Mach, J. P. *Oxford Text Book of Oncology*, **1995**, Oxford Univ. Press, Oxford.

(61) Carpenter, G.; Cohen, *S. Annu. Rev. Biochem*. **1979**, 48.

(62) Carpenter, G.; Cohen, S. *Receptors and Recognition*, **1981**, Series *B 13***,** pp. 41-66, ed. Lefiowitz, R. L., Chapman and Hall.

(63) 2004 Annual Report, LICR.

(64) Harari, P. M.; *Endocrine-Related Cancer* **2004**, *11*, 689.

(65) Walker, F.; Orchard, S. G.; Jorissen, R. N.; Hall, N. E.; Zhang, H. H.; Hoyne, P. A.; Adams, T. E.; Johns, T. G.; Ward, C.; Garrett, T. P. J.; Zhu, H. J.; Nerrie, M.; Scott, A. M.; Nice, E. C.; Burgess, A. W. *J. Biol. Chem*. **2004**, *279*, 22387.

(66) Fabricant, R. N.; De Larco, J. E.; Todaro, G. J. *Proc. Nat Acad. Sci. USA* **1977**, *74*, 565.

(67) Cohen, S.; Carpenter, G.; King, L. Jr. *J. Biol.* Chem. **1980**, *255*, 4834.

(68) Ushiro, H.; Cohen, *S. J. Biol. Chem*. **1980**, *255***,** 8363.

(69) Buhrow, S. A.; Cohen, S.; Staros, J. V. *J. Biol.* Chem. **1982**, *257*, 4019.

(70) Das, M.; Fox, C. F. *Proc. Natl. Acad. Sci. USA.* **1978**, *75*, 2644.

(71) Buhrow, S. A.; Cohen, S.; Staros, J. V. *J. Bio. Chem*. **1982**, *257*, 4019.

(72) Ullrich, A.; Coussens, L.; Hayflick, J.; Dull, T.; Gray. A.; Tam, A.; Lee, J.; Yarden, Y.; Libermann, T.; Schlessinger, J.; Downward, J.; Bye, J.; Whittle, N.; Waterfield, N.; Seeburg, P. *Nature* **1984**, *309*, 418.

(73) Hunter, T.; Ling, N.; Cooper, J. A. *Nature* **1984**, *311*, 480.

(74) Davis, R. J.; Czech, M. P. *Proc. Natl. Acad. Sci. USA*. **1985**, *82*, 1974.

(75) M.W. Russo, T.J. Lukas, S. Cohen, J.V. Staros, *J. Bio. Chem*. **1985**, 260, 5205.

(76) Carpenter, G. *Ann. Rev. Biochem*. **1987**, *56*, 881.

(77) Ferguson, K. M. *Biochemical Society Transactions* **2004**, *32*, 742.

(78) Burgess, A. W.; Cho, H. S.; Eigenbrot, C.; Ferguson, K. M.; Garrett, T. P.; Leahy, D. J.; Lemmon, M. A.; Sliwkowski, M. X.; Ward, C. W.; Yokoyama, S. *Mol. Cell* **2003**, *12*, 541.

(81) Hubbard, S. R. *Cancer cell* **2005**, *7*, 287.

(82) Johns, T. J.; Stockert, E.; Ritter, G.; Jungbluth, A. A.; Huang, H. J.; Cavenee, W. K.; Smyth, F. E.; Hall, C. M.; Watson, N.; Nice, E. C.; Gullick, W. J.; Old, L. J.; Burgess, A. W.; Scott. A. M. *International Journal of Cancer* **2002**, *98(3),* 398.

(83) Luwor, R. B.; Zhu, H. J.; Walker, F.; Vitali, A. A.; Perera, R. M.; Burgess, A. W.; Scott, A. M.; Johns, T. G. *Oncogene* **2004**, *23(36),* 6095.

(84) Walker, Orchard, S. G.; Jorissen, R. N.; Hall, N. E.; Zhang, H. H.; Hoyne, P. A.; Adams, T. E.; Johns, T. G.; Ward, C.; Garrett, T. P.; Zhu, H. J.; Nerrie, M.; Scott, A. M.; Nice, E. C.; Burgess, A. W. *Journal of Biological Chemistry* **2004**, *279(21),* 22387.

(85) Bair, F. E. *Cancer Sourcebook: Basic Information on Cancer Types, Symptoms, Diagnostic Methods, and Treatments, Including Statistics on Cancer Occurrences World (Health Reference Series),* Vol. 1, Omnigraphics, **1990**.

(86) Nakamura, R. M.; Grody, W. W.; Wu, J. T.; Nagle, R. B. *Cancer diagnostics, current and future trend*, Humana Press, **2004**.

(87) Roulston, J. E.; John, M. S. *Molecular Diagnosis of Cancer Methods and Protocols*, 2nd ed., **2004**.

(88) Eleftherios, P. D. *Clinical Chemistry* **2003**, *49*, 1272.

(89) Balmain, A.; Gray J.; Ponder, B. *Nature Genetics* **2003**, *33*, 238.

(90) Sokolov, K.; Aaron, J.; Hsu, B.; Nida, D.; Gillanwater, A.; Follen, M.; Macaulay, C.; Adler-Storthz, K.; Korgel, B.; Discour, M.; Pasqualini, R.; Arap, W.; Lam, W.; Richartz-Kortum, R. *Technology in Cancer Research & Treatment* **2003**, *2(6)*, 491.

(91) Miller, A. B.; Hoogstraten, B.; Staquet, M.; Winkler, A. *Cancer* **1981**, *47(1),* 207.

(92) Lucien Israel, *Conquering Cancer*, Random House, New York, **1978**.

(93) Chen, W. R.; Adamsc, R. L.; Carubellic, R.; Nordquist, R. E. *Cancer Letters* **1997**, *115*, 25.

(94) Chen, W. R.; Adamsc, R. L.; Higginsb, A. K.; Bartefsd, K. E.; Nordquistc, R. E. *Cancer Letters* **1996**, *98*, 169.

(95) D'Cruz, A. K.; Robinson, M. H.; Biel, M. A. *Head & Neck* **2004**, *3*, 232.

(96) McBride, G. *J. Nat. Cancer Inst.* **2002**, *94*, 1740.

(97) Rosenberg, S.A. *Immunity* **1999**, *10(3),* 281.

(98) Weiner, L. M. *Semin Oncol.* **1999,** *26(4 Suppl 12)*, 41.

(99) Jana, N. R.; Gearheart, L.; Murphy, C. J. *J. Phys. Chem. B* **2003**, *105*, 4065.

(100) Jin, R.; Cao, Y.; Mirkin, C. A.; Kelly, K. L.; Schatz, G. C.; Zheng, J. *Science* **2001**, *294*, 1901.

(101) Sun, Y.; Xia, Y. *Science* **2002**, *298*, 2139.

(102) Maillard, M.; Giorgio, S.; Pileni, M.-P. *Adv. Mater.* **2002**, *14*, 1084.

(103) Murray, C. B.; Noms, D. J.; Bawendi, M. G. *J. Am. Chem. Soc.* **1993**, *115,* 8706.

(104) Dabbousi, B. O.; Rodriguez-Viejo, J.; Mikulec, F. V.; Heine, J. R.; Mattoussi, H.; Ober, R.; Jensen, K. F.; Bawendi, M. G. *J. Phys. Chem. B* **1997**, *101,* 9463.

(105) Peng, X.; Schlamp, M. C.; Kadavanich, A. V.; Alivisatos; A. P. *J. Am. Chem. Soc.* **1997**, *119*, 7019.

(106) Guzelian, A. A., Katari, J. E.; Kadavanich, A. V.; Banin, U.; Hamad, K. E.; Juban; A.; Alivisatos; A. P. *J. Phys. Chem.* **1996**, *100*, 7212.

(107) Hines, M. A.; Guyot-Sionnest, P. *J. Phys. Chem.* **1996**, *100,* 468.

(108) Schmid, G. *Clusters and Colloids: From Theory to Application*. Weinheim: VCH New York: Academic, **1994**.

(109) Kamat, P. V; Meisel, D. *Studies in* New York: Wiley. *Surface Science and Catalysis,* Vol. 103. *Semiconductor Nanoclusters—Physical, Chemical, and Catalytic Aspects*. Amsterdam: Elsevier. **1997**.

(110) Edelstein, A. S; Cammarata, R. C. *Nanoparticles: Synthesis, Properties and Applications*. Bristol: Inst. Phys. **1996**.

(111) Hagfeldt, A; Graetzel, M. *Acc. Chem. Res.* **2000**, *33*, 269.

(112) Niemeyer, C. M. *Angew Chem Int Ed Engl,* **2001**, *40*, 4128.

(113) Bruchez, M. Jr.; Moronne, M.; Gin, P.; Weiss, S.; Alivisatos, A. P. *Science* **1998**, *281*, 2013.

(114) Chan, W. C. W.; Nie, S. M. *Science* **1998**, *281*, 2016.

(115) Pathak, S.; Choi, S.K.; Arnheim, N.; Thompson, M.E. *J. Am. Chem. Soc.* **2001**, *123*, 4103.

(116) Elghanian, R.; Storhoff, J.J.; Mucic, R.C.; Letsinger, R.L.; Mirkin, C.A. *Science* **1997**, *277*, 1078.

(117) Dubertret, B.; Calame, M.; Libchaber, A.J. *Nat Biotechnol.* **2001**, *19*, 365.

(118) Reynolds, R. A.; Mirkin, C. A.; Letsinger, R. L. *J. Am. Chem. Soc.* **2000**, *122*, 3795.

(119) Mirkin, C. A.; Letsinger, R. L.; Mucic, R. C.; Storhoff, J. J. *Nature* **1996**, *382*, 607.

(120) Alivisatos, A. P.; Johnsson, K. P.; Peng, X.; Wilson, T. E.; Loweth, C. J.; Bruchez, M. P. Jr.; Schultz, P. G. *Nature* **1996**, *382*, 609.

(121) Bruchez Jr, M.; Moronne, M.; Gin, P.; Weiss, S.; Alivisatos, A. P. *Nature* **1996**, *382*, 609.

(122) West, J. L.; Halas, N. J. *Annu. Rev. Biomed. Eng.* **2003**, *5*, 285.

(123) Paciotti, G. F.; Myer, L.; Weinreich, D.; Goia, D.; Pavel, N.; McLaughlin, R. E.; Tamarkin, L. *Drug Delivery*, **2004**, *11(3)*, 169.

(124) Jain, K. K. *Technol. Cancer Res. & Treat*. **2005**, *4(4)*, 407.

(125) Wu, X.; Liu, H.; Liu, J.; Haley, K. N.; Treadway, J. A.; Larson, J. P.; Ge, N.; Peale, F.; Bruchez, M. P. *Nat. Biotechnol.* **2003**, *21*, 41.

(126) Chan, W. C. W; Maxwell, D. J.; Gao, X.; Bailey, R. E.; Han, M.; Nie, S. *Curr. Opin. Biotechnol*. **2002**, *13*, 40.

(127) Watson, W.; Wu, X.; Bruchez, M. *Bioimaging* **2003**, *34*, 296.

(128) Loo, C.; Lowery, A.; Halas, N.; West, J.; Drezek, R. *Nano letters* **2005**, *5*, 709

(129) El-Sayed, I. H.; Huang, X.; EL-Sayed, M. A. *Nano letters* **2005**, *5*, 821.

(130) El-Sayed, I. H.; Huang, X.; EL-Sayed, M. A. *Cancer letters* **2005**, in press.

(131) Huang, X.; El-Sayed, I.; Qian, W.; El-Sayed, M. A. *JACS*, **2006**, *128*, 2115.

(132) Oldenburg, S.J. et. al., *Chem. Phys. Letters*, **199**8, *288*, 243.

(133) West, J. L.; Halas, N. J. *Cur. Opin. Biotech.* **2002**, *11*, 215.

(134) Loo, C. H.; Lin, A.; Hirsch, L. R.; Lee, M. H.; Barton, J.; Halas, N. J.; West, J.; Drezek, R. A. *Technology in Cancer Research and Treatment* **2004**, *3*, 33.

(135) O'Neal, D. P.; Hirsch, L. R.; Halas, N. J.; Payne, J. D.; West, J. L. *Cancer Letters* **2004**, *209*, 171.

(136) Kreuter, J.; *Colloidal Drug Delivery Systems*, Marcel Dekker, New York, **1994**, pp 219–342.

(137) Song, C.; Labhasetwar, V.; Cui, X.; Underwood, T.; Levy, R. J. *J. Control. Release* **1998**, *54*, 201.

(138) Soppimatha, K. S.; Aminabhavia, T. M.; Kulkarnia, A. R.; Rudzinski, W. E. *Journal of Controlled Release* **2001**, *70*, 1.

(139) Moghimi, S. M.; Hunter, A. C.; Murray, J. C. *Pharmacol. Rev*. **2001**, *53*, 283.

(140) Vinagradov, S. V.; Bronich, T. K.; Kabanov, A. V.; *Adv. Drug Del. Rev*. **2002**, *54*, 223.

(141) Panyama, J.; Labhasetwara, V. *Advanced Drug Delivery Reviews* **2003**, *55*, 329.

(142) Kukowska-Latallo, J. F.; Candido, K. A.; Cao, Z.; Nigavekar, S. S.; Majoros, I. J.; Thomas, T. P.; Balogh, L. P.; Khan, M. K.; Jr. Baker, J. R.; *Cancer Res* **2005,** *65(12),* 5317.

(143) West, J. L.; Halas, N. J. *Cur. Opin. Biotech.* **2002**, *11,* 215- 217.

(144) Daniel, M. C.; Astruc, D. *Chem. Rev.* **2004,** *104*, 293̃.

(145) Thrkevich, J. *Gold Bull*. **1985**, *18*, 86.

(146) Sherman, A. I.; Ter-Pogossian, M. *Cance*r **1953**, *6*, 1238.

(147) Yguerabide, J.; Yguerabide, E. E. *Analy. Biochem.* **1998**, *262*, 157.

(148) Huang, X.; Jain, P. K.; El-Sayed, I. H.; El-Sayed, M. A. *Photochem. Photobiol*., **2006,** *82*, in press.

CHAPTER 2
DETAILS OF THE DIFFERENT EXPERIMENTS CARRIED OUT

2.1 Cell culture

One nonmalignant epithelial cell line, HaCaT (human keratinocytes) and two malignant epithelial cell lines, HOC 313 clone 8 and HSC 3 (human oral squamous cell carcinoma) are obtained from Dr Ivan, a surgeon in Otolaryngology-Head and Neck Surgery, Comprehensive Cancer Center, University of California at San Francisco. Dr Ivan ships the frozen cells (obtained from Prof Randall Kramer's lab, where the cells are originally extracted from patient tissue and cultured and frozen in liquid nitrogen) in dry ice by Fedex. When the frozen cells arrive here, the cells are stored in a -80^{o}C freezer in Prof Paul Edmonds's lab (Department of Biology, Georgia Tech). The chemicals involved in the cell culture are listed in Table 2-1.

Table 2-1: The chemicals used in the cell culture

DMEM medium: Dulbecco's Modification of Eagle's Medium, 1X with 4.5 g/L, L-glutamine, & sodium pyruvate, 6x500mL, *Cellgro*, Cat No: MT10-013-CV.
FBS: Fetal Bovine Serum, *Gem Cell*, Cat No: 100-500.
DPBS buffer: Dulbecco's phosphate-Buffered Saline, W/O Calcium and Magnesium, 1X solution, 6x500 mL, *Cellgro*, Cat No: MT21-031-CV.
Trypsin: 0.25% Trypsin/2.21 mM EDTA in HBSS without sodium bicarbonate, calcium and magnesium, Porcine Paravirus Tested, 6x100mL, *Cellgrow*, Cat No: MT-25-053-CI.
15 mL Falcon Centrifuge Tubes: 17 x 120mm, BD* Falcon* BlueMax* 15mL Graduated Tubes, Qty/pk: 125. *Fisher*, Cat No: 14-959-49B, Falcon No: 352096.
50 mL Falcon Centrifuge Tubes: 30x115mm, BD* Falcon* BlueMax* 50mL Graduated Tubes, Qty/pk: 25, *Fisher*, Cat No: 14-432-22, Falcon No: 352070.

100 x 20 Tissue Culture plates: 100 dia, 20mmH, BD Falcon cell culture dishes, *Fisher*, Cat No: 08-772 E, Falcon No: 353003,
60 x15 Tissue culture plates: 60 dia, 15mmH, BD Falcon cell culture dishes, *Fisher*, Cat No: 08-772B. Falcon No: 353002.
Multiwell culture plates: BD Falcon TM Multiwell culture plates, 12 well flat-bottom with lid, Fisher, Falcon No: 353043, Fisher No: 08-772-29.
Lab marker: Black or blue, *VWR*, Cat No: 52877-150.
Sterile filter: Millex-GV Filter Unit, Millex-GV, 0.22 µm, PVDF 13 mm Ethylene Oxyde, Sterilized, Qty/pk: 100. *Millipore*, Cat No: SLGV013SL.
Sterile filter, 50 mL Steriflip-GP Filter Unit, Steriflip-GP, 0.22 µm, polyethersulfone, gamma irradiated, Qty/Pk: 25, *Millipore*. Cat No: SCGP00525
Sterile Pipette: Falcon* Disposable Polystyrene Serological Pipets, Individually Wrapped in Paper/Plastic, Individually wrapped in paper/plastic package. *Fisher*. 1 mL pipette, Falcon No: 357522, Cat No: 13-675-15C 5 mL pippete, Falcon No: 357543, Cat No: 13-675-22 10 mL pipette, Falcon No: 7551, Cat No: 13-675-20 25 mL pipette, Falcon No: 357525, Cat No: 13-668-2
Tweezers: DUMONT Electronic, blue epoxy-coated Tweezers, *Ted Pella, Inc*, Cat No: 5206.
Cover slips: Fisher band cover glasses. Size: 18mm, Circle, NO.2 -0.17 to 0.25 mm thick, Fisher, Cat No: 12-546.

Before starting cell culture, the cell culture hood, Biosafety Cabinet (Room 140, Department of Biology, Dr Edmonds lab), is sterilized by turning on the UV lights and power switch for at least 30 mins. During this time, FBS (stored frozen at -20^{o}C freezer, top layer of the common refrigerator) and red DMEM medium (stored cold at 4^{o}C, bottom layer of the common refrigerator) are taken out and put in a water bath (set at 37^{o}C) to be warmed up to 37^{o}C. After 30 mins, the UV light is turned off and the light is turned on to start cell culture experiment.

The frozen cells (HaCat, HOC and HSC cells, stored in 2.0 mL cyto tubes)) are taken out from the -80^{o}C freezer, warmed up in the water bath until the cells and liquid

dissolved. The outside of the tubes is sterilized by spraying with 95% ETOH (obtained from stockroom) and the tubes are immediately placed in the Biosafety Hood. Other sterile stuff, such as 15 mL centrifuge tubes and 100x20 mm tissue culture plates are also placed in the hood to get ready to be used. The warm FBS and DMEM bottles are also sterilized by 95 ETOH and placed in the hood. Then 50 mL FBS is transferred to the 500 mL DMEM bottles with 10 mL sterile disposable pipette to make a 10% FBS DMEM medium which is the cell culture medium always used (later referred as medium). The remaining FBS is stored frozen again for the next experiments. The cells are transferred to the 15 mL centrifuge tubes by 1mL sterile disposable pipette and diluted with the medium prepared above (containing 5% FBS) to 5 to 10 mL. The cells are then centrifuged at 0^{o}C or RT, 1000 rpm for 5 mins (Room 310, Edmonds lab). The cells are centrifuged down at the tube bottom and the supernatant contained the medium and the cell frozen solution (the components are explained later). The supernatant liquid is then disposed by the pipette in the hood and the cells are dissolved with the medium.

The cell suspension is transferred to the 100x20 mm tissue culture dishes (2 or three depending on the cell amount), then the medium solution is added to the dishes to make sure to cover at least the dish bottom. The cells are homogenously dispersed in the whole dish by gently swirling the dishes. The cell amount can be checked under a microscope with 10x or 20 x objectives. The cell dishes are then put in the incubator (5% CO_2, 37^{o}C) to grow. The live cells fell down and are attached to the dish bottom within 30 mins and grow within 8 hrs. Any dead cells just floated in the medium solution. If two many dead cells are observed after 8 hrs, the dead cells would have to be removed and rinsed out

with DPBS buffer in the hood and new medium is added. In this way, the live cells can grow healthier and faster.

After 24 hrs, the cells can be cleaved and used for experiments or can be spit into more dishes so the cells keep growing. If no cells are needed, the cells can still keep growing until it reached 80% confluency (80% percentage of the dish bottom is covered by the cells). After 80% confluency, the cells had to be cleaved and separate into more dishes or the cells kept growing and the dish bottom would be fully covered by the cells. When the cells fully covered the plates, the cells might grow layer by layer, or started to change or started to dye. It is not recommended to use the cells if the cells grow full of the dish.

The cells are cleaved off the dishes by using trypsin. When the cell dishes are taken out of incubator, the medium is sucked out by the pipette, and few mL DPBS buffer is added to rinse out the medium. Trypsin is then added to cover the dish bottom and the cell dishes are put in the incubator for about 5 mins. The cell dislodgement is checked under microscope to make sure all the cells come off the dishes (round cells floating and moving in the solution). Few mL medium is then added to the dishes and the cell suspension is collected into 15 mL centrifuge tubes. The cells are then centrifuged down using above parameters. The cell pellet can be dissolved in medium or DPBS buffer for experiment requirement or dissolved into medium to start another round cell culture (spit into several tissue culture dishes and let them grow again in the incubator). The cells are allowed to grow, split and grow again so that a lot of cells are prepared for.

If there are extra cells which are not needed, they can be frozen down and stored for later use so that they did not have to be kept growing if we did not have time to take care

of them. The frozen solution is composed of 25 mL medium without FBS, 22.5 mL FBS and 2.5 mL DMSO. The frozen solution is sterilized by the sterile filter with 50 mL centrifuge tubes attached. After the cells are centrifuged down, the cells are dispersed in the frozen solution (one mL or seral mL depending on the cell amount). The cells in the frozen solution are transferred to the 2 mL cryotubes. The cryotubes are placed into the cryto box which had ETOH at its bottom and then put in -80^{o}C freezer. The scheme of the cryo-holder is shown in Figure 2-1. The ETOH is used to let the cells freeze slowly in the -80^{o}C freezer. If no ethanol solution is present, the cells would freeze too rapidly, which can kill the cells. After overnight, the cells can be taken out from the cryo-holder and put directly in the -80^{o}C freezer and can be stored

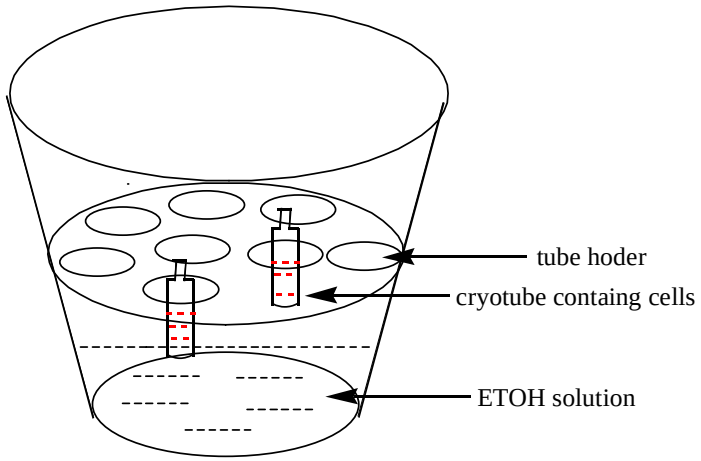

Figure 2-1: Scheme of cell frozen holder.

up to 2 weeks. Some cells would die during long time storage at -80^{o}C. After the cells are frozen, the cells are transferred to liquid nitrogen dewar for long time storage (up to years). When the cells are needed, they are just taken out of the liquid nitrogen and began to be cultured as described above.

In our experiments such as light scattering and photothermal experiments, we need grow cells on small glass coverslips. Coverslips need to be coated with collagen for cell optimum growth. The coverslips are first cleaned in 30%H_2O_2: Conc H_2SO_4 = 1: 3 (v:v) solution at 50 to 60^oC for 30 mins in our lab, then are placed in ETOH solution and transferred to Dr Edmonds lab. The coverslips are then placed in the safety hood and sterilized under UV light for 30 mins. One drop of the collagen solution which is 50 times diluted in DPBS of the pure collagen obtained from Dr Ivan, sterilized with sterile filter, is added on top of the coverslip. The coverslips immersed in collagen solution are then placed in the incubator for at least 30 mins. The top side of the coverslip is coated with collagen which optimizes the cell growth. The extra collagen solution is sucked out or rinsed out by the DPBS buffer and the coverslips are ready to use. Each one of coverslips is put in one well of the 12-well cell culture plates. A drop of cell suspension is added to each cell well and medium is added to fill half or two third level of the well. The culture plates are then placed in the incubator and the cells fell down onto the top side of the coverslips and started to grow on the coverslips.

2.2 Synthesis of gold nanoparticles in different sizes and shapes

Synthesis of 15 nm gold nanospheres

The 15 nm gold nanoparticles are synthesized by the citrate reduction of $HAuCl_4$ (1). A 25 mL tri-neck round bottom bottle is cleaned in aqua regia (3 parts HCl, 1 part HNO3) and rinsed with DDI water. 100 mL of 1mM $HAuCl_4$ solution (0.04g HAuCl4.3H_2O in 100 mL water) is heated to boiling, refluxed while being stirred (see Figure 2-2). Then 10

mL of a 38.8 mM trisodium citrate solution (0.1141 g trisodium citrate in 10 mL water) is added quickly.

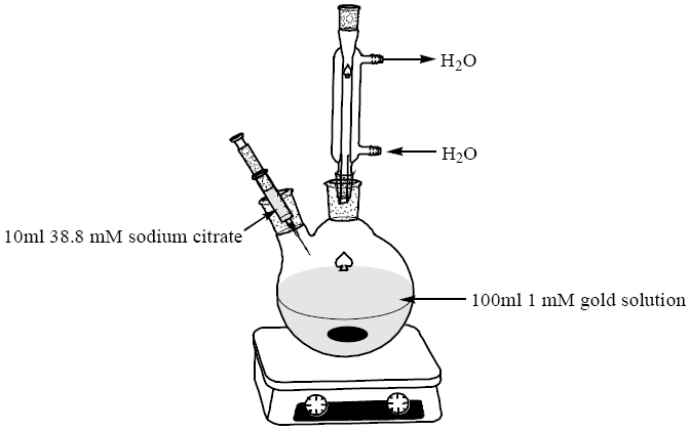

Figure 2-2: Synthesis of 15 nm gold nanospheres.

The solution color changed from yellow to black and to deep red. After the color changed, the solution is refluxed for an additional 15 min, then the heater is turned off and the solution is stirred until it reached cool to room temperature. The nanoparticles made in this way typically have average size around 15 nm.

Synthesis of 20 to 100 nm gold nanospheres

The various sizes of larger nanoparticles are synthesized according the method described by Frens (2). Basically 50 mL of 0.01% $HAuCl_4$ solution (by weight, Exp: 0.01g in 100 mL water) is heated to boiling while stirring in a 100 mL beaker (see Figure 2-3). Then a few hundred μL of 1% (by weight) of trisodium citrate solution is quickly added to the auric solution. The solution changed color within several minuets from yellow to black and then to red or purple color depending on the sizes of the

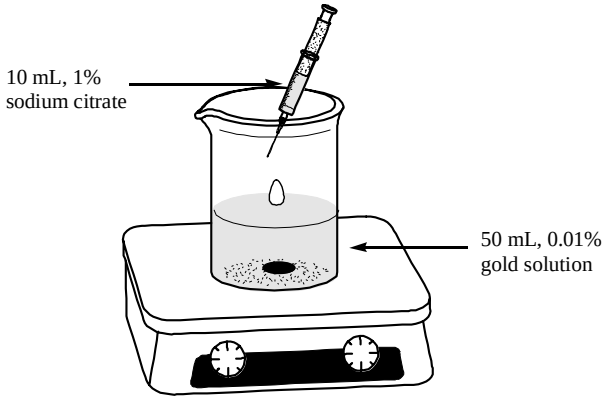

Figure 2-3: Synthesis of gold nanospheres of different sizes.

nanoparticles. The color change is slower for larger nanoparticles than for small nanoparticles. The amount of citrate solution determines the size of the nanoparticles. The approximate amount of citrate and the corresponding sizes of nanoparticles are listed in the following table, but each time the amount of citrate may vary within tens of μL. But it is true that smaller nanoparticles require more citrate solution and larger nanoparticles require less citrate solution. The faster the capping of the nanoparticles by the citrate, the smaller the resulting nanoparticles. (see Page 4, Figure 1-3 for the absorption and TEM spectra of the samples obtained by this method).

Table 2-2: Approximate amount of citrate and the corresponding sizes of nanoparticles

Citrate amount	Surface plasma absorption maximum	NPs size
350 μL	525 nm	30 nm
330 μL	530 nm	40 nm
260 μL	535 nm	50 nm
230 μL	540 nm	60 nm
210 μL	545 nm	80 nm

Synthesis of gold nanorods of different aspect ratios

The nanorods are synthesized according to the seed-mediated growth method by Murphy (3) and Nikoobakht (4) with some modifications. The chemicals used for the synthesis are listed in Table 2-3. The synthesis of gold nanorods is divided into two steps (see Figure 2-4).

Table 2-3: Chemicals used for synthesis of gold nanorods

$HAuCl_4 \cdot 3H_2O$ Gold (III) chloride trihydrate, *Sigma*, Cat No: G4022-5g.
CTAB cetyltrimethylammonium bromide, 98%, *Sigma*, Cat No: 855820-100g.
BDAC Benzyldimethylhexadecylammonium chloride, 98%, Sigma, Cat No: B4136-100g.
$NaHBH_4$ sodium borohydride, 99%, Sigma, Cat No: 213462-100g.
L-ascorbic acid *Sigma*, Cat No: A7506-100g.
$AgNO_3$ Silver Nitrate, *Fisher Scientific Inc*, Cat No: S181 78155, 453g.

Step 1: synthesis of seed solution

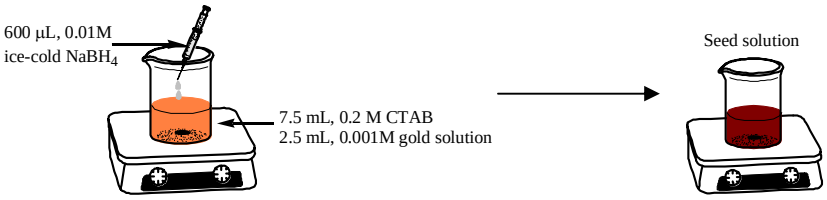

Step 2: Growth of nanorods

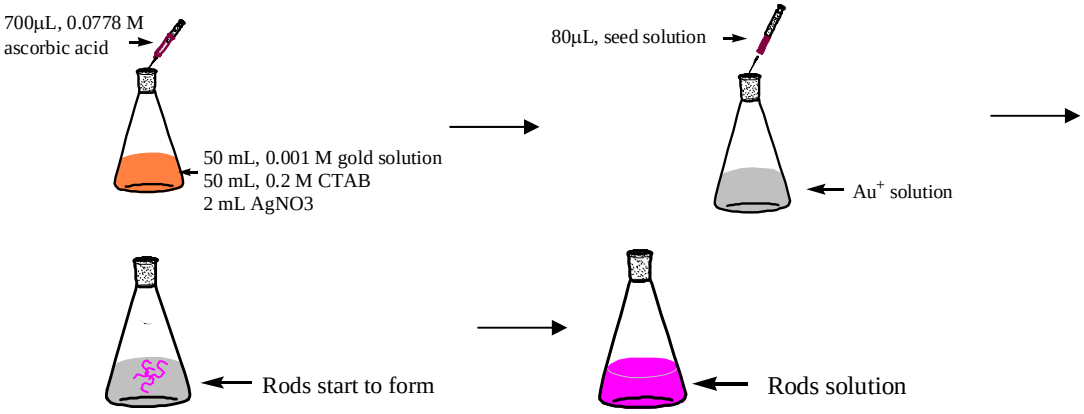

Figure 2-4: Synthesis of gold nanorods of different aspect ratios.

Step 1: Seed (sphere) solution: 7.5 ml of 0.2 M CTAB solution is mixed with 2.5 ml of 0.001 M $HAuCl_4$ in a 40 mL beaker and stirred. To the stirred solution, 0.6 ml of ice-cold 0.01 M $NaBH_4$ is added, which resulted in the formation of a solution with brownish yellow color. Vigorous stirring of the seed solution is continued for 2 minutes. After stirring, the solution is kept at room temperature.

Step 2: Growth of NRs (absorption maximum at 700 nm): 50 ml of 0.001 M $HAuCl_4$ is added to 50 mL of 0.2 M CTAB in a 250 mL flat-bottom flask and the solution changed color from yellow ($HAuCl_4$ dissolved in water) to orange ($HAuCl_4$ dissolved in CTAB). 1mL of 0.004 M $AgNO_3$ solution is added and gentle mixed. Then 700 μl of 0.0788 M ascorbic acid is added to reduced the Au^{3+} ions to Au^{+} and the solution changed to colorless (Au^{+} color) from orange after swirling gently. To this solution, 80 μl of seed solution (make sure the seed solution is clear. Sometimes, the seed nanoparticles crystalize out of the solution which needs to be warmed up to dissolve the nanoparticles before use) is added to the center of the solution. After adding seed solution, the flask should be kept still and never shaken or stirred, so that the seed started to grow in the growth solution. Usually the color of the solution gradually changed within 30 minutes. For longer NRs, the color change took place slower. After overnight, a lot rods are obtained (Optical density is about 0.8 at the longitudinal absorption band). With longer time growth, the rods would get shorter and the optical density would increase. All these experiments are done at room temperature. This pathway produced pure NR solutions with absorption maximum at 700nm.

By changing the concentration of CTAB and BDAC and the amount of silver nitrate, the aspect ratios can be varied. Table 2-4 lists the concentrations used in my experiments in order to produce nanorods of different aspect ratios. (see Page 7, Figure 1-6 for the absorption and TEM spectra of the samples obtained by this mmethod).

Table 2-4: The effect of the relative concentrations on the aspect ratio of gold nanorods:

CTAB	0.2 M	0.12 M	0.2 M	0.12 M	0.2 M	0.12 M	0.2 M
BDAC	0	0.15 M	0.25 M	0.15 M	0.25 M	0.15 M	0.25 M
$AgNO_3$	2 mL	1 mL	1.5 mL	1.5 mL	2 mL	2 mL	2.5 mL
Ascorbic acid	700 μL	700 μL	700 μL	700 μL	700 μL	700 μL	700 μL
Seed solution	80 μL	80 μL	80 μL	80 μL	80 μL	80 μL	80 μL
λmax	650 nm	700 nm	750 nm	800 nm	850 nm	900 nm	950 nm
Aspect ratio	2.4	2.9	3.5	4.0	4.6	5.2	5.7

2-3 Conjugation of gold nanoparticles to anti-EGFR antibodies

Conjugation of gold nanospheres to anti-EGFR antibodies

The conjugation of anti-epidermal growth factor receptor (anti-EGFR) antibodies to gold nanospheres followed the method described by Sokolov (5). Basically, the gold NPs (40 nm) are diluted in 20 mM HEPES (4-(2-Hydroxyethyl)-1-piperazine-ethanesulfonic acid) buffer (pH 7.4, Sigma) to a final concentration with optical density of 0.8 at 530 nm. 40 uL 6 mg/mL anti-EGFR monoclonal antibodies (host mouse; Sigma, clone 29.1) are added to 960 uL of the same HEPES buffer to form 1mL dilute solution. Then 10 mL of the gold solution prepared above is added dropwise to the dilute antibody solution while being stirred. After stirring for 5 mins, the solution is left to react for 20 mins. Right before centrifuge, 0.5 mL of 1% PEG 4000 (polyethylene glycol 4000, PEG 50% W/V, Boehringer Mannheimm, GmbH, 4 mL, 1243268) is added to the mixture to prevent

aggregation and the solution is centrifuged at 6000 rpm for 30 mins. The anti-EGFR/gold pellet is redispersed in PBS buffer (pH=7.4, Cellgro) and stored at 4^{o}C.

It is well known (6) that antibody can be adsorbed onto gold nanoparticle surface at pH = 7.4 and still preserve its function and activity. The binding mechanism is still not quite known although it is suggested (6) that antibody is orientated perpendicular on the nanoparticle surface (see Figure2-5).

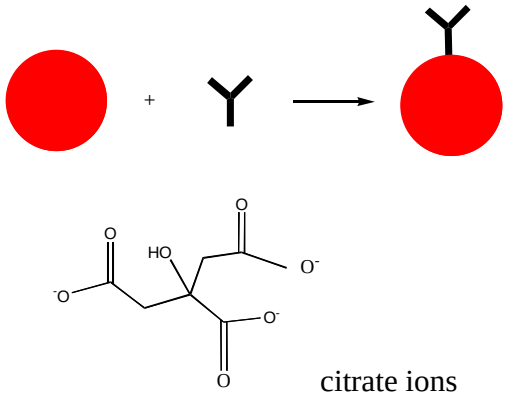

Figure 2-5: Conjugation of gold nanospheres to anti-EGFR antibodies.

The isoelectric point (PI, zero net charge of the protein) of the antibody is near pH 7. Thus at pH = 7.4, the antibody has an overall small net negative charge. The exact PI value of anti-EGFR is not known. Sokolove (5) explained that the preparation of gold bioconjugates is based on noncovalent binding of the anti-EGFR IgG antibodies at their isoelectric point, but did not point out which kind of noncovalant interaction, such as electrostatic interaction or hydrophobic interaction. Gold nanoparticles are capped with citrate and that the surface of the nanoparticles is negatively charged. This suggests that the adsorption of antibody at pH = 7.4 to gold nanoparticles can not be explained by pure electrostatic attraction between the negatively charged citrate on gold surface and the positive segment of the antibody. The hydrophobic interaction of the antibody with the

hydrophobic three carbon region of the citrates (see structure in Figure 2-5) may play an important role.

Conjugation of gold nanorods to anti-EGFR antibodies

The original rods grown by the seed-mediated method are centrifuged at 14000 rpm twice to get rid of the extra free CTAB molecules in solution. The nanorods surface is coated with poly (styrenesulfonate) (PSS, MW=18,000, Polysciences Inc.) polyelectrolyte layers before antibody adsorption. This is done by adding 200 μL of 10 mg/mL PSS to 10 mL stirred rods solution with optical density of 1.0 at the longitudinal absorption maximum. The mixture is let to react for about 15 mins to complete the adsorption process. The extra PSS in solution is separated by centrifuging the rod solution at 8000 rpm and the pellet is redispersed in HEPES solution (pH=7.4). Then the PSS capped nanorods are mixed with antibody solution which is diluted in the same HEPES buffer and left to react for 20 mins. The nanorods that are conjugated with the anti-EGFR monoclonal antibodies are centrifuged and redispersed into PBS (pH=7.4) to form a stock solution with an optical density of around 0.5 at 800 nm. The anti-EGFR/nanorod conjugates are stored at 4^{o}C until use at room temperature.

The possible binding of antibody to the rods surface is shown as in Figure 2-6. The gold nanorod is capped by CTAB bilayers and is positively charged on the surface (7). PSS is a negatively charged polyelectrolyte. According to Lvov et al. (8) and Okahata et al. (9), negatively charged PSS has been used to adsorb the antibody at pH = 7.4 to assemble an immunosensing multilayer. They suggested that besides possible electrostatic interaction between the negative charged PSS and the positively charged

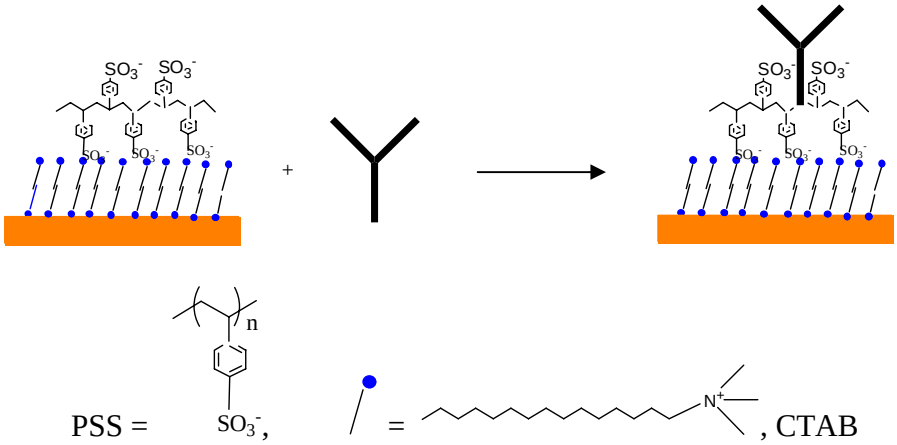

Figure 2-6: Conjugation of gold nanorods with anti-EGFR antibodies.

segment of the antibody (the overall charge of the antibody should be negative charged at pH=7.4, as discussed before), the hydrophobic interaction between these two molecules is dominated. They also found that at pH = 6.0 (the antibody has a net positive charge), the antibody is strongly adsorbed onto PSS layer. We did not use pH = 6.0 condition because the neutralization of the positive charge of the CTAB on the surface of rods by negatively charged antibodies will cause the aggregation of the nanorod solution. Here we used the strong interaction of PSS and antibody to adsorb anti-EGFR antibodies to the nanorods surface. In this way, the outlayer of the nanorods is negatively charged by antibody molecules and thus stable in solution. The aryl portion of the PSS molecules (see structure in Figure 2-6) supports the explanation of the hydrophobic binding.

2.4 Micro-absorption spectroscopy of gold nanoparticles on single cells

The quantification of gold nanoparticles inside or on the surface of single cells is carried out by using the micro-absorption spectrometer in Prof Mohan's lab. This is a S.E.E. 1000 MSP visible-NIR micro-spectrometer running the SEEScope version 4.0.0 software package (S.E.E. Inc, Middleboro, MA). The micro-spectrometer has a

wavelength range of 400-1100 nm thus the surface plasma absorption spectra of gold nanospheres and nanorods can be measured. The 20X objective used in these experiments has a sampling area of 8 μm squared. Since on average the cells grown on cover slips are usually larger than 10 μm, 20X objective is the best one to use. Also different areas on a single cell can be examined individually. All data taken is saved as .spc files and exported in ASCII format so that the data can be opened by Oringin or Excell software. If the baseline is to be subtracted, the data is saved as .spc files and opened in the ONMIC v 5.2 software package (Nicolet Instrument Corp, Madison WI), where the baseline can be smoothed or subtracted easily. After subtraction, the data is saved as .csv files and opened with the Origin or Excell software for plotting. Since Sept 2005, the SEES Microscope software has changed to CRAIC software because SEE company has been shut down. A CCD color camera has been added to the microscope so that more than one spectrum can be recorded and identified.

Under 20X objective, the distance between the objective and the sample is very small (several mms) so the absorption spectra can not be measured in buffer, which means absorption spectrum can not be taken on living cells. So after colloidal nanoparticles or nanoparticle bioconjugates incubation, the cells needed to be fixed and sealed before measurement (see Figure 2-7). This is carried out as follows: First, the cells on the coverslips are rinsed with PBS beffer, then several drops of 1% paraformaldehyde (the 16% paraformaldehyde are obtained from Dr Ivan and then diluted with PBS buffer to 1%) are added on top of the cells and left for at least 5 mins to fix the cells. The cells are then stopped to grow. The extra paraforamaldehyde is rinsed off with DDI water.

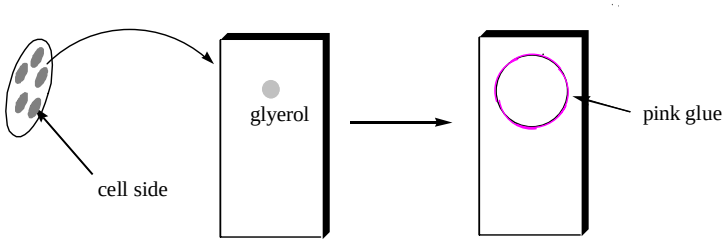

Figure 2-7: Cell fixation and sealing.

On a separate larger rectangular coverslip (50 x 24 mm), a small drop of glycerol is added. The small coverslip with cells on them is placed onto the rectangular coverslip with cells between the two coverslips and the glycerol homogenouly distributed between the two coverslips. Then the Hard as Nails glue is used to seal the edge of the two coverslips so that the glycerol did not leak out. In this way, the cells can be stored at room temperature for several months.

2.5 **Cellular imaging in bright and dark field**

The pictures of cells are taken in both bright and dark field using a simple optical microscope. In our lab, the Inverted Olympus IX70 can realize both functions with a DP11 color camera (for bright field images) and an Olympus film camera (for dark field images, borrowed from Prof Robert Dickson at Department of Chemistry and Biochemistry, Georgia Tech).

Bright field images are taken when light from a tungsten lamp is focused by a bright field condenser at the sample, and the objective collected the transmitted light and focused at the camera (see scheme on the left in Figure 2-8). Bright field microscopy is used when there is enough contrast in the subject matter or if artificial staining techniques

are employed. In our lab, we have 10X, 60X and 100X objectives for bright field images. But under 100X, oil immersion is needed for better focus and resolution.

The dark field is very useful in revealing very fine details in the cells which are hard to resolve with bright field images. The condenser must have a numerical aperture higher

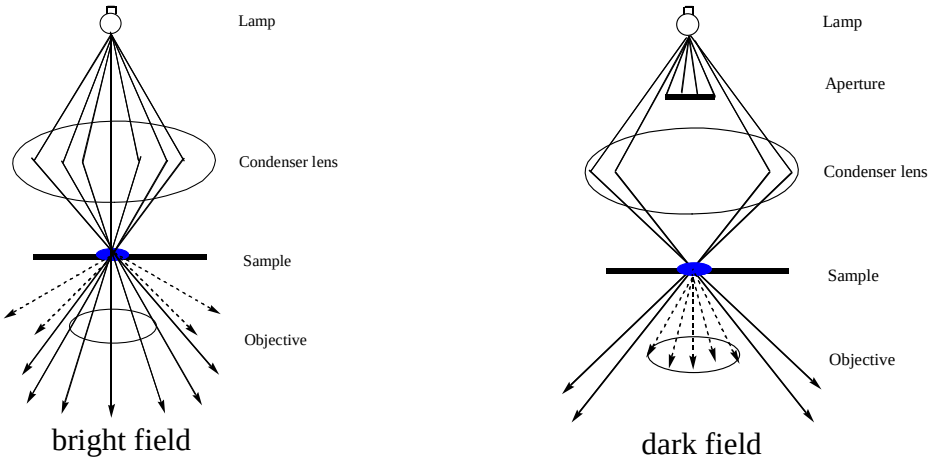

Figure 2-8: Scheme of bright (left) and dark (right) field imaging.

than the objective. In our lab, a dark field condenser (U-DCW) with high numerical aperture (0.9-1.2) delivers a very narrow beam of white light from a tungsten lamp on the top of the sample. A 100x/1.35 oil Iris objective (UPLANAPO) is used to collect only the scattered not the transmitted light from the samples. When the focus is optimized, the center of illuminating beam is blocked from entering the light collection cone of the microscope objective and only the scattered light of the side beam is collected (see right half scheme of Figure 2-8). This presents an image of bright object in a dark background. This is most useful for samples with very higher scattering crossection as in the case for the plasmonic nanoparticles. Figure 2-9 shows an example of the pictures taken under bright and dark field.

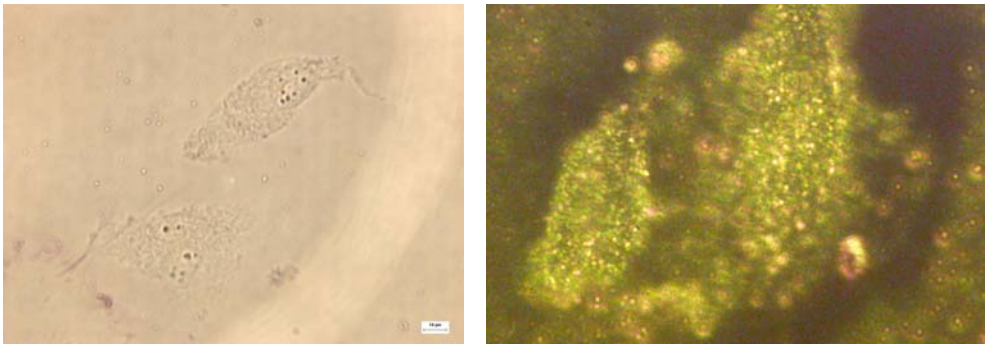

Figure 2-9: bright (left, 50X) and dark field (right, 100X) images of HOC cancer cells incubated with anti-EGFR antibody conjugated gold nanoparticles.

2.6 Laser irradiation of gold nanoparticle conjugated cells with cw lasers

For the laser irradiation experiments, the 514 nm line of the cw argon ion laser is used to heat up gold nanoparticles that have plasmon absorption at 520 nm. The argon laser at 514 nm is reflected down to the sample direction by a reflection mirror. The laser beam is focused by a lens (f = 10 cm) to form a small spot with 1 mm in diameter on the sample position where the coverslip with the cells is placed (Figure 2-10). The coverslips with the cells is immersed in PBS buffer in a Petri dish which is placed on

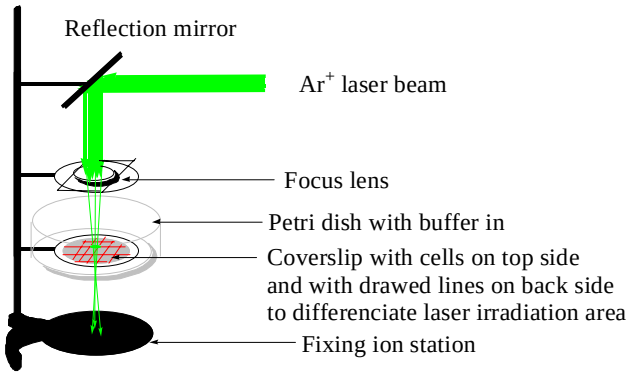

Figure 2-10: Laser irradiatin experiment setup.

the ion ring of the ion station. The coverslip is previously marked with lines to form many frames by a lab marker on the back side so that each laser irradiation position can be differentiated. After one position is irradiated for 4 mins, the laser beam is blocked and the Petri dish is moved so that the next cell frame is exposed to the laser beam and the beam power is changed. In the same way, multiple regions on the coverslips are exposed to argon laser light of different power densities for 4 min each. After the laser irradiation, the coverslip is taken out of the buffer from the Petri dish and a few drops of 0.4 % trypan blue (Sigma) solution is added on top of the cells and left to be stained for 10 mins. The trypan blue dye is used to test cell viability. Dead cells accumulated the dye and stained blue while live cells pumped the dye out and remained clear. After staining, the cells are rinsed with buffer and immersed in buffer in a petrish for bright field imaging under 10X.

When the gold nanorods are used which have their longitudinal plasmon absorption at 800 nm, a cw Ti: Sapphire laser at 800 nm is used (similar setup, with the help from Dr Wei in our lab). This wavelength is in the NIR region at which the tissue has low absorption. The red laser at 800 nm is also focused to a 1 mm diameter spot on the sample position. Multiple regions on the slides are exposed to the laser light at different power densities for 4 min each and then stained with 0.4 % trypan blue (Sigma) for 10 min to test cell viability. After staining, the samples are imaged under 10X in bright field setup.

2.7 Steady and time-resolved fluorescence spectroscopy of NADH, collagen and cells

The fluorescence spectrum of NADH solution is excited at 325 nm with a Shimadzu RF-5301PC spectrofluorophotometer in a 1cm quart cuvete. For NADH solution with higher concentrations, a 2-mm quartz is used at an angle of 45^{o} to the excitation beam so that the fluorescence came just from the front surface of the sample. The time-resolved fluorescence spectrum of NADH in the presence and absence of nanoparticles is obtained with a PTI fluorimeter with a nitrogen laser and PMT detector.

The fluorescence spectra of the living cell suspensions are obtained with the PTI fluorimeter in a 1-cm quartz cuvette. After each spectrum is taken, the cells are shaken strongly to make sure the cells do not settle at the bottom. Excitation is chosen to be at three wavelengths, one in the protein absorption region at 280 nm, another one at the NADH absorption region at 340 nm and the third at the flavor and other chromatins absorption wavelength at 370 nm. When the cells are extracted from the tissue culture dishes, the cells are put on ice and carried to our lab to measure the fluorescence immediately.

2.8 Surface enhanced Raman spectroscopy of biomolecules and cells

The Surface enhance Raman experiments are carried out on a Holoprobe series 5000 Micro-spectrometer (Kaiser optical systems, Inc, Ann Arbor, MI). The excitation wavelength is at 785 nm from a diode laser. The red laser does not damage the cells as the 514 nm argon ion laser does. Focusing on single cells is set under bright field exposure of the microscope using the 10X objective or 50X objective. The bright field is turned off and the cell is kept on the stage of the Raman microscope in the dark for data collection. The Raman microscope is housed in a black felt-lined Plexiglass box to

prevent the entrance of stray light. When the 10X objective is used, the laser power at the sample position is 2-6 mW, the focus area is 15 μm in diameter and the power density is 2800 W/cm^2. When the 50X objective is used, the laser power at the sample position is 2-3 mW, the focus area is 3 μm in diameter, and the laser density is 42000 W/cm^2.

2.9 References

(1) Grabar, K. C.; Freeman, R. G.; Hommer, M. B.; Natan, M. J. Anal.Chem. 1995, 67, 735.

(2) Frens, G. *Nat. Phys. Sci.* **1973**, *241*, 20.

(3) Murphy, C. J.; Jana, N. R. *Adv. Mater.* **2002**, *14*, 80.

(4) Nikoobakht, B.; El-Sayed, M. A. *Langmuir* **2001**, *17*, 6368.

(5) Sokolov, K.; Aaron, J.; Hsu, B.; Nida, D.; Gillanwater, A.; Follen, M.; Macaulay, C.; Adler-Storthz, K.; Korgel, B.; Discour, M.; Pasqualini, R.; Arap, W.; Lam, W.; Richartz-Kortum, R. *Technology in Cancer Research & Treatment* **2003**, *2(6)*, 491.

(6) Hayat, M. A. *Colloidal gold: principles, methods and applications*; Vol 1. ed; Academic Press: San Diego, **1989**.

(7) Nikoobakht, B.; El-Sayed, M. A. *Langmuir* **2001**, *17*, 6368.

(8) Ai, H.; Fang, M.; Jones, S. A.; Lvov, Y. M. *Biomacromolecules* **2002**, *3*, 560.

(9) Caruso, F.; Niikura, K.; Furlong, D. N.; Okahata, Y. *Langmuir* **1997**, *13*, 3427.

CHAPTER 3
SURFACE PLASMON ABSORPTION STUDIES OF ANTI-EGFR CONJUGATED GOLD NANOSPHERES AND NANORODS ON CANCER AND NONCANCER CELLS

Abstract

Gold nanospheres of various sizes and gold nanorods of various aspect rations are synthesized according to the citrate reduction and the seed-mediated growth methods, respectively. Gold nanospheres are directly bound to the anti-epidermal growth factor receptor (anti-EGFR) monoclonal antibodies. The gold nanorods are bound to the antibodies through poly (styrenesulfonate) (PSS) polyelectrolyte linker. The conjugation is characterized from the surface plasmon absorption spectra of the nanoparticles. The anti-EGFR/Au nanosphere and nanorod conjugates are bound to one nonmalignant epithelial cell line, HaCaT (human keratinocytes) and two malignant epithelial cell lines, HOC 313 clone 8 and HSC 3 (human oral squamous cell carcinoma). The surface plasmon absorption spectra of gold nanoparticles on the single cells are measured to qualitatively and quantitatively characterize the binding of the conjugates with the healthy and cancer cells. The anti-EGFR/Au nanospheres are found to have a surface plasmon absorption maximum at 545 nm when bound to the cancer cells but at 552 nm when added onto the normal cells, suggesting that absorption spectroscopy can be used for cancer diagnostics with this technique in the visible region of the spectrum. Due to the broad nature of the gold nanorod spectrum, its absorption spectroscopy does not offer a clear method for cancer diagnostics. The work has been published in Nano Letters, 2005, 5 (5), 829 and JACS, 2006, 128 (6), 2115.

3.1 Introduction

As we have learnt in Chapter 1, gold nanoparticles show a strong surface plasmon absorption band in the spectrum when the frequency of the electromagnetic field is in resonance with the coherent electron motion (see Chapter 1, Page 1-5). The wavelength maximum of the surface plasmon absorption band is dependent on many parameters including the size and shape of the metal nanoparticles. As the size increases, the absorption maximum red shifts. The surface plasmon absorption of gold nanoparticles is also dependent on the dielectric constant of the metals as well as that of the medium surrounding the particles. This provides a great possibility for the nanoparticle to be used as a sensitive biosensor.

The surface plasmon absorption band of gold nanorods splits into two bands: A strong long wavelength band due to the longitudinal oscillation of electrons and a weak short wavelength band around 520nm due to the transverse electronic oscillation (see Chapter 1, Page 5-9). The longitudinal absorption band shifts from the visible to longer wavelength as the rod's aspect ratio increases. This tunable optical property of gold nanorods makes them useful in many biological applications such as photothermal cancer therapy.

Gold nanoparticles have been conjugated to many biomolecules such as DNA (1-4), proteins (5-9) and sugars (10). Chad Mirkin used surface absorption spectra of gold nanospheres to monitor the hybridization of complimental DNA. When thiolated DNA single strand DNA is bound to the surface of gold nanospheres, the absorption maximum is shifted from 519 nm to 524 nm due to the Au-S bond formation (See Figure 3-1, absorption spectra A). After being hybridized with another complimentary DNA which is

also conjugated to nanoparticles, the nanoparticles aggregate and the surface plasmon absorption band decreases in intensity and red shifts in position (See Figure 3-1, absorption spectra B).

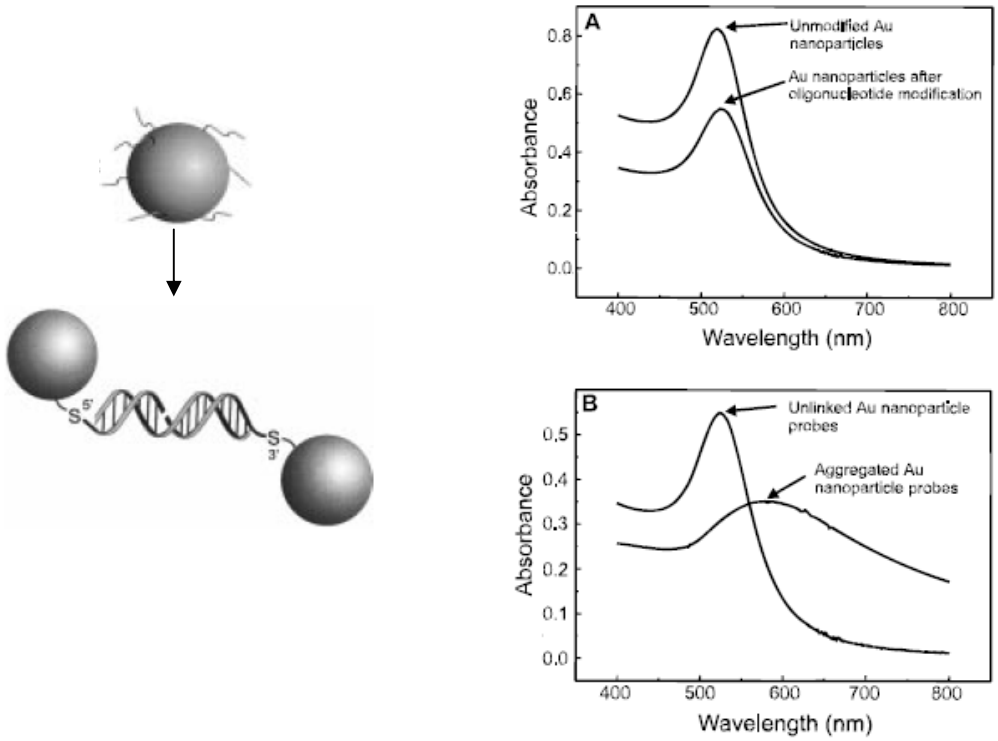

Figure 3-1: DNA assembly of gold nanoparticles (left) and comparison of UV-vis spectra during DNA assembly (right) (2).

Mann et al. uses the longitudinal absorption band of gold nanorods to monitor the hybridization of DNA (3). When complementary DNA is bound to rods in advance is duplexed, the longitudinal absorption band of gold nanorods decreases in peak intensity and blue shifts in peak position (see Figure 3-2).

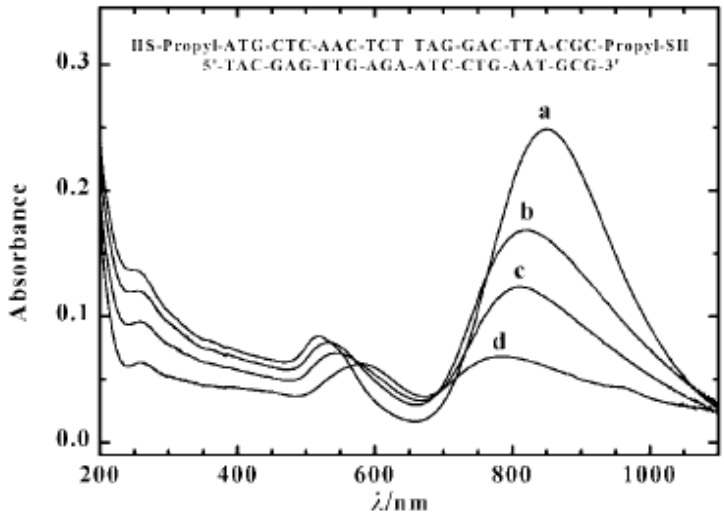

Figure 3-2: UV–VIS spectra of a suspension of non-complementary DNAfunctionalised nanorods. (a) 0 s, (b) 10 min, (c) 1 h, (d) 2 h after duplex initiation arising from the addition of the third complementary strand. Sequences of the three oligonucleotides are shown in the insert (3).

Gold nanoparticles have been conjugated to various antibodies for biological applications such as staining studies since 1950s' (11). The conjugates are simply formed by noncovalant interactions between the citrate capping molecules and the antibodies (see Figure 3-3). The binding is in such a way that the bioactivity of the antibodies are preserved and thus the conjugates can be used for further biofunctional studies such as imaging cancer biomarker (12) and probing pathologic bacteria (13). Very recently,

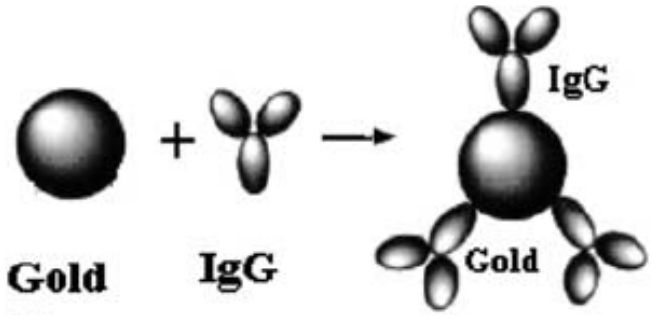

Figure 3-3: The binding of antibody to gold nanoparticles (14).

gold nanorods have been reported to be bound to antibodies and characterized for biological applications (15) (see Figure 3-4).

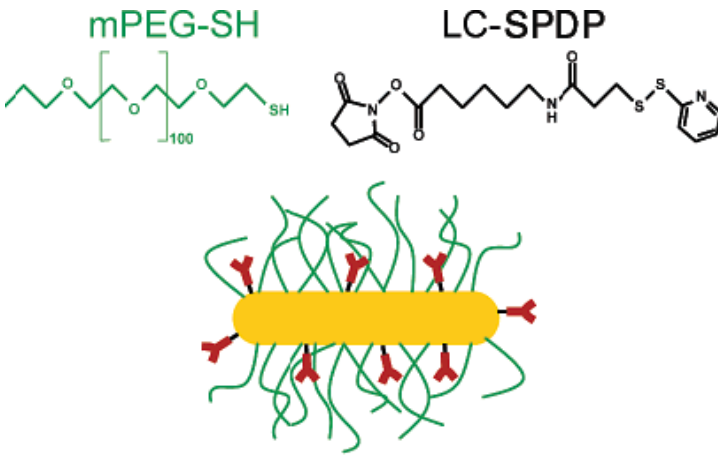

Figure 3-4: The binding of antibody to gold nanorods (15).

They replace the stabilized surfactant bilayer by thiol terminated methoxypoly(ethylene glycol) so that the nanorods are stable in buffer solutions free of surfactant. Nanorod bioconjugation is accomplished with a heterobifunctional cross-linker, LC-SPDP. Nanorod bioconjugates are characterized by independent measurements of the nanorod and antibody concentrations.

In the present study, anti-EGFR monoclonal antibodies are conjugated with gold nanospheres using the method describe by Sokolov et al (12). The nanorods are firstly coated with a negatively charged PSS layer and then bound to antibodies. All these conjugates are incubated with the HaCat (human keratinocytes) healthy cells and HOC 313 and HSC 3 (human oral squamous cell carcinoma) cancer cells. The absorption spectra of the conjugates and after bound to cell surfaces are measured and discussed.

3.2 Experimental

Gold nanospheres and nanorods in different sizes are synthesized according to the procedures described in detail in Chapter 2, Page 54-59. The sizes are determined from their absorption spectrum and TEM (see Page 4, Figure 1-3, Page 7, Figure 1-6). Three sizes of gold nanospheres with the absorption maximum at 519, 529 and 535 nm and one size of gold nanorods with longitudinal absorption maximum around 800 nm arechosen for the conjugation with the anti-epidermal growth factor receptor (anti-EGFR) monoclonal antibodies (House, clone29.1, Sigma).

The conjugation procedure of gold nanoparticles with anti-EGFR antibodies is described in detail in Chapter 2, Page59-62. The success of binding of the antibody to the gold nanospheres which is capped by citrate is not only confirmed by the red shift of the absorption maximum (discussed later), but also by the fact the antibody bound gold nanospheres are stable in PBS buffer (while the bare gold nanospheres are very unstable and aggregate in the same buffer). The success of binding of the gold nanorods is confirmed by the fact that the conjugates can be centrifuged down (before conjugation, the nanorods have been centrifuged twice to get rid of free CTAB molecules) and dispersed in buffer while the bare gold nanorods can not be centrifuged at the third time and they are not stable in buffer.

After the gold nanoparticles are conjugated with the antibodies, they are dispersed in PBS buffer at some concentration for their incubation with the living cells. For nanospheres, the optical density at the absorption maximum is adjusted to a value between 1.5 to 2.0. For gold nanorods, the optical density at the longitudinal absorption

maximum is adjusted to a value between 0.8 to 1.0. The use of lower concentration for the nanorods might be due to the higher affinity of antibody to nanorods which is due to the contribution of the hydrophobic interaction of the PSS and the antibody (16, 17). After the cells are grown on coverslips (see Chapter 2, Page 49-54, cell culture for detail procedure) for 2 or 3 days, the cells are taken out from Prof Edmonds' lab to our lab, rinsed with PBS buffer and then a few drops of the nanoparticles are added on top of the cells and wait for 40 mins. For gold nanorods, 30 mins incubation is found to be sufficient. For the nanorods, you can see the cells are stained red within 5 mins which is due to the binding of gold nanorods onto the cells. After the incubation, the free nanoparticles are rinsed out with PBS buffer and the cells are fixed with paraformaldehyde and coated with glycerol and sealed with glue. Then the cells are taken to Prof Mohan's lab to measure absorption spectra of gold nanoparticle on single cells.

For comparison, the gold nanospheres are also incubated into cells by putting the nanoparticles (several drops of nanopsrticles with optical density at 3.5 at the absorption maxiumum in the well of the 12-well plates) in the medium while the cells are growing (the coveslip is put in the well and the cells are grown on the coverslip). In this way the nanoparticles diffuse into cells by endocytosis. The absorption spectra of the nanoparticles inside the cells are compared with the nanoparticles bound on the cell surface.

3. Results and discussion

3.3.1 Gold nanospheres

By just changing the citrate amount, various sizes of gold nanoparticles from 15 nm to 100 nm can be prepared (see Chapter 2, Page 55-56). Figure 3-5 shows the absorption spectrum and the TEM of the nanospheres used for the study.

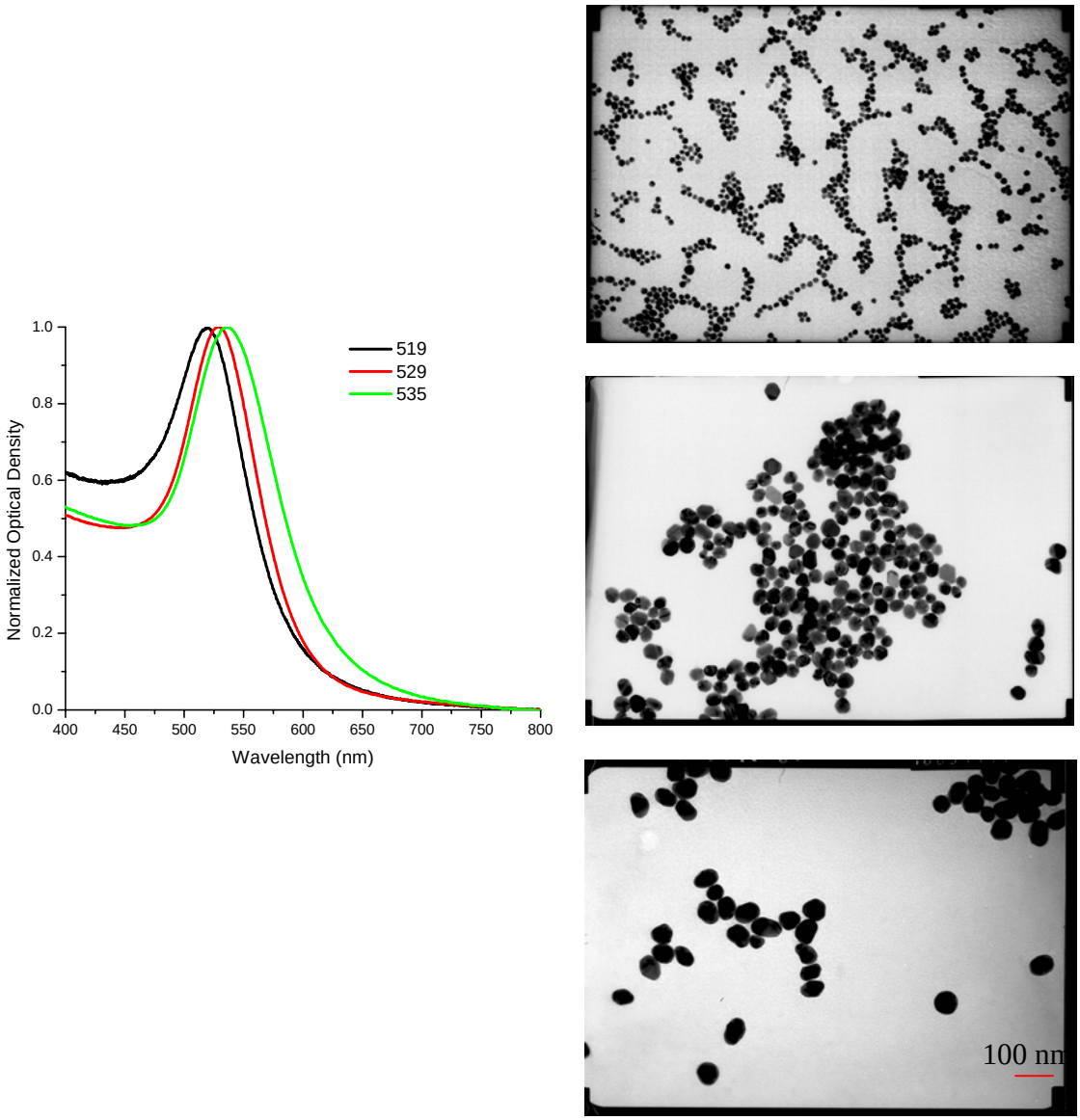

Figure 3-5: Gold nanospheres of different sizes obtained by changing citrate amount. Left: absorption spectra, right: TEM of the samples with absorption maximum at 519nm (top, 15 nm), 529 nm (middle, 35 nm) and 535 nm (bottom, 50nm).

The surface plasmon absorption maxima of the anti-EGFR antibody conjugated gold nanoparticles are shown in Figure 3-6. Among all the three sizes, the absorption maximum shows obvious red shift. For the 15 nm (λ_{max} = 519 nm), the absorption maximum shifts by 6 nm, for the 35 nm gold nanoparticles (λ_{max} = 529 nm), the absorption maximum shifts by 7 nm and for the 50 nm gold nanoparticles (λ_{max} = 535 nm), the absorption maximum shifts by 12 nm. This red shift is due to the change in the dielectric constant of the medium around gold nanoparticles. Antibody binding changed the local environment and thus the surface plasmon absorption of the nanoparticles is changed.

For binding the cells, the sizes of 35 nm are chosen after experimental determination of the cellular labeling efficiency and the light scattering experiment of the nanoparticles (describe in the next Chapter). Smaller nanoparticles have smaller light scattering crossection than larger nanoparticles. They also give more greenish scattered color which cannot be easily resolved from the scattered green light of the cellular organelles. Larger nanoparticles have higher scattering crossection but have smaller labeling efficiency possibly due to steric hindrance.

Figure 3-7 shows the absorption spectra of conjugated gold nanoparticles after binding to cells. Statistically 25 cells are measured. Each spectrum is from the sample area of 8 μm in diameter. The cells are over 10 μm. So each spectrum is from part of a cell. From Figure 3-7 we can see that the nanoparticles bound to all types of cells red shift greatly compared to the conjugated nanoparticles in solution in Figure 3-6.

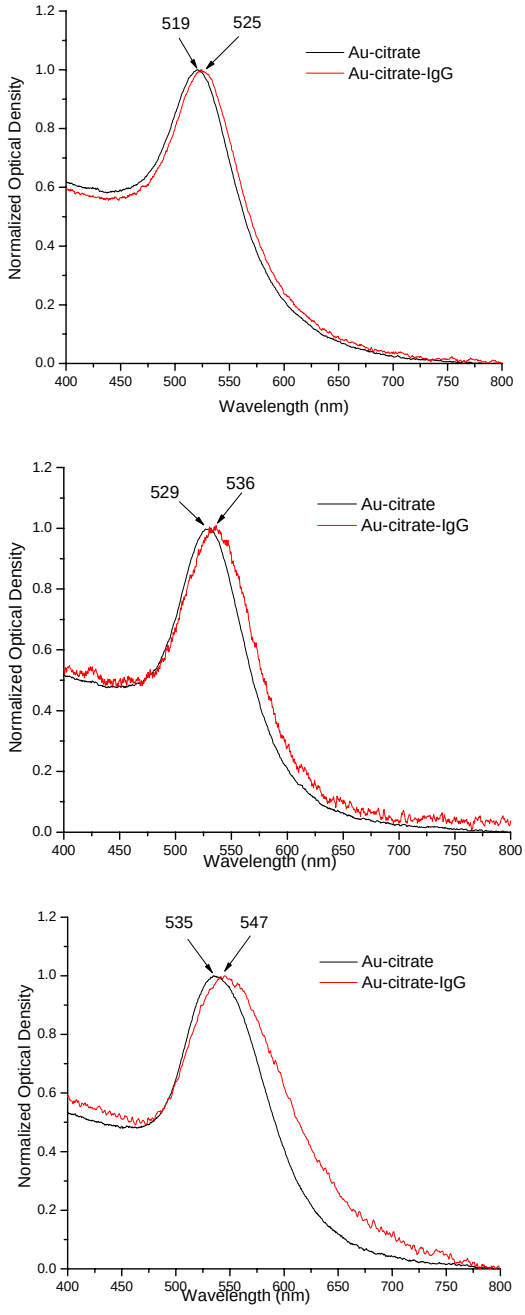

Figure 3-6: The absorption spectra of gold nanoparticles and the conjugates of gold nanoparticles with anti-EGFR antibody.

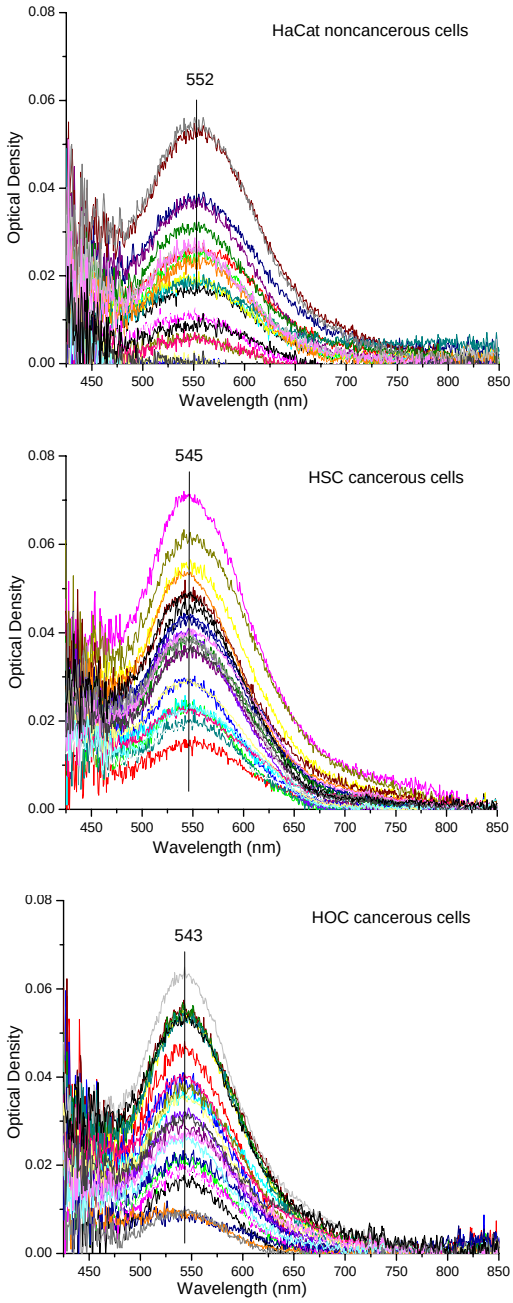

Figure 3-7: The absorption spectra of anti-EGFR antibody conjugated gold nanoparticles on single cells.

HOC and HSC cancer cells have similar absorption maxima at around 545 nm which is 9 nm red shifted compared to the isolated anti-EGFR/Au solutions at 536 nm. This red shift could be due to the specific binding of the anti-EGFR antibodies on the gold surface to EGFR on the cell surface. One can use the maximum at 545 nm to characterize the conjugated nanoparticle binding to the EGFR on the cell surface. For HaCaT noncanerous cells, the nanoparticles have their maximum at 552 nm. The maximum difference indicates the difference in the dielectric constant of the local environment around gold nanoparticles of the healthy cells compared to cancer cells. The well organized nanoparticles on the cancer cell surface have a different environment than that on the noncancerous cell surface which has a heterogeneous environment.

For comparison, the nanoparticles inside the cells is also measured. Figure 3-8 shows the absorption spectrum of the nanoparticles in the three types of cells. To statistically characterize the surface plasmon absorption of the gold nanoparticles inside the cells, 25 cells of each kind are measured. The NPs inside all cells have a major peak around 545 nm characteristic of the surface plasmon absorption of the individual nanoparticles inside the cytoplasm of the cells. This is red shifted by 16 nm compared from that of the colloid nanoparticles suspension (at 529 nm). This suggests that the nanoparticle surface has a different dielectric environment when present inside the cells. The broad absorption around 700 nm of the gold nanoparticles inside the cells is characteristic of the aggregated gold nanoparticles. Aggregation of the nanoparticles is likely induced by the salts in both the growth medium and the cytoplasm of the cells. The capping material of citrate molecules could be dissolved inside cells and thus leads to aggregation of the resulting metallic nanostructures.

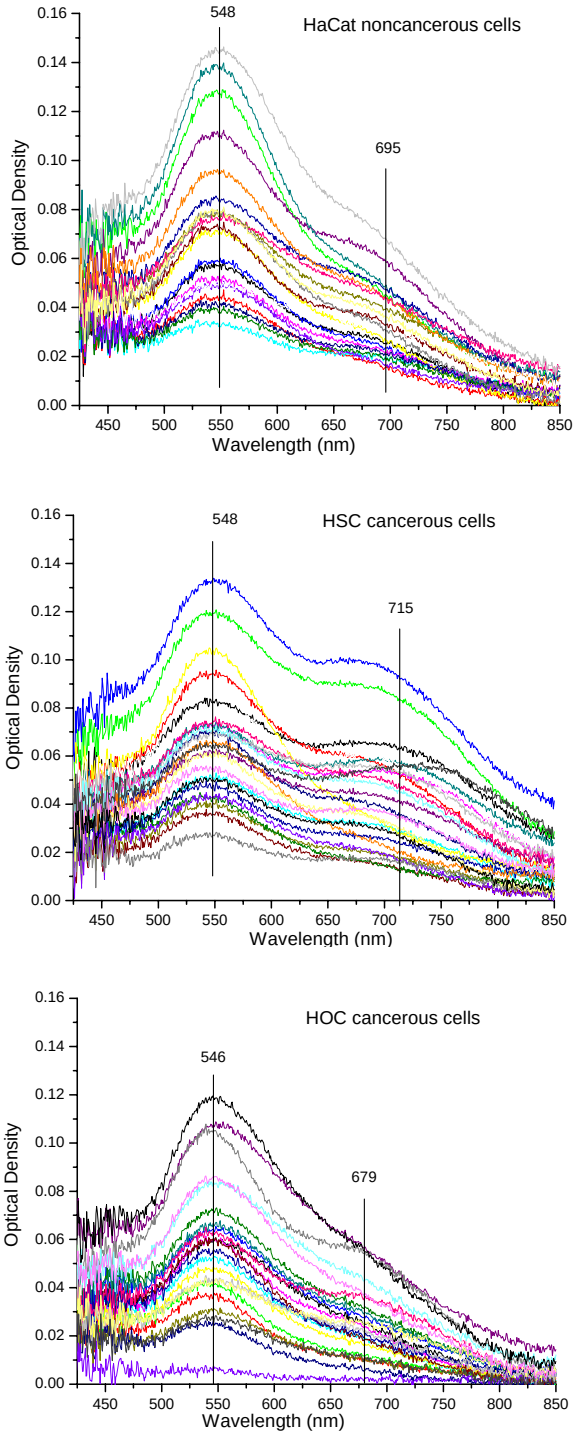

Figure 3-8: The absorption spectra of colloidal gold nanoparticles inside single cells.

In HSC cells, the aggregates have the absorption maximum at 715 nm. In HaCaT cells, the size of these large aggregates is smaller as concluded from the shorter wavelength surface plasmon absorption maximum. The absorption of the aggregates inside HOC is not as resolved due to the shorter wavelength (679 nm) which is close to the absorption maximum of the surface plasmon absorption of the individual nanoparticles. The different sizes of the aggregates inside different kinds of cells may reflect the difference in the cell cytoplasm medium. The ability to resolve aggregates within cells by SPRA spectroscopy suggests that different capping agents could be utilized to monitor intracellular processes as the aggregates are formed.

3.3.2 Gold nanorods

By changing the silver amount during the rod preparation process (see Chapter 2, Page 57-59 for details), the aspect ratios of gold nanorods can be changed (see Page 7, Figure 1-6 for the absorption spectra and TEM images).

The nanorods with aspect ratio of 3.9 is chosen for the conjugation with antibodies and with cells due to the overlapping of the absorption longitudinal maximum of the rods with the NIR Ti:Sapphire laser wavelength (800 nm) which will be used for the photothermal therapy (describe later). Figure 3-9 shows the absorption spectra during the change of the surface charge by PSS and the antibody binding process. From Figure 3-9, we can see that there is no shift in the absorption maximum after PSS coating. After the antibody binding to the PSS laser, there is 10 nm blue shift of the longitudinal absorption maximum, while there is no shift in the absorption maximum of the transverse band during the whole process. The intensity of the transverse absorption maximum increased

slightly after PSS coating and antibody binding. When PSS is bound, it does not affect the gold nanoparticle absorption much due to the covalently capped thick bilayer of the CTAB molecules (see structure in Figure 3-9). When antibody is bounded, it may cause conformation changing in the PSS and the CTAB layers and thus shifts the absorption maximum.

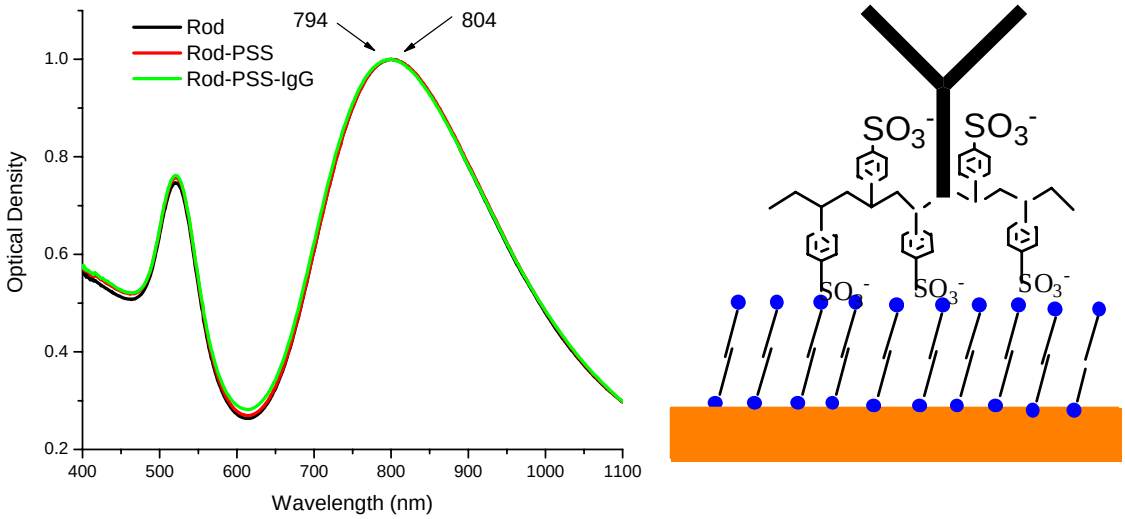

Figure 3-9: The absorption spectra of bare gold nanorods, PSS coated nanorods and antibody bounded nanorods (left) and the structure of the conjugates (right).

Figure 3-10 shows the absorption spectra of conjugated gold nanorods after binding to the three types of cells. Compared to the conjugates in solution (Figure 3-9), the peak maximum of the longitudinal absorption band is red shifted by about 80 nm. This is probably due to the interparticle interaction resulting from the assembly of nanoparticles on the cell surface. This interplasmon interaction of nanorods has also been observed on carbon nanotube surfaces and in solution (16-18).

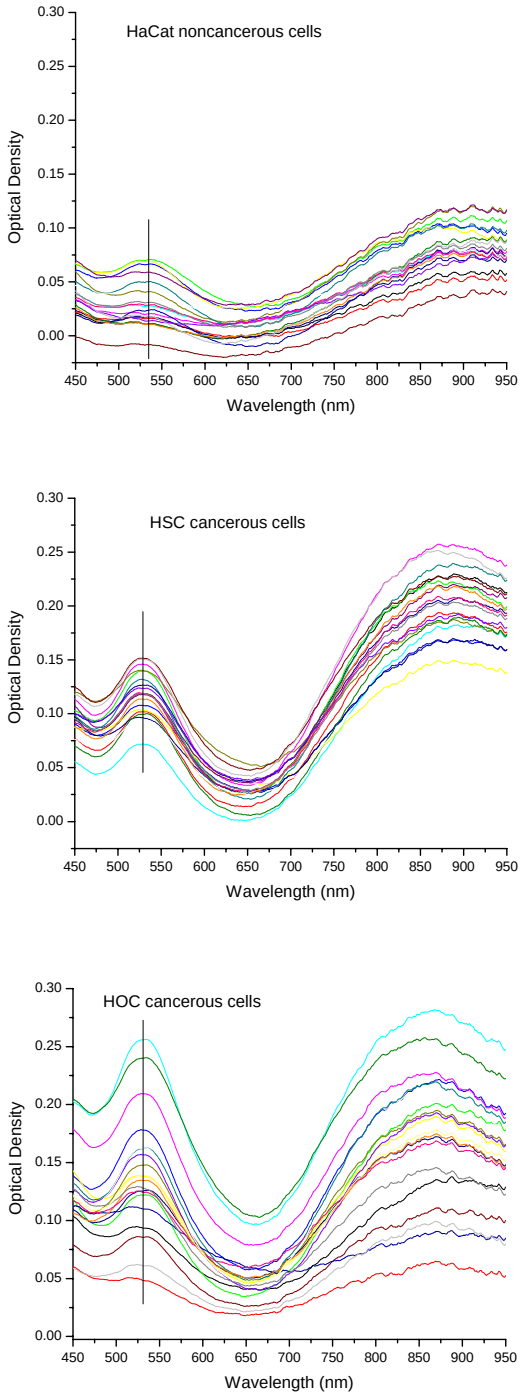

Figure 3-10: The absorption spectra of anti-EGFR antibody conjugated gold nanorods on single cells.

Due to the broadening of the longitudinal absorption band, its peak position can not be used to differentiate the cancer and noncancer cells. However, the transverse band is sharper and shows difference in the wavelength maximum. In the cancer cells, the maximum is at 530 nm while in the noncancer cells it red shifts to 535 nm and is broader. Compared to the spheres shown in Figure 3-7, the optical density of the nanorods are much higher for each type of cells. This might be due to the higher affinity of antibody to the PSS molecules on the nanorods than that between antibodies to citrate molecules. The higher affinity of PSS with antibody is due to the strong hydrophobic interaction between antibody and the aryl portion in the PSS molecules. Another reason might be that the nanorods have higher absorption coefficient (~ 10^9) than spheres (~10^8) so they giver higher optical density for the same amount of nanoparticles between nanorods and nanospheres.

From Figure 3-10 we can also see that statistically the amount of gold nanorods on the two cancerous cells is about double of the amount of nanorods on the noncancerous cells. This is due to the specific binding of the antibodies to the overexpressed EGFR on the cancerous cells. But the nanorods amount can not be attributed to the amount of EGFR amount on the cancerous and healthy cells because of the nonspecific binding of antibodies to the healthy cells.

3.4 References

(1) Storhoff, J. J.; Elghanian, R.; Mucic, R. C.; Mirkin, C. A.; Letsinger, R. L. *J. Am. Chem. Soc.* **1998**, *120*, 1959.

(2) Mucic, R. C.; Storhoff, J. J.; Mirkin, C. A.; Letsinger, R. L. *J. Am. Chem. Soc.* **1998**, *120*, 12674.

(3) Dujardin, E.; Hsin, L. B.; Wang, C. R.; Mann, S. *Chem. Commun.* **2001**, 1264.

(4) Niemeyer, C. M. *Angew. Chem. Int. Ed.* **2001**, *40*, 4128.

(5) Connolly, S.; Fitzmaurice, D. *Adv. Mater.* **1999**, *11*, 1202.

(6) Caswell, K. K.; Wilson, J. N.; Bunz, U. H. F.; Murphy, C. J. *J. Am. Chem. Soc.* **2003**, *125*, 13914.

(7) Grabar, K. C.; Freemant, R. G.; Hommer, M. B.; Natan, M. J. *Anal. Chem.* **1995**, *67*, 735.

(8) Tsai, C. S.; Yu, T. B.; Chen, C. T.; *Chem. Commun.*, **2005**, 4273.

(9) Chah, S.; Hammond, M. R.; Zare, R. N. *Chemistry & Biology*, **12**, 323.

(10) Barrientos, A. G.; de la Fuente, J. M.; Rojas, T. C.; Fernandez, A.; Penades, S. *Chem. Eur. J.* **2003**, *9*, 1909.

(11) Hayat, M. A. *Colloidal gold: principles, methods and applications*; Vol 1. ed; Academic Press: San Diego, **1989**.

(12) Sokolov, K.; Follen, M.; Aaron, J.; Pavlova, I.; Malpica, A.; Lotan, R.; Richartz-Kortum, R. *Cancer Res.* **2003**, *63*, 1999.

(13) Ho, K. Ch.; Tsai, P. J.; Lin, Y. S.; and Chen, Y. C. *Anal. Chem.* **2004**, *76*, 7162.

(14) Zhang, C. X.; Zhang, Y.; Wang, X.; Tang, Z. M.; Lu, Z. H. *Analytical Biochemistry* **2003**, *320*, 136.

(15) Liao, H.; Hafner, J. H. *Chem. Mater.* **2005,** *17*, 4636.

(16) Ai, H.; Fang, M.; Jones, S. A.; Lvov, Y. M. *Biomacromolecules* **2002**, *3*, 560.

(17) Caruso, F.; Niikura, K.; Furlong, D. N.; Okahata, Y. *Langmuir* **1997**, *13*, 3427.

CHAPTER 4
BRIGHT AND DARK FIELD IMAGING OF CANCEROUS AND NONCANCEROUS CELLS INCUBATED WITH GOLD NANOPARTICLES

Abstract

Bright field (light transmission mode) and dark field (light scattering mode) imaging of HaCat normal cells, HSC and HOC cancer cells with and without gold nanospheres and nanorods incubation are discussed. Two methods are used to incubate the gold nanospheres with the cells: One is to add colloidal gold to the cell growth medium and the cells are left to grown for overnight in the presence of the nanospheres. In this way, the nanospheres enter into cells by endocytosis process. The other method is to incubate anti-EGFR antibody conjugated gold nanospheres with the cells for 40 mins and the nanospheres are bound to cells through EGFR on the cell surface. For incubation with gold nanorods, only anti-EGFR/Au nanorod conjugates are incubated with the cells and located on the cell surface by specific binding between antibody and the EGFR on the cell surface. Both transmission and light scattering imaging are used to characterize the gold nanoparticles inside the cells or on the surface of the cells. From the light scattering images, the cancer cells are clearly distinguishable from the healthy cells by using either gold nanospheres or nanorods. This is due to the specific binding of the anti-EGFR/Au conjugates to the overexpressed EGFR on the cancer cell surface. The work has been published in Nano Letters, 2005, 5 (5), 829 and JACS, 2006, 128 (6), 2115.

4.1 Introduction

Cellular and tissue imaging is one of the most important ways for the detection of pathosis in biology and medicine. Radiographic imaging modalities such as CT scan and MRI can delineate the deep extent of carcinomas (1). But they are not sufficiently sensitive to detect small, earlier intraepithelial lesions which are more readily cured. Cellular imaging utilizing microscope techniques provides anatomic details of cells and tissue architecture important for cancer diagnostics and research. Currently used optical probes include chemiluminescent, fluorimetric and colorimetric techniques (2). Optical imaging is a relatively new modality which enables real time, non-invasive, high resolution imaging of epithelial tissue (3-7).Optical imaging systems are inexpensive, robust and portable because of advances in computing, fiber optics and semiconductor technology.

Imaging the molecular features of cancer requires molecular specific contrast agents which can safely be used in vivo as well as cost-effective imaging systems to rapidly and noninvasively imaging the uptake, distribution and binding of these agents in vivo. One of the earlier contrast agents is the conventional organic dyes (8-9). They are bright and can be used for both cytoplasmic and nuclear labeling due to the small size molecules. But one of the problems is that they are not photostable. After one minuets irradiation with a laser, they are totally bleached and can not be used anymore (10). Thus, the fluorescent semiconductor nanoparticles emerged, which is called quantum dots (11-13). Quantum dots have wide absorption ranges and unique size dependent fluorescence properties. They are highly fluorescent and photobleach resistant. They can provide

single excitation for multicolor images which is not possible for molecular fluorophors because of their narrow excitation spectra.

Another kind of contrast agents is metal nanoparticles which use the bright light reflectance properties (14-17). Metal nanoparticles have the ability to resonantly scatter visible and near infrared light upon the excitation of their surface plasmon oscillation. The scattering light intensity is extremely sensitive to the size and aggregation state of the particles. Preliminary studies have reported their use as contrast agents for biomedical imaging using confocal scanning optical microscopy (17), multiphoton plasmon resonance microscopy (15), optical coherence microscopy (18) and third-harmonic microscopy (19).

In the present work, we use a very simple and inexpensive conventional microscope with proper rearrangement of the illumination system and the light collection system to imaging cells which are incubated with colloidal gold or with anti-epidermal growth factor receptor (anti-EGFR) antibody conjugated gold nanoparticles. The optical properties of the gold nanoparticles incubated in single living cancerous and noncancerous cells are compared for different incubation methods.

4. 2 Experimental

The detail bright and dark field procedures as well as their principles have been described in detail in Chapter 2, Page 64-66. In bright field imaging, the light goes through the samples and the transmitted light is detected. In dark field imaging, the light is scattered by the samples and the transmitted light is blocked and only scattered light is

detected. In this way, the background is dark and the sample which scatters strongly gives very bright images. Under the illumination with a beam of white light, multicolor images can be seen due to the differently scattered light wavelength. Both the bright and dark field images are taken with our inverted Olympus IX70 microscope (some dark field pictures are taken with Olympus IX70 in Prof Robert Dickson's lab).

The nanospheres are incorporated with living cells (grown on coverslips) with two methods. One is to add 40 nm colloidal gold into the cell growth medium and the cells are left to grown overnight in the presence of the nanoparticles. In this way, the nanoparticles are incorporated inside cells by endocytosis process during cell division and proferlitation. In the other method, gold nanospheres are conjugated anti-EGFR antibodies and then incubated with living cells in buffer at room temperature outside incubator for 40 mins (see Chapter 2, Page 59-61 for detail information). In this way, the nanoparticles are mostly stay at cell surface due to the short incubation time and the specific binding of anti-EGFR to the EGFR on the cell surface. Then the cells with gold nanoparticles incorporated are fixed and sealed with another coverslip with a layer of glycerol filled between and then used for bright and dark field imaging.

The nanorods are incorporated with cells only after conjugation with antibodies. The nanorods are coated with PSS polyelectrolyte and conjugated with anti-EGFR antibodies (see Chapter 2, Page 61-62 for detail information). The conjugated nanorods are incubated with living cells at room temperature for 30 mins in buffer outside incubator. The cells are then fixed, sealed and then used for bright and dark field imaging. The nanorods have problems to be incorporated inside cells because the nanorods aggregate in

the cell growth medium and mess up the cell growth environment. Thus the cells can not grow. The cell death is also caused by the cytotoxicity of the free CTAB molecules in the nanorods solution. The cytotoxicity of the free CTAB molecules has been reported by some other group (20).

4.3 Results and discussion

4.3.1 Bright field imaging (light transmission mode)

The nanoparticles we used for both incubation inside cells and conjugation with antibodies are 40 nm in diameter. Figure 4-1 shows the absorption spectrum and the TEM images of the nanoparticles.

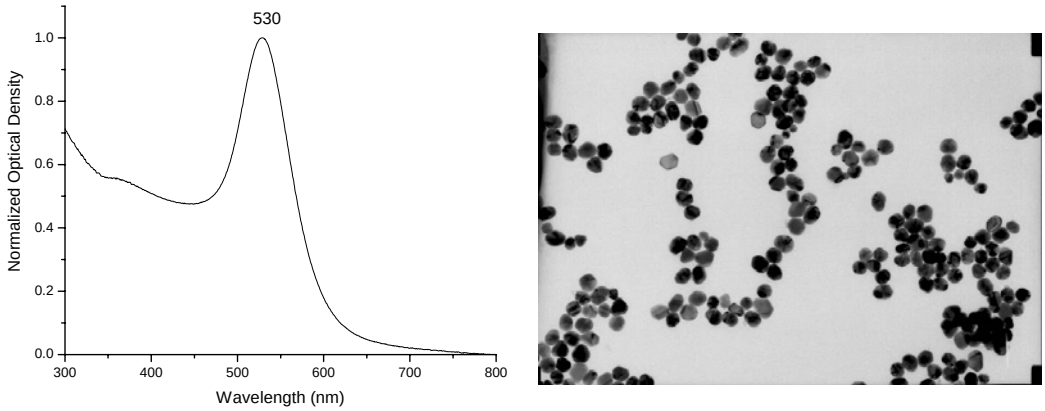

Figure 4-1: Absorption spectrum (left) and TEM image (right) used for the treatment of gold nanospheres with cells.

Figure 4-2 shows the bright field images of both cancer and healthy cells without gold nanoparticle (control cells, top row), with colloidal gold incubated (middle row) and with anti-EGFR/Au nanosphere conjugates incubated (bottom row). In the bright field, the camera detects the transmitted light trough the sample, the coverslip background shows very bright color and thus the fine structures of the cells can not be recognized.

From this figure we can see that the three types of cells have different structure character. HOC cancer cells are almost 4 times larger than HaCaT or HSC cells. HaCaT and HSC cells show almost homogenous diamond shapes while HOC cells have other shapes. The HaCat normal cells grow in a different way. They like to grow in a clump style. Usually no individual cells are observed during HaCat grow process while the other two cancer cells can grow individually.

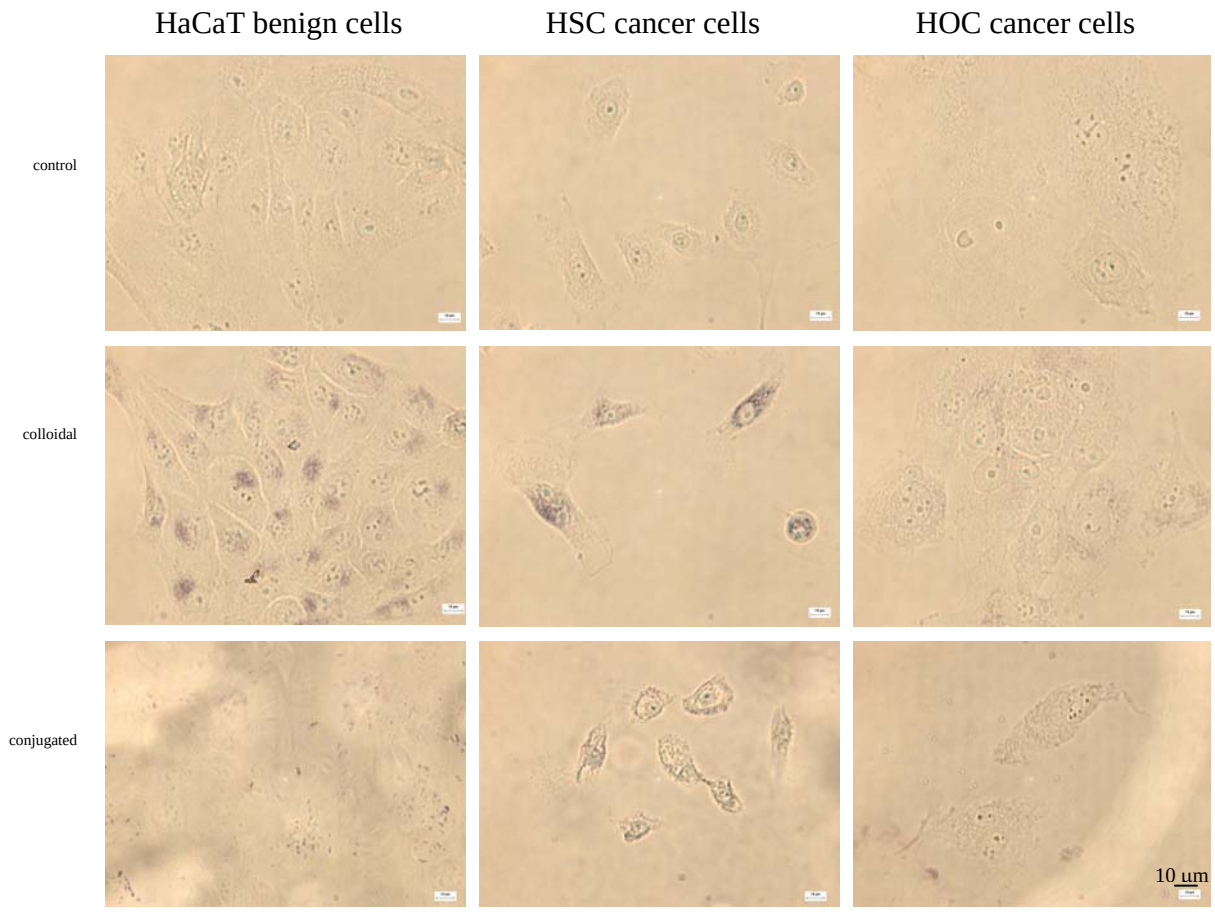

Figure 4-2: The bright field images of HaCaT normal cells (left column), HSC cancer cells (middle column) and HOC cancer cells (right column) without gold (top row), with colloidal gold incubated inside cells (middle row) and with anti-EGFR/Au nanosphere conjugates (bottom row) bound on the cell surface. Magnification: 50x.

When incubated in the presence of nanoparticles, the cells grow as usual and the nanoparticles are accumulated inside the cells. The gold nanoparticles can be seen clearly under 50x as red spots inside the cells. It can be seen that gold nanoparticles are predominantly accumulated inside the cytoplasm of the cells. It is well known that gold nanoparticles enter into cells by endocytosis process. In most HaCaT noncancerous cells (middle, left image) the gold nanoparticles demonstrate a spotted pattern inside the cytoplasm while the nanoparticles are homogenously distributed in the cytoplasm of HSC (middle image) and HOC (middle, right image) cancer cells. The difference of the distribution of nanoparticles inside cells may reflect the difference of the cell differentiation and proliferation processes. It can also be seen that the HOC cancer cells take less nanoparticles than the other two types of cells. This could be due to the slower growth speed of this type of cells than the HaCat and HSC cells.

When anti-EGFR antibodies (optical density of 2.5 at 530 nm) are conjugated to gold nanoparticles, the nanoparticles can not be recognized in bright field. The HaCaT noncancerous cells could not be identified individually (bottom left image). This is due to the poor labeling of the cells by the nanoparticles. The HSC (bottom middle image) and HOC (bottom right image) cancerous cells show better contrast than the control cells, which is due to the binding of the anti-EGFR/Au conjugates to the surface of the cancer cells. This contrast difference between the normal and cancer cells is due to the specific binding of overexpressed EGFR on the cancer cells with the anti-EGFR antibodies on the gold surface.

Figure 4-3 shows the absorption spectrum and TEM image of the gold nanorods used in the experiment. The nanorods have an absorption maximum of the longitudinal band at 800 nm with an aspect ratio of 3.9.

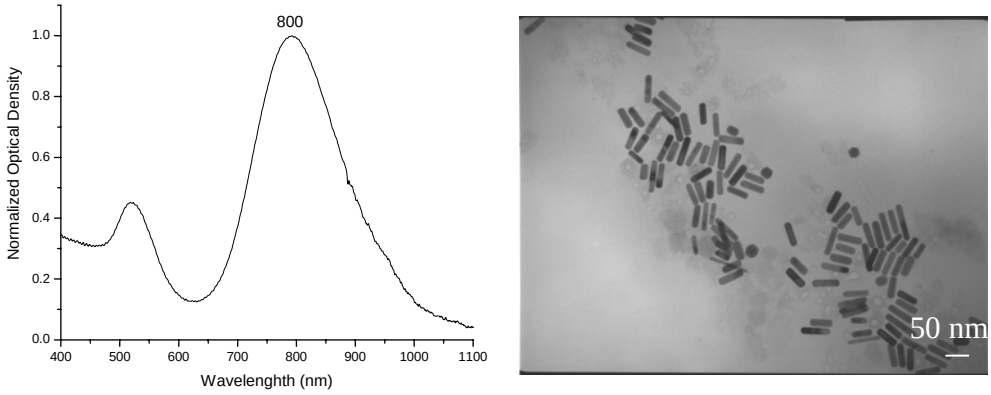

Figure 4-3: Absorption spectrum (left) and TEM image (right) used for the incubation of gold nanorods with cells.

Figure 4-4 shows the bright field images of both cancerous and noncancerous cells without gold nanoparticle and with anti-EGFR/Au nanorod conjugates incubated. For better comparison, we choose 10x and 60x to image the cells. The top two rows show the images of the control cells. The middle two rows show the images after incubated with anti-EGFR/Au nanorod conjugates with optical density of 0.6 at 800 nm (the absorption maximum of the longitudinal band). The bottom two rows show the images after incubation with anti-EGFR/Au nanorod conjugates with optical density of 1.2 at 800 nm. From this figure we can see that at lower concentration of the conjugates, the HaCat healthy cells can not be clearly identified individually but the two cancer cells can be seen clearly. This is consistent with the results when using gold nanospheres. When the concentration of the conjugates doubled, the HaCat normal cells can be recognized, but the gold nanorods (red color on the cells) show different pattern from the two cancer cells.

10x
control

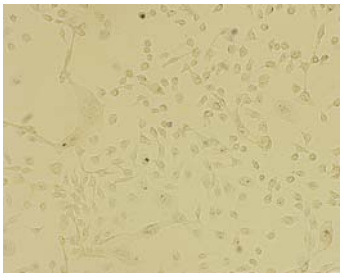
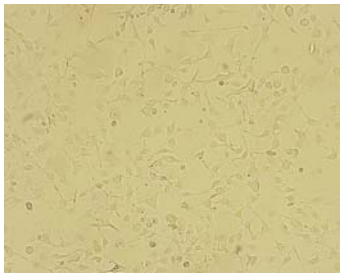
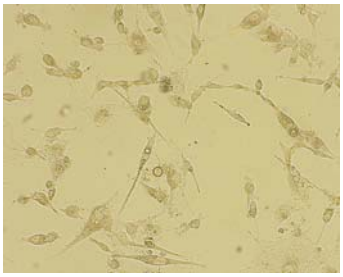

60x
control

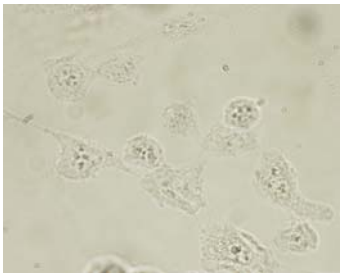
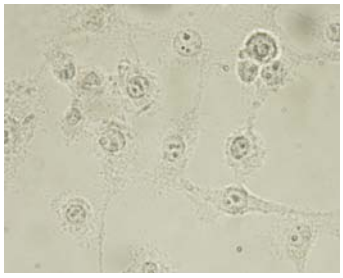


10x
lower conc

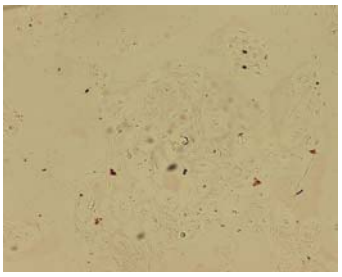
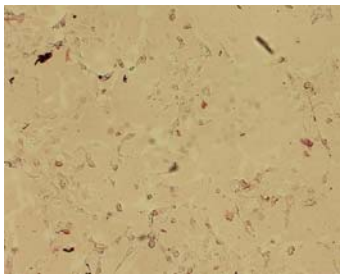
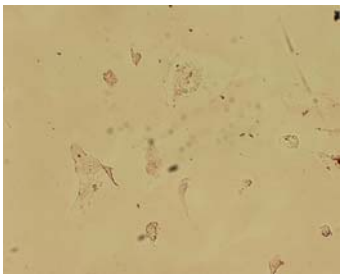

60x
lower conc

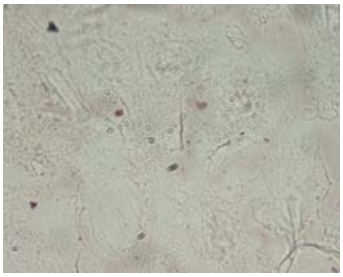
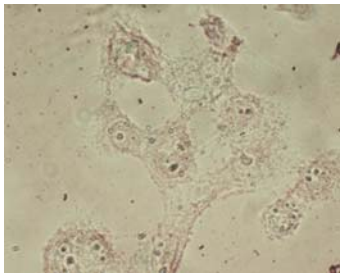
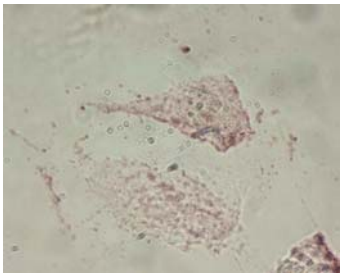

10x
higher conc

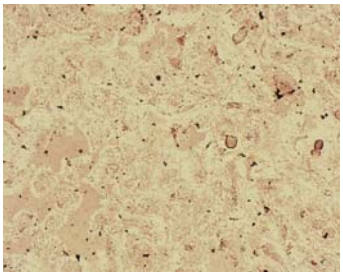
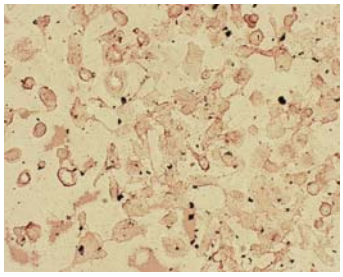
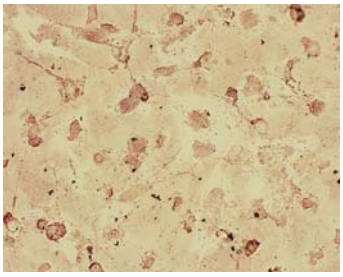

60x
higher conc

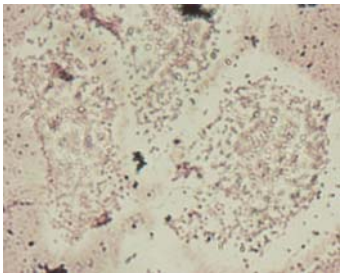
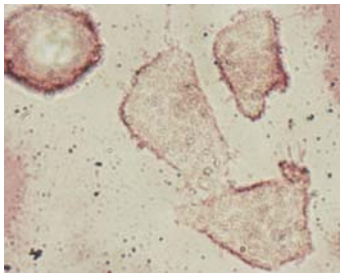
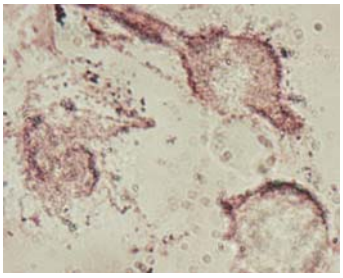

Figure 4-4: The bright field images of both cancer and health cells without gold nanoparticle treatment and with anti-EGFR/Au nanorod conjugates. row 1: 10x; row 2: 60x; row 3: lower concentration of conjugates (OD_{800} = 0.6), 10x; row 4: lower concentration of conjugates, 60x; row 5: higher concentration of conjugates (OD_{800} = 1.2), 10x, row 4: higher concentration of conjugates, 60x.

The nanorods on the two cancer cells show deeper and smooth red color than the healthy cells. Also on the edge of the cells (cell cytoplasmic membrane) the nanorods show higher concentration on the cancer cells so that the cells look like rings. This contrast difference of gold nanorods on the cancerous and noncancerous cells is due to the specific binding of anti-EGFR antibodies to the overexpressed EGFR on the cancer cell surface. Due to the nonspecific binding, the nanorods heterogenously distributed on the surface of the HaCat healthy cells. This indicates that when anti-EGFR/Au nanorod conjugates are used, the simple bright field images can be used to distinguish the cancer cells from the healthy cells.

It is well known that citrate-capped gold nanospheres have no cytotoxicity for the cells. But the toxcicity of CTAB-capped gold nanorods is not known. So after we incubate the rod conjugates with cells, we stained with trypan blue dye to test the cell viability. The dead cells accumulate trypan blue dye and stained blue while the live cells get rid of the dye and stain colorless. For comparison, the conjugates are incubated with the cells in several different ways (Figure 4-5). First, the cells are incubated with nanorods (with PSS^- capped) in buffer at room temperature for 30 mins (using HSC cancerous cells for this experiment) and then stained with trypan blue (see the image on the first row). The cells are stained blue and the rods (without antibody) also go to the cell surface. In addition the nanorods attachment on the cells caused the cell dislodgment from the cover slips.

HSC cancer cells after incubated with PSS⁻/rods in buffer for 30 mins at RT, TB 10 mins Cell dislodgment Blue No Rod aggregate	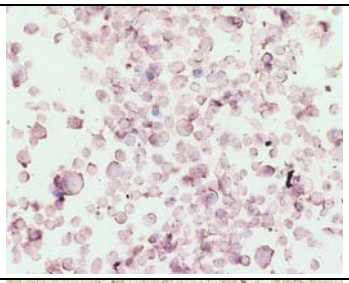	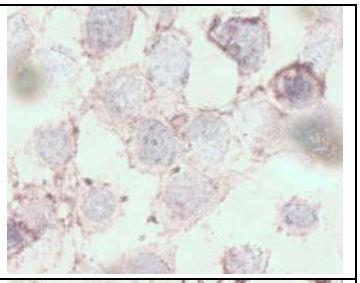
HSC cancer cells after incubated with PSS⁻/rods in medium for 15 mins at 37°C, TB 8 mins. No cell dislodgment Almost not blue Rod aggregate	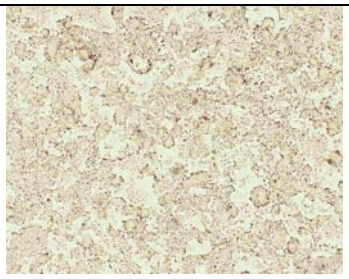	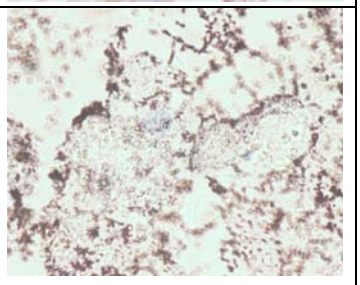
HSC cancer cells after incubated with rod/IgG in buffer for 30 mins at RT, TB 10 mins. No cell dislodgment blue No Rod/IgG aggregate	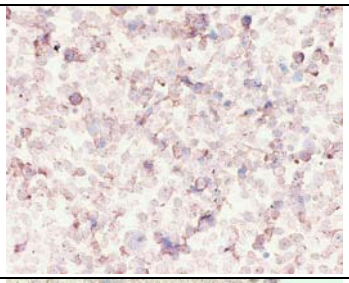	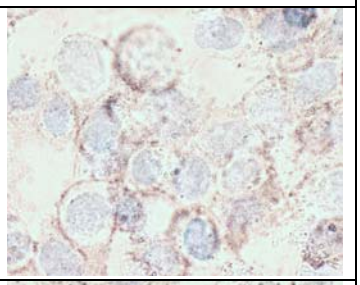
HSC cancer cells after incubated with rod/IgG in buffer for 20 mins at 37°C, TB 8 mins. Cell dislodgment Blue Rod/IgG aggregate	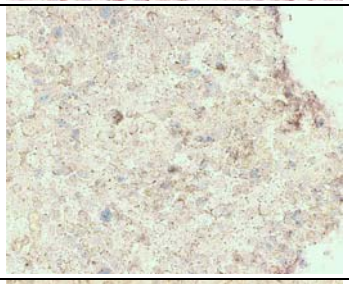	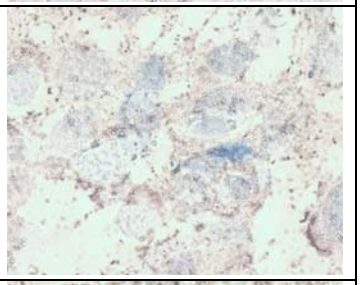
HSC cancer cells after incubated with rod/IgG in medium for 30 mins at 37°C, TB 8 mins. No cell dislodgment Almost not blue Rod/IgG aggregate	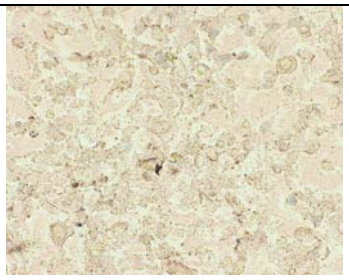	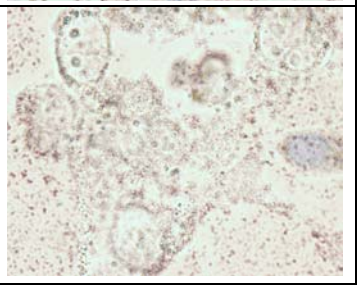
HSC cancer cells after incubated with rod/IgG in buffer for 30 mins at RT, then immersed in medium and put back into incubator at 37°C for 2.5 hs, TB 8 mins **No cell dislodgment** **Almost not blue** **No Rod/IgG aggregate**	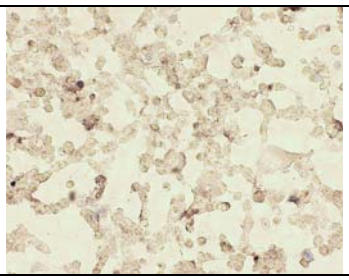	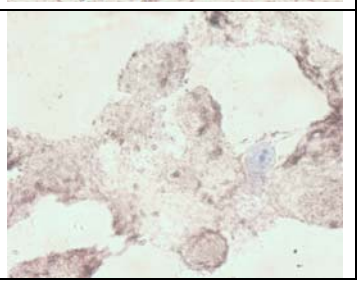

Figure 4-5: The cell viability after binding anti-EGFR/Au nanorod conjugates in different ways.

This indicates that the nanorods without antibody also bind to the cells but they injure the cells. If the rods (with PSS^- capped) are incubated with the cells in medium at 37^{o}C for 15 mins, the cells are not stained blue and no cell dislodgement (second row images) but the nanorods aggregate on the cells so that the cells can not be individually recognized. This indicates that when the cells are taken out from incubator, the cells are getting unhealthy due to lack of medium and the lower temperature (cells need 37^{o}C for grow).

For the incubation of antibody conjugated gold nanorods, four methods are tried. One is to incubate the rods in buffer at room temperature for 30 mins (third row images). Another method is to incubate the rods in buffer at 37^{o}C for 20 mins (fourth row). The third way is to incubate the rods in buffer at RT for 30 mins (this is the usual way we incubated the conjugates with cells, fifth row images) and the last one is to incubate the rods in buffer at RT for 30 mins and then immerse the cells in medium and put back into incubator and let cells grow for 2 hrs (bottom row images). From the results of these four incubation ways, we can see that again the cells are getting unhealthy when taken out of their incubator environment. Another point we can see is that the cells are best labeled with the conjugates in buffer at RT. Either the medium or the temperature affects the labeling of the rods on the cells. In addition, after the incubation of the conjugates, if the cells are put back into its growth environment (immersed in medium) and let them grow for several hours in incubator, the cells will recovered totally and become healthy again (not blue stained). This indicates that the anti-EGFR/Au nanorod conjugates have no cytotoxcity to the cells.

4.3.2 Dark field imaging (light scattering mode)

Figure 4-6 shows the dark field (light scattering) images of the HaCaT noncancerous cells, HOC cancerous cells and HSC cancerous cells without nanoparticles (A), with colloidal gold nanospheres incubated inside cells (B), with lower concentration of anti-EGFR/Au nanosphere conjugates incubated (OD_{530} = 1.0, C) and with higher concentration of anti-EGFR/Au nanosphere conjugates incubated (OD_{530} = 2.5, C). All the cells without gold nanoparticles show dim greenish light. This green light is due to autofluorescence and scattered light from the cell organelles in cell cytoplasm and membrane. The cell morphogy is much clearer than the bright field images (Figure 2, top row images). We can see obviously that the three types of cells have different structure characteristics. HOC cancer cells are larger than the other two types of cells.

The incorporated gold nanoparticles scatter strong yellowish light and make individual cells easily identifiable. It is very clear that gold nanoparticles are predominantly accumulated inside the cytoplasm of the cells. In most HaCaT and HSC noncancerous cells (left column) the gold nanoparticles demonstrate a spotted pattern inside the cytoplasm while the nanoparticles are homogenously distributed in the cytoplasm of HOC cancerous cells. The HaCat and HSC specimens give stronger scattering light which is due to the large amount of accumulated gold nanoparticles.

The light scattering pattern of gold nanoparticles is significantly different when anti-EGFR antibodies are conjugated to gold nanoparticles. When the conjugates concentration is lower (OD_{530} = 1.0), almost no nanoparticles are bound to the healthy cells (C row, left image). But a lot of nanoparticles are accumulated on the surface of

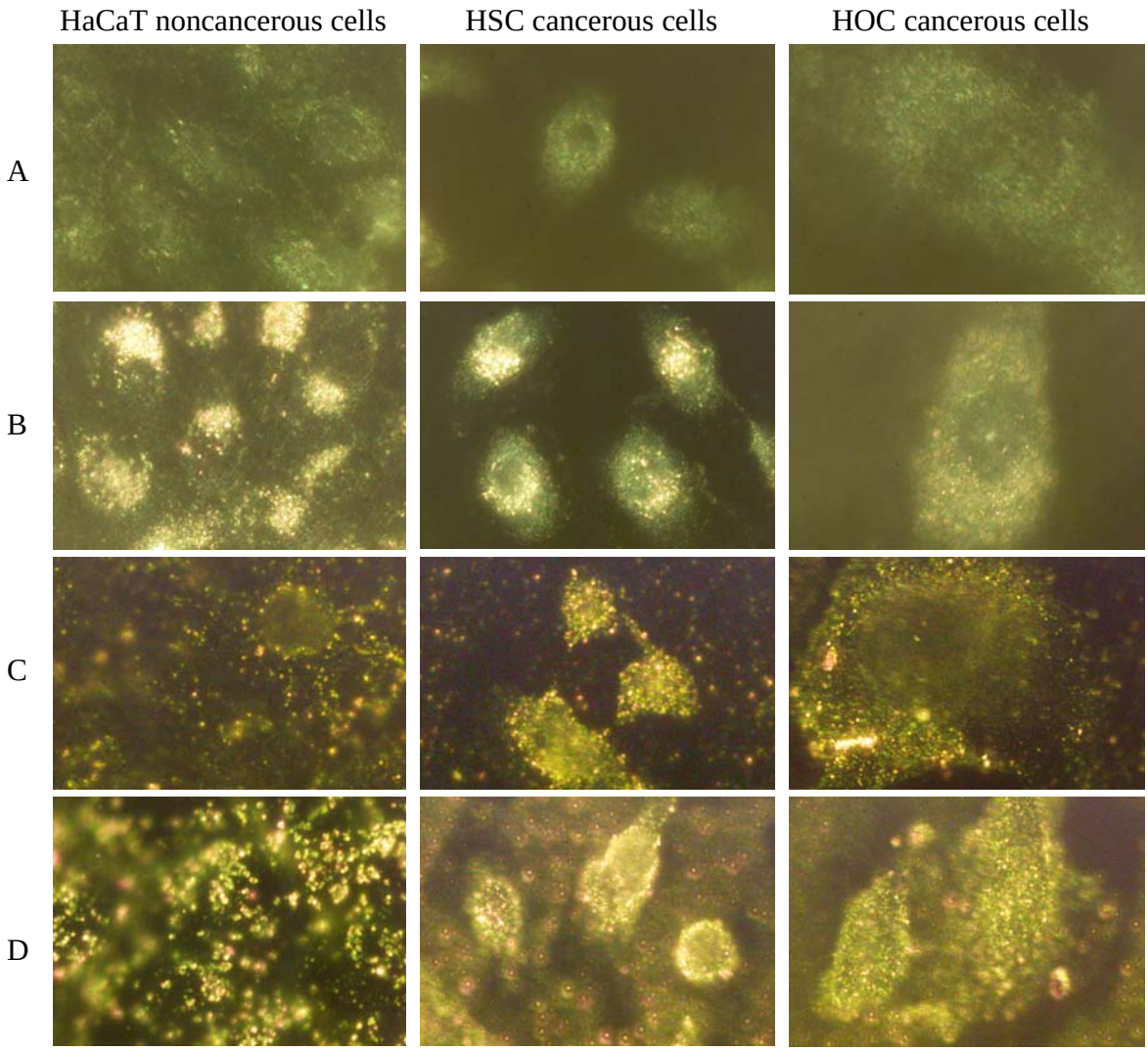

Figure 4-6: The dark field (light scattering) images of the HaCaT noncancerous cells, HOC cancerous cells and HSC cancerous cells without nanoparticles (A), with colloidal gold nanospheres incubated inside cells (B), with lower concentration of anti-EGFR/Au nanosphere conjugates incubated (OD_{530} = 1.0, C) and with higher concentration of anti-EGFR/Au nanosphere conjugates incubated (OD_{530} = 2.5, C).

the two cancer cells (C, right two images). When the conjugates concentration increases (OD_{530} = 2.5), some nanoparticles are bound to the healthy cells (D row, left image). And even more nanoparticles are accumulated on the surface of the two cancer cells (D, right two images). At this time, some gold nanoparticles also stick to the coverslip background

(the coverslip is coated with collagen). This is due to the nonspecific binding of gold nanoparticles to the collagen background. The nanoparticles are also bound to the healthy cells due to part of the specific binding, but mostly due to the nonspecific interactions between the antibodies and the proteins on the cell surface and thus the nanoparticles are randomly distributed on the whole cells. This predominant nonspecific interaction makes the cells not be identified individually. This contrast difference in both conjugate concentrations is due to the specific binding of overexpressed EGFR on the cancer cells with the anti-EGFR antibodies on the gold surface.

The nanorods scatter strongly orange to red light due to their strong longitudinal surface plasmon oscillation with a frequency in the NIR region (Figure 4-7). As the nanosphere conjugates, the anti-EGFR/Au nanorod conjugates bind specifically to the two types of malignant cells (right two columns) and give them distinguished imaging difference from the noncancerous cells. The individual noncancerous cells are hardly identified due to the predominant nonspecific interactions between the nanoparticles and the cells. The light scattering images with higher concentration of conjugates (OD_{800} = 1.6) as shown in the bright field images is not shown here. Because too much nanorods accumulated on the cells make the focus very difficult. The nanoparticles located at different part of the cells can not be focused at the same time because they are not on the same focus layer while in the dark field imaging (100x) only a very thin layer of particles can be focused.

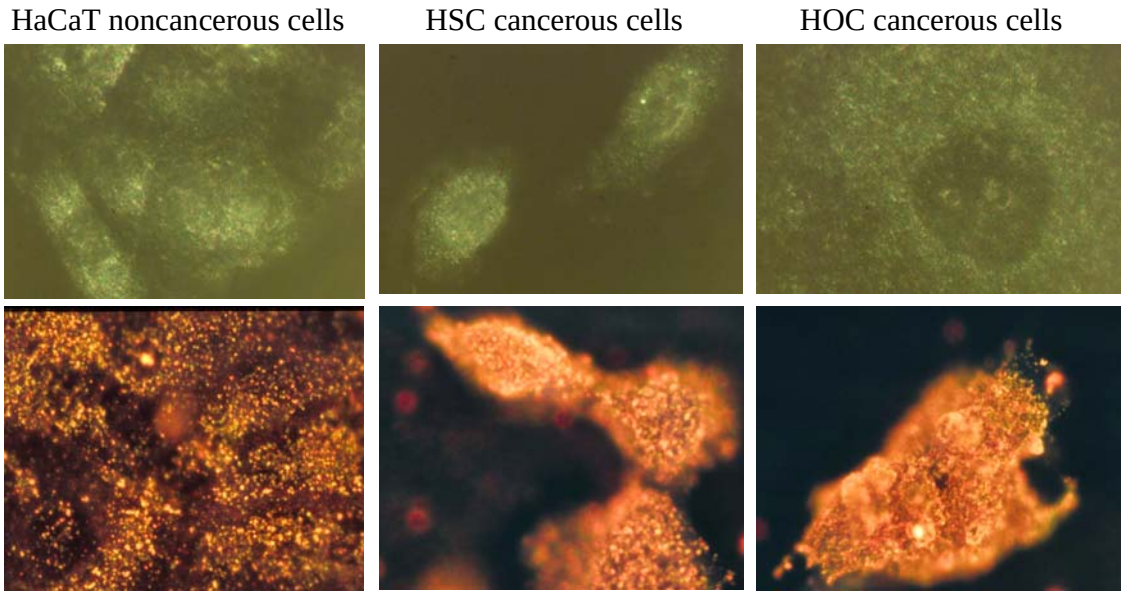

Figure 4-7: The dark field (light scattering) images of the HaCaT noncancerous cells, HOC cancerous cells and HSC cancerous cells without nanoparticles (top row), and with anti-EGFR/Au nanorod conjugates incubated (OD_{800} = 0.8, bottom row).

4.4 References

(1) Pomper, M. G. Academic Radiology 2001, 8, 1141.

(2) Roda, A.; Pazzagli, M.; Kricka, L. J.; Stanley, P. E. *Bioluminescence and Chemiluminescence: Perspectives for the 21st Century*; Wiley: Chichester, **1999**.

(3) Rajadhyaksha, M.; Anderson, R. R.; Webb, R. H. *Applied Optics* **1999**, *38*, 2105.

(4) Rajadhyaksha, M.; Anderson, R. R.; Webb, R. H. *J. Invest. Dermatol.* **1999**, *113*, 293.

(5) Selkin, B.; Rajadhyaksha, M.; Gonzalez, S.; Langley, R. G. *Dermatologic Clinics* **2001**, *19*, 369.

(6) White, W. M.; Rajadhyaksha, M.; Gonzalez, S.; Fabian, R. L.; Anderson, R. R *Laryngoscop* **1999**, *109*, 1709.

(7) Gonzalez, S.; Rajadhyaksha, M.; Gonzalez-Serva, S.; White, W. M.; Anderson, R. R. J. Cutan Pathol. 1999, 26, 201.

(8) Haugland, R. P. *Handbook of Fluorescent Probes and Research Chemicals*, Molecular Probes, Eugene, OR, ed. 6, 1995.

(9) Waggoner, A. *Methods Enzymol*. **1995**, *246*, 362.

(10) Wu, X.; Liu, H.; Liu, J.; Haley, K. N.; Treadway, J. A.; Larson, J. P.; Ge, F.; Peale, F.; Bruchez, M. P. *Nat. Biotech*. **2003**, *21*, 41.

(11) Alivisatos, A.P. *Science* **1998**, *281*, 2013.

(12) Chan, W.C.W; Nie, S. *Science* **1998,** *281*, 2016.

(13) Gao,X.; Cui, Y.; Levenson, R. M.; Chung, L. W. K.; Nie, S. *Nat. Biotechnol.* **2004**, *22(8)*, 969.

(14) Xu, X. H; Brownlow, W. J.; Kyriacou, S. V.; Wan, Q.; Viola, J. J. *Biochemistry* **2004**, *43*, 10400.

(15) Yelin, D.; Oron, D.; Thiberge, S.; Moses, E.; Silberberg, Y. Optics Express **2003**, *11(12)*, 1385.

(16) Sokolov, K.; Aaron, J.; Hsu, B.; Nida, D.; Gillanwater, A.; Follen, M.; Macaulay, C.; Adler-Storthz, K.; Korgel, B.; Discour, M.; Pasqualini, R.; Arap, W.; Lam, W.; Richartz-Kortum, R. *Technology in Cancer Research & Treatment* **2003**, *2(6)*, 491.

(17) Sokolov, K.; Follen, M.; Aaron, J.; Pavlova, I.; Malpica, A.; Lotan, R.; Richartz-Kortum, R. *Cancer Research* **2003**, *63*, 1999.

(18) Raub, C. B.; Orwin, E. J.; Haskell, R. *J. Biomech. Eng.* **2003**, *125*, 1.

(19) Yelin, D.; Oron, D.; Korkotian, E.; Segal, M.; Silberberg, Y. *Apply. Phys. B: Lasers and Optics* **2002**, *74 (Suppl.)*, S97.

(20) Connor, E. E.; Mwamuka, J.; Gole, A.; Murphy, C. J.; Wyatt, M. D. *Small* **2005**, *1*, 325.

CHAPTER 5
PHOTOTHERMAL CANCER CELL THERAPY IN VISIBLE REGION USING ANTI-EGFR ANTIBODY CONJUGATED GOLD NANOSPHERES

Abstract

Two oral squamous carcinoma cell lines (HSC 313 and HOC 3 Clone 8) and one benign epithelial cell line (HaCaT) are incubated with anti-epithelial growth factor receptor (EGFR) antibody conjugated gold nanoparticles and then exposed to continuous visible argon ion laser at 514 nm. It is found that the cancer cells require less than half the laser energy to be photo-destructed than the benign cells after incubation with anti-EGFR antibody conjugated Au nanoparticles. No photothermal destruction is observed for all types of cells in the absence of nanoparticles at four times energy required to destroy the malignant cells with ant-EGFR/Au conjugates bonded. By oven-heating the cells (either cancerous or noncancerous cells), it is found that the cells are thermally destructed between 70-80°C. This temperature range is in agreement with the local temperature rise calculated by Prashant (another member in our group) from the amount of gold loading at the threshold laser power. The work has been published in Cancer Letters, in press and Photochem. Photobiol., 2006, 82, in press.

5.1 Introduction

It is known that the tradition cancer treatment includes surgery, radiation, hormone therapy and more recently chemotherapy, immunotherapy and combines strategies (1). Surgery is limited to tumors that are known to be surgically respectable and accessible. Chemotherapy may have significant side effects (2) and is subject to the development of resistance by the tumor, rendering agents ineffective. Radiotherapy can cause damage to healthy tissue close to the tumor or in the path of the radiation beam (3). Rapid advances in immunology suggests the potential of immunotherapy as a promising treatment, however its development is still in the nascent stage (4). Thus the searching for more effective cancer therapy is still underway.

Photodynamic therapy (PDT) is an attractive alternative to the traditional treatment methods with less morbidity and can preserve the anatomic and functional integrity of many organs such as the tongue or larynx (5). PDT uses molecules that are preferentially taken up by the tumor cells. Light delivered to tumor site to convert the molecules into singlet oxygen that chemically injures the cell. However, these agents are only relatively selective and risk of severe burns over the entire body when exposed to light for long time.

Thermal therapies (hyperthermia) for cancer have been widely investigated as a minimally invasive alternative (6). Thermal therapies induced cellular injury/death above 40°C appears due to protein denaturation (7-9). A variety of heat sources have been used including ultrasound (10), microwaves (11, 12), magnetic heating (13, 14) and radio frequency (11, 15). However, the thermal therapy affects both healthy and cancerous

tissue. In order to attain success as a sole therapeutic agent, the thermal heat must be specifically targeted to the tumor with much less heat produced in the surrounding tissue.

The use of lasers for thermal treatment of tumors can target the tumors by fine cable (16-18). However, pigments in healthy tissue absorb energy in the light path, thus reducing the speed and effectiveness of the heat deposition within tumor cells and increasing nonspecific injury of adjacent healthy tissue. Photosensitizers such as dyes (19, 20) located within a tumor allow for increased heat production within the tumor at lower incident energies.

Nanotechnology has engendered a range of novel materials with unique properties unlike their bulk counterparts and raised the possibility of designing molecularly targeted photothermal agents. Recently, silica coated gold nanoshells with a tunable absorption in the near infrared (NIR) region have been used as both imaging and therapy agents (21-24). Nanoshells have generated considerable interest as a photothermal agent due to its wavelength selectivity, strong near infrared absorption efficiency and photo-stability compared to the conventional dyes. By adjusting the relative gold layer thickness and the size of the silica core, the absorption band can be tuned to NIR wavelength, a region of light where optical penetration through tissue is optimal.

Metallic noble nanoparticles devoid of any coating have received widespread interest in their use in biotechnological systems for diagnostic application and biological imaging due to its easy preparation, ready bioconjugation and highly controlled optical properties (25-31). Colloidal gold nanoparticles are well known safe and their safety in human cells have been characterized (32). The absorption maximum of Au nanoparticles is tunable

from the mid visible region into the infrared region based on the size, shape, and material. Our group has determined that the absorbed light by Au nanoparticles is converted into heat on the picosecond time scale (33, 34). Thus Au nanoparticles are potential very practical and efficient phothermal agents in therapeutic applications.

In this work the efficiency of gold nanospheres as photothermal agent near its plasmon resonance absorption (530 nm) is demonstrated in vitro by selectively delivering gold nanoparticles to oral squamous carcinoma cells that overexpress EGFR, a clinically related cancer biomarker. Thermal therapy by oven heating is also carried out for comparison.

5.2 Experimental

Au nanoparticles are prepared by the citrate reduction of $HAuCl_4$ as described in Chapter II, part 2. The measured absorption maximum of the nanoparticles is 530 nm. TEM showed the average particle size of 40 nm. The anti-EGFR/gold conjugates are prepared according to the method described in Chapter II, part 3. Briefly, the gold NPs are diluted in 20 mM HEPES buffer (pH = 7.4, Sigma) to a final concentration with optical density of 0.8 at 530 nm. 50 uL anti-EGFR monoclonal antibodies (host mouse; Sigma) are diluted in 500 uL of the same HEPES buffer. Then 10 mL of the Au solution prepared above are mixed with the dilute antibody solution for 20 mins. 0.5 mL of 1% polyethyleneglycol (MW = 4000, Boehringer Mannheim) is added to the mixture to prevent aggregation and the solution is centrifuged at 6000 rpm for 18 mins. Then the anti-EGFR/Au pellet is redispersed in PBS buffer (pH = 7.4, Cellgro) and stored at 4^oC.

One benign epithelial cell line, HaCaT (human keratinocytes), and two malignant epithelial cell lines (human oral squamous cell carcinoma) , HOC 313 clone 8 and HSC 3, are cultured on 18 mm diameter glass cover slips in a 12-well tissue culture plate in DMEM plus 5% FBS at 37°C under 5% CO_2. The cover slips are coated with collagen type I (Roche) in advance for optimum cell growth.

For the laser irradiation experiment the CW argon laser is chosen due to wavelength overlapping with the absorption band of the nanoparticles. The cell monolayer is immersed into the conjugated nanoparticles solution (~ 0.2 nM) for 40 min, rinsed with PBS buffer and then exposed to argon laser light at various power densities. The argon laser at 514 nm is focused by a lens (f = 10 cm) to form a round spot with 1 mm in diameter on the sample position. Multiple regions on the slides are exposed to argon laser light at different power densities for 4 min each and then stained with 0.4 % trypan blue (Sigma) for 10 mins to test cell viability. Dead cells will accumulate the dye and stain blue while live cells will pump out it and remain clear. After staining, the samples are imaged under 10x in a transmission mode.

In the thermal destruction experiment, cells without any gold nanoparticles are heated in an oven at different temperatures ranging from 50-90˚C with intervals of 10°C. After 7 mins, the cells are taken out, cooled down to room temperature and stained with trypan blue for 10 mins. The cells are then rinsed with PBS buffer and imaged under a microscope.

5.3 Results and discussion

5.3.1 Photothermal Therapy

Control cells (without nanoparticles) have been exposed to laser light at several power values to test the photothermal stability of the cell themselves as controls. Laser power energy of 600 mW (76 W/cm^2), 500 mW (64 W/cm^2), 400 mW (50 W/cm^2), 300 mW(38 W/cm^2), 200 mW (25 W/cm^2) and 150 mW (19 W/cm^2) are used to irradiate cells at different regions for 4 mins each and then stained with trypan blue. After staining, no blue cells are observed for all of the area exposed to laser irradiation. Figure 5-1 shows the pictures of the cells irradiated at 600 mW. It is obvious that even at high laser energies, no death is observed for both cancer and healthy cells.

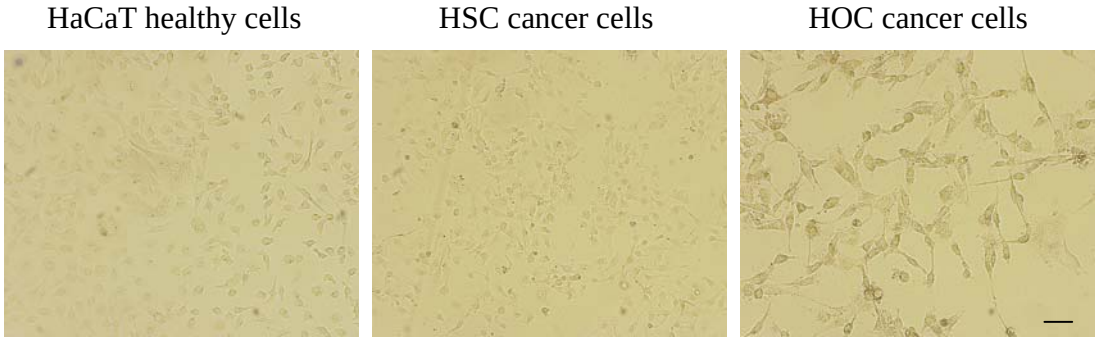

Figure 5-1: HaCaT benign cells, HSC malignant cells and HOC malignant cells without nanoparticles treatment irradiated at 600 mW (76 W/cm^2) and then stained with trypan blue. No cells are killed up to this laser power. Scale bar: 60 μm.

After incubation with anti-EGFR antibody conjugated gold nanoparticles, cells are exposed to laser power value from 600 mW to 250 mW at an interval of 50 mW at different regions for 4 mins each to test their photothermal stability. After exposure to the argon laser at and above 450 mW, cells within the laser spots became blue while at lower energy values only a few or no blue cells are detected. Figure 5-2 shows the pictures irradiated at some selected laser energy. Other images are not shown for space.

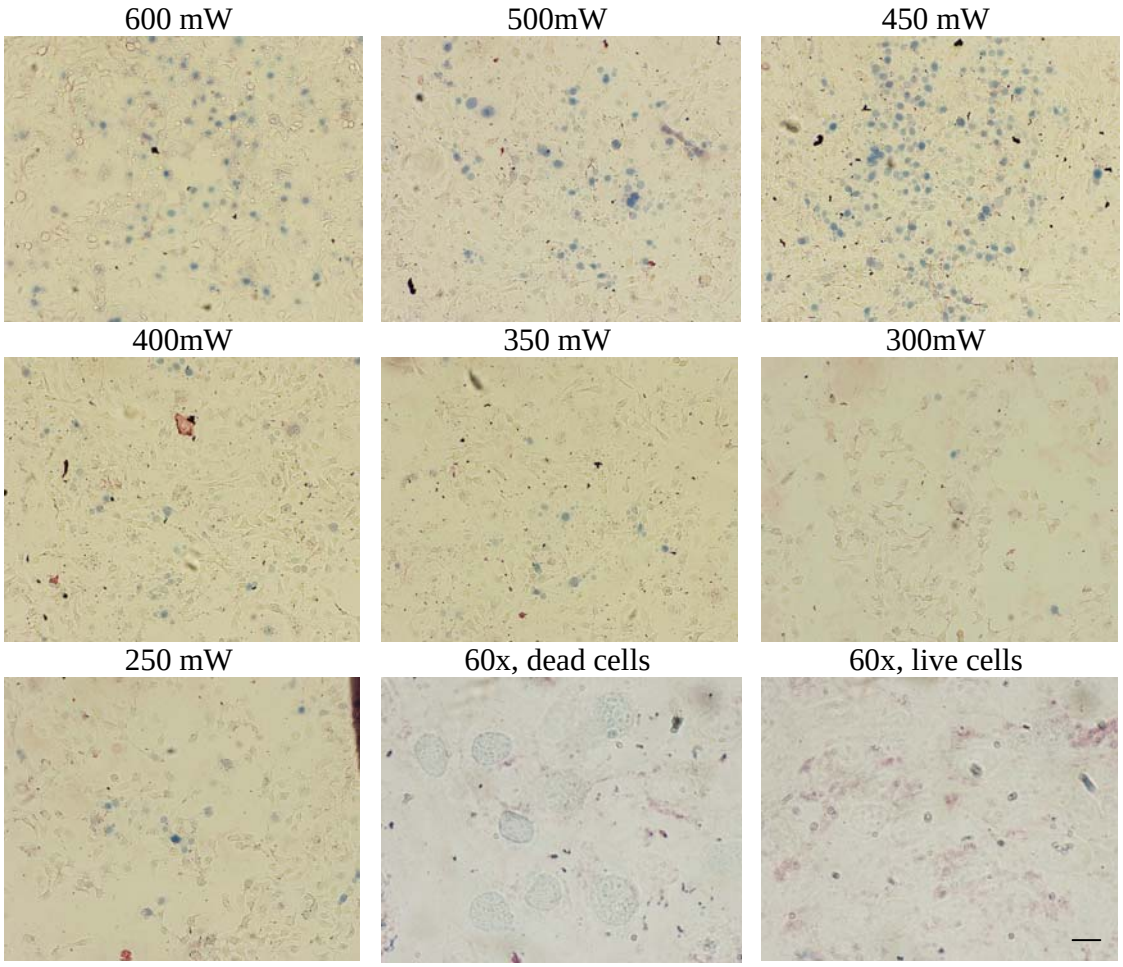

Figure 5-2: HaCaT noncancerous cells irradiated at different laser powers and then stained with trypan blue. Scale bar: 60 μm for 10x images and 10 μm for 60x images.

It is obvious that the HaCaT cells after incubation with anti-EGFR antibody conjugated gold nanoparticles suffered photothermal destruction when the laser has density at or higher than 450 mW in a 1mm laser spots (57 W/cm^2). This is due to the introduction of the Au nanoparticles which binds to EGFR on the cell surface. The Au nanoparticles served as a photo-absorbers due to the overlapping of its absorption band (λ_{max} = 530 nm) and the argon ion laser wavelength at 514 nm. From Figure 5-2 we can also see that even at energy equal and higher than 450 mW, some cells are still colorless. This means some

cells are not killed by the laser although majority of cells are photodamaged. This indicates that the gold nanoparticles do not homogeneously distribute on the cell monolayer. Some cells take nanoparticles, some not. Some cells may take more nanoparticles and some cells take less. This is because that although part of nanoparticles are bound to the cells by EGFR on the cell surface, but mostly the nanoparticles are bound to cell surface by nonspecific interactions of the antibody on the surface of gold nanoparticles and the proteins on the surface of healthy cells.

The malignant HSC cells suffered irreversible photothermal injury at a much lower power density (see Figure 5-3). Cell death occurred within the laser spots after exposure to laser at and above 200 mW while no cell death are observed at lower power density than 150 mW. The energy threshold to cause death of the HSC cells is about half that which caused the photothermal death of the benign HaCaT cells. This indicates that the gold amount on the HSC cancer cells are much more than that on the healthy cells, which results in the lower laser energy required to cause the cell destruction.

The HOC malignant cells also undergo photothermal destruction at a much lower power density than that required for HaCaT noncancerous cells (Figure 5-4). Cell death within the laser spots is observed at the laser power of 250 mW (19 W/cm^2) and no cell death is observed at lower power density than 100 mW (13 W/cm^2). The transmission images at 60x reveal that more Au nanoparticles (reddish color) are bound to the surface of the HOC cell surface allowing for the lower energy required to cause cell death than HSC cells. This indicates that HOC may have more EGFR on their cell surface than HSC cells at this cell phase. It is well known that EGFR functionizes in the initiation of cell

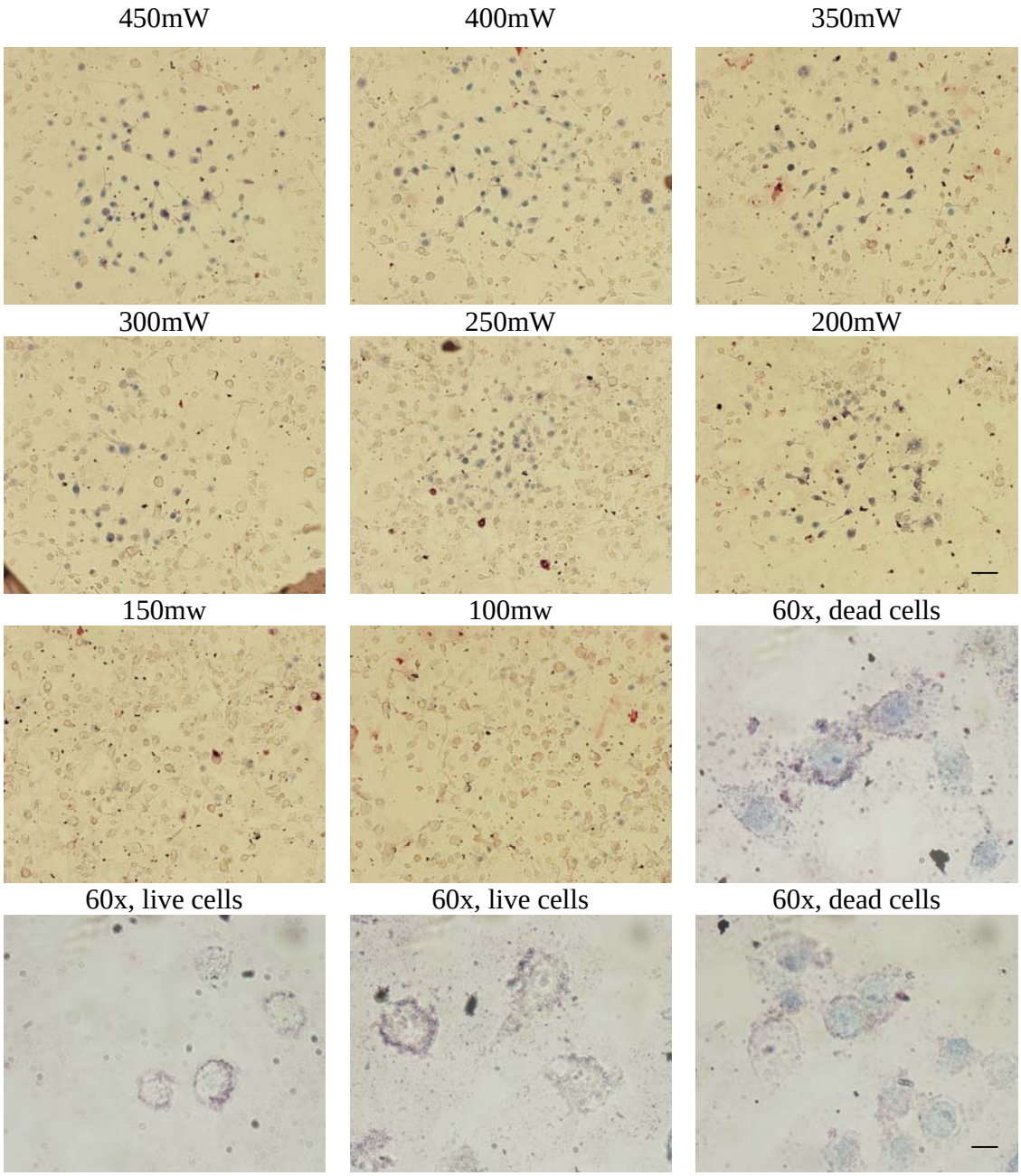

Figure 5-3: HSC cancer cells irradiated at different laser powers and then stained with trypan blue. HSC cancer cells are killed at and above 200 mW (57 W/cm^2). Scale bar: 60 μm for 10x images and 10 μm for 60x images.

growth processes by binding with EGF. Before bound to EGF, EGFR change its conformation and form an activated state so that EGF can bind to EGFR (35). Upon binding of a specific growth factor ligand to its extracellular ligand-binding domain,

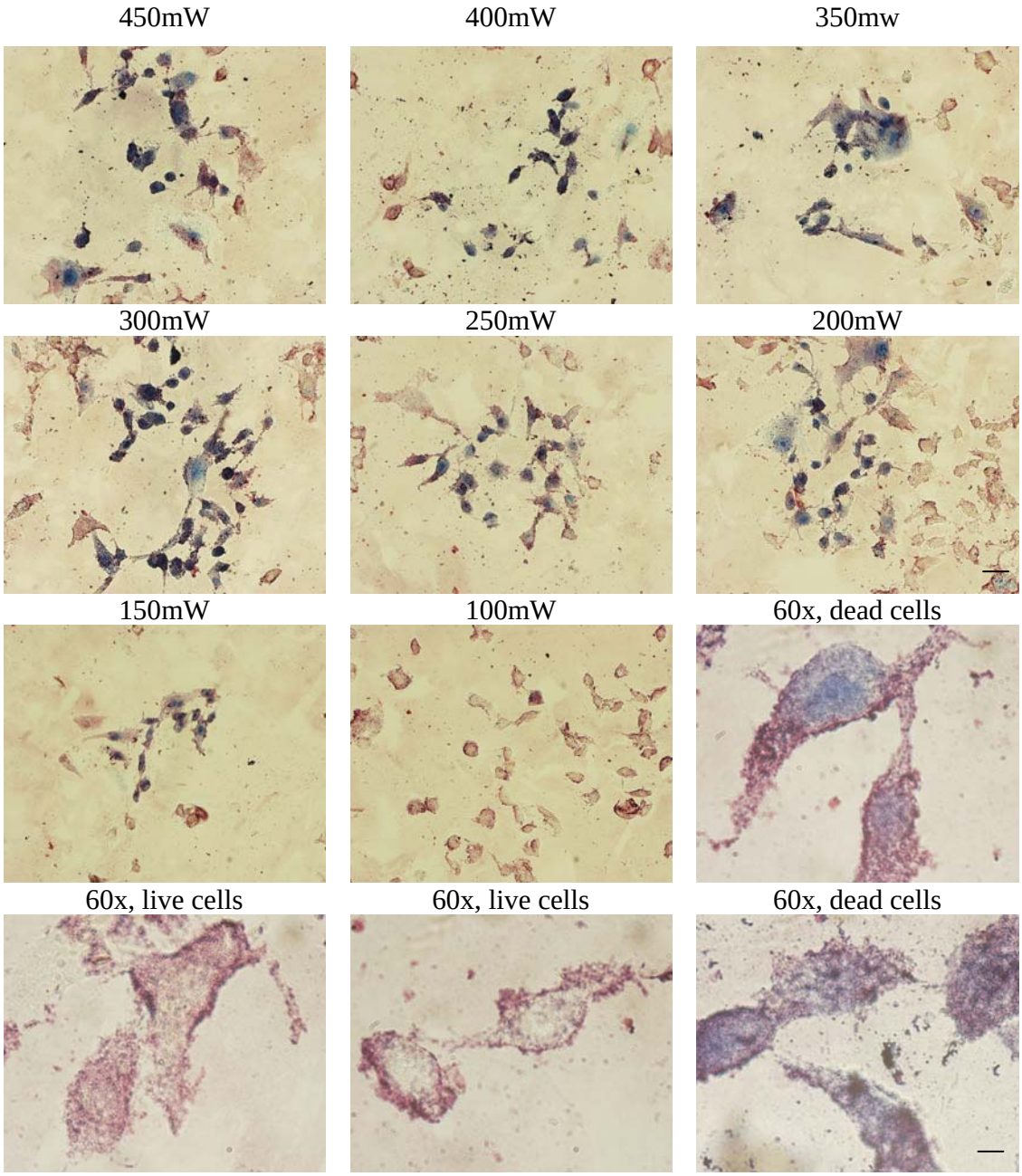

Figure 5-4: HOC cancer cells irradiated at different laser powers and then stained with trypan blue. HOC cancer cells are killed at and above 150 mW (19 W/cm^2). Scale bar: 60 μm for 10x images and 10 μm for 60x images.

the EGFR receptor pairs, or 'dimerizes', with another ErbB family members. So at the time of gold nanoarticles bound to the EGFR, EGFR might be in an unactivated

monomer state, might be in an activated state and might be in dimmer state. It is not known when the antibody on the gold surface bound to EGFR. Does it bound to all the states or some states? These factors will affect the amount of gold nanoparticles eventually adsorbed on the cell surface. So at different phase of cell growth, the binding of antibody to EGFR may vary at some extent.

5.3.2 Thermal destruction of cells by oven heating

Figure 5-5 shows images of the cells which are heated in the oven at 70°C and 80°C for 7 min. These results indicate that for all three cell lines, cell damage began at 70°C while the cell samples underwent complete destruction at 80°C. The error in the temperature measurement is 5°C. Thus a threshold temperature in the range of 70-80°C is required for the thermal destruction of cells of all three lines.

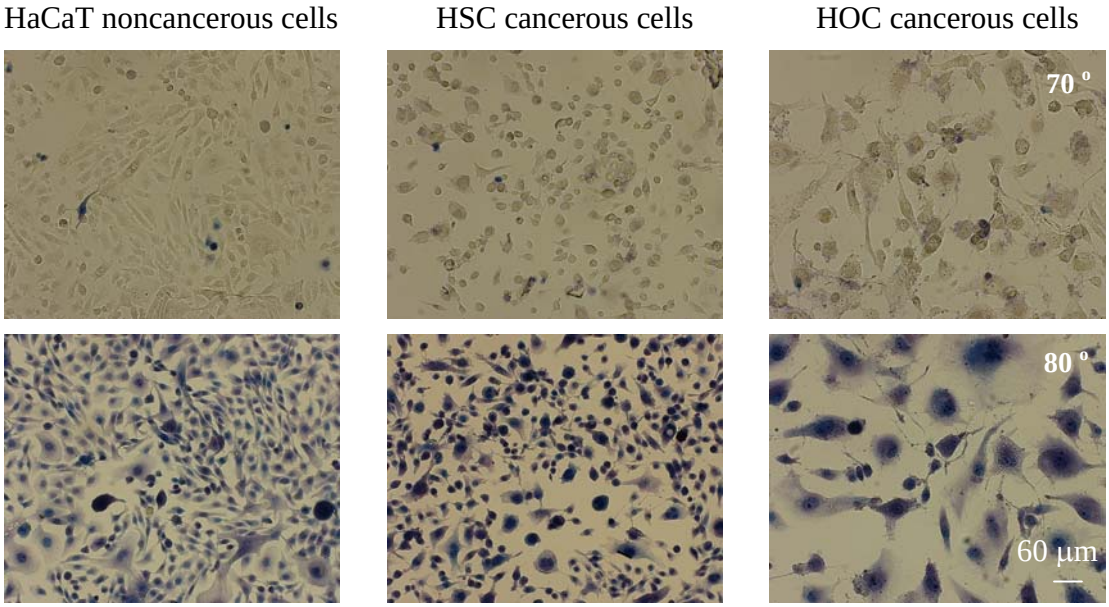

Figure 5-5: HaCaT noncancerous cells (top row), HSC cancerous cells (middle row) and HOC cancerous cells (bottom row) heated in an oven at 70˚C (left column) and 80˚C (right column). For all three lines, the cell damage began at 70˚C while complete cell destruction is achieved at 80˚C. The error in the temperature measurement is 5˚C.

Using a numerical model, Prashant, another member in our lab, calculated the relationship of the minimum local temperature rise on the cells with the laser power values according to the gold loading on each type of cells (36). He found that the temperature rise is lineally dependent on the laser power. At the threshold power value for the photothermal destruction of each type of cells (see results in 5.3.1), he found that the local temperature rise for HaCat cells is 77^{o}C, 73^{o}C for HSC cancer cells and 74^{o}C for HOC cancer cells. These results indicate that the minimum temperature to cause cell phothermal destruction is between 70^{o} and 80^{o}C, which is in great agreement with the temperature range to cause cell thermal destruction. It is also interesting to notice that that Hirsch *et. al*. (22) has reported that a temperature of ~ 74^{o}C (measured by MRTI analysis) is reached in the photothermal destruction of breast tumor *in vivo* using gold nanoshells. Although the heating dissipation in photothermal and thermal therapy of cancer cells *in vitro* as well as in the photothermal therapy of tumor tissue *in vivo* might be different, a similar threshold temperature in the range of 70-80°C is required for the destruction of the cells.

This study demonstrates that Au nanoparticles are a novel class of photothermal agents causing cell injury and death through conversion of the strongly absorbed light to thermal energy. After exposure of these cells treated with anti-EGFR antibody conjugated Au nanoparticles to a visible CW argon laser at 514 nm, different laser power densities are observed to cause photothermal destruction among these three types of cells. The two malignant cells require less than half the energy needed to kill the benign cells incubated with gold nanoparticles and more than four times energy required to kill the cells in the absence of nanoparticles. Thermal destruction by oven-heating showed that a threshold

temperature in the range of 70-80˚C is required to destroy cancerous as well as noncancerous cells. This temperature range is in great agreement with the calculated minimum temperature rise to cause the photothermal destruction of cells which is done by Prashant, another member in our lab.

5.4 References

(1) Miller, A.B.; Hoogstraten, B.; Staquet, M.; Winkler, A. *Cancer*. **1981,** *47(1)*, 207.

(2) Hamilton, A.; G. Hortobagyil *J. Clin. Oncol*. **2005**, *23*, 1760.

(3) Partridge, A. H.; Burstein, H. J.; Winer, E. P. *J. Natl. Cancer Inst. Monogr*. **2001**, *30*, 135.

(4) Donaldson, S.S. *Cancer Res*. **1977**, *37*, 2407.

(5) Schweitzer, V.G. *Lasers in Surgery and Medicine* **2001**, *29*, 305.

(6) Overgaard, J. *Int. J. Radiat. Onco.l Biol. Phys*. **1989**, *16*, 535.

(7) Kamisawa, T.; Tu, Y.; Ishiwata, J.; Karasawa, K.; Matsuda, T.; Sasaki, T.; Funata, N.; Tsuruta, K.; Okamoto, A.; Takahashi; T. *Hepatogastroenterology* **2005**, *52*, 1005.

(8) He, X.; Wolkers, W.; Crowe, J. H.; Bischof, J. C. *Ann. Biomed. Eng.* **2004**, *32*, 1384.

(9) Henriques, F. C. Jr. *Arch. Pathol*. **1947**, *43***,** 489.

(10) Jolesz, F.A.; Hynynen, K. *Cancer J.* **2002**, *8 (suppl. 1)*, S100.

(11) Mirza, A.N.; Fornage, B.D.; Sneige, N.; Kuerer, H.M.; Newman, L.A.; Ames, F.C.; Singletary, S.E. *Cancer J.* **2001**, *7*, 95.

(12) Seki, T.; Wakabayashi, M.; Nakagawa, T.; Imamura, M.; Tamai, T.; Nishimura, A. *Cancer* **1999**, *85*, 1694.

(13) Hilger, I., Andrä, W.; Bähring, R.; Daum, A.; Hergt, R.; Kaiser, W. A. *Invest. Radiol*. **1997**, *32*, 705.

(14) Hilger, I.; Hiergeist, R.; Hergt, R.; Winnefeld, K.; Schubert, H.; Kaiser, W. *Invest. Radiol*. **2002**, *37*, 580.

(15) Gazelle, G. S.; Goldberg, S. N.; Solbiati, L.; Livraghi, T. *Radiology (Easton, Pa.)* **2000**, *217*, 633.

(16) Amin, Z., J. J. Donald, A. Masters, R. Kant, A. C. Steger, S. G. Bown and W. R. Lees *Radiology (Easton, Pa.)* **1993**, *187*, 339.

(17) Nolsoe, C. P.; Torp-Pedersen, S.; Burcharth, F.; Horn, T.; Pedersen, S.; Christensen, N. E.; Olldag, E. S.; Andersen, P. H.; Karstrup S.; Lorentzen, T. *Radiology (Easton, Pa.)* **1993**, *187*, 333.

(18) Vogl, T. J.; Mack, M. G.; Müller, P. K.; Straub, R.; Engelmann K.; Eichler, K. *Eur. Radiol.* **1999**, *9*, 1479.

(19) Chen, W. R.; Adams, R. L.; Carubelli, R.; Nordquist, R. E. *Cancer Lett.* **1997**, *115*, 25.

(20) Chen, W. R.; Adams, R. L.; Higgins, A. K.; Bartels, K. E.; Nordquist; R. E. *Cancer Lett.* **1996**, *98*, 169.

(21) Loo, C.; Lowery, A.; Halas, N.; West, J.; Drezek, R. *Nano letters* **2005**, *5*, 709.

(22) Hirsch, L. R.; Stafford, R. J.; Bankson, J. A.; Sershen, S. R.; Rivera, B.; Rrice, R. E.; Hazle, J. D.; Halas, N. J.; West, J. L. *PNAS* **2003**, *100*, 13549.

(23) Loo, C.; Lin, A.; Hirsch, L.; Lee, M.; Barton, J.; Halas, N.; West, J.; Drezek, R. *Technology in Cancer Research & Treatment* **2004**, *3*, 33.

(24) O'Neal, D.P.; Hirsch, L.R.; Halas, N. J.; Paynea, J. D.; West, J. L. *Cancer Letters* **2004**, *209*, 171.

(25) El-Sayed, M. A. *Acc. Chem. Res.* **2001**, *34*, 257.

(26) Yguerabide, J.; Yguerabide, E. E. *Analy. Biochem.* **1998**, *262* , 137.

(27) Yguerabide, J.; Yguerabide, E. E. *Analy. Biochem* **1998**, *262*, 157.

(28) Daniel, M.C.; Astruc, D. *Chem. Rev.* **2004,** *104*, 293.

(29) Niemeyer, C.M. *Angew. Chem. Int. Ed.* **2001**, *40*, 4128.

(30) Parak, W.J.; Gerion, D.; Pellegrino, T.; Zanchet, D.; Micheel, C.; Williams, S.C.; Boudreau, R.; Le Gros, M.A.; Carolyn, A.; Alivisatos, A. P. *Nanotechnology* **2003**, *14*, R15.

(31) Sokolov, K.; Follen, M.; Aaron, J.; Pavlova, I.; Malpica, A.; Lotan, R.; Richartz-Kortum, R. *Cancer Res.* **2003**, *63*, 1999.

(32) Connor, E. E.; Mwamuka, J.; Gole, A.; Murphy, C. J.; Wyatt, M. D. *Small* **2005**, *1*, 325.

(33) Link, S.; El-Sayed, M. A. *Annu. Rev. Phys. Chem*. **2003**, *54*, 331.

(34) Link, S.; El-Sayed, M. A. *International Reviews in Physical Chemistry* **2000**, *19*, 409.

(35) Hubbard, S.R. *Cancer cell* **2005**, *7*, 287.

(36) Huang, X.; Jain, P. K., EL-Sayed, I. H.; EL-Sayed, M. A. *Photochem. Photobiol*. **2006**, *82*, in press.

CHAPTER 6
PHOTOTHERMAL CANCER CELL THERAPY IN NEAR-INFRARED REGION USING ANTI-EGFR ANTIBODY CONJUGATED GOLD NANORODS

Abstract

Due to strong electric fields at the surface, the absorption and scattering of electromagnetic radiation by noble metal nanoparticles are strongly enhanced. These unique properties provide the potential of designing novel optically active reagents for simultaneous molecular imaging and photothermal cancer therapy. It is desirable to use agents that are active in the near infrared (NIR) region of the radiation spectrum to minimize the light extinction by intrinsic chromophores in native tissue. Gold nanorods with suitable aspect ratios (length divided by width) can absorb and scatter strongly in the NIR region (650-900 nm). In the present work, we provide an in vitro demonstration of gold nanorods as novel contrast agents for the photothermal cancer therapy. Nanorods are synthesized and conjugated to anti-epidermal growth factor receptor (anti-EGFR) monoclonal antibodies and incubated in cell cultures with a nonmalignant epithelial cell line (HaCat) and two malignant oral epithelial cell lines (HOC 313 clone 8 and HSC 3). The anti-EGFR antibody conjugated nanorods bind specifically to the surface of the malignant type cells with a much higher affinity due to the overexpressed EGFR on the cytoplasmic membrane of the malignant cells. After exposure to continuous red laser at 800 nm, it is found that malignant cells require half the laser energy to be photothermally destroyed than the nonmalignant cells. Thus selective photothermal therapy is realized in the NIR region. The work has been published in JACS, 2006, 128 (6), 2115.

6.1 Introduction

Reducing a material's size to the nanometer length scale (which is the length scale of the electronic motion that determines the material's properties) makes it sensitive to further reduction in size or a change in shape. In semiconductor nanoparticles, the property change results from quantum confinement of the electronic motion (1). In metals the properties of the surface become dominant and give nanoparticles new properties (2). In noble metals the coherent collective oscillation of electrons in the conduction band induces large surface electric fields which greatly enhance the radiative properties of gold and silver nanoparticles when they interact with resonant electromagnetic radiation (3). This makes the absorption crossection of these nanoparticles orders in magnitude stronger than the strongest absorbing molecules (4) and the light scattering crossecction orders in magnitude more intense than organic dyes (5). Thus these particles act as excellent sensors and novel contrast agents for optical detection due to their enhanced absorption and scattering, respectively. In addition, when it is realized that the strong absorbed radiation is converted efficiently into heat on a picosecond time domain due to electron-phonon and phonon-phonon processes (6), their potential use in photothermal therapy becomes obvious.

The use of nanoparticles in medicine is one of the important directions that nanotechnology is taking at this time. Their applications in drug delivery (7-9), cancer cell diagnostics (10-13), and therapeutics (14) have been active fields of research. The scattering properties of gold nanospheres have been used for cancer cell imaging using confocal microscopy (13, 15) and simple dark field microscopy (16). Recently

photothermal therapy using the absorption properties of antibody conjugated gold nanoshells (17) and solid gold nanospheres (18) have been demonstrated to selectively kill cancer cells leaving the healthy cells unaffected.

In order to use long wavelength laser irradiation that penetrates tissue optimally (can be over 10 cm in penetration depth depending on tissue types) for in vivo photothermal treatment (650-900 nm) (19, see Figure 6-1), the absorption band of the nanoparticles has to be in the near infrared region. The absorption band of core-shell particles has been

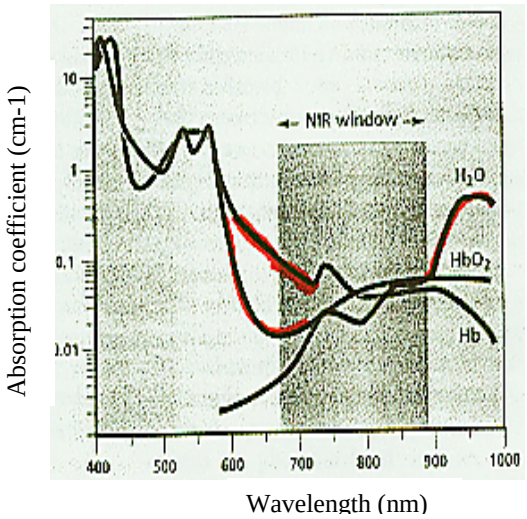

Figure 6-1: NIR window (19).

tuned by adjusting the ratio of the thickness of the gold shell to the diameter of the silica core (about 120 nm in diameter) and thus enables photothermal therapy in this region. Carbon nanotubes absorb naturally in this region and have recently been proposed as near-infrared therapy agents (20). It is important to mention that surface plasmon field enhancement of the absorption of nanorods is predicted to be the strongest of all the different shapes of gold and silver nanoparticles (21, 22). By changing the shape of gold nanoparticles to gold nanorods, not only can one change the absorption and scattering

wavelength from visible to the NIR region, but also increase their absorption and scattering crossections.

In the present work, we demonstrate the potential use of gold nanorods as a novel contrast reagent for selective photothermal therapy of cancer cells using a near infrared low energy cw laser. Solid gold nanorods have several advantages over other photothermal contrast agents. The synthesis of gold nanorods with various aspect ratios which enables tunable absorption wavelength in the near infrared region (4, 23, 24) is quite simple and well-established. The appropriate size of the nanorods is quite small and is potentially useful in applications such as drug delivery and gene therapy. In addition, the biosafety of metallic gold is well known and they have been used in vivo since the 1950's (25) and recently the noncytotoxicity of gold nanoparticles in human cells has been studied in detail by Wyatt et al (26).

6.2 Experimental

The nanorods are synthesized according to the seed-mediated growth method described in Chapter 2, page 57-59. The nanorods with aspect ratio of 3.9 are chosen for this experiment due to the efficient overlapping of the longitudinal absorption maximum which overlapped the red laser wavelength at 800nm. The nanorods prepared above are coated with poly (styrenesulfonate) (PSS, MW=18,000, Polysciences Inc.) and then conjugated with the anti-EGFR antibodies according to the methods described in Chapter 2, Page61-62. The nanorods conjugated with anti-EGFR monoclonal antibodies are centrifuged and redispersed into PBS (pH=7.4) to form a stock solution with the optical density around 1.0 at 800 nm.

HaCaT healthy cells and HOC and HSC 3 cancer cells are cultured in DMEM (Dulbecco's Modification of Eagle's Medium, Cellgro) plus 10% FBS (Fetal Bovine Serum, Gem Cell) at 37°C under 5% CO_2. Then the cells are cleaved by trypsin and replated onto 18 mm glass coverslips in a 12-well tissue culture plate and are allowed to grow for 3 days. The cover slips are coated with collagen type I (Roche) in advance for optimum cell growth. The cell monolayer on the cover slips is taken out of the medium from the incubator and rinsed with PBS buffer and then immersed into the anti-EGFR conjugated nanorods solution for 30 min at room temperature. After the nanorods incubation, the cell monolayer is rinsed with PBS buffer, and immersed in PBS buffer in a 60x15mm Petri dish for the photothermal experiments.

For the laser irradiation experiment, a cw Ti: Sapphire laser at 800 nm is used. This wavelength is in the NIR region at which the tissue has low absorption. It also overlaps efficiently with the longitudinal absorption band of the nanorods. The cell monolayer is immersed into the conjugated nanoparticle solution (OD_{800nm} = 0.5) for 30 min, rinsed with PBS buffer and then exposed to the red laser light at various power densities. The red laser at 800 nm is focused to a 1 mm diameter spot on the sample. Multiple regions on the slides are exposed to the laser light at different power densities for 4 min each and then stained with 0.4 % trypan blue (Sigma) for 10 min to test cell viability. Dead cells accumulated the dye and are stained blue while living cells got rid of it and remained clear. After staining, the samples are imaged under 10x in bright field.

6.3 Results and Discussion

Our previous work (see Chapter 5) demonstrates that antibody conjugated gold nanospheres of 35 nm in diameter act as efficient and selective photo thermal absorbers for destroying cancer cells with a visible argon ion laser without affecting the surrounding nonmalignant cells (18). The laser wavelength at 514 nm overlaps the surface plasmon absorption of the spherical nanoparticles which has an absorption maximum at 520 nm. By conjugation with anti-EGFR monoclonal antibodies that specifically target the molecular marker EGFR, the malignant cells can be destroyed with less than half the laser energy required to kill the normal cells due to the overexpresssion of the EGFR on the surface of malignant cells. However, at this wavelength, tissue penetration of the light is very low (less than 500 μm, (19)). While this may be useful for superficial lesions, to treat cancer in vivo it is desirable to have deeper tissue penetration. The near infrared region of the spectrum provides maximal penetration of light due to relatively lower scattering and absorption from the intrinsic tissue chromophores. In this region, the light penetration depth is up to ten centimeters depending on the tissue types (19).

Since the absorption band of metallic noble nanoparticles is tunable by altering the nanoparticle shape or size, designing photothermal absorbing agents in the near infrared region is possible. Other shapes of gold nanoparticles, such as branched (27), pentagon (28) and large prisms nanoparticles (29) have the surface plasmon absorption in near infrared region. Nanorods are better candidates for this application due to the accurate control of the absorption maximum to the required wavelength by changing the aspect ratio, which can be realized by simply changing the silver ion concentration during the gold nanorod growth process. However, other properties such as binding affinity of

different nanoshapes and their capping molecules to the antibodies should also be considered in the future.

Figure 6-2 shows the absorption spectrum (left) and TEM image (right) of the gold nanorods used for the selective photothermal therapy of cancer cells in this work. Nanorods with an aspect ratio of 3.9 are chosen due to their absorption overlapping with a region of minimum extinction of the human tissues. The absorption band of the nanorods also overlaps the cw Ti:Sapphire red laser wavelength at 800 nm which we used in our lab.

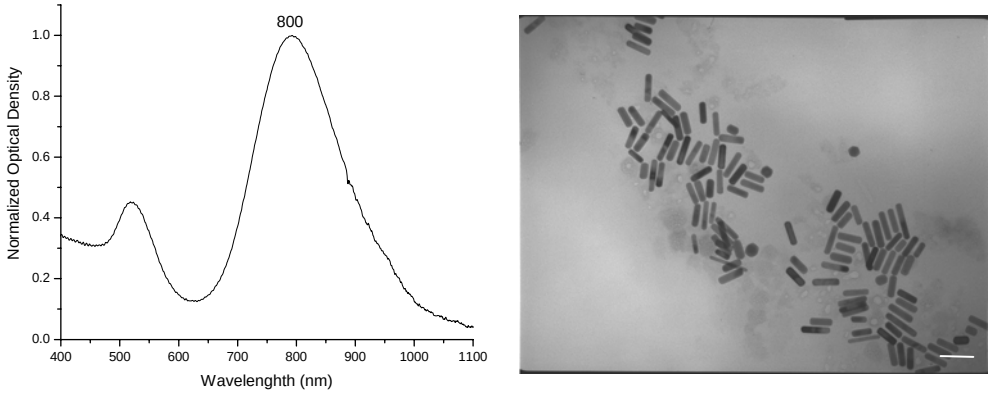

Figure 6-2: Absorption spectrum (left) and TEM image (right) of the gold nanorods with aspect ration of 3.9 used for the selective photothermal therapy of cancer cells. Scale bar: 60 μm.

After incubation with anti-EGFR antibody conjugated gold nanorods for 30 minutes, cells are exposed to cw Ti:Sapphire laser irradiation at power values of 40, 80, 120, 160, and 200 mW with a focus spot of 1 mm in diameter for 4 minutes each. The cells are then stained with trypan blue to test for their photothermal stability. Figure 6-3 shows images of irradiated HaCat healthy cells at different laser energies.

Exposure to the red laser at 800 nm at and above 160 mW (20 W/cm^2) caused photodestruction of all HaCat normal cells, which is detected by the cell viability test with trypan blue. Cell death is shown as a blue spot in a circular region that matches the laser spot size. The cells outside the laser spot are viable as indicated by their ability to get rid of the trypan blue. This also indicates that the anti-EGFR/Au nanorods themselves are not cytotoxic. Reducing the laser energy to 120 mW decreases the proportion of blue cells in the laser spot. At this energy, only the laser spot center contains a sufficiently high enough energy density to cause cell destruction. The energy density at the edge of the laser spot is not high enough to cause cell injury and thus the blue death cell spots become smaller than at higher energies.

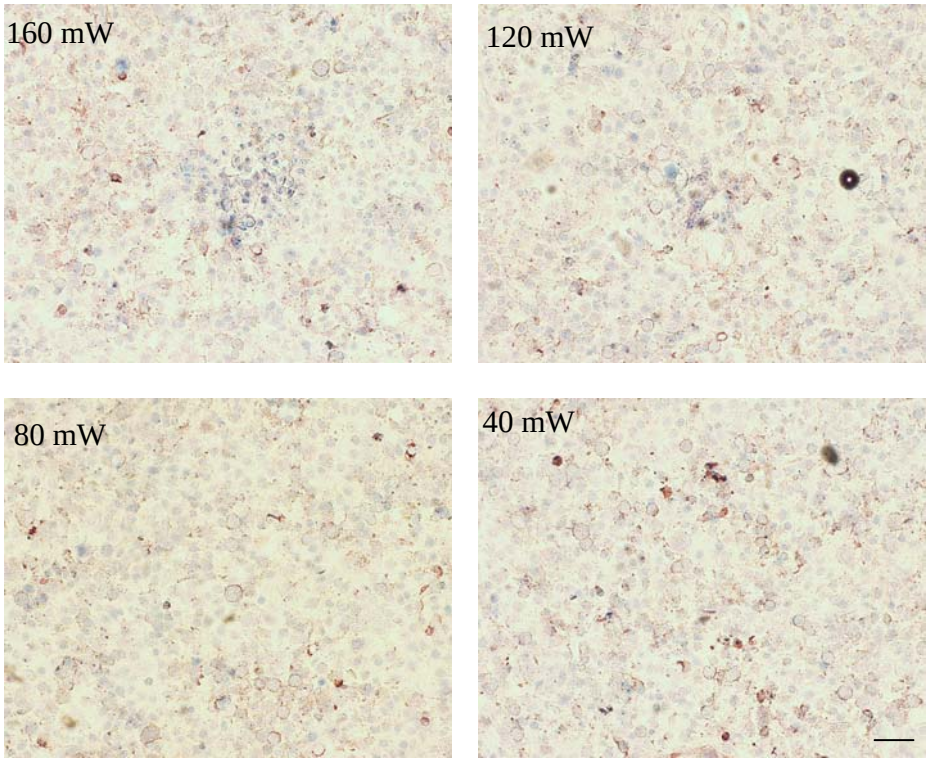

Figure 6-3: HaCat noncancerous cells irradiated at different laser powers and then stained with trypan blue. HaCatC noncancerous cells are killed at and above 160 mW (20 W/cm^2). Scale bar: 100 μm.

Figure 6-4 shows that the malignant HSC cells suffer photothermal injury at a lower laser power. Cell death occurs within the laser spots after exposure to the laser at and above 80 mW, which corresponds to 10 W/cm^2. The energy threshold for cell death of the HSC cells is about half that needed to cause cell death of the nonmalignant HaCaT cells. The dim blue color shown in the HSC cell images outside the laser spot is due

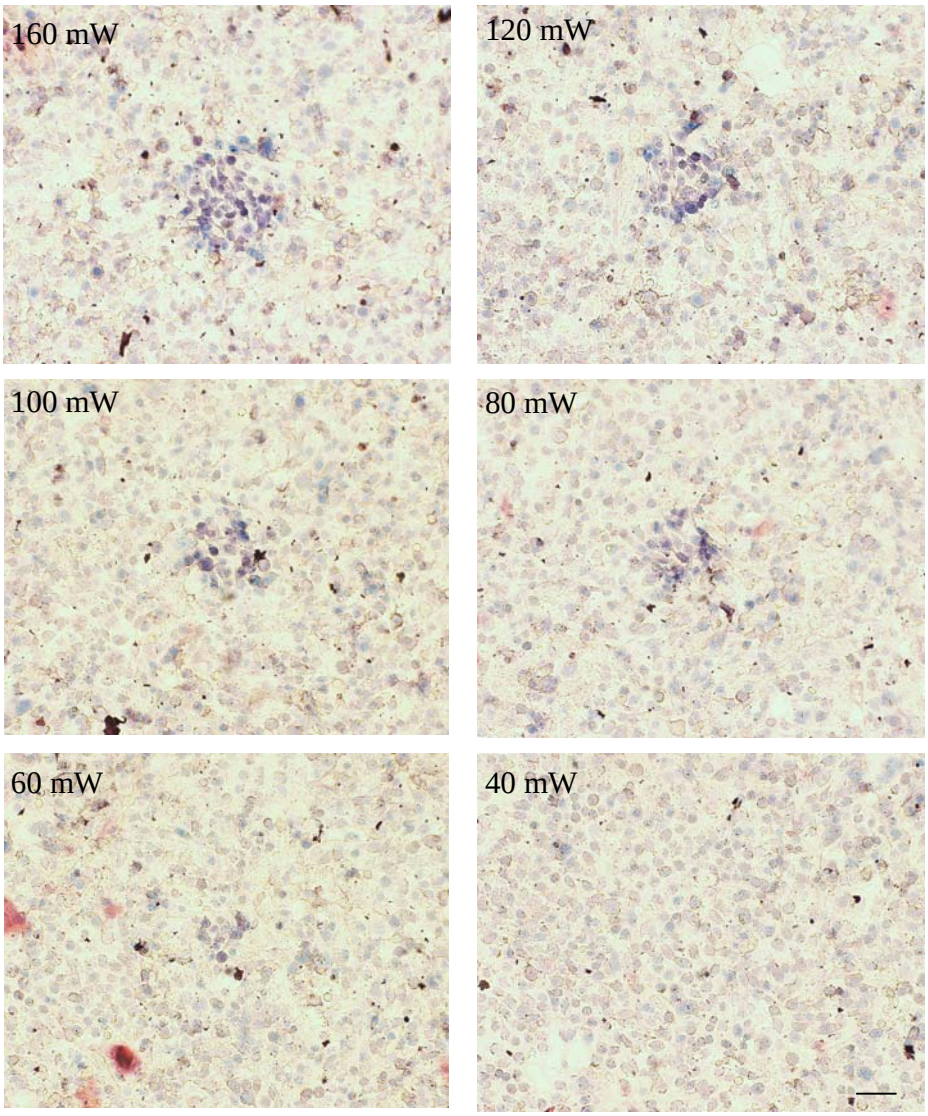

Figure 6-4: HSC cancer cells irradiated at different laser powers and then stained with trypan blue. HSC cancer cells are killed at and above 80 mW (10 W/cm^2). Scale bar: 100 μm.

to cells that died from prolonged exposure of the cells in buffer solution outside the cell incubator.

The HOC malignant cells also undergo photothermal destruction at and above 80 mW while no cell death is observed at lower power (Figure 6-5). The two malignant cells require less than half the energy needed to kill the nonmalignant cells, which is due to the overexpression of EGFR on the cancer cells and the corresponding higher amount of anti-EGFR antibody conjugated gold nanorods which absorb the light and convert it into heat at the cell surface. From the absorption spectra of the three types of cells in Figure 6-3, it can be seen that the amount of nanorods on the two malignant cells is over 2 times higher than that on the nonmalignant cells. The photothermally hot nanorods thus deliver more heat to the malignant cell membrane leading to cell death at lower energy than that for the nonmalignant cells.

The above results suggest that nanorods conjugated to antibodies can be used as a selective and efficient photothermal agent for cancer cell therapy using low energy harmless near infrared laser. Thus, for further in vivo applications, it is expected that the tumor tissue will be selectively destroyed at laser energies which will not harm the surrounding normal tissue due to the higher concentration of nanorods selectively bound to the tumor tissue. The threshold energy to kill the cancer cells in our work is found to be 10 W/cm^2, which is lower than that needed in the case of the core-shell particles (14). This difference can result from either higher absorption crossection, higher binding affinity constant of the gold nanoparticles to the antibody or higher affinity constant of the antibody to the cancer cell surface used.

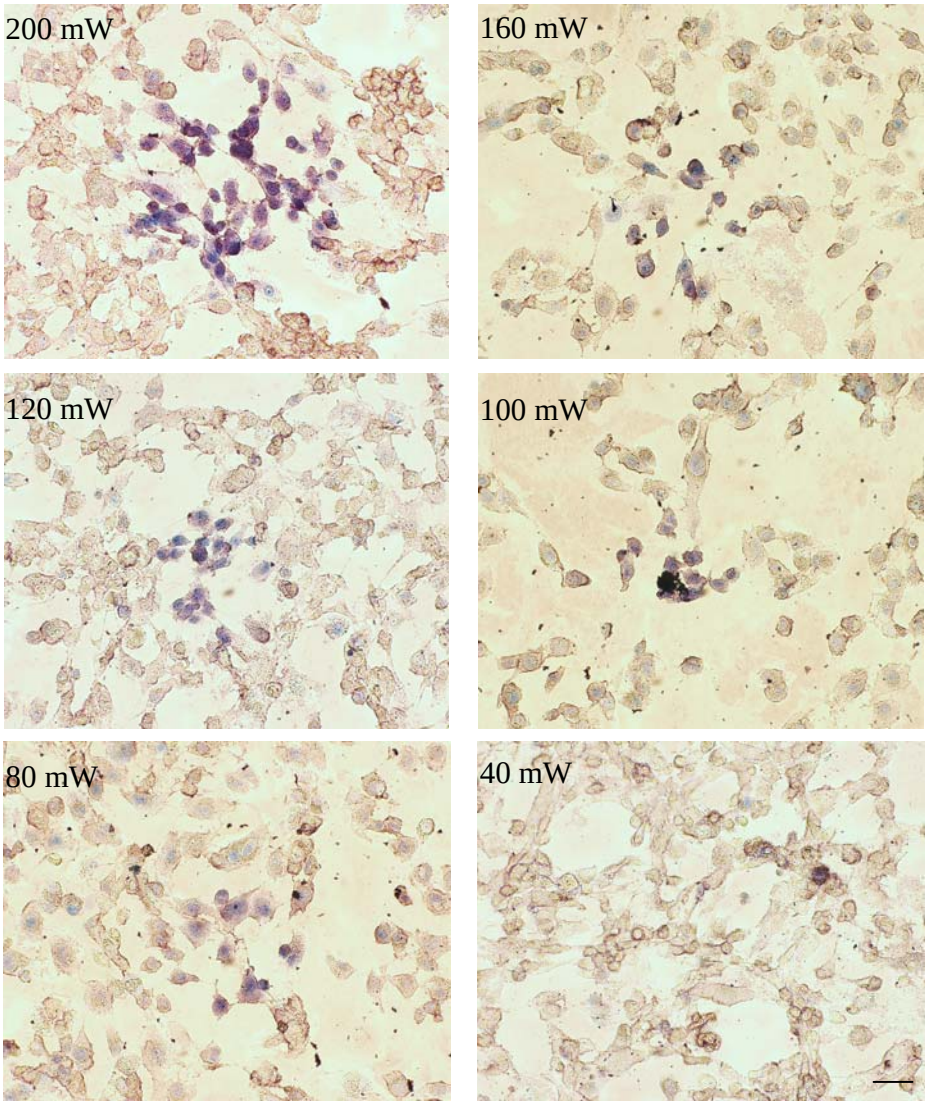

Figure 6-5: HOC cancer cells irradiated at different laser powers and then stained with trypan blue. HOC cancer cells are killed at and above 80 mW (10 W/cm^2). Scale bar: 100 μm.

It is known that many solid tumors including brain, bladder, stomach, breast, lung, endometrium, cervix, vulva, ovary, esophagus, stomach, prostate, renal, pancreatic, glioblastoma, and squamous cell carcinoma cells, overexpress EGFR on the cell cytoplasm membrane to different degrees (30). Targeting this specific molecule on the cell surface allows selective delivery of the nanorods with much higher concentrations to

carcinoma cells and allow for selective photothermal therapy with a near infrared laser for many types of cancer cells. The strong scattering of gold nanorods enables them to be imaging contrast agents as well. Thus gold nanorods offer a new dual diagnostic imaging/therapy method in biomedical sensing and cancer therapy tunable to be used in the visible and near infrared region.

6.4 References

(1) Alivisatos, A. P. *Science*, **1996**, *271*, 933.

(2) Kreibig, U.; Vollmer, M. *Optical Properties of Metal Clusters;* New York: Springer, **1995**.

(3) El-Sayed, M. A. *Acc. Chem. Res.* **2001**, *34(4)*, 257.

(4) Link, S.; El-Sayed, M. A. *J. Phys. Chem. B* **1999**, *103*, 8410.

(5) Yguerabide, J.; Yguerabide, E. E. *Anal. Biochem.* **1998**, *262*, 137.

(6) Link, S.; El-Sayed, M. A. *Int. Rev. Phys. Chem.* **2000**, *19*, 409.

(7) West, J. L.; Halas, N. J. *Annu. Rev. Biomed. Eng.* **2003**, *5*, 285.

(8) Paciotti, G. F.; Myer, L.; Weinreich, D.; Goia, D.; Pavel, N.; McLaughlin, R. E.; Tamarkin, L. *Drug Delivery*, **2004**, *11(3)*, 169.

(9) Jain, K. K. *Technol. Cancer Res. & Treat.* **2005**, *4(4)*, 407.

(10) Wu, X.; Liu, H.; Liu, J.; Haley, K. N.; Treadway, J. A.; Larson, J. P.; Ge, N.; Peale, F.; Bruchez, M. P. *Nat. Biotechnol.* **2003**, *21*, 41.

(11) Chan, W. C. W; Maxwell, D. J.; Gao, X.; Bailey, R. E.; Han, M.; Nie, S. *Curr. Opin. Biotechnol*. **2002**, *13*, 40.

(12) Alivisatos, A. P. *Nat. Biotechnol*. **2004**, *22(1)*, 47.

(13) Sokolov, K.; Aaron, J.; Hsu, B.; Nida, D.; Gillanwater, A.; Follen, M.; Macaulay, C.; Adler-Storthz, K.; Korgel, B.; Discour, M.; Pasqualini, R.; Arap, W.; Lam, W.; Richartz-Kortum, R. *Technol. Cancer Res. & Treat.* **2003**, *2(6*), 491.

(14) Hirsch, L. R.; Stafford, R. J.; Bankson, J. A.; Sershen, S. R.; Rivera, B.; Rrice, R. E.; Hazle, J. D.; Halas, N. J.; West, J. L. *Proc. Natl. Acad. Sci. USA* **2003**, *100*, 13549.

(15) Sokolov, K.; Follen, M.; Aaron, J.; Pavlova, I.; Malpica, A.; Lotan, R.; Richartz-Kortum, R. *Cancer Res*. **2003**, *63*, 1999.

(16) El-Sayed; I. H.; Huang, X.; El-Sayed, M. A. *Nano Letters* **2005**, *5 (5)*, 829.

(17) Loo, C.; Lowery, A.; Halas, N.; West, J.; Drezek, R. Nano letters **2005**, *5(4)*, 709.

(18) El-Sayed, I. H.; Huang, X.; El-Sayed, M. A. *Cancer Letters*, **2005**, in press.

(19) Weissleder, R. *Nat. Biotechnol*. **2001**, *19*, 316.

(20) Shi Kam, N. W.; O'Connell, M.; Wisdom, J.A.; Dai, H. *Proc. Natl. Acad. Sci. USA* **2005**, *102*, 11600.

(21) Hao, E.; Schatz, G. C. *J. Chem. Phys.* **2004**, *120*, 357.

(22) Hao, E.; Schatz, G. C.; Hupp, J. T. *J. Fluorescence* **200**4, *14*, 331.

(23) Murphy, C. J.; Sau, T. K.; Gole, A. M.; Orendorff, C. J.; Gao, J.; Gou, L.; Hunyadi, S. E.; Li, T. *J. Phys. Chem. B* **2005**, *109 (29)*, 13857.

(24) K. Lance Kelly, Eduardo Coronado, Lin Lin Zhao, and George C. Schatz, *J. Phys. Chem. B* **2003**, *107 (3)*, 668.

(25) Sherman, A. I.; Ter-Pogossian, M. *Cancer* **1953,** *6*, 1238.

(26) Connor, E. E.; Mwamuka, J.; Gole, A.; Murphy, C. J.; Wyatt, M. D. *Small* **2005**, 1, 325.

(27) Hao, E.; Bailey, R. C.; Schatz, G. C.; Hupp, J. T.; Li, S. *Nano Letters* **2004**, *4(2)*, 327-330.

(28) Malikova, N.; Pastoriza-Santos, I.; Schierhorn, M.; Kotov, N. A.; Liz-Marzan, M. L. *Langmuir* **2002**, *18*, 3694-3697.

(29) Huang, W.; Qian, W.; El-Sayed, M. A. *Nano Letters* **2004**, *4(9)*, 1741-1747

(30) Herbst, R. S.; Shin, D. M. *Cancer* **2002**, *94***,** 1593-1611.

CHAPTER 7
CATALYTIC PROPERTY OF GOLD NANOPARTICLES FOR THE OXIDATION OF NADH TO NAD^+

Abstract

Nicotinamide adenine dinucleotide is an important coenzyme involved in the production of ATP, the fuel of energy, in every cell. It alternates between the oxidized form NAD^+ and the reduced form dihydronicotinamide adenine dinucleotide (NADH) and serves as a hydrogen and electron carrier in the cellular respiratory processes. In the present work, the catalytic effect of gold nanoparticles on the oxidization of NADH to NAD^+ is investigated. The addition of gold nanoparticles is found to quench the NADH fluorescence intensities but had no effect on the fluorescence lifetime. This suggested that the fluorescence quenching is not due to coupling with the excited state, but due to changing the ground state of NADH. The intensity of the 340 nm absorption band of NADH is found to decrease while that of the 260 nm band of NAD^+ is found to increase as the concentration of gold nanoparticles increases. This conversion reaction is further supported by nuclear magnetic resonance and mass spectroscopy. The effect of the addition of NADH is found to slightly red shift and increase the intensity of the surface plasmon absorption band of gold nanoparticles at 520 nm. This gives strong support that the conversion of NADH to NAD^+ is occurring on the surface of the gold nanoparticles, i.e. NADH is surface catalyzed by the gold nanoparticles. The catalytic property of this reaction might have important future applications in biological and medical fields. The work has been published in J. Photochem. Photobiol. B: Biology, 2005, 81, 76.

7.1 Introduction

Nicotinamide adenine dinucleotide is one of the most important coenzymes found in every cell. It is involved in the production of energy in all cells, and is needed to oxidize all foods including carbohydrate, fats, and amino acids to produce ATP which is used by every cell in the body (1). It serves as a hydrogen and electron carrier and alternates between the oxidized state NAD^+ and the reduced state – dihydronicotinamide adenine dinucleotide (NADH) in cellular respiratory and metabolic processes (2). The extra hydrogen on position 4 of the planar pyridine ring in NADH results in the significant spectral differences between NADH and NAD^+ (Figure 1). In contrast with oxidized NAD^+, the reduced coenzyme NADH absorbs strongly around 340 nm and fluoresces in the blue spectral region with a maximum around 460 nm (3). This reduced fluorescent form is one of the major endogenous fluorophores on cellular fluorescence (4) and the absorption and fluorescence of which have been widely used to monitor enzymatic reactions (5) or to detect enzyme-coenzyme complex formation (6).

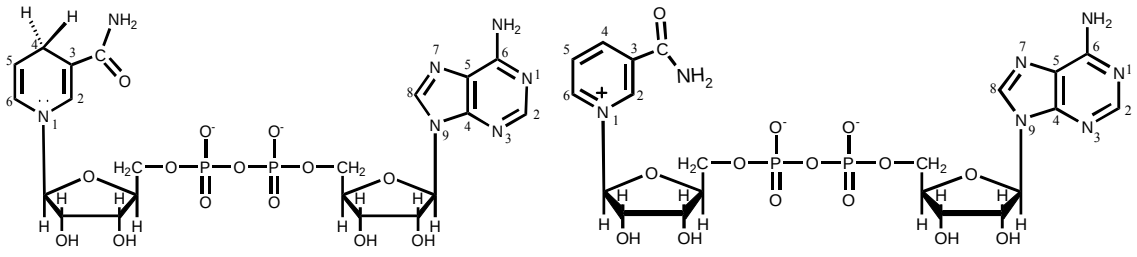

Dihydronicotinamid Adenine Dinucleotide (NADH)

Nicotinamid Adenine Dinucleotide (NAD^+)

Figure 7-1: Structure of NADH and NAD+.

Metal nanoparticles have been shown to catalyze some redox reactions such as the electron transfer reaction of hexacyanoferrate(III) ions and thiosulfate ions catalyzed by platinum nanoparticles (7) and the Suzuki reaction between phenylboronic acid and iodobenzene catalyzed by PVP-Palladium nanoparticles (8). The large surface to volume ratio and the enhanced surface atomic catalytic activity make metallic nanoparticles attractive catalysts compared to bulk materials. In this paper, the effect of gold nanoparticles on NADH is systematically investigated by following the change in the UV/Vis absorption and fluorescence spectroscopy, ^{1}H nuclear magnetic resonance and mass spectroscopy. A catalytic function of gold nanoparticles to the biologically important reaction of NADH to NAD^{+} is found. This catalytic property of gold nanoparticles to NADH might have future importance in biochemical and medical applications.

7.2 Experimental

NADH disodium salt is obtained from CALBIOCHEM Co. Gold nanoparticles are prepared by the citrate reduction of $HAuCl_4$ (9, 10). Briefly, 10mL of 38.8 mM sodium citrate is quickly injected into 100 mL of 1 mM $HAuCl_4$ vigorously stirred in a 250 mL round-bottom flask equipped with a condenser. The color is quickly changed from pale yellow to burgundy. The heating is continued for 10 min. Then the solution is kept stirring for 15 min without heating. After it reached room temperature, the solution is filtered through a 0.45 μm Gelman Nylon filter. The gold nanoparticles made in this way have the absorption maximum at 520 nm. TEM showed the average particle size of 15 nm. A series of Au and NADH mixed solution are prepared by simply adding 1.0 to 2.5

mL of the stock gold solutions (OD = 1.0) and 0.03 mL to 0.9 mL of the stock NADH solution (1mM) as well as water to form a final solution in a total volume of 3.0 mL. The final concentrations of gold nanoparticles are calculated according to the extinction coefficient calculated by Stephan Link ($\varepsilon = 7.2 \times 10^8$ for 15 nm gold nanoparticles) (11). The Au nanoparticle and NADH mixed solution is kept in dark for later NMR and MS measurements and time experiments. The mixed solutions are stable for about one week in cold and dark.

The absorption spectrum of each sample is measured on a Shimadzu UV-3101PC spectrometer in a quartz cell. The fluorescence spectrum excited at 325 nm is measured on a Shimadzu RF-5301PC spectrofluorophotometer. For NADH with higher concentrations, a 2-mm quartz is used at an angle of 45^o to the excitation beam so that the fluorescence just came from the front surface of the sample. PTI fluorimeter with a nitrogen laser and PMT detector is used to obtain the time-resolved fluorescence spectrum. Mass spectrum is obtained from a LCQ Advantage mass spectrometer in a negative mode with electrospray ionization (ESI). The NADH (0.2 mM) or the NADH-Au mixed solution (0.2 mM NADH are mixed with 0.46 nM Au solution and let sit in dark for 3 days before measurement) is diluted by about a factor of 5 using water/acetonitrile/ammonia before injection. Nuclear magnetic resonance spectra are obtained from a Varian Inova 600MHz NMR spectrometer equipped with a chili cryoprobe. 225 μl of NADH (1.0 mM) or NADH-Au mixed solutions (1.0 mM NADH are mixed with 2.0 nM Au solution and let sit in dark for 3 days before measurement) are mixed with 25 μl of D_2O and then used for NMR experiment.

7.3 Results and discussion

7.3.1 Fluorescence results

The spectra effect of Au nanoparticles on NADH is followed by the change of fluorescence intensities of NADH when different concentrations of Au nanoparticles are just mixed with NADH solution, shown in Figure 7-2. Figure 7-2(a) shows that when Au

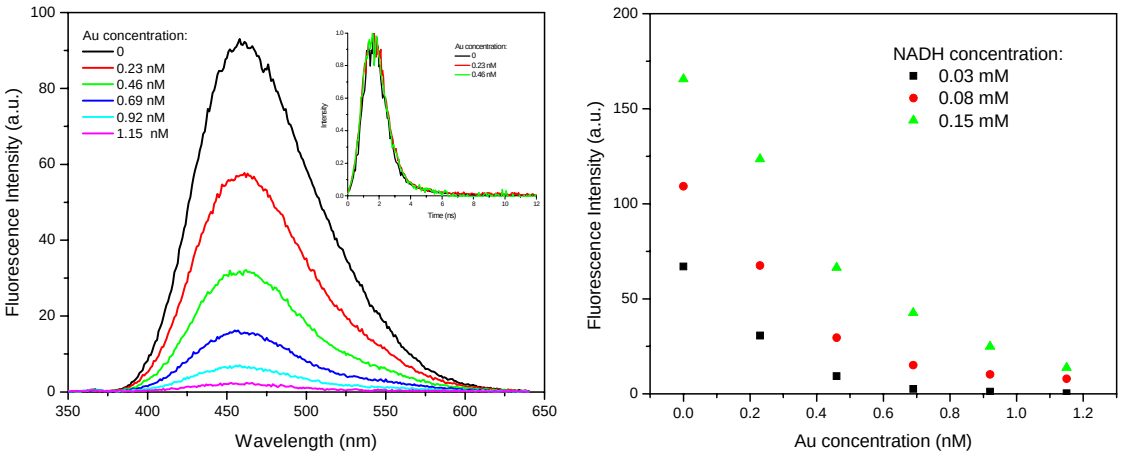

(a) (b)

Figure 7-2: (a) Fluorescence spectra of NADH (0.08 mM) at different concentrations of gold nanoparticles (λ_{exci} = 325 nm). Inset is the time-resolved fluorescence decay spectra of NADH at 460 nm at different concentrations of gold nanoparticles. The lifetime of NADH fluorescence obtained by a monoexponential fitting is about 0.85 ns which is the same for all samples; (b) The quantitative relationship of the fluorescence intensity of NADH at 460 nm with the concentration of gold nanoparticles.

nanoparticles are added into NADH, the fluorescence of NADH with a maximum at 460 nm (λ_{exci} = 325 nm) is quenched. The quenching effect is increased with the increasing of the concentration of Au nanoparticles. The same quenching effect is also observed at other concentrations of NADH. Figure 7-2 (b) shows a quantitative relationship of the fluorescence intensities at 460 nm with the concentration of Au nanoparticles at different concentrations of NADH. It can been seen that for 0.03 mM NADH, 0.92 nM Au

nanoparticles (the final concentration of gold nanoparticles when 2.0 mL gold (OD = 1.0) are mixed with 0.09 mL of 1mM NADH solution and 0.91 mL water) induced the fluorescence to be totally quenched while for 0.08 and 0.15 mM NADH more Au nanoparticles are needed to lead to the same effect. To find out the reason for the quenching effect, the fluorescence lifetime of pure NADH as well as NADH in Au solutions is measured. The normalized fluorescence decay in inset of Fig. 2(a) shows that the fluorescence lifetimes for these three samples are the same as that of pure NADH. This suggests that the quenching effects are not due to the coupling of Au nanoparticles with the excited states of NADH, but due to the change of their ground states. So the absorption spectra of NADH should change. By a monoexponential fitting of the fluorescence decay of NADH, the fluorescence lifetime is about 0.85 ns. There exists variation on the absolute value of the life time as the instrument is most sensitive to time scale of over nanosecond region.

7.3.2 Absorption results

The absorption spectra are measured right after Au nanoparticles are added into NADH solution. Figure 7-3(a) solid line shows that NADH has three absorption bands at UV-Vis region. The band at 340 nm is from the n-π* transition of the dihydronicotinamide part which has a coplanar conformation with the carboxamide moity and thus the electrons are conjugated between these two parts (12, 13). The stronger band at 260 nm is from the π-π* transition of the adenine ring. The strongest band around 205 nm is from the π-π* transition of the dihydronicotinamide part. From Figure 7-3 we can see that when the concentration of Au nanoparticles are linearly increased, the absorption

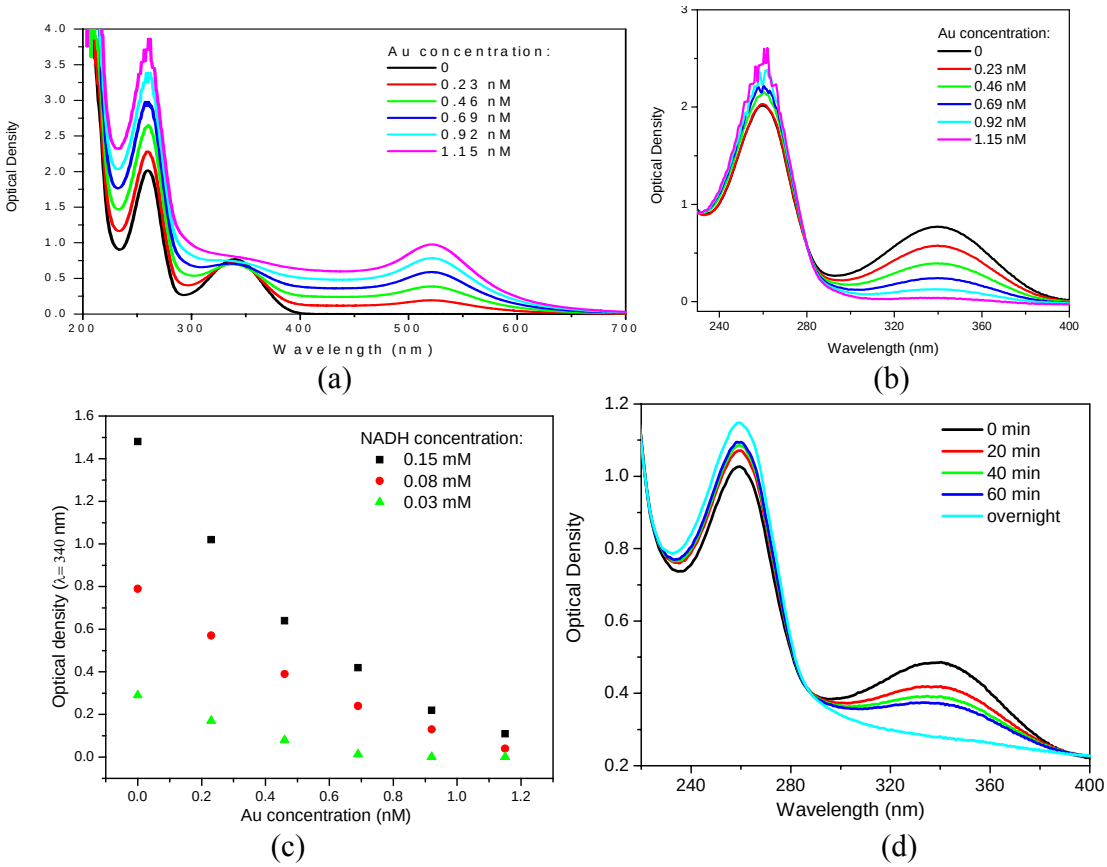

Figure 7-3: Absorption spectra of the mixed solutions of NADH (0.08 mM) and gold nanoparticles at different concentrations; (b) The absorption spectra of NADH after subtraction of the absorption contribution from gold nanoparticles; (c) The quantitative relationship of the absorption intensity of NADH at 340 nm with the concentration of gold nanoparticles; (d) The absorption spectra of NADH (0.08 mM) at different time after gold nanoparticles (0.46 nM) are added.

intensities of both 260 nm of NADH and 520 nm of Au nanoparticles linearly increased while the intensities of the 340 nm band didn't change much. The intensities of 205 nm band are too strong to be resolved. Due to the contribution of Au nanoparticles, the absorption of the mixed solution is subtracted by the absorption of pure Au nanoparticles at the same concentration as in the mixed solution on considering of no obvious change on the gold absorption spectra and thus the change only from NADH absorption can be resolved, as shown in Figure 7-3(b). It is obvious that when Au nanoparticles are added,

the intensity of the 340 nm band greatly decreased while the intensity of the 260 nm band slightly increased. More Au nanoparticles induced further decrease on the former band and further increase on the latter band. Since the 340 nm band is from the electron transition on the coplanar structure of dihydronicotinamide and carboximate, the intensity decrease of this band suggests that the structure of this part is changed due to the addition of gold nanoparticles, i.e NADH must be converted to some other species. The intensity increase of the 260 nm band which is due to the adenine ring indicates that the adenine is not destroyed by the Au nanoparticles, but conversely this band has higher extinction coefficient than that in NADH. It has been reported that NAD^+, the oxidized state of NADH has larger extinction coefficient at 260 nm (18×10^{-3}) than that of NADH (14.4 $\times10^{-3}$) due to the contribution of oxidized nicotinamide (14). It doesn't have the 340 nm band due to a twisted and cisoid conformation between the oxidized nicotinamide and carboxamide (15). So the changes of the absorption spectra of NADH due to the effect of Au nanoparticles indicate that NADH might be oxidized to NAD^+, and thus the decrease of the 340 nm band could be due to the decrease of the amount of NADH and the increase of the 260 nm band is due to the production of NAD^+ which had higher molar extinction coefficient than that of NADH. Further experiments are carried on other NADH concentrations. The quantitative relationship of the absorption intensities at 340 nm with the concentration of Au nanoparticles are shown in Figure 7-3(c). Since the 340 nm band is specific for NADH, the absorption intensity of this band represents the amount of NADH. From Figure 7-3(c) we can see that 0.92 nM Au nanoparticles can lead to the complete reaction of 0.03 mM NADH according to the absorption intensity of the NADH. This is consistent with the fluorescence results shown in Figure 7-2 that 0.92

nM Au nanoparticles lead to the complete reaction of 0.03 mM NADH according to the fluorescence intensity of NADH.

The effect on the absorption spectra of NADH by the addition of Au nanoparticles also depended on time, which is shown in Figure 7-3(d). Figure 7-3(d) shows that as the time increased, the intensity of 340 nm band decreases while that of the 260 nm band increases. The band at 340 nm totally disappeared after overnight and the band at 260 nm became strongest among all the time. This suggests that more and more NADH is reacted with gold nanoparticles until complete reaction after overnight.

7.3.3 Mass spectra and nuclear magnetic resonance results

If NADH is converted into NAD^+, then the mass spectra of pure NADH and NADH in Au solutions should shown the differences of their molecular ion peak and NMR of these two samples should shown the difference of the chemical shifts of protons from the oxidized and reduced nicotinamide rings. A soft ionization mode - Electron Spray Ionization is used in the mass spectra measurement and the signals are detected in a negative mode. The strongest peak in NADH in Figure 7-4 represents the molecular ion of NADH (FW = 663). Due to the two negative charges on the NADH (see Figure 7-1), a proton is added to the molecule to form a single negative charged ion. So the molecular ion appeared at 664.2. The peak at 686.2 is from the NADH · Na ion. And the double charged NADH ion is detected at 331.7. While in the NADH and Au mixed solution, only one peak is detected in the range from 250 to 700. This peak at 661.9 represented the molecular ion peak of the product. While NAD^+ (FW = 662, single negative charged)

should have a molecular ion at 662, the product is possibly NAD^+. As electron spray ionization is a kind of soft ionization, no other fragment peaks are observed.

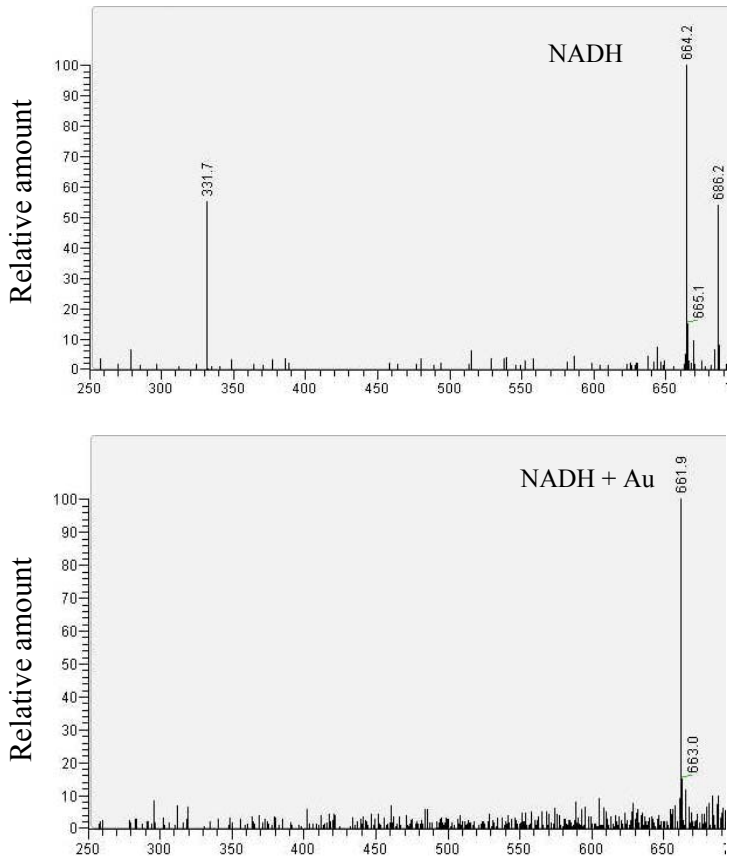

Figure 7-4: ESI - MS of pure NADH (0.2 mM) and NADH with gold nanoparticles mixed (0.46 nM) using a negative detection mode. The peak at 664.2 is the molecular ion of NADH (FW = 663) plus a proton for the detection in the negative mode. The peak at 661.9 is the molecular ion of NAD^+ (FW = 662).

Figure 7-5 shows the ^1H NMR of NADH and NADH-Au mixed solutions. The Au nanoparticles are mixed with NADH solution for three days and absorption spectra had shown that there are no NADH left. The signals between 4.0 to 5.8 ppm are cut off due to the strong and broad peak from water. The peak assignments of protons on the carbons of the nicotinamide, adenine and ribose C1' are listed in the Table 7-1. The chemical shifts of the protons on NADH and NAD^+ reported by Catterall et.al (16) at pH = 7.2 (which is

the same condition in our samples) are also listed for comparison. The results of NADH agree very well with those from Catterall et.al.

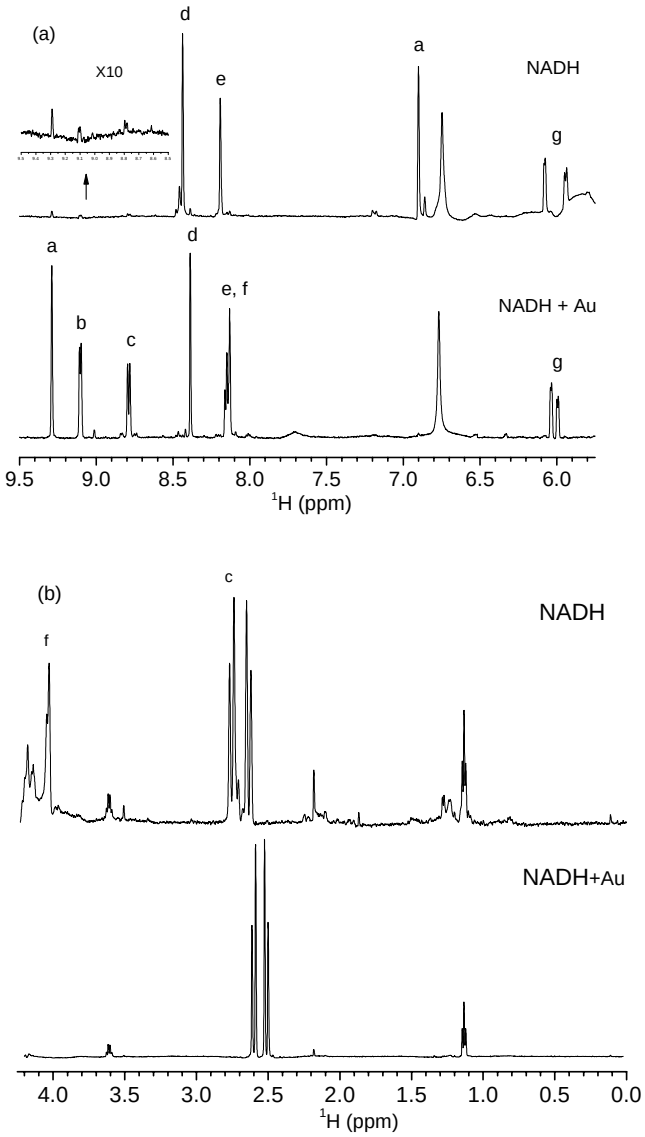

Figure 7-5: ^{1}H NMR of NADH (1.0 mM) and NADH with gold nanoparticles (2 nM) mixed (10% D_2O) at the region from 9.5 to 5.8 ppm (a) and the region from 4.2 ppm to zero (b). The region between 4.2 to 5.6 ppm is not shown due to the strong signals from water. The inset in NADH spectrum from 6 to 9.5 ppm is the enlarged signals between 8.5 and 9.5 ppm in NADH. The assignments of the labeled peaks are listed and compared with the NMR of NADH and NAD^+ from reference in Table 7-1.

Table 7-1: Some of the ^{1}H-NMR peak assignments of NADH and NADH in gold nanoparticle solutions. The data reported by Catterall et al (16) are listed for comparison.

Number	H position	NADH (ppm)	NADH (16) (ppm)	NADH in Au NPs solution (ppm)	NAD^+ (16) (ppm)
a	N-C-2-H	6.90	6.98	9.30	9.32
b	N-C-6-H	Buried by H_2O peak	-	9.10	9.17
c	N-C-4-H	2.75	2.8	8.80	8.84
d	A-C-8-H	8.44	8.45	8.39	8.41
e	A-C-2-H	8.19	8.20	8.14	8.11
f	N-C-5-H	4.04	-	8.15	8.21
g	Ribose-C-1'-H	5.95, 6.08	6.09, 6.12	6.00, 6.04	6.05, 6.13

By the comparison of the chemical shifts of the protons on NADH in Au solutions with those of protons on NAD^+, we can see that they are in a great agreement. These indicate that the NADH in Au solutions is actually NAD^+. The oxidization at the C-4 position of NADH (c peak in Fig. 5) led to the far down shift of the chemical shift of the protons at this position from 2.8 ppm to 8.8 ppm in NAD^+. And the oxidization of the dihydronicotinamide to nicotinamide also resulted in the big change of the chemical shifts of other protons on the nicotinamide rings (a,b and f peaks). The chemical shifts of the protons on adenines are the same in NADH and NAD^+ (d and e peaks). The chemical shift of the ribose C-1' which is bond to the adenine ring (g, left peak) didn't change, but the chemical shift of the ribose C-1' which is bond to the nicotinamide ring (g, right peak) of NAD^+ is obviously down shifted. From the zoom-in region between 8.5 and 9.5 ppm in the NADH spectrum, we can see that those peaks in the mixed solution also showed up in the pure NADH solution in which there are no Au nanoparticles at all. This means that there is about 1% NAD^+ impurities in the pure NADH stock solution.

7. 3.4 Explanation of the oxidation reaction

So why the oxidation reaction of NADH to NAD^+ happens after the addition of Au nanoparticles? What induces this redox reaction? Since Au nanoparticles are obtained by sodium citrate reduction of $HAuCl_4$, there might some $HAuCl_4$ molecules left and they could cause the reaction. But this reason is excluded because it is also found that Au nanorods synthesized by the electrochemical method (no $HAuCl_4$ acid is added and gold metal is converted from the anode to from gold nanoparticles) shows the same spectroscopic changes as induced by the Au nanoparticles although in a much slower reaction speed, shown in Figure 7-6 (a). This indicates that it is not $HAuCl_4$ inducing the conversion of NADH to NAD^+ in the Au nanoparticle solution. The slower reaction speed in Au nanorods than in nanospheres could be due to their differences in the shape, size and surface capping materials of the nanoparticles. Another possibility might be the $HAuCl_2$ left in solution which is due to the incomplete reduction of $HAuCl_4$. This reason is also excluded because the reduction of $HAuCl_2$ solution (0.17 mM) by NADH (Figure 7-6 (b)) is much slower than that caused by Au nanoparticles (the $HAuCl_2$ is obtained by reduction of $HAuCl_4$ in CTAB solution with ascorbic acids. The $HAuCl_2$ concentration is selected by assuming 100% $HAuCl_4$ is converted to $HAuCl_2$ during the synthesis of gold nanoparticles).

From the absorption spectra of Au nanoparticles in Figure 7-6 (c) we can see that after 24 h the gold surface plasmon band red shifted by 3 ~ 4 nm and the intensities increased about 4%. This indicates that Au nanoparticles are involved in the reactions. From Figure 7-6 (d), it can be seen that the initial reaction rate determined by using the absorption

intensity of NADH at 340 nm depends on Au concentration linearly in the range used (0.23 to 1.17 nM). This, together with the absorption changes of the Au surface plasmon band, suggests that the catalytic reaction occurs at the surface of Au nanoparticles.

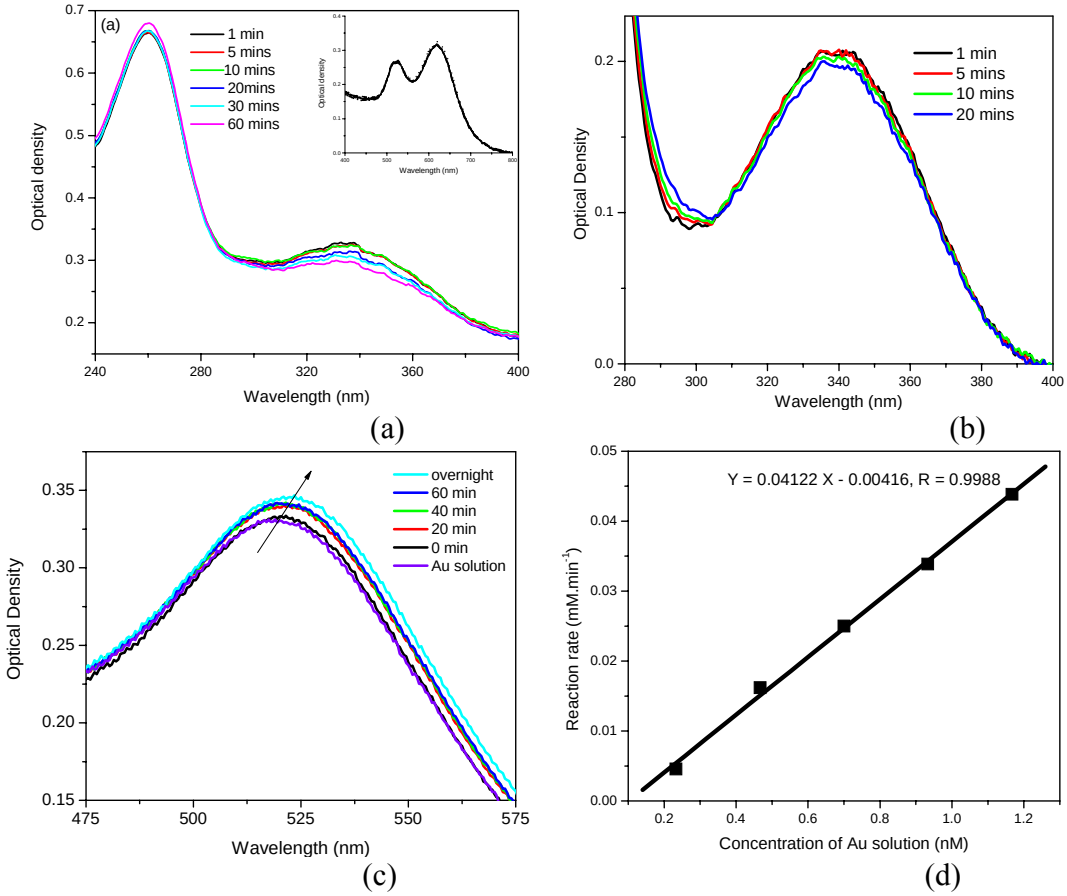

Figure 7-6: Absorption spectra of NADH (0.05 mM) at different time after gold nanorods (0.3 nM) are added. The gold nanorods are synthesized by the electrochemical method. Inset is the absorption region of gold nanorods between 400 to 800 nm; (b) Absorption spectra of NADH (0.05 mM) at different time after $HAuCl_2$ solution (0.17 mM) is added. The $HAuCl_2$ solution is obtained by reduction of $HAuCl_4$ in CTAB solution with ascorbic acids; (c) Absorption spectra of gold nanoparticles (0.46 nM) at different time after NADH (0.05 mM) is added; (d) Initial reaction rate of the NADH oxidization vs concentration of gold nanoparticles. The reactions are taken at the same initial NADH concentration (0.08mM). The initial reaction rates are determined by the decreased amount of NADH within the first one minute after gold nanoparticles are added.

The Au^{+} on the surface of Au nanoparticles could be one reason due to the incomplete reduction of Au^{3+}. The Au nanoparticles must catalyze the reduction of Au^{+} on the surface of Au nanoparticles if this is the case because much higher concentration of $HAuCl_2$ (assuming 100% $HAuCl_4$ is converted to $HAuCl_2$ in the synthesis of Au nanoparticles) solution shows slower reduction (Figure 7-6 (b)). Thus the oxygen molecules adsorbed on the surface of Au nanoparticles is the possible reason due to the high surface-to-volume ratio of the Au nanoparticles. It has been reported that many important reactions involving oxygen as the oxidant are catalyzed by Au nanoparticles, such as the low-temperature CO oxidation (17-19), propylene epoxidation (20, 21), combustion of hydrocarbons (22, 23), NOx reduction (24, 25), hydrogenation reactions (26), etc.

In our work, the fact that oxygen is involved as the oxidant and Au nanoparticles as the catalyst for the NADH oxidation reaction is supported by the nitrogen flush experiment. When Au nanoparticles are flushed with nitrogen gas for several minutes before they are mixed with NADH solution, the reaction speed (the slope of the fitting curves) is obviously slowed compared to the reaction in oxygen (Figure7-7). So the addition of Au nanoparticles simultaneously introduced the catalysts and the oxidant.

In this work it has been shown that Au nanoparticles catalyze the oxidation reaction of the biofluorophore nicotinamide adenine dinucleotide which is one of the most important coenzymes in every cell. The decrease of the absorption intensities at 340 nm is due to the decrease of the NADH amount and the increase of the absorption intensities at 260 nm is due to the formation of NAD^{+}. As NAD^{+} is not fluorescent, the conversion reaction

induces the quenching of the fluorescent intensities of NADH. The change of the surface plasmon absorption band of Au nanoparticles indicates NADH is surface catalyzed by the Au nanoparticles. The oxygen on the surface of Au nanoparticles possibly reacts with NADH and produces NAD^+. This catalytic effect of Au nanoparticles on NADH could have future importance in biochemical and medical applications.

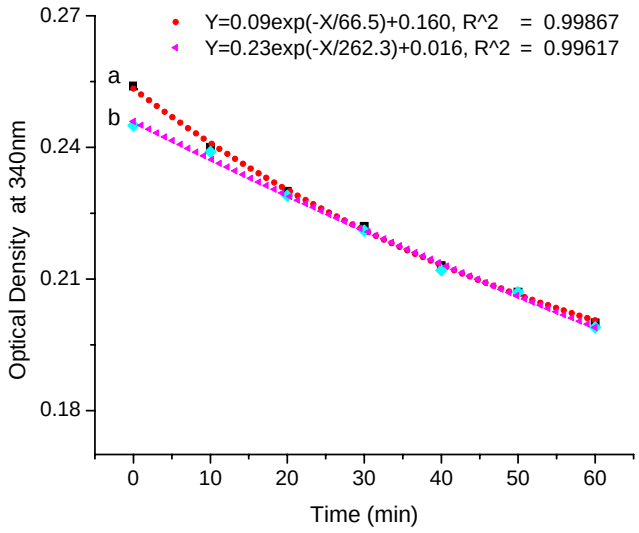

Figure 7-7: Comparison of the reaction speed of NADH oxidation in O_2 (a) and in N_2 (b). The data are fitted by first order of the exponential decay.

7.4 References

(1) Jeffrey, J. *Dehydrogenases Requiring Nicotinamide Coenzymes*, Birkhgoldser Verlag, Basel, Boston and Stuttgart, **1980**.

(2) Dolphin, D.; Poulson, R.; Avramovic, O. *Pyridine Nucleotide Coenzymes*, Wiley, New York, **1987**.

(3) White, A.; Handler, P.; Smith, E. L.; Hill, R. L.; Lehman, I. R. *Principle of Biochemistry*, McGraw-hill, New York, **1978**.

(4) Köng, K.; Bers, M. W.; Tromberg, B. *J. Photochem. Photobio. B: Biol*. **1997**, *37,* 91.

(5) Bergmeyer, H. U. *Methoden der enzymatischen Analyse*, Verlag Chemie, Weinheim, **1962**.

(6) Pfleiderer, G.; Hohnholz, E. *Z. Biochem.* **1959**, *331*, 254.

(7) Narayanan, R.; El-Sayed, M. A. *J. Phys. Chem. B* **2003**, *107*, 12416.

(8) Narayanan, R.; El-Sayed, M. A. *J. Am. Chem. Soc*. **2003**, 125, 8340.

(9) Grabar, K. C.; Freeman, R. G.; Hommer, M. B.; Natan, M. J. *Anal. Chem.* **1995**, *67*, 735.

(10) Frens, G. *Nat. Phys. Sci.* **1973**, *241*, 20.

(11) Link, S.; El-Sayed, M. A. *J. Phys. Chem. B* **1999**, *103*, 8410.

(12) Fisher, P.; Fleckenstein, J.; Hönes, J. *J. Photochem. Photobio*. **1988**, *47*, 193.

(13) Bgoldmgarten, B.; Hönes, J. *J. Photochem. Photobio*. **1988**, *47*, 201.

(14) Campbell, I. D.; Dwek, R. A. *Biological Spectroscopy*, Menlo Park, CA: Benjamin Cummings, **1984**.

(15) Hofmann, H. J.; Kuthan, J. *Collect. Czech. Chem. Commun*. **1979**, *44*, 2633.

(16) Catterall, W. A.; Hollis, D. P.; Walter, C. F. *Biochem*. **1969**, *8*, 4032.

(17) Valden, M.; Lai, X.; Goodman, D. W. *Science* **1998**, 281, 1647.

(18) Okamura, M.; Nakamura, S.; Tsubota, S.; Nakamura, T.; Azuma, M.; Haruta, M. *Catal. Lett.* **1988**, *51*, 53.

(19) Griesel, R. J. H.; Nieuwenhuys, B. E. *J. Catal.* **2001**, *199*, 48.

(20) Stangland, E. E.; Stavens, K. B.; Andres, R. P.; Delgass, W. N. *J. Catal*. **2000**, 191, 332.

(21) Sinha, A. K.; Seelan, S.; Tsubota, S.; Hayashi, M. *Topics in Catalysis* **2004**, *29*, 95.

(22) Griesel, R. J. H.; Kooyman, P. J.; Nieuwenhuys, B. E. *J. Catal.* **2000**, *191*, 430.

(23) Waters, R. D.; Weimer, J. J.; Smith, J. E. *Catal. Lett*. **1995**, *30,* 181.

(24) Salama, T. M.; Ohnishi, R.; Ichikawa, M. *Chem. Commun*. **1997**, 105.

(25) Lee, J. Y.; Schwank, J. *J. Catal*. **1986**, *102*, 207.

(26) Sakurai, H.; Tsubota, S.; Haruta, M. *Appl. Catal. A* **1993**, *102*, 125.

CHAPTER 8
FLUORESCENCE STUDIES OF THE INTERACTION OF GOLD NANOPARTICLES WITH COLLAGEN AND LIVING CELLS

Abstract

The fluorescence properties of collagen and whole cells are studied with and without the presence of gold nanospheres and nanorods. The fluorescence of collagen solution is quenched by the addition of Au nanospheres and nanorods due to the re-absorption of the fluorescence by the Au nanoparticles. The protein fluorescence of HaCat healthy cells, HSC and HOC cancer cells are the same but the NADH fluorescence of the three types of cells are different, which makes the diagnostics of the cancer cells possible by using fluorescence spectroscopy. When the nanospheres and nanorods are incorporated into cells or by mixing with the cell solutions, the fluorescence of both protein and NADH bands are quenched by the nanoparticles. This is due to the re-absorption of the cellular fluorescence or the excitation light by the gold nanospheres and nanorods.

8.1 Introduction

Fluorescence spectroscopy is a widely used tool in biochemistry and molecular biology as a novel minimal-invasive method. It is a well established analytical technique that can be used to provide chemical sensing in dilute nonscattering samples. It is very helpful to provide information about biochemical, structural and functional changes of biomolecule related complexes (1-3). It is becoming a dominant method in medical diagnostics such as cancer detection. In fluorescence spectroscopy, absorption of light by a molecule excites it from a vibrational level in the electronic ground state to one of the many vibrational levels in the electronic excited state, usually a singlet state. Collisions with other molecules cause the excited molecule to lose vibration and electric energy and fall to the lowest vibrational level of this state. Fluorescence occurs when the molecule returns to the *electronic* ground state, from the excited singlet state, by emission of a photon. The molecule will also partition the excess energy to other possible modes (see Figure 8-1, (4)) of vibration and rotation if in the gas phase.

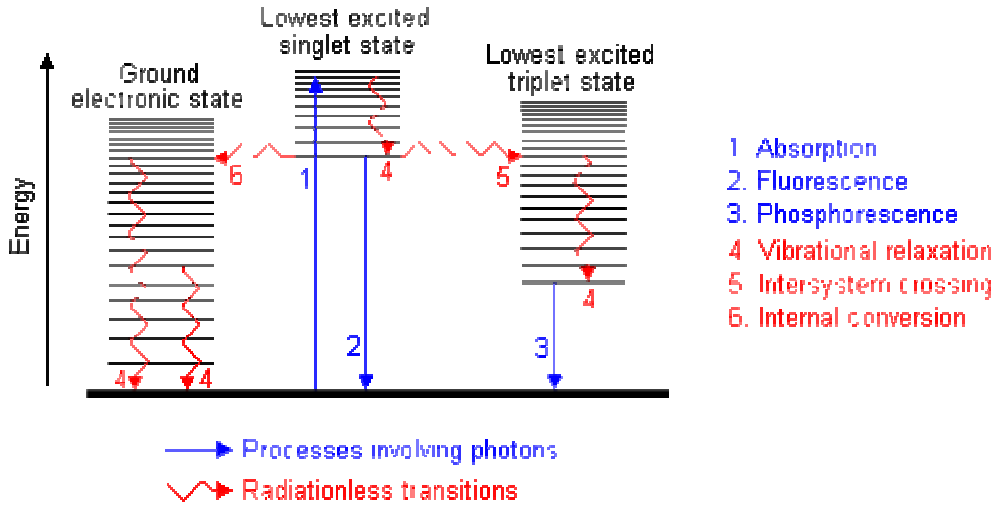

Figure 8-1: Fluorescence process (4).

Tissues contain a lot of different intrinsic fluorophores which are characterized by their absorption and emission spectra. Table 8-1 lists the Endogenous fluorophores in tissue (5). Figure 8-2 shows the absorption and emission spectra of some of the important autofluorophores in tissue (6). These endogenous fluorescences are very important for optical assessment of the tissue metabolic status. Among those autofluorophores, NADH, collagen, elastin and flavins plays dominant roles due to their strong fluorescence upon excitation between 335 nm and 360 nm. Protein fluorescence is contributed by amino acids including tryptophan, tyrosine and phenylalaine (7, 8).

Table 8-1: Endogenous fluorophores (5) at physiologica pH.

Chromophore	Absorption maxima	Molar extinction coefficient	Excitation maxima	Emission maxima	Fluorescence quantum yield
HP, collagen, elastin	325 nm (83)		325 nm (83)	400 nm (83)	
LP, collagen, elastin			325 nm (86)	400 nm (86)	
Collagen powder			280 nm, 265 nm, 330 nm, 450 nm (88)	310 nm, 385 nm, 390 nm, 530 nm (88)	
Elastin powder			350 nm, 410 nm, 450 nm (88)	420 nm, 500 nm, 520 nm (88)	
Tryptophan	280 nm (82)	5.6×10^{-3} (82)	280 nm (66)	350 nm (82)	0.2 (82)
Tyrosine	275 nm (82)	1.4×10^{-3} (82)		300 nm (82)	0.1 (82)
Phenylalanine	260 (nm) (82)	2×10^{-4} (82)		280 nm (82)	0.04 (82)
Pyridoxine (PN)	324 (94)		332 (94)	400 (94)	
Pyridoxal (PL)			330 (94)	380 (94)	
Pyridoxamine (PM)	326 (94)		335 (94)	400 (94)	
Pyridoxal 5′-phosphate (PLP)			330 (94)	400 (94)	
4-Pyridoxic acid (PA)	307 (94)		315 (94)	425 (94)	
NADH	260 nm 340 nm (82)	14.4×10^{-3} 6.2×10^{-3} (82)	290 nm (77) 340 nm (66)	440 nm (77), 450 nm (66)	
NAD+	260 (82)	18×10^{-3} (82)			
FAD			450 nm	515 nm	
Ceroid			340–395 nm (97, 102)	430–460 nm, 540–640 nm, (97, 100, 102)	
Lipofuscin			340–395 nm (97, 102)	430–460 nm, 540–540 nm, (97, 100, 102)	
Eosinophils—circulating			370 nm, 500 nm (107)	440 nm, 550 nm (107)	
Eosinophils—granules			380 nm, 450 nm (108, 109)	520 nm (108, 109)	

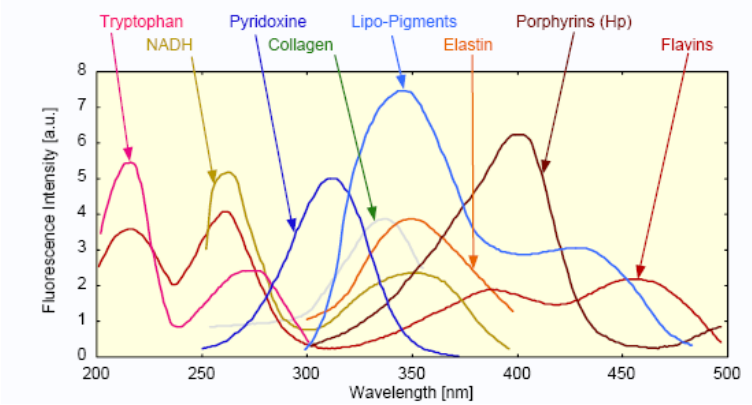

(a) Excitation spectra of some biomolecules

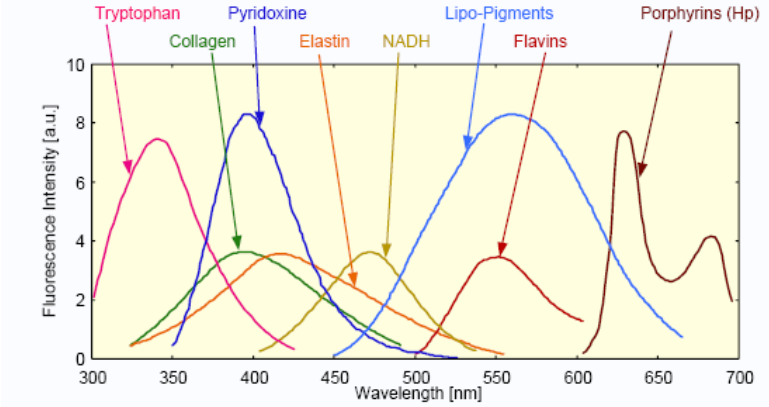

(b) Emission spectra of some biomolecules

Figure 8-2: Excitation (a) and emission (b) spectra of some biomolecules (6).

Collagen is a fibrous component of bone, teeth, cartilidge, tendons, blood vessels and matrix of skin. It contains 3 protein chains forming triple helix (see Figure 8-3, (9)). All the three helix contains GLY-X-Y-repeating sequence (X often Pro, Y often Hyp). Collagen fluorescence is associated with two types of cross-links. One is hydroxylysyl pyridinoline (HP) and another is lysyl pyridinoline (LP) (Figure 8-4, 10). Both are autofluorescent with emission maximum at 400 nm at excitation of 325 nm.

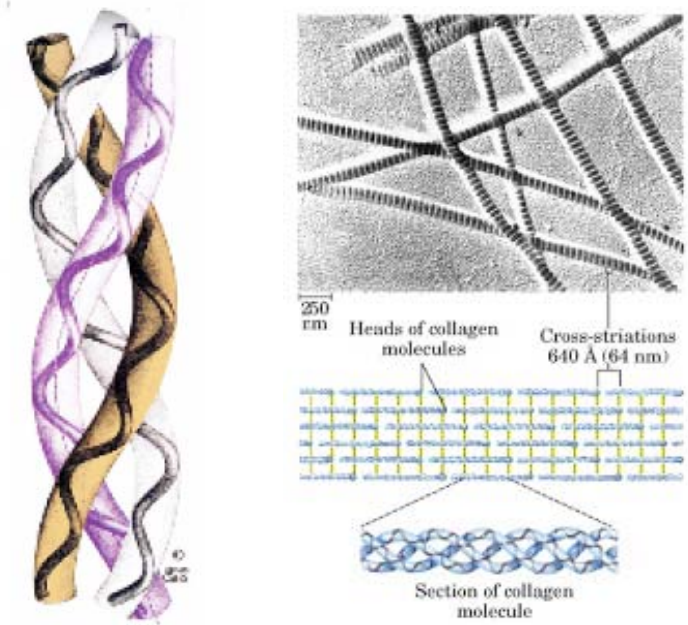

Figure 8-3: Structure of collagen (9).

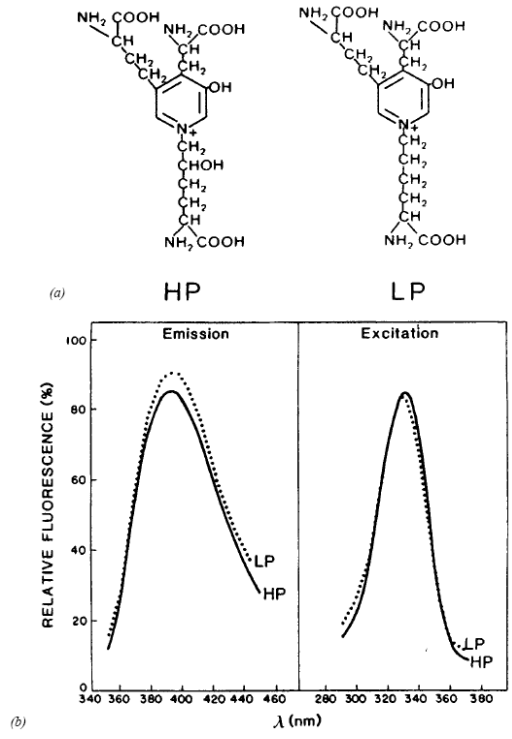

Figure 8-4: Fluorescence components in collagen (10).

With the wide application of nanotechnology in biology and biomedine, the use of metal surfaces to manipulate the spectral properties of fluorophores has gained increased interests due to their effects on the fluorophores such as increasing or decreasing the rates of radiative decay and the rates of resonance energy transfer (RET) (11,12). Au nanoparticles have been applied to biomedine for cancer cells diagnostics and photothermal therapy (13-16). But there is no report on the research on its interaction with the fluorescence of cellular compoents. In order to understand the potential application of Au nanoparticles in fluorescence studies as an optical diagnostic tool, we characterized the interaction of Au-NP's with the optical properties of the component fluorophores and whole cells of an oral squamous cell carcinoma cell culture model.

8.2. Experimental

Acid soluble type I collagen (White rabbit skin, Sigma-Aldrich) is dissolved in 0.5 M acetic acid. Collagen is mixed with Au nanospheres with 15 nm in diameter and AU nanorods with aspect ratio of 2.4 in various concentrations and put in a 1cm (for dilute specimen) and/or 5 mm quartz cuvette for absorption and fluorescence experiments. The concentration of collagen is held constant as the nanoparticle concentrations are increased over several trials.

The effect of 15 nm Au nanospheres on whole cell fluorescence is characterized using two malignant oral squamous cell lines (HOC 313 clone 8 and HSC 3) and one non-malignant epithelial cell line (HaCat). HSC 3 is a malignant, aggressive, metastatic line of oral carcinoma. HOC 313 clone 8 is a less aggressive malignant oral carcinoma with less metastatic potential. HaCat is a line of nonmalignant line of epithelial tissue origin.

Au NPs are applied in two ways. First they are added directly to cell suspensions and compared to control cells without nanoparticles from the same suspension that are equally diluted with Dulbeccos' buffered phosphate saline (DPBS). The cells are spun down at 1000 rpm and 0^{o}C C for 5 mins to get rid of DMEM medium which will interference the fluorescence signals of cells. The cell pellets are reconstituted with DPBS and then centrifuged two more times in DPBS to remove all DMEM. Second, they incubated into cells for 12, 24 and 48 hours and compared to control cells derived from the same sample and incubated concurrently.

The absorption spectrum of each sample of NADH and collagen are measured in 1cm (for dilute solutions) or 5mm quartz cuvette on a Shimadzu UV-3101PC spectrometer. Fluorescent spectra of collagen are obtained using a PTI fluorimeter with a Xenon lamp and PMT detector. Spectra of cell suspensions are measured in a 5mm quartz cuvettte on a Molecular Devices Spectramax M5 fluorimeter. Data of cellular fluorescence is recorded into Soft Max Pro 4.8 software and transferred to Microsoft Excel 2002 database on Windows XP for data processing.

Preliminary spectra from whole cell suspensions are evaluated at several excitation wavelengths over several trials to identify optically active areas and peak maximum values is graphed out by cell type and length of incubation and analyzed visually for consistency. The optical density and cell count are compared to ensure data integrity. Clumping of the cells during specimen preparation could decrease the fluorescence by removing cells from the light path. Data is evaluated for differences among the cell types and by method of nanparticle application. The average difference of fluorescence

between untreated and treated cells is determined and graphed using Micorsoft Excel as a proportion of the total fluorescence of the control cells without the nanoparticles. The mean value of fluorescence of the two groups (with and without nanoparticles) is calculated and the significance determined using the *paired T test* for the matched samples.

8.3 Results and discussion

8.3.1 Interaction of gold nanoparticles with the collagen suspension

Figure 8-5 shows the results of the effect of Au nanospheres on the absorption and fluorescence of collagen solution. Figure 8-5(a) shows that the addition of Au nanospheres did not affect the absorption spectra of collagen. Figure 8-5 (b) shows that the absorption spectra did not change with the time when Au nanospheres are mixed with the collagen solution. Figure 8-5 (c) shows that Au nanoparticles quench the fluorescence of collagen. As the concentrations of Au nanoparticles increase, the quenching of the fluorescence increases. The time-resolved fluorescence spectra in Figure 8-5 (d) show that the presence of Au nanospheres does not affect the fluorescence decay of collagen solution.

This is unlike the effect of Au nanoparticles on NADH fluorophore. As discussed in Chapter VII, Au nanoparticles catalyzed the oxidation of NADH to NAD+. But when Au nanospheres are mixed with collagen solution, the absorption spectra of collagen do not change. This indicates that collagen is not converted to other species. The fluorescence decrease after addition of Au nanoparticles indicates that Au nanoparticles quenched

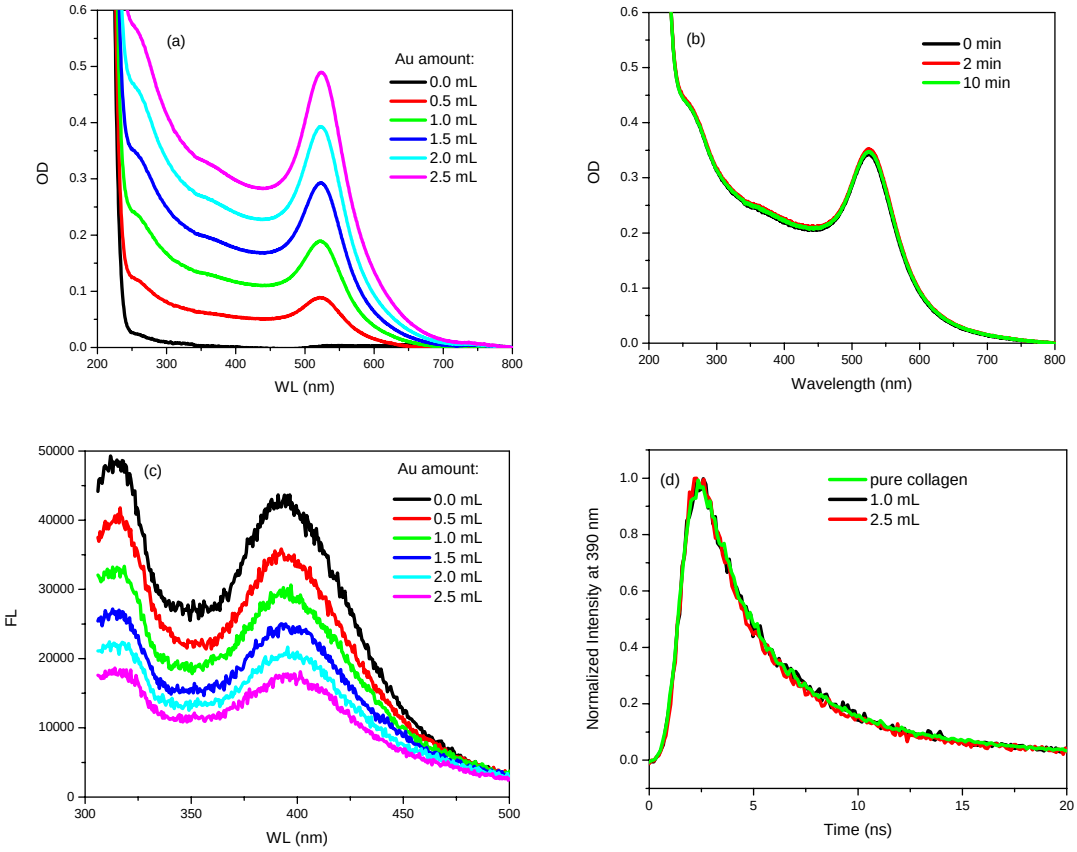

Figure 8-5: Interaction of collagen suspension with Au nanospheres. (a) Absorption spectra of collagen in various amount of Au nanospheres (OD=1.0); (b) Absorption spectra of collagen with Au nanospheres at different time; (c) Fluorescence spectra of collagen in various amount of Au nanospheres (OD=1.0). λ_{exci} = 280 nm. (d) The fluorescence decay of collagen at 390 nm in different amount of Au nanospheres (λ_{exci} = 280 nm). The lifetime of collagen fluorescence obtained by a monoexponential fitting is about 2.4 ns which is the same for all samples.

the fluorescence of collagen. This could be due to the filter effect of the gold nanoparticles, the re-absorption of collagen fluorescence by Au nanoparticles or due to energy transfer from collagen molecule to the Au nanoparticles. The same fluorescence decay of collagen is not affected by the addition of Au nanoparticles suggesting that there is no energy transfer process taking place between collagen and the nanoparticles. Thus

the fluorescence quenching is caused by the simple absorption of the fluorescence of collagen or the exciting light by Au nanoparticles.

The gold nanorods have similar effects on the collagen absorption and fluorescence spectra, shown in Figure 8-6. Au nanorods quenched the fluorescence of the collagen

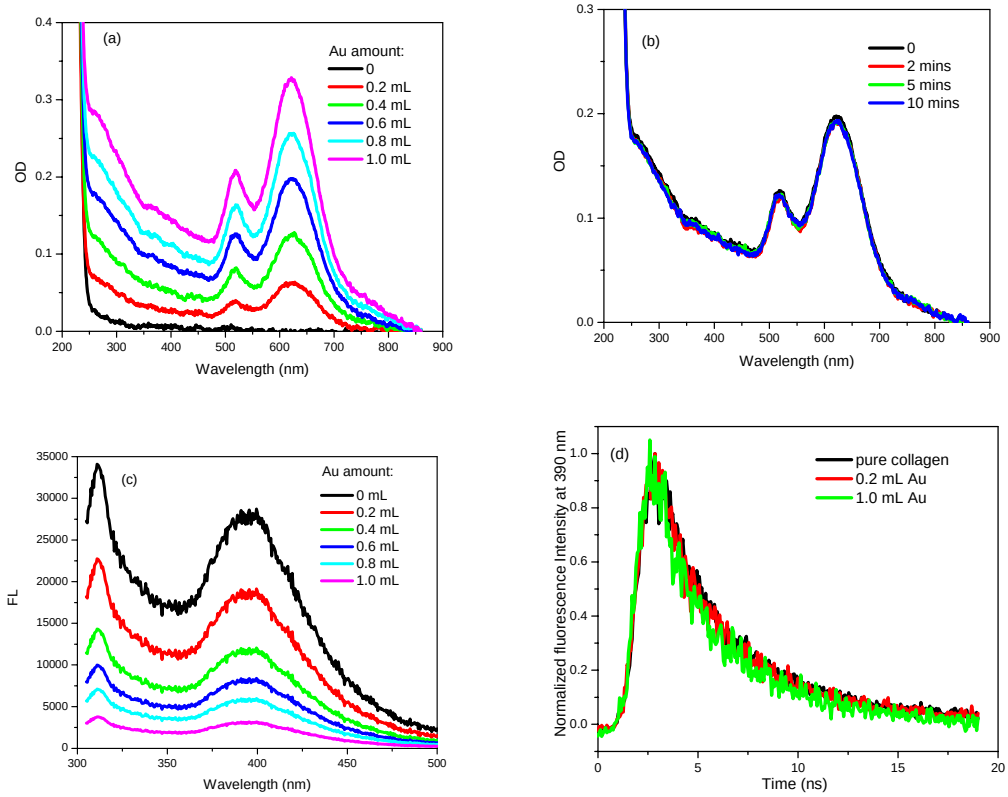

Figure 8-6: Interaction of collagen suspension with Au nanorods. (a) Absorption spectra of collagen in various amount of Au nanorods (OD=1.6); (b) The absorption spectra of collagen with Au nanorods at different time; (c) Fluorescence spectra of collagen in various amount of Au nanorods (OD=1.6). λ_{exci} = 280 nm; (d) The fluorescence decay of collagen at 390 nm in different amount of Au nanorods (λ_{exci} = 280 nm. The lifetime of collagen fluorescence obtained by a monoexponential fitting is about 2.4 ns which is the same for all samples.

solution, but they did not change the absorption spectra or the fluorescence decay of the collagen solution. The fluorescence quenching effects is due to the re-absorption of the fluorescence or the exciting light by Au nanorods.

8.3.2 Interaction of gold nanoparticles with the cell suspension

The absorption and fluorescence spectra of cells without nanoparticles are shown in Figure 8-7. For comparison, all data are normalized. All three types of cells have absorption maximum at 280 nm which is from the protein absorption (Figure 8-7(a)).

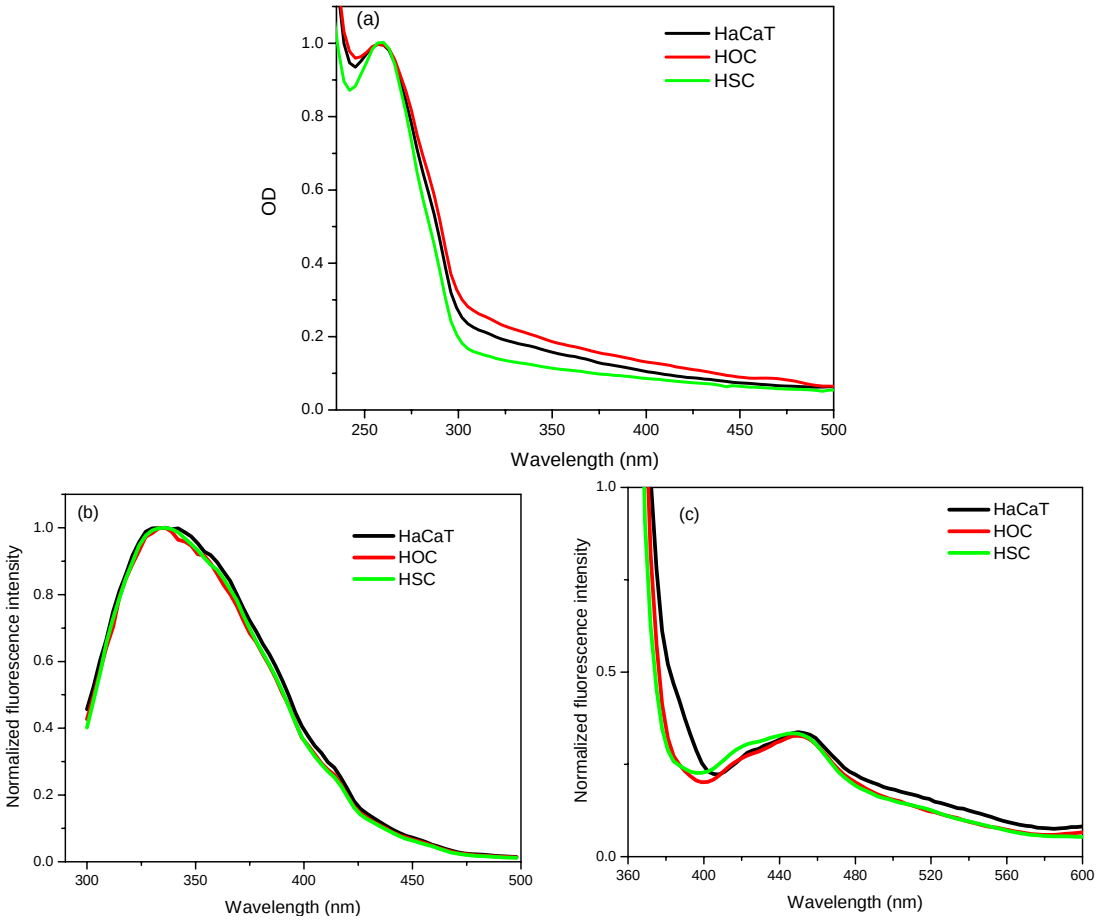

Figure 8-7: Absorption (a) and fluorescence spectra (b, c) of different types of cells without nanoparticles. (b): λ_{exci} = 280 nm, (c): λ_{exci} = 340 nm.

The protein fluorescence profile is similar for all three cells lines after normalization. When excited at the protein absorption maximum of 280 nm, the cells show a very strong and similar fluorescence band around 336 nm (Figure 8-7 (b)). When excited at the NADH absorption maximum around 340 nm, they show a weaker band around 450 nm compared to their protein fluorescence bands (Figure 8-7 (c)). From Figure 8-7 (c) we can see that the normalized profile for each type of cells is different. The normal HaCat cells have higher fluorescence at wavelength shorter than 400 nm and higher wavelength over 480 nm regions. HSC cancer cells have higher fluorescence intensity from 420nm to 450 nm. Collagen fluorescence (380nm region) and flavin (520nm region) in HaCaT noncancerous cells are stronger than that in HOC and HSC cancerous cells. Elastin fluorescence (420nm region) is stronger in HSC cancerous cells than that in HaCaT noncancerous cells and HOC cancerous cells. Upon mixing NPs with cell suspension, NPs quenched both protein and NADH fluorescence of all three cell lines. After incubation inside the cells, NPs quenched the protein fluorescence of all three kinds of cells. Interestingly, NPs also quenched the NADH fluorescence of HaCaT noncancerous cells, but enhanced the NADH fluorescence of HOC and HSC cancerous cells.

The effects of Au nanoparticles on the absorption and fluorescence of all three type of cells are shown in Figure 8-8 (Au nanoparticles are mixed with cell suspension). From Figure 8-8 it can be seen that Au nanoparticles quenched the fluorescence of cells at their protein and NADH bands when they are mixed with the cell suspensions.

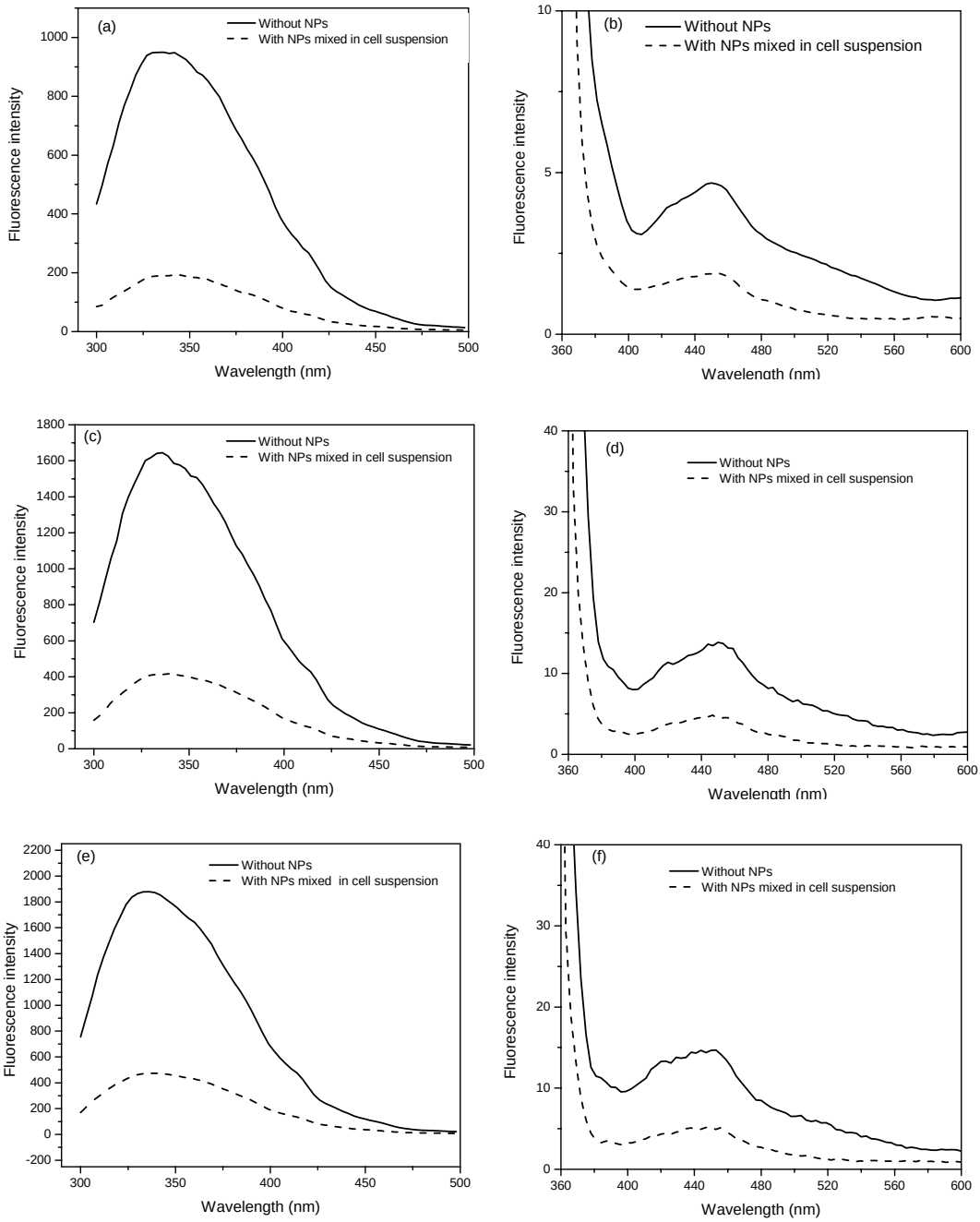

Figure 8-8: The comparison of fluorescence spectra of whole cells with and without nanospheres mixed in solution. λ_{exci} = 300 nm for (a), (c) and (e); λ_{exci} = 330 nm for (b), (d) and (f). (a) and (b): HaCat cells; (c) and (d): HSC cells; (e) and (f): HOC cells.

The effects of Au nanoparticles on the absorption and fluorescence of HSC cells incubated with nanoparticles are shown in Figure 8-9 (data are obtained by Ivan H. EL-Sayed at University of San Francisco). From Figure 9 it can be seen that Au nanoparticles quench the cellular fluorescence at their protein and NADH bands. Other types of cells have similar results and thus not shown here. Further review of the data revealed there is no obvious difference if the gold nanoparticles incubated for longer times (12 to 48 hours).

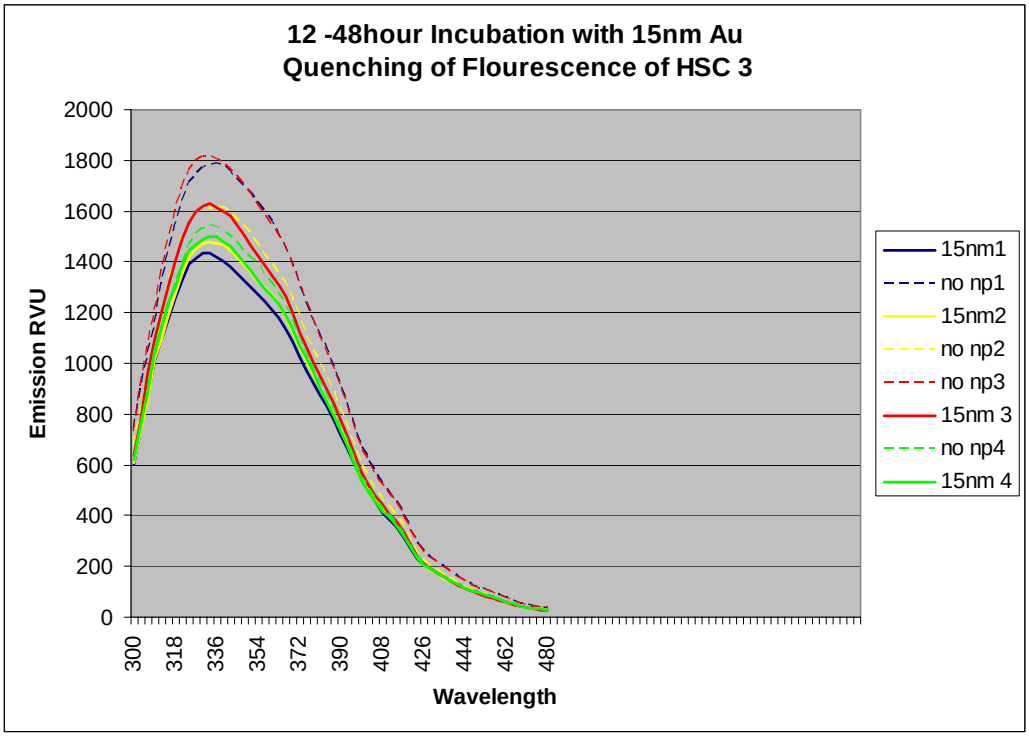

Figure 8-9: Representative fluorescence spectra of whole cells incubated with nanospheres using HSC 3 in solution. λ_{exci} = 280 nm. Au nanospheres decrease the fluorescence of cells. The pilot data is similar for all 3 cells both for those incubated with and without nanoparticles, and for those mixed in suspension with nanoparticles (Obtained by Ivan H. EL-Sayed, at University of San Francisco).

Statistically many samples are run for checking the data of reproduction. A similar number of cells have a wide range of fluorescence. This may be attributable to varying metabolic conditions of the cells. However, each test sample and control is paired as they are seeded with the same starting cells and grown under equal conditions. Overall, Dr Ivan H. EL-Sayed's student, Fema checked 32 samples. He grouped the cells together and the mean fluorescence of the two groups is compared (Figure 8-10). There are not enough specimens to perform subgroup analysis. Thirty eight specimens are obtained overall. Two specimens are excluded due to technical difficulties with sample preparation and clumping of cells determined visually along with abnormal OD and cell counts. A box and whisker plot is created determining two outliers in either direction of the mean, and these 4 samples are removed from analysis. Twenty six of 32 samples demonstrated a decrease in fluorescence. Comparison of the mean fluorescence value at the peak maximum of 333 nm revealed a mean relative value unit of 1244 (no nanoparticles) and 1059 (nanoparticles). The difference between means revealed an average quenching of 15% ($p<.00005$). Thus from this percent decrease fluorescence analysis, statistically Au nanopartices quench the fluorescence of living cells. This is the first report we know of to characterize the effect of Au NPs on the cellular autofluorescence. While Au NPs effects on fluorescence in many dry processes is a field of active investigation, the addition of a physiologic fluidic environment introduces many unknown variables to the system that have not been well studied. Many variables exist that may effect the optical properties of Au NP such as the acidity, the ions in solution, enzymes, and proteins. Therefore, any effects of Au nanoparticles in these conditions must be characterized experimentally. We

demonstrate that Au NPs decrease the fluorescence of two of the main fluorophores of cancer (NADH and Collagen) and also of whole cells (excitation at 280 nm).

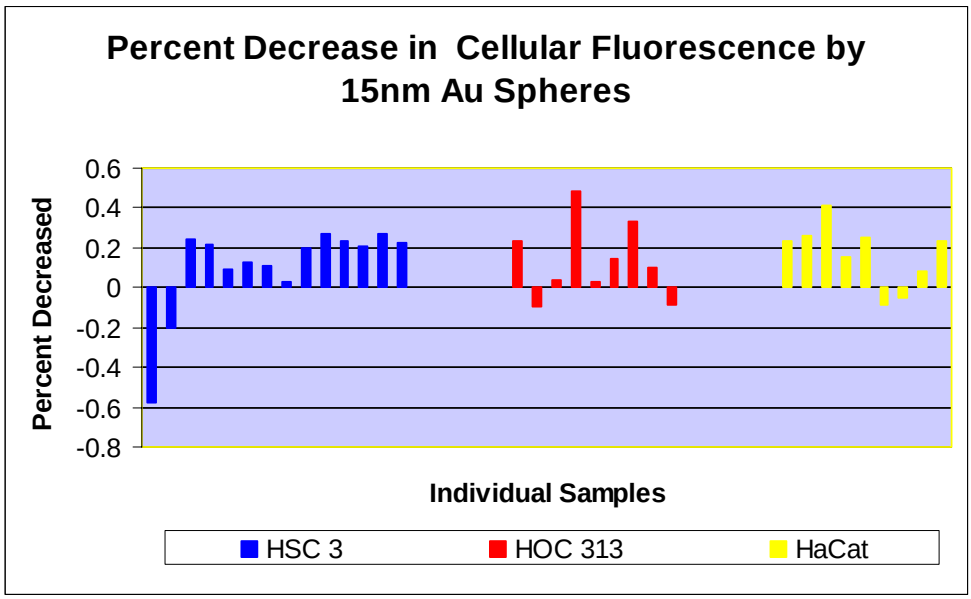

Figure 8-10: Percent of fluorescence decreased for all samples (no incubation and incubation). No difference is observed for samples incubated with particles and mixed with particles in solution just prior to measurements with sample size. Some samples demonstrate increased fluorescence. With this small sample size, no difference can be determined between cell types or incubation times with nanoparticles. (Obtained by Ivan H. EL-Sayed, at University of San Francisco).

Much research has been conducted on the florescence of oral cancer. While LIFE (17) is FDA approved for pulmonary and GI screening, the oral cavity and upper aerodigestive tract stand to benefit tremendously by improved screening methods. While the UADT is generally accessible for visual inspection, the eye lacks sensitivity and specificity. Further, at risk patients, including those with a previously diagnosed cancer, often have abnormal areas of dysplastic or scarred tissue from prior surgery and radiation, which is followed clinically. An accurate noninvasive technique to diagnose cancer and dysplasia in these patients would guide the treating physician tremendously. In conjunction with our prior work, we have now demonstrated that Au NPs effect three optical parameters

useful for spectroscopic cancer diagnostics; absorption, scattering, and fluorescence. These may be useful as optical probes for application with confocal endoscopy in the scattering or fluorescent mode, TMS, or LIFE.

Current fluorescent based techniques are not specific, but are capable of being coupled with camera imaging technology for screening wide areas. Thus fluorescent technology complements the fiberprobe technologies which offer specific diagnosis. Despite consistent changes in tissue fluorescence, many variables exist in the oral mucosa that affects interpretation of the spectra. The tissue thickness and keratinization varies with each site in the oral cavity, and factors such as increased vascularity or inflammation may create extra signals from porphyrins in hemoglobin or bacteria. Thus, many investigators have stressed that baseline florescence must be determined on a patient to patient basis. This complicated process could be bypassed by developing a agent that could be applied to mucosa and stick to malignant cells. Measurements of fluorescence before and after can be imaged and significant decrease in fluorescence identified by comparing images. Au nanoparticles are easily conjugated to a variety of chemicals, proteins and antibodies to allow for molecular targeting which should increase the fluorescence quenching significantly.

This pilot study suggests a potential role for Au nanoparticles as an optical probe to be used in conjunction with optical biopsy techniques employing fluorescence spectroscopy. In combination with its other optical properties, Au nanopoarticles represent a unique multifunctional particle to increase sensitivity of detection, specificity of diagnosis, and tumor destruction with photothermal therapy via heat conversion of absorbed light.

Further, this work raises the possibility of new avenues of optical sensing in vivo using Au NPs with fluorescence based technologies.

8.4 References

(1) Fang, Q.; Papaioannou, T.; Jo, J. A.; Vaitha, R.; Shastry, K. Rev. Sci. Instrum. 2004, 75 (1), 152.

(2) Lakowicz, J. R. *Principles of Fluorescence Spectroscopy*, 2nd ed. Kluwer, Academic/Plenum, New York, **1999**.

(3) Richards-Kortum R.; Sevick-Muraca, E. M. *Annu. Rev. Phys. Chem*. **1996**, *47*, 555.

(4) http://www.shu.ac.uk/schools/sci/chem/tutorials/molspec/lumin1.htm.

(5) Richards-Kortum, R.; Sevick-Muraca, E. *Annu. Rev. Phys. Chem.* **1996**, *47*, 555.

(6) www.gfmer.ch/Presentations_En/ Pdf/Instrumentational_**setup**.pdf.

(7) Lakowicz, J. R. *Principles of Fluorescence Spectroscopy.* New York: Plenum, **1985**.

(8) Campbell, I. D; Dwek, R.A. *Biological Spectroscopy.* Menlo Park, CA: Benjamin Cummings. **1984**.

(9) www.udel.edu/chem/robinson/ courses_doc/527_S05/lecture_4.ppt.

(10) Eyre, D.; Paz, M. *Annu. Rev.Biochem.* **1984**, *53*, 717.

(11) Lakowicz, J. R. *Analytical Biochemistry* **2001,** *298,* 1.

(12) Lakowicz, J. R.; Shen, Y.; D'Auria, S.; Malicka, J.; Fang, J.; Gryczynski, Z.; Gryczynski, I. *Analytical Biochemistry* **2002**, 301**,** 261.

(13) Sokolov, K.; Follen, M.; Aaron, J.; Pavlova, I.; Malpica, A.; Lotan, R.; Richartz-Kortum, R. *Cancer Res.* **2003**, *63*, 1999.

(14) El-Sayed, H. I.; Huang, X.; El-Sayed, M. A. *Nano letter* **2005**, *5 (5),* 829.

(15) El-Sayed, H. I.; Huang, X.; El-Sayed, M. A. Cancer letter, in press.

(16) Huang, X.; El-Sayed, H. I.; Qian, W.; EL-Sayed, M. A. JACS 2006, 128, 2115.

(17) Muller, M. G; Valdez, T. A.; Georgakoudi, I.; Backman, V.; Fuentes, C.; Kabani, S., Laver, N.; Wang, Z.; Boone, C. W.; Dasari, R. R.; Shapshay, S. M.; Feld, M. S. Cancer **2003,** *97*, 1681.

CHAPTER 9
SURFACE ENHANCED RAMAN SPECTROSCOPY OF CELLS USING GOLD NANOPARTICLES

Abstract

Surface enhanced Raman spectroscopy (SERS) are carried out on several different systems using a micro-Raman spectrometer with a NIR excitation laser at 785 nm. Colloidal Au nanoparticles (Au NPs) are incubated inside cells and Raman spectra from both single cells and cell pellet are collected. Colloidal Au NPs are also mixed with the cell suspension and the cell pellets. The HaCat healthy cells, HSC and HOC cancer cells are measured and compared. SERS are also measured on mercaptoacetic acids and anti-EGFR antibodies which are adsorbed onto monolayer of prismatic gold nanoparticles assembled on quartz substrate. The SERS of R6G and BSA molecules are recorded on a film of gold nanorods.

9.1 Introduction

Raman spectroscopy has been used for biological application since the first interpretable laser-excited Raman spectrum of a native protein is obtained from lysozyme by Lord and Yu at the MIT Spectroscopy Laboratory in 1970 (1). Raman spectroscopy can provide the most detailed information about the chemical composition of the tissue under study among the molecular level optical spectroscopy such as absorption, fluorescence, reflectance and Raman scattering (2). But most biological molecules have small Raman scattering cross-section which results in very weak signals, possibility of sample damage and the strong fluorescence background from cells and tissues (3). The problem of sample damage and strong florescence background can be addressed by shifting the excitation laser wavelength from UV-Visible to NIR region. The enhancement of Raman signals mostly relies on the surface-enhancement Raman spectroscopy.

In 1974, surface-enhanced Raman spectroscopy (SERS) are observed by Fleischmann on pyridines adsorbed on an Ag electrode roughed by oxidation-reduction cycles (4). But they attribute the signal enhancement to the big surface area of the electrode. In 1977, Van Duyne (5) and Creighton (6) firstly recognized the large intensity is due to the electromagnetic field effect. Now it is believed that SERS is due to two major enhancements: the electromagnetic field enhancements and the chemical enhancement. When molecules are adsorbed to metallic nanostructures, resonances of the applied optical fields with the surface plasmon oscillation of the nanostructures, the local optical fields of these structures are greatly enhanced and results in the enhanced Raman signals

(7-11). This electromagnetic field enhancement plays the most important role in the SERS. In addition, the electronic interaction of the adsorbed molecules and the metal surface can results in an increase in the Raman cross-section of the molecules (12-15). In many experiments on metal surfaces this “chemical or electronic” effect provides a very small contribution compared to the electromagnetic enhancement.

In early 1980’s, SERS are observed on small and large biomolecules such as DNA and protein. Three groups, Koglin and Sequaris (16), Cotton et al. (17-19) and Nabiew (20) and coworkers have lead to a great development of SERS on the biomolecules during this period. Later many researchers have continued to demonstrate the great potential of SERS applications in the fields of biochemistry, biophysics, and molecular biology.

In early 1990’s, SERS are performed using metallic nanoparticles on living cells (21-24). In these experiments, colloidal silver nanoparticles are incorportated inside cells and used to probe the interaction of drugs and DNA complex. But only drug signals are observed. In 2002, Field et al. directly incorporated 60 nm colloidal gold nanoparticles into living cells and observed the celluar constitutes (25). Figure 9-1 shows the SERS signals of the cell DNA and proteins and the signal mapping. On the cell monolayer, different spectra are obtained on different spots. These distinct spectra reflect the inhomogenorosity of the cell composition. But also the nanoparticles aggregated inside cells, which might also results in the signal difference due to different degree of aggregation. Recently, Kneipp et al used indocyanine green dye conjugated gold nanoparticles as probe to determine the cellular components (26). When indocyanine green dye conjugated gold nanoparticles are incorporated into cells,

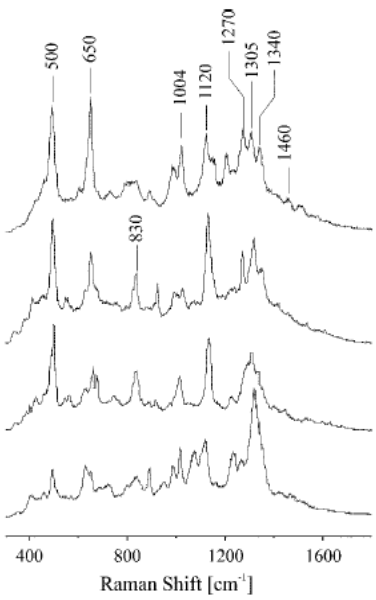

Typical unprocessed surface-enhanced Raman spectra measured with 1-mm spot size at different places on a cell monolayer incubated with colloidal gold (25).

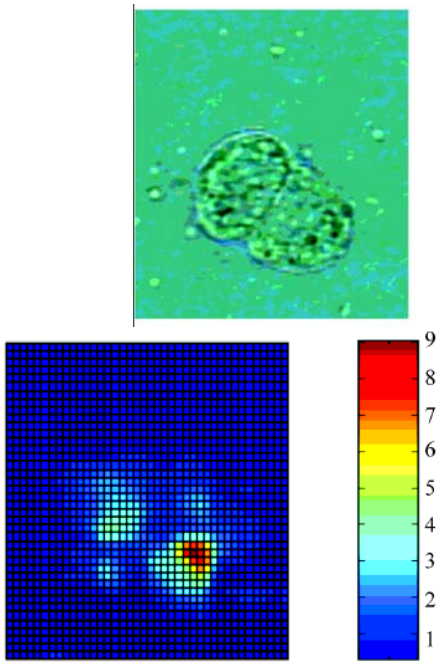

Phase contrast image of two living cells (top) and the image of the total SERS signal (bottom) (25).

Figure 9-1: SERS from single living cells using gold nanoparticles incorporated inside cells (left) and the images of the total SERS signals (right) (25).

the probe not only gave Raman signals of indocyanine green molecules, but also signals from cell constitutes (Figure 9-2). In this way, nanoparticle aggregation is avoided and the data is more consistent. But they did not compare the difference between cancer and healthy cells.

In the present work, 60 nm colloidal gold nanoparticles are also incorporated inside both healthy and cancer cells and Raman signals from single cells are obtained and compared between the noncancerous and cancerous cells. Due to the signal difference from different laser focus spots, the cells pellet after incorporation of the gold nanoparticles are also used to obtain SERS of whole cells. In addition, gold nanoarray

and gold nanorods film are also used to obtain SERS of small molecules, large biomolecules and living cells.

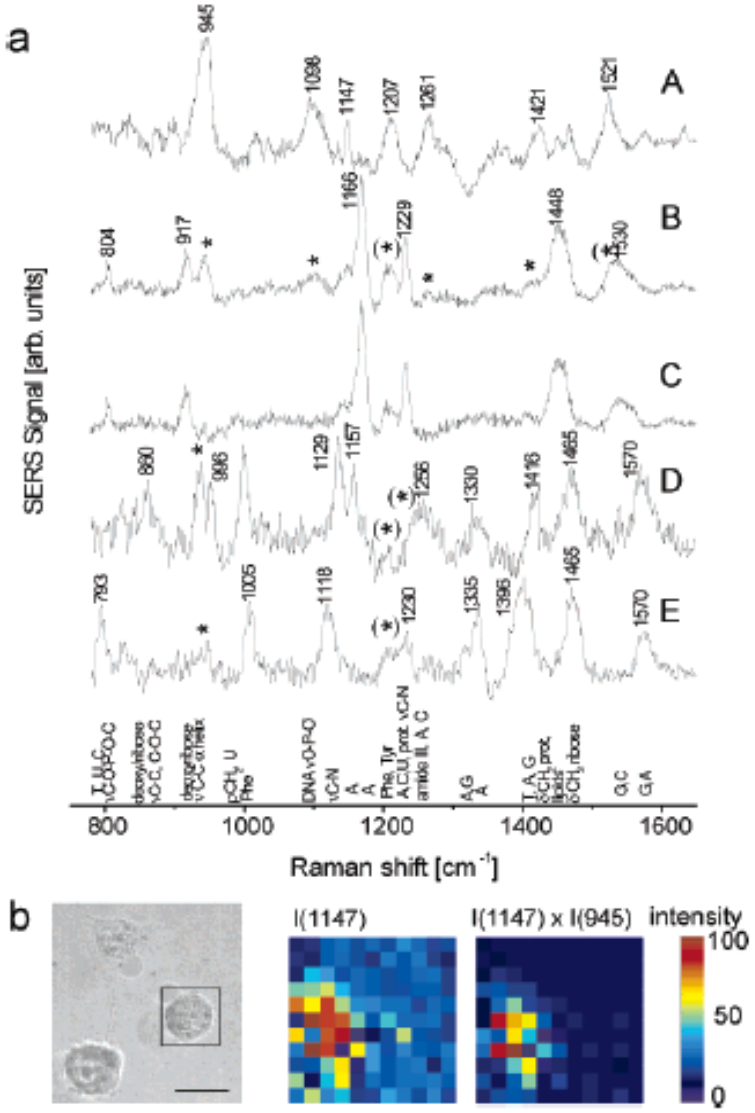

Figure 9-2: (a) Examples of SERS spectra measured in single living cells incubated with the ICG-gold nanoprobe. Trace A represents the ICG signature. Assignments of major bands in spectra B-E are given below spectrum E. ICG bands are marked with an asterisk, while an asterisk in parentheses indicates contribution of both ICG and cell. Trace C shows the difference between spectra B and A and displays only Raman lines of the cell. (b) Spectral map of the ICG-gold nanoprobe in a cell based on 1147-cm-1 ICG line and on the product of two ICG lines at 1147 and 945 cm^{-1} (26). Scale bar 20 μm.

9.2 Experimental

Au nanoparticles of 60 nm in diameter are synthesized by the citrate reduction method as described in Chapter 2, Page 55-56. Then several drops of these nanoparticles are added in the medium in a well of a 12-well plate in which cells are grown on a cover slip. The nanoparticles are incubated with the cells for 2 days. Then the cells on coverslips are take out of the incubator and fixed with 1.6% paraformaldehyde and sealed with another coverslips and used for Raman measurement.

To make the cell pellet for Raman experiment, the cells are grown in 60x15mm tissue culture dishes. The 60 nm Au nanoparticles are added into the medium and let incubate with the cells for 2 days. The cells are then cleaved with trypsin and centrifuged at 1000 rpm for 5 mins to get cell pellet. The cell pellet is resispersed in DPBS buffer and centrifuged again to rinse out the medium which might interfere the Raman signals. Then the cell pellet on the bottom of the centrifuge tubes is placed on the ice and carried to Raman lab for Raman experiment. The cell pellet are taken out by a glass pipette and placed onto a foil film and used for Raman measurement.

60 nm Au NPs are also mixed with cell suspension and shaken for 30 mins and then centrifuged down to get cell pellet. In this way, the NPs are adsorbed onto the surface of the cells and SERS signals from the cell surface protein can be obtained.

Au nanoarray is also used for SERS of adsorbed molecules. The nanoarray is prepared by Wenyu Huang, a member of our group. Different molecules are adsorbed onto the nanoarray for SERS measurement. Nanoarray is also autoclaved and used a substrate for cell growth. The Raman experiment of the cells grown on Au array is carried out in PBS buffer.

Au nanorods film is also prepared on which molecules are adsorbed for the SERS experiment. The procedure to make the rod film is similar to that described by Yamada et al. (27) and shown in Figure 9-3. Briefly, 10 mL hexane is added to 10 mL rod solution (λ_{max} = 2.0). Then 2.5 mL acetonitrile is added dropwise on top of the hexane. During the addition of the acetonitrile, the nanorods are adsorption onto the interface of the hexane and nanorod solution. After the acetonitrile is completely added, a thick layer of nanorod film is formed at the interface. The film is then lifted up by inserting a quartz plate and the film is transferred onto the quartz plate.

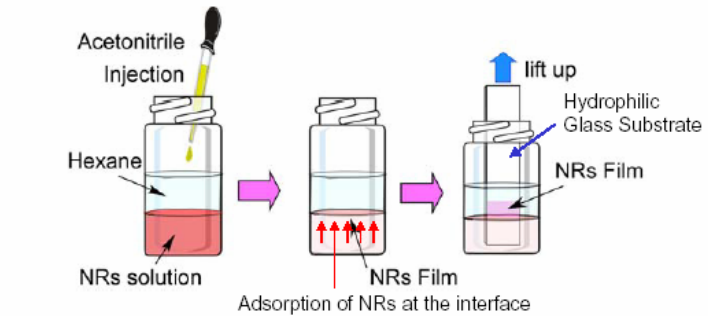

Figure 9-3: The preparation of nanorods film (27).

Rrodmine 6G, Bovine Serum Album and anti-EGFR antibodies are drop added on the film for Raman measurement. After 2 mins of R6G addition on the film, Raman spectra are collected. After overnight of BSA and anti-EGFR antibodies are added, Raman spectra are collected.

9.3 Results and Discussion

Since Au nanoparticles are capped with and mostly close to citrate molecules, it is important to know the citrate Raman SERS signals. Figure 9-4 shows the Raman spectra of a drop of 60 nm Au NPs concentrated solution on a foil film and a dried 60 nm Au

NPS film. From this Figure, we can see that very strong SERS signals of citrate on the surface of Au NPs are observed. And also the signals from monodispersed Au NPs and aggregated dried film are different. These Raman bands from citrate should be considered when molecules or cells are adsorbed onto the surface of Au NPs. The assignment of the bands can be obtained from reference 28. The major bands at 890, 1126, 1266, 1446 and 1492 cm^{-1} are possibly assigned for υ (C4-O), υ (C-C), υ_a (OCO), υ_s (COO) and υ_{as} (COO), respectively.

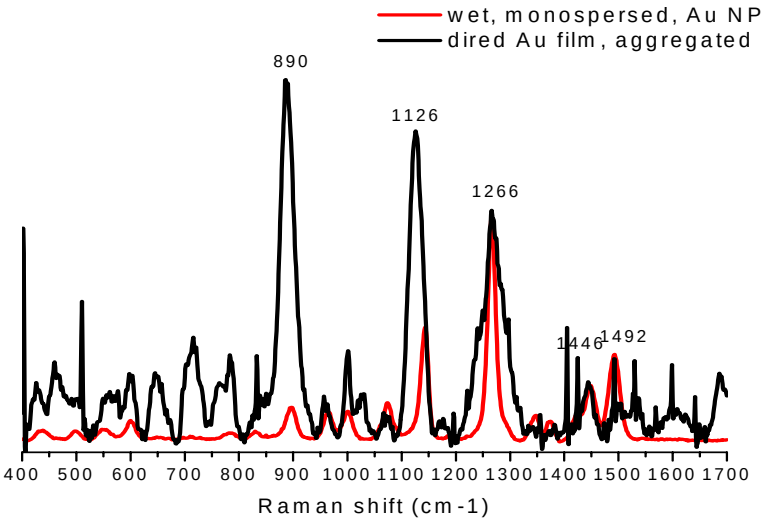

Figure 9-4: Citrate SERS signals adsorbed on Au NPs.

9.3.1 Colloidal gold incubated inside cells – SERS from single cells

Colloidal Au are incubated inside cells, fixed and used for Raman measurement. But the problem is that the spectra are not quite reproducible. Different age of Au NPs used and different incubation time gave different Raman signals. Figure 9-5 shows the SERS from part of single cells (8 μm in diameter) obtained by different time. The NPs are incubated inside cells for 2 days for all samples.

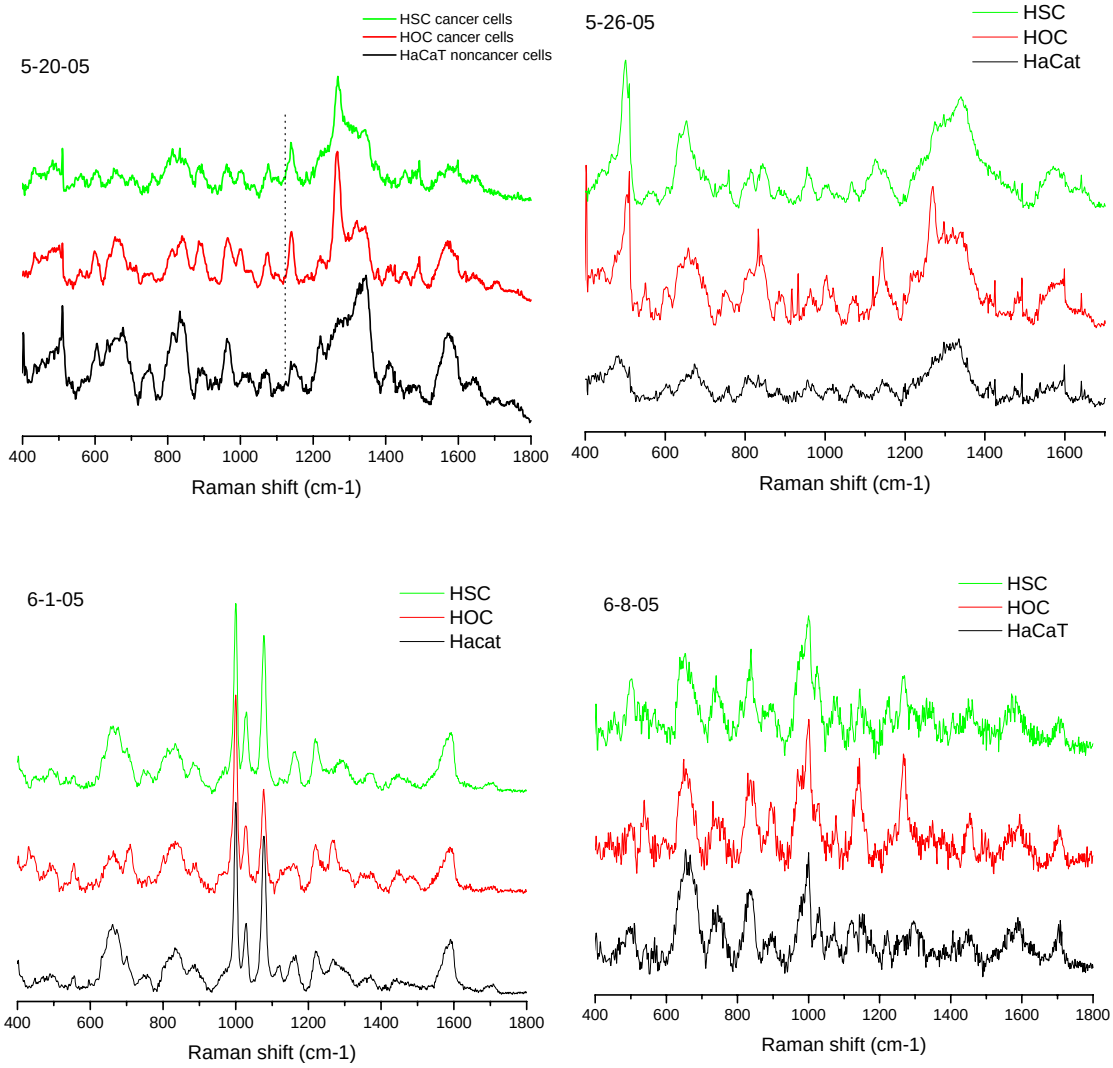

Figure 9-5: SERS signals from single cells. 60 nm Au NPs are incubated inside cells.

From Figure 9-5 we can see that the Raman signals for each type of cells are different when the experiments are done at different time. This is mostly due to the different patches of Au NPs used. The Au NPs used on May 26 are the same patches of NPs used on May 20, but aged 6 more days. The Au NPs used on June 1 is different patches of Au NPS used on June 8. As we have seen from Figure 9-4 that for nanoparticles themselves, aggregation give different spectrum. So it is obviously that the degree of Au NPs aggregation affects the signals observed from cells. Each time, Au nanoparticles are

incubated inside cells, the NPs are aggregated. Different aggregation will get different signals. Even in the solution of Au NPs before addition to the medium, there might also aggregation of NPs. And also compared to Figure 9-4, most signals from cells are actually from citrate molecules. So it is hard to get a consistent conclusion what are the difference between the cancer and healthy cells.

If the cells are not fixed, the living cells are immersed into PBS buffer and measure signals from single cells, the signals from each spot from one cell are different. And also the signals on one spot are changing even after several seconds under 50x. We originally thought that this is due to the laser damaging the cells. However, if the cells are fixed, the signals are not changed within mins. This indicates that the change in the signal with time is due to the motion of the living cells in the buffer. Under each second, the cell molecules are moving and the Au nanoparticles inside cells are also moving. So it is hard to reproducible signals from each part of the cells.

9.3.2 Colloidal gold incubated inside cells – SERS from cell pellet

Since it is hard to get reproducible results from signals on single cells, the cell pellet after incubated with Au NPs solution is used. In this way, each cell pellet gives one spectrum from a lot of cells under the focused spot (10x, 15 μm focus area). Since the aggregation of Au NPS affects the signals, the Raman spectra from samples of different incubation time are also measured for comparison. Figure 9-6 shows the Raman signals from cell pellets pre-incubated with 60 nm Au NPs. It can be seen that the Raman profile are quite reproducible for each type of cells. Also the changes of the signals due to

aggregation of the Au NPs (long time incubation) are consistent for the three types of cells. The assignments of the peaks are listed in Table 9-1 according to references (29-32).

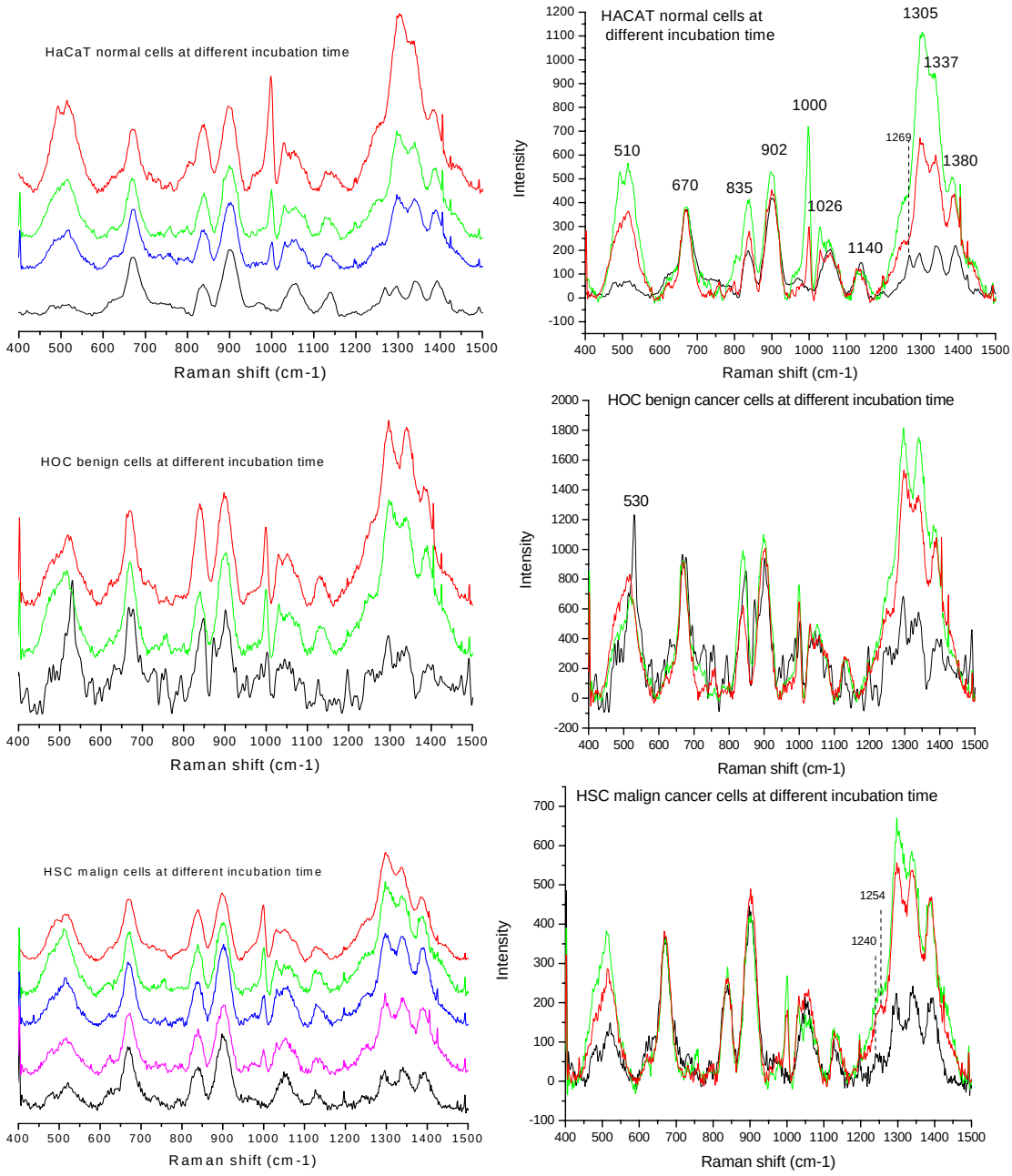

Figure 9-6: Raman spectra of cell pellet incubated with NPs at different time. From up to bottom the incubation time increases. Right spectra are the time peaked for 2 days, 4 days and 6 days incubation and normalized at 670 cm-1 for comparison.

Table 9-1: Peak assignment of the bands in Figure 9-6 according to references (29-32).

510: Au-S	1026: Phe
670: cys and or T, G	1140: trp
755: T	1303: phe, try, trp and/or A, P: CH def
836: DNA: RP, try	1337: trp and/or A, P: Ch def
897: DNA Bkb: C-C str	1384: T, A, G?
1000: Phe ring vib	

From Figure 9-6 and Table 9-1 we can see that some differences between the three types of cells are observed. The phe contents in HaCat normal cells are higher than that in HSC and HOC cancer cells. At 6 days incubation, there is a peak at 1267 cm-1 (try and/or citrate molecules) in HaCat normal cells while this peak is absent in the other two cancer cells. At 6 days incubation, the Au-S band in HOC cancer cells is extremely strong compared to the other two types of cells. Also the intensity ratios of the two peaks around 500 nm are different for each type of cells. These differences might be useful in the diagnosis of the different types of cells.

9.3.3 Colloidal gold mixed with cell suspension

Another method to measure the SERS of cells is to mix colloidal Au with the cell suspensions in buffer. In this way, the Au NPs aggregate in the buffer and also are adsorbed onto the cell surface. Some of the NPs enter into cells by endocytosis. The mixture is centrifuged down and the cell pellet is used for the Raman experiment. Figure 9-7 shows the results of the three types of cells and Table 9-2 lists the assignment of the major peaks according to reference (29-32). One issue need to be pointed out is that the ratio of the cell numbers and the Au NPs amount determine the intensity of the observed signals. Too much Au NPs give mostly citrate signals and too many cells give too weak

SERS signals to be detected. Figure 9-7 is the optimum signals obtained. From Figure 9-7 we can see that the 1263 cm-1 peak (tyr) in HOC is very strong while it is absent in HaCat and HSC cells. The largest difference is due to the two peaks at 1546 (trp) and 1586 (trp, phe) cm-1. The intensity ratio of the 1546 cm-1 to 1586 cm-1 is in the following order: HOC > HSC > HaCat. This might be a fingerprint for differentiation of the three cells from.

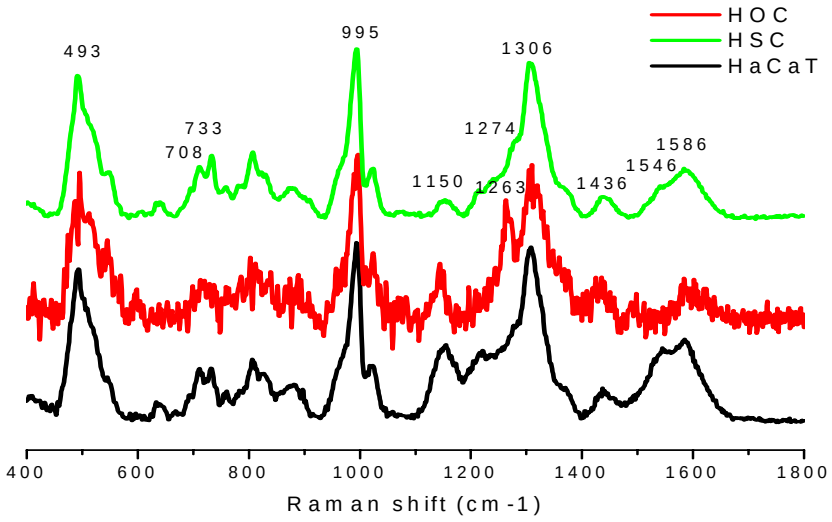

Figure 9-7: SERS of cell pellets with Au NPs mixed.

Table 9-2: Peak assignments of the bands in Figure 9-7 according to references (29-32).

493: Au-S	1263: tyr and/or citrate
708: trp	1306: phe, try, trp
733: cys	1436: phe
995: Phe	1546: trp
1150: trp	1586: trp, phe

9.3.4 SERS using gold nanoarray

The reason we use array is try to see anti-EGFR SERS signals. We have tried to bind anti-EGFR antibodies onto the Au nanosphere solution and did not see the antibody

signals due to the interference from the strong citrate signals. So it is better to use nanoarray since the gold nanoparticles are made without capping materials under the method of nanosphere lithograpy on a quart substrate. These adsorbed molecules onto the surface of the nanoprisms would give strong Raman signals. We have tried different molecules and also cells grown and dropped onto the array surface. Figure 9-8 is SERS of the mercaptoacetic acid chemically adsorbed onto the Au array.

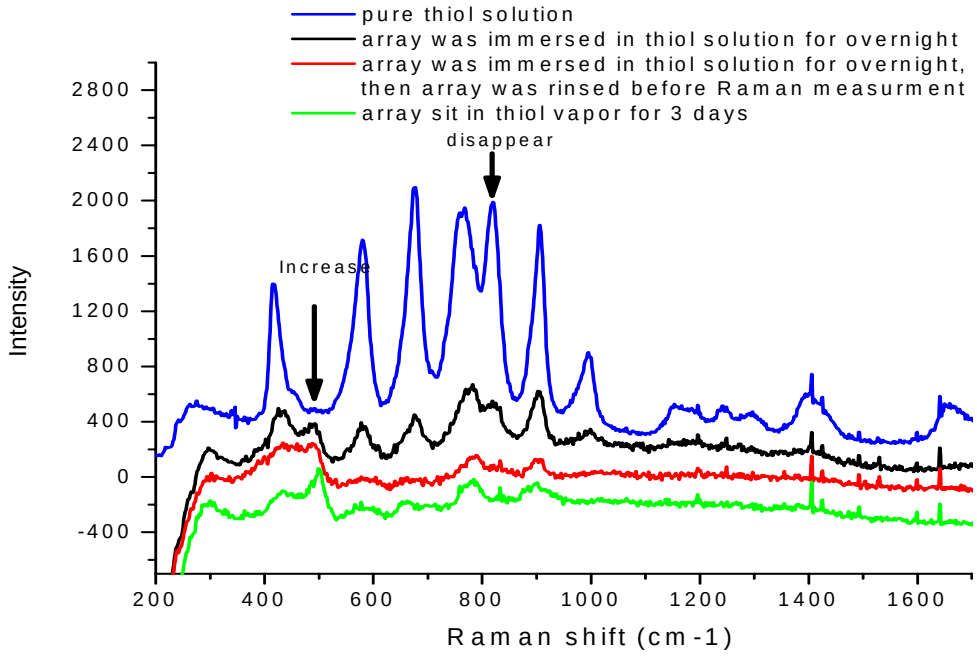

Figure 9-8: SERS of the mercaptoacetic acid adsorbed onto the Au array.

The mercaptoacetic acid (MPA) is chemically bound to the Au surface via Au-S bound and thus strongly enhanced by the Au nanoarray. Even the Au nanoarray is exposed to the vapor of the acids, the thiol molecules will be adsorbed onto the Au array and strong Raman peaks are observed.

After MPA are adsorbed onto Au surface, anti-EGFR antibodies are adsorbed onto the MPA surface by electrostatic interaction between the negatively charged acid surface on

the MPA and the positively charged antibodies. The Raman spectra after addition of antibodies are shown in Figure 9-9. From this Figure, it can be seen that there is no more peaks observed after addition of the antibodies. The increase of the intensity around 954 cm^{-1}, 676 cm^{-1}, 800 cm^{-1} and 1138 cm^{-1} may also indicate the antibody signals, but it is weak and can not be confirmed. This might be because the antibody molecules are far away from the Au surface and thus they are not enhanced. Thus we tried to directly put the antibodies onto the array surface and Raman signals are observed.

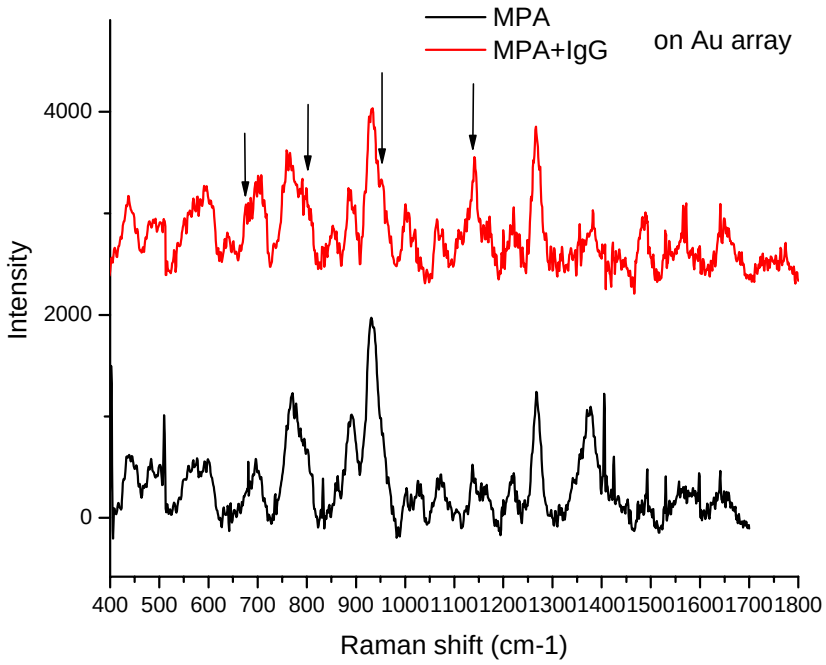

Figure 9-9: SERS of mecaptoacidic acid as well as after addition of anti-EGFR antibodies.

Figure 9-10 shows the Raman spectrum of antibodies on the Au array. From Figure 10 we can see that some peaks such as 674 cm^{-1}, 1150 cm^{-1} and 1264 cm^{-1} showed up after addition of antibodies, which indicate the signals from antibody. The array is immersed into the antibody solution (10 μM) overnight. So the antibody is adsorbed onto

the Au array by some chemical bounds and physical adsorption between the amino acids on the antibodies and the Au surface.

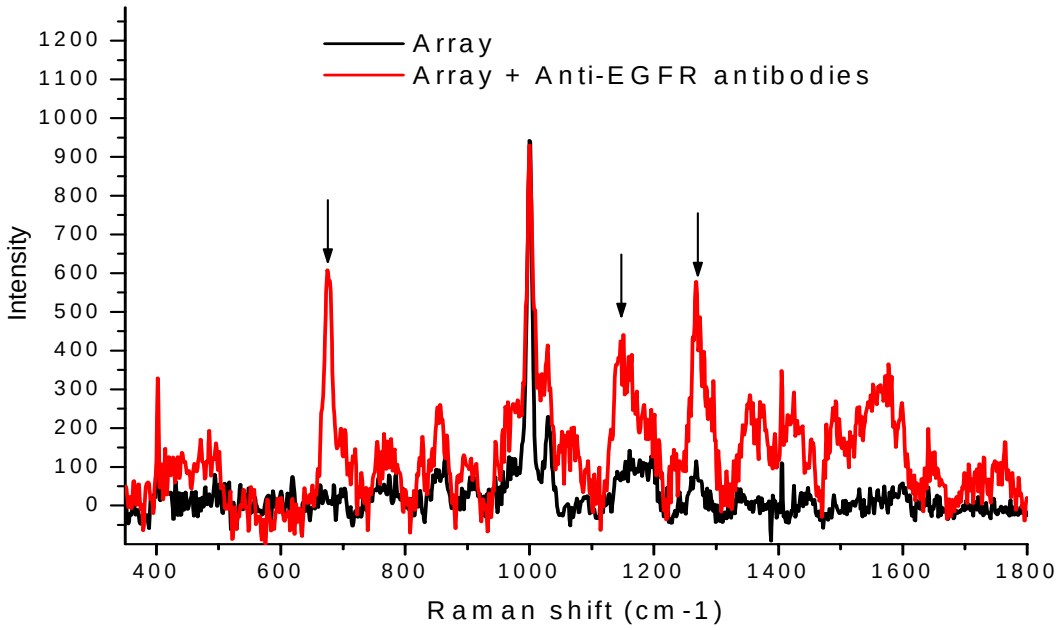

Figure 9-10: The SERS of antibodies on the Au array. The background signals from array itself are also shown for comparison.

9.3.5 SERS of R6G dye using gold nanorod film

To obtain the SERS of the antibodies, gold nanorods are also used. In this method, gold nanorods film is prepared on quartz plates. To test the SERS of the rod film, R6G molecules are drop added onto the film and Raman spectrum are measured. I used R6G because the molecules would not evaporate when they are dropped onto the film and also many people use R6G as a test of Raman enhancement. Figure 9-11 shows the Raman spectra of the Rods themselves and the rods with different concentration of R6G adsorbed.

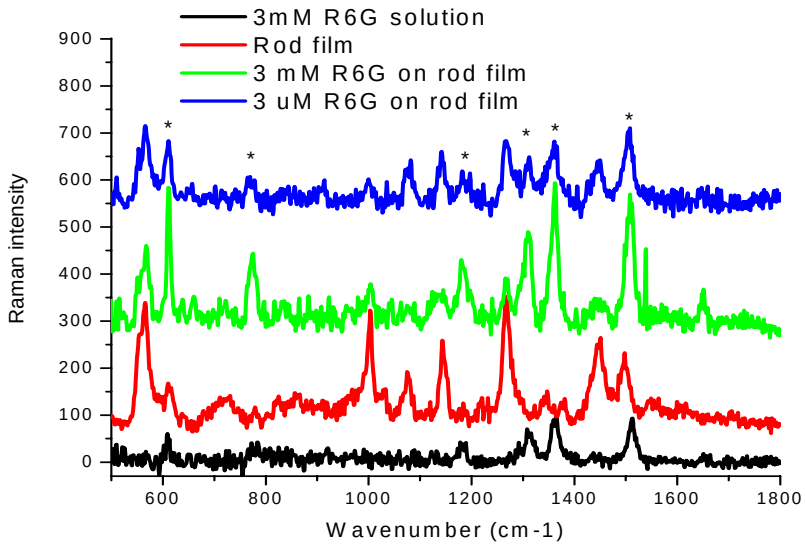

Figure 9-11: The SERS of R6G on Au nanorods film.
*: R6G signals enhanced by the gold nanorods.

In Figure 9-11 green and blue curves show the Raman signals of R6G on the rod film. The 3mM R6G in ethanol is checked for comparison. It can be seen that the Raman intensity of 3mM R6G on nanorods is much stronger than that of 3mM R6G film. When the R6G concentration decreased to 3 μm, the R6G signals are still strong and the intensity is similar to the 3mM R6G film. So the nanorods definitely enhanced the R6G signals. Compared to literature using gold nanospheres (33), which hardly give signals when R6G increased to 10^{-6} M, the rod film give much better enhancement.

Then Bovine Serum Album molecules are drop added onto the rod film to see if the rod can enhance the Raman signals of big biomolecules. 15 μM BSA are added onto rod film and let it sit for 4h before checking Raman signals. The Raman signal is shown in red in Figure 9-12. Compared to the Rod film itself shown in black at the bottom, it seems some very weak peaks are observed such as the peak at 1426 cm-1. To see if these peaks are from BSA protein, the concentration of the BSA and the time of the Rod film

immersed into the protein solution are increased. When the rod film is immersed in the BAS solution for overnight in 5 mg/mL (75 μM) concentration, some new peaks are obvious: 500cm-1, 550cm-1, 890 cm-1, 960 cm-1 and 1426 cm-1. To immerse the rod film into the BSA at 10mg/mL for 3 days, these peaks slightly increased. It indicates that after overnight incubation, the absorption of BSA onto rod film is saturated. The peak at 500 cm-1 is from phe Au-N bond and 550 cm-1 is from tryp Au-N bond.

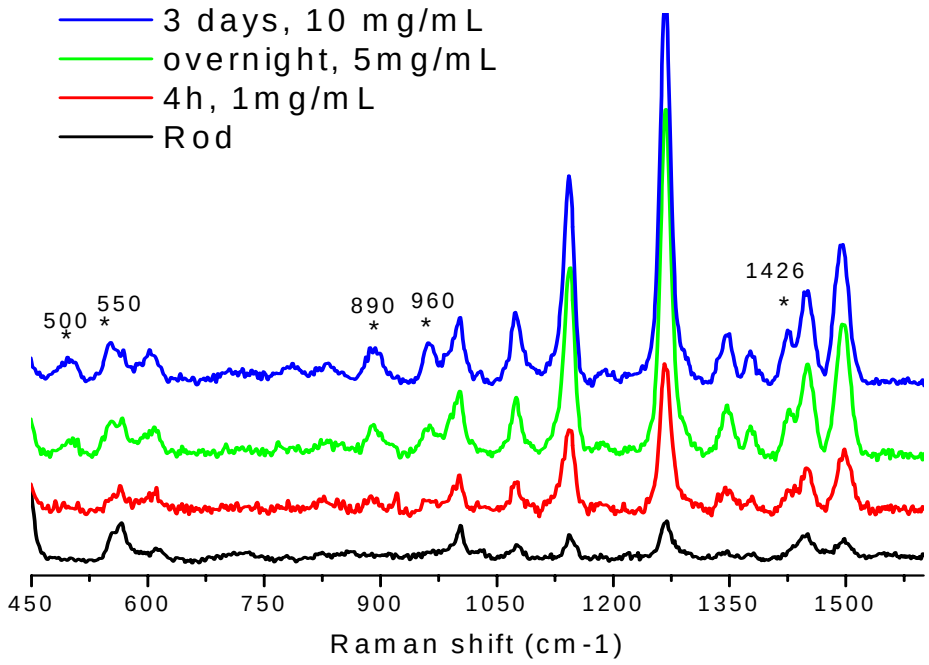

Figure 9-12: Surface Enhanced Raman Shift of bovine serum album on gold nanorod film. *: R6G signals enhanced by the gold nanorods. The nanorods are capped with CTAB.

This is first time that large protein SERS is observed on gold nanorod films. So this means that if cells can be ruptured (just by immerse the cells into water, the membrane ruptures and the nucleaus and proteins inside cells can flow out), the Raman signals of the protein and DNA could be enhanced by the rod film. In this way, the data will be very reproducible because the rods form a monodispersed film. They are not aggregates. I

have tested that from different spots of a nanorod film, the signals from both capping materials and adsorbed moelucles (R6G and BSA), they are almost the same. And also the signals do not change upon laser exposure. In addition, the anti-EGFR antibody SERS on the nanorods film should also be detected. But unfortunately, the Raman instrument is broken and the antibody Raman experiment can not be done.

9.4 References

(1) Lord, R.C.; Yu, N.T. *J Mol Biol.* **1970**, 50(2), 509.

(2) Hanlon, E. B.; Manoharan, R.; Koo, T. W.; Shafer, K. E.; Motz, J. T.; Fitzmaurice, M.; Kramer, J. R.; Itzkan, I.; Dasari, R. R.; Feld, M. S. *Phys. Med. Biol.* **2000**, *45* R1.

(3) Nabiev, I.; Chourpa, I.; Manfait, M. *J. Raman. Spectro*. **1994**, *25*, 13.

(4) Fleischman, M.; Hendra, P. J.; Mcquillan, A. J. *J. Chem. Soc., Chem. Commun*. **1973**, 80.

(5) Jeanmaire, D. L.; Van Duyne, R. P. *J. Electroanal. Chem*., **1977**, *84*, 1.

(6) Albercht, M. G.; Creighton, J. A., *J. Am. Chem. Soc*., **1977**, *99*, 5215.

(7) Kneipp, K.; Kneipp, H.; Itzkan, I.; Dasari, R. R.; Feld, M. S. *Chem. Rev*. **1999**, *99***,** 2957.

(8) Cardona, M.; Guntherodt, G. Eds, *Light Scattering in Solids IV*, Springer-Verlag, Berlin, Germany, **1984**.

(9) Moskovits, M. *Rev. Mod. Phys*. **1985**, *57***,** 783.

(10) Kneipp, K. *Experimentelle Technik der Physik* **1990**, *38***,** 1.

(11) Campion, A.; Kambhampati, P. *Chem. Soc. Rev*. **1998**, *27***,** 241.

(12) Kneipp, K.; Wang, Y.; Kneipp, H.; Perelman, L. T.; Itzkan, I.; Dasari, R. R.; Feld, M. S. *Phys. Rev. Lett*. **1997**, *78***,** 1667.

(13) Kneipp, K.; Kneipp, H.; Itzkan, I.; Dasari, R. R.; Feld, M. S. *Proc. SPIE-Int. Soc. Opt. Eng.* **2001,** *4258***,** 50.

(14) K. Kneipp, H. Kneipp, V. B. Kartha, R. Manoharan, G. Deinum, I. Itzkan, R. R. Dasari, and M. S. Feld, Phys. Rev. E: Stat. Phys., Plasmas, Fluids, Relat. Interdiscip. Top. **57,** R6281 (1998).

(15) Kneipp, K.; Kneipp, H.; Deinum, G.; Itzkan, I.; Dasari, R. R.; Feld, M. S. *Appl. Spectrosc*. **1998**, *52***,** 175.

(16) Koglin, E.; Sequaris, J. M. *Top. Curr. Chem*. **1986**, *134*, 1.

(17) Cotton, T. M. *In Surface and Interfacial Aspects of Biological Polymers*, edited by J. Andrade, Vol.2, Plenum Press, New York, **1985**.

(18) Cotton, T. M. *In Spectrocopy of Surfaces*, edited by R.J.H. Jek and R.E. Hester, PP91-153. Wiley, New York, **1988**.

(19) Cotton, T. M.; Kim, J. M.; Chumanov, G. D. *J Raman Spectroscopy*, **1991**, *22*, 729.

(20) Nabiev, I.; Efremov, R. G.; Chumanov, G. D. *Sov. Phys*. **1988**, *31*, 241.

(21) Manfait, M.; Morjani, H.; Millot, J. M.; Debal, V.; Angiboust, J. F.; Nabiev, I. *Proc. SPIE-Int. Soc. Opt. Eng*. **1990**, *1403***,** 695.

(22) Manfait, M.; Morjani, H.; Nabiev, I. *J. Cell. Pharmaco*. **1992**, *3***,** 120.

(23) Nabiev, I.; Morjani, H.; Manfait, M. *Eur. Biophys. J*. **1991**, *19***,** 311.

(24) Morjani, H.; Riou, J. F.; Nabiev, I.; Lavelle, F.; Manfait, M. *Cancer Res.* **1993**, *53***,** 4784.

(25) Kneipp, K.; Haka, A. S.; Kneipp, H.; Badizadegan, K.; Yoshizawa, N.; Boone, C.; Shafer-Peltier, K. E.; Motz, J. T.; Dasari, R. R.; Feld, M. S. *Appl. Spectrosc.* **2002**, *56(2),* 150.

(26) Kneipp, J.; Kneipp, H.; Rice, W. L.; Kneipp, K. *Anal. Chem.* **2005**, *77*, 2381.

(27) Suzuki, M.; Niidome, Y.; Terasaki, N.; Kuwahara, Y.; Inoue, K.; Yamada, S. *Jpn. J. Appl. Phys.* **2004**, *43*, L554.

(28) Kerker, M.; Siiman, O.; Bumm, L. A.; Wang, D.-S. *Applied Optics* **1980**, *19 (19)*, 3253.

(29) Keipp, K.; Pohle, W.; Fabian, H. *J. Molecu. Struc*. **1991**, *244*, 183.

(30) Rava, R. P.; Spiro, T. G. *J. Phys. Chem*. **1985**, *8*9, 1856.

(31) Vidugiris, G.-J. A.; Gudavicius, A. V.; Razumas, V. J.; Kulys, J. J. *Eur. Biophys. J.* **198**9, *17*, 19.

(32) Stewart, S.; Fredericks, P. M. *Spectrochimica Acta Part A* **199**9, *55*, 1641.

(33) Suzuki, M.; Niidome, Y.; Kuwahara, Y.; Terasaki, N.; Inoue, K.; Yamada, S. *J. Phys. Chem. B* **2004**, *108*, 11660.

CHAPTER 10
NUCLEUS TARGETING OF GOLD NANOPARTICLES BY SONICATION METHOD AND INTRACELLULAR FORMATION

Abstract

Gold nanoparticles are targeted into the nucleus of humam epithelial HaCat cells by the sonication after incorporation of the nanoparticles inside cytoplasm by incubation of the nanoparticles in the cell medium during the cell growth process. In addition, gold nanoparticles are formed inside both nucleus and cytoplasm part of the cells by the reduction of auric acid with the cellular reducing proteins. The gold nanoparticles formation inside cells are more efficient by using the paraformaldehyde or glycerol reducing agents after the accumulation of gold ions inside cells. Light scattering imaging and micro-absorption spectroscopy are used to identify the nanoparticles in the cells.

10.1 Introduction

Nuclea rtarget of nanoparticles is very important because of the genetic information inside nucleus (1, 2). But nuclear targeting is a difficult task because the nanoparticles have to pass both cytoplasmic membrane and the nuclear membrane. Most of studies of intracellular tracking by metal, semiconductor and polymer nanoparticles are on the cytoplasmic entry (3-6). Some studies realize nuclear targeting by microinjection or chemical modification of cells (7, 8).

Feldheim et al. (9, 10) have tried to use several different peptides to modify gold nanoparticles and found that the nanoparticles modified with peptide from both adenovirus RME and adenovirus NLS went into nucleus efficiently when they are incubated with intact HepG2 cells in the cell culture medium (See Figure 10-1).

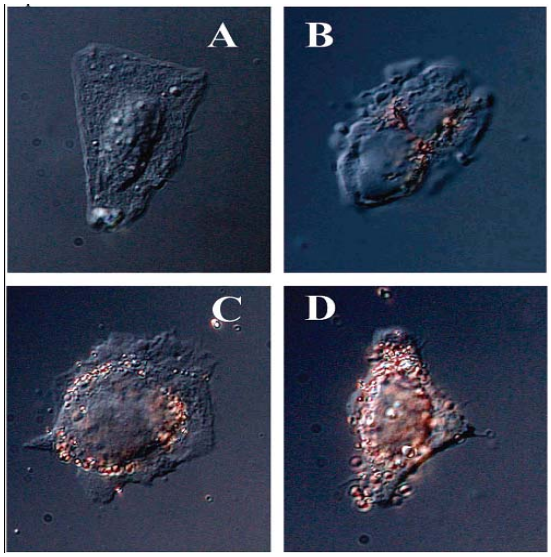

Figure 10-1: Nanoparticle-peptide complexes incubated with HepG2 cells for 2 h: #2 (A), #3 (B), #4 (C), and #2/#3 (D).
1: CGGGPKKKRKVGG, origin: SV40 large T NLS;
2: CGGFSTSLRARKA, origina: adenoviral NLS;
3: CKKKKKKSEDEYPYVPN, origina: adenoviral RME;
4: KKKKKKKSEDEYPYVPNFSTSLRARKA, origina:adenoviral fiber protein. (8).

In our work, when we incubate colloidal gold nanoparicles with cells in the cell culture medium, the majority of nanoparticles go into the cytoplasm of the cells which are identified by the light scattering imaging. It is well known that nanoparticles can also enter into cells by sonication which ruptures the cell membrane and then the membrane will be recovered after the nanoparticle entry. Thus from this idea, it is interesting to see if nanoparticles can go into the nucleus by the sonication if the nanoparticles are already present inside the cytoplasm of the cells. By the sonication, the nucleus membrane may also rupture and allow nanoparticle incorporation.

In addition, recent reports have shown that gold and silver nanoparticles can be formed inside cells by mixing the auric acid or silver nitrate solution with the cell suspension (11-17). As shown in Figure 10-2 when auric acid is added to the bacteria biomass, the Au nanoparticles are formed after 24 hours. The particles distribute inside both cytoplasmic and nuclear part of the cells (Figure 10-3). In this manner, the nanoparticles can be directly formed inside the nucleus. In our work, we try the method for incubation the nanoparticles inside the nucleus of both cancer and healthy human cells.

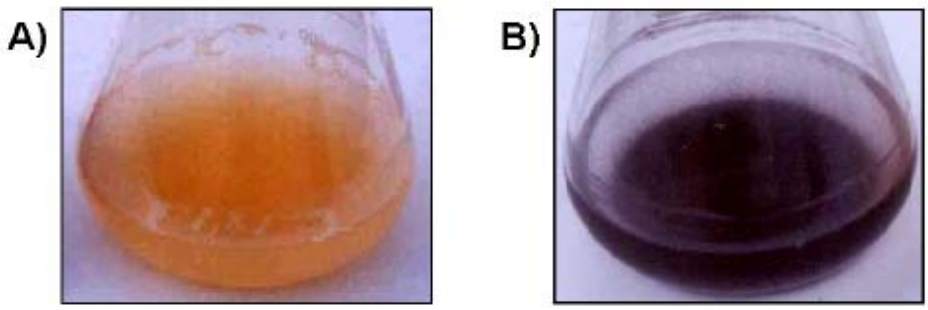

Figure 10-2: (A) *Rhodococcus* sp. biomass after removal from the culture medium. (B) *Rhodococcus* sp. actinomycete cells after exposure to 10−3 M aqueous solution HAuCl4 for 24 h.

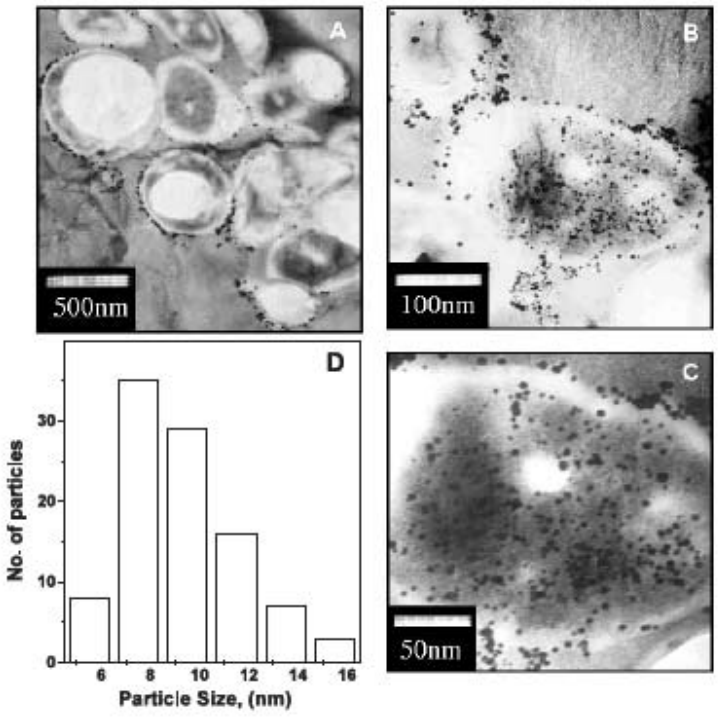

Figure 10-3: (A)–(C) Representative TEM micrographs recorded at different magnifications from thin sections of stained *Rhodococcus* cells after reaction with AuCl−4 ions for 24 h. (D) A particle size distribution histogram determined from the TEM micrograph shown in figure 3(C).

10.2 Experimental

15 nm gold nanoparticles are added to the DMEM cell culture medium and incubated with cells in culture dishes for 2 days. Then the cells is cleaved with trypsin and dispersed in DMEM in the centrifuge tube and carried to our lab for sonication. The sonication time is 20s, 40s and 60 s to see find out the best time for the nuclear entry of the nanoparticles. In too long time the cells might be killed due to the rupture of the membrane and too short time the nanoparticles entry might not be efficient. Right after

sonication, the cells are taken back and replated onto cover slips and let them grow at least for 4 hours. Then the cells are fixed and sealed and used for dark field imaging.

To try to see the distribution of small nanoparticles (3nm), nanoparticles are made by the reduction of auric acid using NADH solution. These small nanoparticles are tried because they might directly penetrate into nucleus due to their small sizes. Equal amount of NADH solution (10 mM) and auric acid (5 mM) are mixed together. The solution became dark red immediately. The nanoparticles are left sit overnight to allow for the complete capping of the nanoparticles, probably by NAD^+. The absorption spectrum show that the nanoparticles have an absorption maximum at 523 nm and the TEM show that the nanoparticles are about 3 nm (Figure 10-4). If the nanoparticles are allowed to sit for longer time, the absorption maximum red shifted about several nanometers due to the aggregation and growing of the nanoparticles.

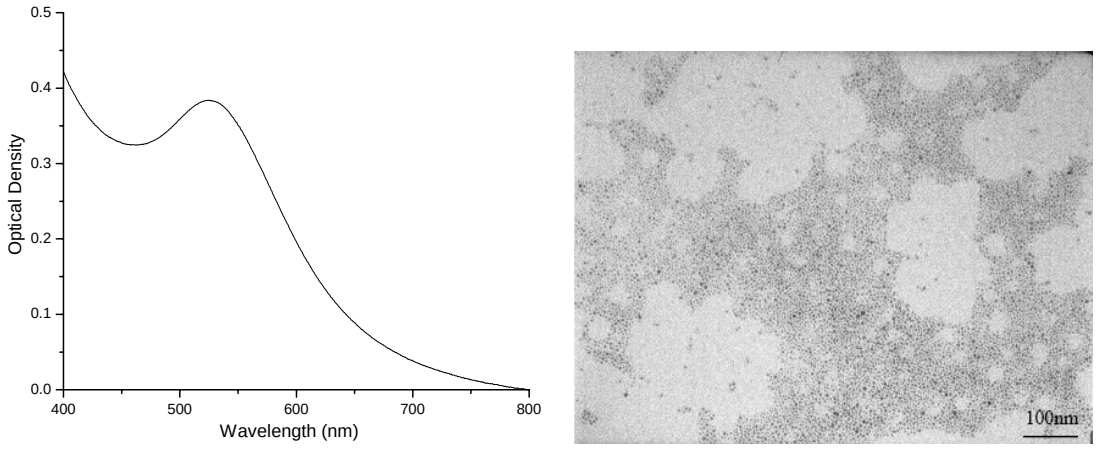

Figure 10-4: Absorption and TEM of NADH made Au nanoparticles.

The intracellular formation of Au nanoparticles are carried out according to the method by Pradeep et al (11) who synthesizes Au nanoparticles inside human cells. Briefly, the

cells are grown on cover slips for 3 days. Then the medium are rinsed out and immersed with DPBS buffer with 1 mM auric acid. The cells with 1mM auric acid in the buffer are put back in the incubator for 7 days. The cells are then taken out and fixed and used for micro-absorption spectrum measurement and dark field imaging.

10.3 Results and discussion

10.3.1 Nucleus entry of gold nanoparticles by sonication

According to our previous experience, gold nanoparticles go mostly into cytoplasma portion of the cells. We do not see much or did not see at all gold nanoparticles inside nucleus. One simple experiment is to sonicate the cells after incubation of gold nanoparticles. Figure 10-5 shows the comparison before and after sonication for 40s.

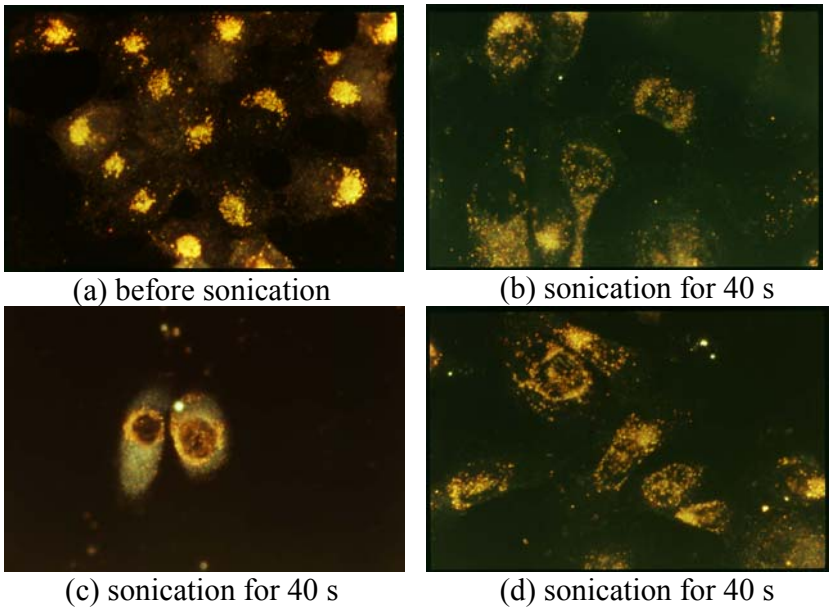

(a) before sonication (b) sonication for 40 s

(c) sonication for 40 s (d) sonication for 40 s

Figure 10-5: Comparison of gold nanoparticles inside cells without (a) and with sonication (b), (c), and (d).

From this Figure it can be seen that before sonication, the nanoparticles aggregate together and are located in someplace inside the cytoplasm. After sonication, the nanoparticles are more dispersed and widely distributed everywhere in the cytoplasm (b), (c) and (d). Also they are located inside the nucleus. The cells are viable after sonication and continue to grow in the growth medium and in the incubator.

Another interesting experiment is to incubate NADH made Au nanoparticles with cells. Au nanoparticles of different sizes can be prepared by reduction of NADH. No citrate is required to cap the nanoparticles. So NAD^+ must cap the nanoparticles and the nanoparticles are very stable up to several weeks. Since NADH and NAD+ are more biocompatible and also NADH made Au nanoparticles do not aggregate in buffer, so the nanoparticle distribution must be different from the colloidal citrate capped nanoparticles. The light scattering pictures and micro-absorption spectra after incubation with NADH to make gold nanoparticles are shown in Figure 10-6.

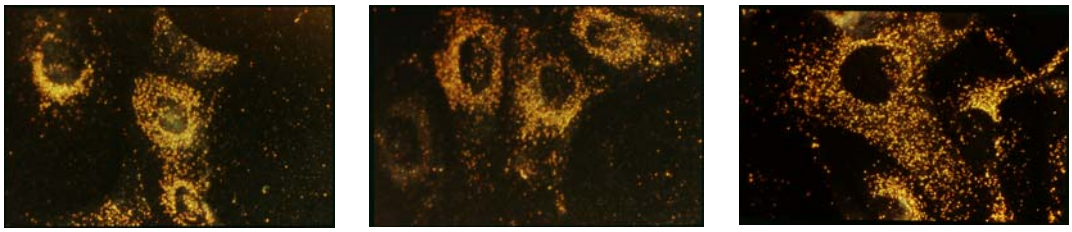

(a) (b) (c)

Figure 10-6: Au NPs made by the NADH reduction incubated into cells. Au nanoparticles are distributed homogeneously inside cytoplasm of the cells. Some Au nanoparticles go into nucleus (a).

Compared to the colloidal nanoparticles, it can be seen that the nanoparticles are homogenously distributed inside the cytoplasm part of the cells and the dark nucleus can be clearly seen. In this picture, the nanoparticles are about 30nm because the

nanoparticles are aged for 3 days after preparation. From the picture (a) it can be seen that some of nanoparticles went into nucleus. Compared to the citrate made Au nanoparticles, the NADH made nanoparticles do not aggregate. So the monodispersed NADH made nanoparticles went into cells more easily than the aggregated citrate made nanoparticles.

10.3.2 Nucleus entry of gold nanoparticles by intracellular formation

Recently it has been reported that gold nanoparticles can be formed inside cancer and noncancer human cells by adding auric acid in the buffer solution (11). We follow this method for the HaCat healthy cells. In order to imaging cells, the cells need be taken out and sealed with another coverslips. So fixation and glycerol are needed for general procedures. But unfortunately, fixation solution-paraformaldehyde and glycerol are both reductive and so they might reduce Au^{3+} inside the cells and form gold nanoparticles. Thus a series of experiments are carried out to exam this possibility. The data are shown in Figure 10-7.

Figure 10-7 (A) is the image of the cells incubated only with 1mM auric acid for 7 days and taken out of incubator and imaged immediately. No paraformadehyde or glycerol is used. Figure 10-7 (B) is the image of the cells incubated with 1 mM auric acid for 2 days and then paraformaldehyde is used to fix the cells and then wait for 2 days for cell imaging. So only paraformaldehyde is used. Figure 10-7 (C) is the image of the cells incubated with 1 mM auric acid for 2 days and then paraformaldehyde is used to fix the cells, glycerol is used to seal the cells and then wait for 2 days for cell imaging. So both paraformaldehyde and glycerol are used. From these pictures we can see that if

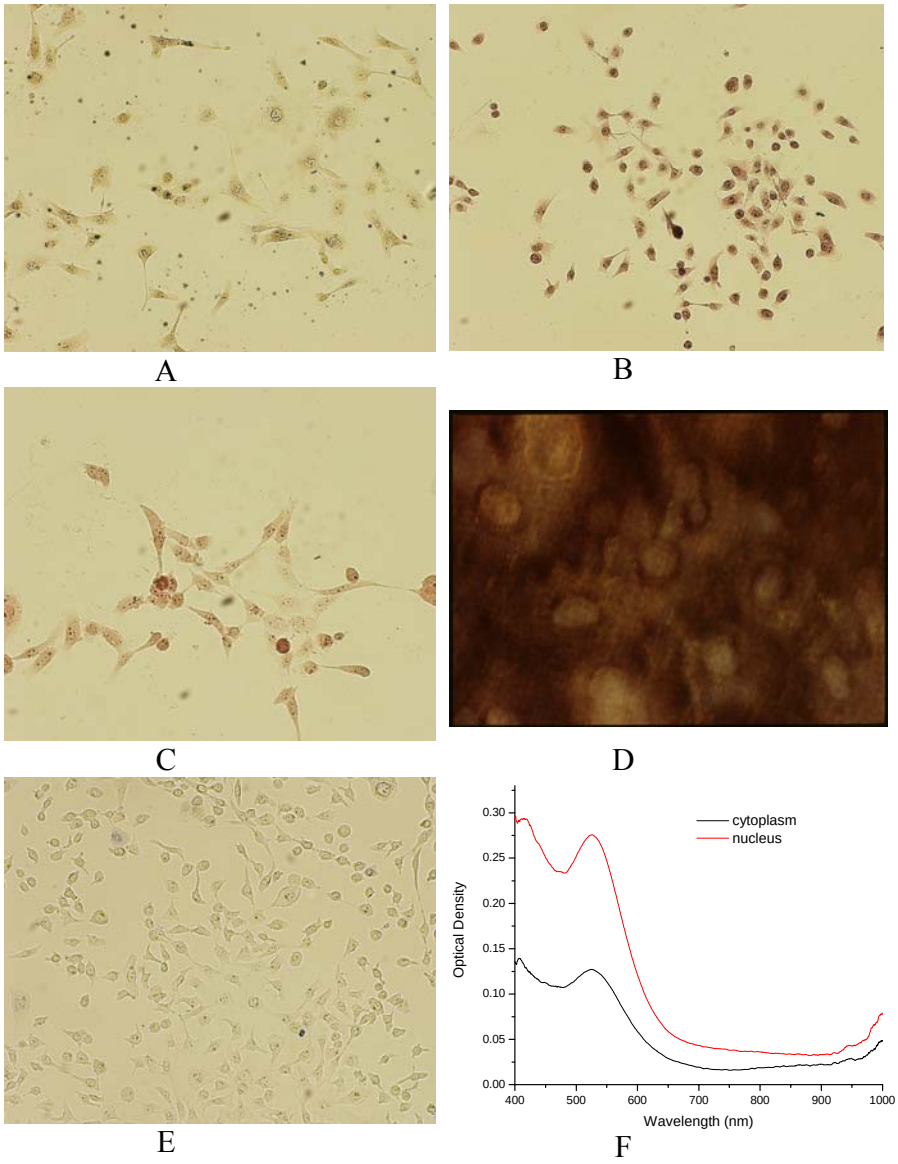

Figure 10-7: Au nanoparticles formation inside the cells. A: Cells incubated with 1 mM Au^{3+} for 6 days and take out for bright field imaging immediately. B: Cells incubated with 1 mM Au^{3+} for 2 days, them take out fixed with paraforaldehyde and sealed with water and measured their bright field images; C: Cells incubated with 1 mM Au^{3+} for 2 days, then take out fixed with paraforaldehyde and sealed with glycerol and then imaged. D: the light scattering image of D; E: cells without auric acid; F: the micro-absorption spectra of Au NPs from nucleus and cytoplasm of a typical single cell in sample C.

paraformaldehyde and glycerol are used, a lot of gold nanoaprticles are formed (red color in the bright field images), but if no paraformaldehyde and glycerol are involved, it is hard to see nanoparticles (Figure 10-7(A)). The cells look more yellowish, which means that a lot of Au^{3+} ions are accumulated inside cells (at Au^{3+} ion solution is yellow). Only under dark field, some gold nanoparticles can be seen inside cells (Figures not shown). So it means that gold nanoparticles can be formed inside cells by the cellular reducing agents. By using paraformaldehyde and glycerol, the Au^{3+} ions inside cells are reduced very quickly to forma nanoparticles. But the nanoparticles must be very small because they can not be identified under dark field. The absorption spectra show that the nanoparticles amount inside nucleus is almost double those in the cytoplasmic portion. This indicates that Au^{3+} contents ($AuCl^{4-}$ actually) are much higher inside nucleus than that in the cytoplasm.

10.4 References

(1) Kole, R.; Sazani, P. *Curr. Opin. Mol. Ther.* **2001**, *3*, 229.

(2) Bilbao, G.; Gomez-Navarro, J.; Curiel, D. In *Targeted Adeno*V*iral Vectors for Cancer Gene Therapy*; Walden, P., et al., Eds.; Plenum Press: New York, **1998**; Vol. 57, pp 365-374.

(3) West, J.; Halas, N. *Curr. Opin. Biotechnol.* **2000**, *11*, 215.

(4) Hogemann, D.; Ntziachristos, V.; Josephson, L.; Weissleder, R. *Bioconjugate Chem.* **2002**, *13*, 116.

(5) Bruchez, M.; Moronne, M.; Gin, P.; Weiss, S.; Alivisatos, A. *Science* **1998**, *281*, 2013.

(6) Liu, J.; Zhang, Q.; Remsen, E.; Wooley, K. *Biomacromolecules* **2001**, *2*, 362.

(7) Marinakos, S. M.; Anderson, M. F.; Ryan, J.; Martin, L. D.; Feldheim, D. L. *J. Phys. Chem. B* **2001**, *105*, 8872.

(8) Feldherr, C.; Lanford, R.; Akin, D. *Proc. Natl. Acad. Sci. U.S.A.* **1992**, *89*, 11002.

(9) Tkachenko, A. G.; Xie, H.; Coleman, D.; Glomm, W.; Ryan, J.; Anderson, M. F.; Franzen, S.; Feldheim, D. L. *J. AM. CHEM. SOC.* **2003**, *125*, 4700.

(10) Tkachenko, A. G.; Xie, H.; Liu, Y.; Coleman, D.; Ryan, J.; Glomm, W. R.; Shipton, M. K.; Franzen,S.; Feldheim, D. L. *Bioconjugate Chem.* **2004,** *15,* 482.

(11) Anshup; Venkataraman, J. S.; Subramaniam, C.; Kumar, R. R.; Priya, S.; Kumar, T. R. S.; Omkumar, R. V.; John, A.; Pradeep, T. *Langmuir,* ASAP.

(12) Mukherjee, P.; Ahmad, A.; Mandal, D.; Senapati, S.; Sainkar, S. R.; Khan, M. I.; Ramani, R.; Parischa, R.; Ajayakumar, P. V.; Alam, M.; Sastry, M.; Kumar, R. *Angew. Chem. Int. Ed*. **2001**, 40(19), 3585.

(13) Ahmad1, A.; Senapati, S.; Khan, M. I.; Kumar, R.; Ramani, R.; Srinivas, V.; Sastry, M. *Nanotechnology* **2003**, *14*, 824.

(14) Mukherjee, P.; Senapati, S.; Mandal, D.; Ahmad, A.; Khan, M. I.; Kumar, R.; Sastry, M. *ChemBioChem* **200**2, *5*, 461.

(15) Sastry, M.; Ahmad, A.; Khan, M. I.; Kumar, R. *CURRENT SCIENCE*, 2003, 85 (2), 162.

(16) Mukherjee, P.; Ahmad, A.; Mandal,D.; Senapati, S.; Sainkar, S. R.; Khan, M. I.; Parishcha, R.; Ajaykumar,|P. V.; Alam, M.; Kumar, R.; Sastry, M. *Nano Lett.,* **2001**, *1* (10), 515.

(17) Ahmad, A.; Mukherjee, P.; Senapati, S.; Mandal, D.; Khan, M. I.; Kumar, R.; Sastry, M. *Colloids and Surfaces B: Biointerfaces* **2003**, *28*, 313.